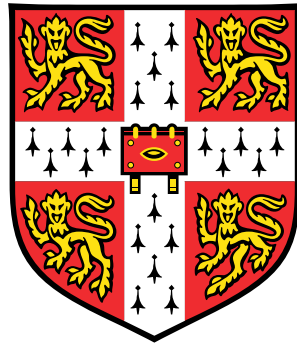


Physical Insights of Non-Premixed MILD Combustion using DNS



Nguyen Anh Khoa Doan

Department of Engineering
University of Cambridge

This dissertation is submitted for the degree of
Doctor of Philosophy

To all my friends, still present or not, here and everywhere, and to my family

Declaration

I hereby declare that except where specific reference is made to the work of others, the contents of this dissertation are original and have not been submitted in whole or in part for consideration for any other degree or qualification in this, or any other university. This dissertation is my own work and contains nothing which is the outcome of work done in collaboration with others, except as specified in the text and Acknowledgements.

This dissertation contains approximately 62000 words, 82 figures and 12 tables.

Nguyen Anh Khoa Doan
September 2018

Acknowledgements

I would like to express my gratitude to the numerous people I have met and who have, in one way or another, supported me during this PhD journey. Without them, I would probably not have made it to the end with my sanity (more or less) intact. The few words written here will never be enough to express their importance to my life in Cambridge and the influence they have had on me.

First, I would like to thank Prof. Swaminathan for taking me as his PhD student and for his continuous guidance throughout my PhD. His constant availability and patience have proven to be invaluable. I have learned a lot through our many discussions and he managed to not make me quit academia for which I will be forever grateful. Mr. Benie also receives my thanks for helping me set up and maintain my huge workstation, **charden**. I would also like to acknowledge the (remote) help of Yuki Minamoto. Having inherited his pile of "crap" as he likes to call it, his assistance was extremely useful for starting this PhD.

I am also particularly grateful to all my friends from Division A and the (too social) Hopkinson Lab for their company and friendships. From ISO-15, Phil will always be remembered fondly for our shared love of fine food (and for occasionally feeding me); Golnoush also receives my thanks for helping me discover the limits of my patience and also for having, as my desk neighbour, stood up with me; The many discussions I have had with Zhi about science or academic life in general have also been greatly appreciated; Despite the fact that it took Ivan one year to start talking to me, his sense of independence has been a source of inspiration and I also thank him for allowing me to share the paternity of our joint LD-D model. Finally, the support of Pedro (through his coffee and hipsterness) and Steve (as a desk neighbour) were greatly appreciated.

Prior to sitting in ISO-15, I also had the chance to share the same office as Nick (my favourite aussie), Richard (forever remembered as the founding president of the CUBS) and Rob (the least PC Canadian I have ever met) who all have my gratitude for making the "graveyard" a bit less of an actual graveyard. The advice and many discussions about science, life and the why of the universe, I have had with our senior postdocs, Andrea and Luca, are also particularly appreciated. Luca in particular has all my thanks for the opportunity and trust he has given me. Over the last period of my PhD, the (not so new) newcomers of the Hopkinson Lab, in particular Hans and Ingrid, also have my

thanks for keeping that time interesting and eventful. Alessandra's friendship has also been a most appreciated late surprise to my time in Cambridge.

From Darwin and since the very first week of my PhD, I have had the chance to meet amazing people among whom Amani will always be remembered fondly for her continuous motherly kindness. Fabio and Adam are also thanked for our geek Star Wars related discussions. During my time in Darwin, the company and friendship of Ann and Wojtek, members of our FoF's group, has also been greatly appreciated.

Priyanka and Harika deserve some special thanks for making my life in Cambridge so unpredictable. Priyanka's spontaneity has been a constant source of wonder and inspiration and Harika's company at all those classical concerts was greatly enjoyed.

A few people have truly been invaluable to me during my time in Cambridge for which they receive my most sincere gratitude. In alphabetical order:

Anjali has been my most steadfast lunch and coffee break companion and also an amazing friend ever since the very beginning of our PhDs.

Avnita has been of special support to me during my first year in Cambridge. Despite whatever she said, she is a wonderful person who taught me much more than what she thinks and made my life full of tea at all time of the day and night.

Francesca has been a constant source of wonder and support by her true and sincere understanding of me. She has also constantly inspired me to do better and I would not have achieved half as much without her presence.

Nabil has been a long-time companion in my studies, without whom I would not have made it to Cambridge. His friendship has been and still is a constant source of support, for work and all the rest.

Finally, the support of my family, my parents, sisters and brother and their occasional visits have also been of particular importance to me.

The Qualcomm European Research Studentship, Darwin College, the UKCTRF, the Combustion Institute, the British Section of the Combustion Institute, EPSRC and SIAM are acknowledged for their financial support. EPSRC and EPCC are also acknowledged for recognising this work by awarding me the "Best Use of ARCHER award". This work used the ARCHER UK National Supercomputing Service (<http://www.archer.ac.uk>) using CPU time provided by EPSRC under the project number e419 and by the UKCTRF (e305). I would like to thank M. Yokokawa, T. Ishihara, K. Itakura, A. Uno, Y. Kaneda, P. K. Yeung, N. Chakraborty, M. Tanahashi and Y. Minamoto for providing the additional DNS data used in this thesis. Useful discussion with Prof. Davidson is acknowledged. Prof. Cant is also acknowledged for providing the code SENG2 used in this thesis work.

Abstract

Moderate or Intense Low-oxygen Dilution (MILD) combustion is a combustion technology that can simultaneously improve the energy efficiency and reduce the pollutant emissions of combustion devices. It is characterised by highly preheated reactants and a small temperature rise during combustion due to the large dilution of the reactant mixture with products of combustion. These conditions are generally achieved using exhaust gas recirculation. However, the physical understanding of MILD combustion remains limited which prevents its more widely spread use.

In this thesis, Direct Numerical Simulation (DNS) is used to study turbulence, premixed flames and MILD combustion to obtain these additional physical insights. In a first stage, the scale-locality of the energy cascade is analysed by applying a multiscale analysis methodology, called the bandpass filter method, on DNS of homogeneous isotropic turbulence. Evidence supporting this scale-locality were obtained and the results were found to be similar for Reynolds numbers ranging from 37 to 1131. Using the same method in turbulent premixed flames, the scale-locality of the energy cascade was still observed despite the presence of intense reactions. In addition, it was found that eddies of scales larger than the laminar flame thickness were imparting the most strain on the flame.

In a second part, a methodology was developed to conduct the DNS of MILD combustion with mixture fraction variations. This methodology included the effect of mixing of exhaust gases with fuel and oxidiser in unburnt, burnt and reacting states. In addition, a specific chemical mechanism that includes the chemistry of OH^* was developed. From these DNS, the role of radicals on the inception of MILD combustion was studied. In particular, due to the reactions initiated by these radicals, the initial temperature rise in MILD combustion was occurring concurrently with an increase in the scalar dissipation rate of mixture fraction which is contrasting to conventional combustion.

The reaction zones in MILD combustion were also analysed and extremely convoluted reaction zones were observed with frequent interactions among them. These interactions yielded the appearance of volumetrically distributed reactions. Furthermore, the adequacy of some species to identify these reaction zones was assessed and OH showed a poor

correlation with regions of heat release. On the other hand, OH^* , HCO or $\text{OH} \times \text{CH}_2\text{O}$ were found to be well correlated. Through the study of the flame index, the existence of non-premixed and premixed modes of combustion were also highlighted. The premixed mode was observed to be dominant but the contribution of the non-premixed mode to the total heat release was non negligible.

Because of the presence of radicals and high reactant temperatures, auto-igniting regions and propagating reaction zones are both observed locally. The balance between these phenomena was investigated and it was found that this was strongly influenced by the typical lengthscale of the mixture fraction field, with a smaller lengthscale favouring sequential autoignition. Finally, using the bandpass filtering method, the effect of heat release rate in MILD combustion on the energy cascade was studied and this showed that the energy cascade was not unduly affected.

Table of contents

List of figures	xv
List of tables	xxiii
Nomenclature	xxv
1 Introduction	1
1.1 Motivation	1
1.2 Background on MILD combustion	3
1.2.1 On the definitions of MILD combustion	3
1.2.2 Experimental explorations	8
1.2.3 Investigations based on laminar model reactors	12
1.2.4 Turbulent calculations	16
1.3 Outstanding issues and modelling challenges	24
1.4 Aims and objectives	26
1.5 Thesis structure	28
2 Direct Numerical Simulation	29
2.1 Governing equations	29
2.1.1 Thermodynamic and transport quantities	31
2.1.2 Reaction rate	32
2.2 Non-premixed MILD combustion	34
2.2.1 Numerical flow configuration	34
2.2.2 Generation of initial and inflow fields	35
2.2.3 Combustion mechanism	41
2.2.4 MILD combustion conditions	45
2.2.5 On the choice of laminar configuration	47
2.3 Summary	49

Table of contents

3	Multiscale Analysis of Turbulence and Premixed Flames	51
3.1	Background and objectives	51
3.2	DNS data used	52
3.2.1	Homogeneous isotropic turbulence	52
3.2.2	Turbulent premixed flames	54
3.3	Bandpass filtering method	55
3.4	Energy cascade in turbulence	57
3.4.1	Scale decomposition and interactions analysis	59
3.4.2	Morphology descriptor	62
3.4.3	Morphology of the turbulent vortices	63
3.4.4	Energy and enstrophy transfer	65
3.4.5	Vorticity - strain rate alignment	68
3.4.6	Summary	71
3.5	Interactions of scales in turbulent premixed flames	72
3.5.1	Instantaneous features	74
3.5.2	Vorticity-strain rate analysis	76
3.5.3	Multiscale analysis of tangential strain-rate	78
3.5.4	Summary	80
3.6	Implications for MILD combustion	80
4	Inception of MILD combustion	83
4.1	Motivation	83
4.2	Role of radicals on MILD combustion inception	85
4.3	Summary	91
5	Reaction Zones Structure and Combustion Modes in MILD Combustion	93
5.1	General combustion features and evolution	93
5.2	Features of the instantaneous reaction rate	94
5.3	Markers of heat release rate	97
5.4	Structure of reaction zones in mixture fraction space	101
5.5	Premixed and non-premixed behaviours of reaction zones	108
5.6	Summary	113
6	Autoignition and Flame Propagation in Non-Premixed MILD Combustion	115
6.1	Balance of reaction and convection/diffusion effects	115

6.2	Lagrangian evolution	116
6.3	Statistical behaviour	124
6.4	Summary	130
7	Multiscale Analysis in MILD Combustion	131
7.1	Energy cascade and vortex stretching	131
7.1.1	Energy transfer	132
7.1.2	Vortex stretching	134
7.2	Summary	136
8	Conclusions and Future Work	139
8.1	Scales interactions in turbulence and premixed flames	139
8.2	Physical insights of MILD combustion	140
8.3	Future work	141
	References	143
	Appendix A Initial Turbulent Kinetic Energy and Scalar Spectrums	159
A.1	Turbulent energy spectrum	159
A.2	Scalar spectrum	160
	Appendix B Description of the Chemical Mechanism	163
	Appendix C List of Publications	169

List of figures

1.1	World energy consumption by fuel type (quadrillion Btu in ordinate, year in abscissa) from EIA [2013]	1
1.2	S-shaped curves illustrating the conditions of premixed conventional and MILD combustion (as in [Oberlack et al., 2000]).	4
1.3	Combustion types diagram with typical examples shown. Feedback combustion is from de Joannon et al. [2000] . Piloted case is from Dunn et al. [2010] , HiTAC case is from Fujimori et al. [1998] and MILD cases are from Medwell et al. [2007] and de Joannon et al. [2000]	5
1.4	S-shaped curves illustrating the conditions of conventional non-premixed and MILD combustion (as in [Evans et al., 2017c ; Pitsch & Fedotov, 2001]).	7
1.5	Combustion regime map for MILD combustion according to the definitions of Cavaliere & de Joannon [2004] (in black), of Oberlack et al. [2000] (in dashed-dotted blue) and Evans et al. [2017c] (dashed red).	7
1.6	Evolution of temperature (black) and heat release rate (gray) with mixture fraction for an undiluted case (full lines) and a MILD combustion case (5% in volume of fuel or air) (dashed lines) in the counterflow flame configuration associated. The temperature mixing line is plotted using a dotted line.	14
2.1	Schematic illustration of DNS steps followed for MILD combustion of inhomogeneous reactant mixture field obtained with internal recirculation of exhaust gases. Steps 1-5 are discussed in section 2.2.2	35
2.2	Species mass fractions of MILD premixed flames parametrized on Z and c used for the MILD combustion DNS pre-processing stage (step 2).	37
2.3	Representative spatial variation of (a) $\widehat{c_Y}$ and (b) \widehat{Z} , obtained at the end of Step 3 for case AZ1. The results are shown for the mid x - y plane. The pdfs of $\widehat{c_Y}$ and \widehat{Z} for the sample from the entire domain are shown in (c) for all cases.	38

List of figures

2.4	Spatial variation of (a) $\widehat{c_Y}$, (b) \widehat{Z} , (c) $\widehat{Y_{O_2}}$ and (d) $\widehat{Y_{OH}}$ in the mid x - z plane at the end of Step 5 for case AZ1.	40
2.5	Spatial variation of (a) $\widehat{c_Y}$, (b) \widehat{Z} , (c) $\widehat{Y_{O_2}}$ and (d) $\widehat{Y_{OH}}$ in the mid x - z plane at the end of Step 5 for case AZ2.	40
2.6	Spatial variation of (a) $\widehat{c_Y}$, (b) \widehat{Z} , (c) $\widehat{Y_{O_2}}$ and (d) $\widehat{Y_{OH}}$ in the mid x - z plane at the end of Step 5 for case BZ1.	41
2.7	Pdf of (a) $\widehat{c_Y}$ and (b) \widehat{Z} for the initial and inflowing mixture fields (after Step 5) used for combustion DNS.	42
2.8	Pdf of τ_{ign} for the initial and inflowing mixture field (after Step 5) used for combustion DNS.	42
2.9	Comparison of computed and measured laminar flame speeds at standard conditions. Experimental data are taken from Vagelopoulos & Egolfopoulos [1998] ; Vagelopoulos et al. [1994]	43
2.10	Ignition delay time for CH ₄ -air mixture at atmospheric pressure and for (a) $\phi = 0.5$, (b) $\phi = 1.0$ and (c) $\phi = 2.0$. Experimental data are from Hu et al. [2015]	44
2.11	Ignition delay time for CH ₄ -air mixture at 4 atm and for (a) $\phi = 0.5$ and (b) $\phi = 1.0$. Experimental data are from Snyder et al. [1965]	45
2.12	Species mass fractions distribution for MILD premixed flames or MILD PSR.	48
2.13	Species mass fractions for a counterflow flame (dashed-dotted) with minimum and maximum of the associated premixed flame (cross) or PSR (circle).	49
3.1	Combustion regime diagram showing conditions of flames in [Rutland & Cant, 1994] \times , [Minamoto et al., 2014a] \circ , [Gao et al., 2014] $\triangle, \nabla, \square$	55
3.2	Iso-surfaces of enstrophy (red) and straining (green) structures with a threshold value of $\mu + 2\sigma$, where μ is the mean and σ is the rms. Panels (a) & (b) are for $Re_\lambda = 140$ and (c) & (d) are for $Re_\lambda = 1131$. In (a) and (c) $L_s = 24\eta$ and $L_\omega = 5\eta$, in (b) $L_s = 75\eta$ and $L_\omega = 24\eta$ and in (d) $L_s = 750\eta$ and $L_\omega = 150\eta$	64
3.3	(a) Isolated single iso-surface of enstrophy (red) and dissipation (green) structures with a threshold value of $\mu + 2\sigma$ extracted from the case $Re = 1131$. (b) The associated mid x - y plane distribution.	65
3.4	Joint-pdf of planarity, \mathcal{P} , and filamentarity, \mathcal{F} , of the strained (or enstrophy) structures seen in Fig. 3.2.	65
3.5	Normalised energy transfer function, $\widehat{\Pi}_{V,b}^{L \rightarrow S}$, for various cases.	66

3.6	Normalised enstrophy flux, $\hat{F}_b^{L \rightarrow S}$, for various cases.	67
3.7	Ratio (a) $(S/L)_{\max}^E$ and (b) $(S/L)_{\max}^\Omega$ yielding the maximum energy or enstrophy transfer from eddies of a scale L to a scale S	67
3.8	Pdf of alignment between the vorticity filtered at scale $L_\omega = 5\eta$ and the principal directions of the strain filtered at scales L_s . Solid line α and dashed line β . The gray lines are for the case $Re_\lambda = 1131$ computed using unfiltered fields.	68
3.9	Variation of probability of near perfect alignment of ω with α versus \mathcal{L} with (a) $L_\omega = 5\eta$ and (b) $L_\omega = 45\eta$	69
3.10	Ratio $\mathcal{L}^* = L_s/L_\omega$ yielding the highest probability for perfect alignment of ω with the α strain rate (lines). The shaded region shows the minimum and maximum values of $(L/S)_{\max}^E$ yielding the highest energy transfer for the associated Re_λ	70
3.11	Reaction rate of c with bandpass filtered strain rate $S_{ij}^{L_s}$, at $L_s \approx 3.3\delta_{th}$ and enstrophy Ω^{L_ω} , at $L_\omega = \delta_{th}$, fields for $u'/s_L = 11.25$ case in Table 3.2, x - z and x - y cuts are shown.	75
3.12	Compensated energy spectrum for unfiltered and filtered at $L = 15\eta$, 10η and 5η (left to right) velocity fields and unfiltered progress variable. . . .	76
3.13	Pdf of the magnitudes of direction cosines between vorticity at $L_\omega = \delta_{th}$ and principal strain rates at L_s in the case with $u'/s_L = 11.25$	77
3.14	Probability of perfect alignment between the vorticity at L_ω and α strain rate at $L_s = \mathcal{L}L_\omega$	77
3.15	Probability of perfect alignment between the vorticity at L_ω and α strain rate at $L_s = \mathcal{L}L_\omega$ conditioned on $\dot{\omega}^+$ with the maximum probability shown (white line) for case with initial $u'/s_L = 11.25$	78
3.16	(a) Surface averaged tangential strain rate from eddies of scale L_s^+ normalised by total contribution and (b) its cumulative integral.	79
3.17	Comparison of various cutoff scales.	79
4.1	Variations of major, X_M , and minor, X_m , species mole fractions with T for $0.1 \leq \phi \leq 5$ using the same oxidiser and fuel compositions, as in [Evans et al., 2017c; Medwell et al., 2008].	84
4.2	Typical iso-surfaces of normalised heat release rate $\dot{Q}^+ = 2.0$ at $t = 1.5\tau_f$ for cases (a) AZ1, (b) AZ2 and (c) BZ1, coloured by $\log(N_Z)$. The temperature field is shown on the bottom and side surfaces.	85
4.3	Variation of normalised temperature with SDR. This variation for Z_{st} is also shown.	86

List of figures

4.4	Typical variation of \hat{Q} in the mid x - y plane for case AZ1 at $t = \tau_f$. Dashed black lines enclose regions with $\hat{N}_Z > 0.2$	87
4.5	Variation of (a) \hat{Y}_{OH} and (b) \hat{Y}_{CH_2O} in the mid x - y plane for case AZ1 at $t = \tau_f$. Isolines of $\hat{Q} = 0.2$ (full black lines) and $\hat{N}_Z = 0.2$ (dashed) are also shown.	88
4.6	Variation of $\widehat{\Delta Y}_{OH}$ in the mid x - y plane for case AZ1 at $t = \tau_f$. Isolines of $\hat{Q} = 0.2$ (full black lines) and $\hat{N}_Z = 0.2$ (dashed) are also shown. . . .	89
4.7	Variation of ΔY_{OH} with θ for points with $\hat{N}_Z > 0.2$ and axial locations $0 \leq x/L_x \leq 0.05$ for case AZ1 at $t = \tau_f$. The corresponding conditional average $\langle \theta \Delta Y_{OH} \rangle$ is plotted as full black line.	90
5.1	Comparison of volume rendered temperature field at $t = 1.5\tau_f$ of (a) conventional turbulent premixed combustion (case with $u'/s_L = 2.19$ of Table 3.2) and (b) non-premixed MILD combustion (case AZ1 from the present work, see Table 2.2).	94
5.2	Mean axial profiles of (a) temperature, (b) Y_{CH_4} , (c) Y_{O_2} and (d) Y_{CO_2} for all cases.	95
5.3	Typical iso-surface of normalised heat release rate $\dot{Q}^+ = 2.0$, at $t = 1.5\tau_f$ for cases (a) AZ1, (b) AZ2 and (c) BZ1. The temperature field is shown on the bottom and side surfaces.	96
5.4	Variation of \dot{Q}^+ in the mid x - y plane for cases (a) AZ1, (b) AZ2 and (c) BZ1 at $t = 1.5\tau_f$	96
5.5	Variation of \dot{Q}^* , $Y_{CH_4}^*$, $Y_{O_2}^*$, Y_{OH}^* , $Y_{OH^*}^*$ and c_T with normal distance d marked in Fig. 5.4a for locations marked using (a-b) filled and (c-d) open circles. The location corresponding to peak \dot{Q}^* is $d = 0$. (a) and (c) are for $t = 1.46\tau_f$ and (b) and (d) are for $t = 1.5\tau_f$	98
5.6	Contours of (a) \dot{Q}^* , (b) S_{OH}^* , (c) S_{HCO}^* and (d) $S_{OH}^* \times S_{CH_2O}^*$ in the mid x - y plane for case AZ1 (dark to light gray lines are for isocontours at 0.1, 0.2, ..., 0.9).	100
5.7	Variations of (a) $[OH^*]^*$, (b) S_{OH}^* , (c) S_{HCO}^* and (d) $S_{OH}^* \times S_{CH_2O}^*$ with \dot{Q}^* for case AZ1 in the mid x - y plane. Points are coloured by their streamwise locations. Black lines are the conditional averages.	101
5.8	Variations of (a) $[OH^*]^*$, (b) S_{OH}^* , (c) S_{HCO}^* and (d) $S_{OH}^* \times S_{CH_2O}^*$ with \dot{Q}^* for case AZ2 in the mid x - y plane. Points are coloured by their streamwise locations. Black lines are the conditional averages.	102

5.9	Variations of (a) $[\text{OH}^*]^*$, (b) S_{OH}^* , (c) S_{HCO}^* and (d) $S_{\text{OH}}^* \times S_{\text{CH}_2\text{O}}^*$ with \dot{Q}^* for case BZ1 in the mid x - y plane. Points are coloured by their streamwise locations. Black lines are the conditional averages.	102
5.10	Variations of conditionally averaged temperature, T , with Z for case AZ1 (black) and BZ1 (gray). Counterflow flame results are shown using dash-dotted. Mixing line is shown as dashed line. The results are shown for two instances at two streamwise locations as marked above.	103
5.11	Variations of conditionally averaged temperature, T , with Z in case AZ1 for five streamwise locations $x/L_x \approx 0.03, 0.27, 0.50, 0.73$ and 0.97 . Counterflow flame result is shown using dash-dotted line. Mixing line is shown in dashed line.	105
5.12	Variations of conditionally averaged \dot{Q} [W/m^3] with Z for case AZ1. Counterflow flame result is shown using dash-dotted line.	106
5.13	Variations of conditionally averaged Y_{CH_4} (black) and Y_{O_2} (gray) with Z for case AZ1. Counterflow flame results are shown using dash-dotted lines.	107
5.14	Variations of conditionally averaged Y_{OH} (black) and $Y_{\text{CH}_2\text{O}}$ (gray) with Z for case AZ1. Counterflow flame results are shown using dash-dotted lines.	108
5.15	Flame Index shown in regions with $\dot{Q}^+ \geq 1.0$ for cases (a) AZ1, (b) AZ2, (c) BZ1 at $t = 1.5\tau_f$. The results are shown in the mid x - y plane.	110
5.16	Pdf of the flame index for all cases at $t = 1.5\tau_f$	111
5.17	Ratio $\dot{Q}_{\text{NP}}/\dot{Q}_{\text{tot}}$ presented in regions where $\dot{Q}^+ \geq 1$ with isoline of $ FI = 0.1$ at $t = 1.5\tau_f$. The regions bounded by these contours has $ FI < 0.1$	113
6.1	Typical spatial variations of \mathcal{B} field shown in regions with \dot{Q}^+ , normalised heat release rate, larger than 1.0 at $t = 1.5\tau$ for cases (a) AZ1, (b) AZ2 and (c) BZ1.	117
6.2	Typical trajectories of Lagrangian particles tracked for $\tau_f \leq t \leq 1.5\tau_f$ for all cases. Lines are coloured with the value of \mathcal{B} along the trajectory. Arrows indicate trajectories which will be further studied.	118
6.3	Projection on the x - y and x - z planes of the trajectories of Fig. 6.2a. Lines are coloured with the value of \mathcal{B} along the trajectory. Annotated trajectories are further discussed in Fig. 6.4.	119
6.4	Evolutions of \dot{Q}^* , ϕ , $Y_{\text{CH}_4}^*$, $Y_{\text{O}_2}^*$, $ \nabla Z ^*$, $ \nabla c_T ^*$, ΔT^* , (left axis) and \mathcal{B} (right axis) along the trajectory of three particles for case AZ1.	121
6.5	Evolutions of \dot{Q}^* , ϕ , $Y_{\text{CH}_4}^*$, $Y_{\text{O}_2}^*$, $ \nabla Z ^*$, $ \nabla c_T ^*$, ΔT^* (left axis) and \mathcal{B} (right axis) along the trajectory of three particles for case AZ2.	123

List of figures

6.6	Evolutions of \dot{Q}^* , ϕ , $Y_{\text{CH}_4}^*$, $Y_{\text{O}_2}^*$, $ \nabla Z ^*$, $ \nabla c_T ^*$, ΔT^* , (left axis) and \mathcal{B} (right axis) along the trajectory of three particles for case BZ1.	124
6.7	Logarithm of the joint-pdf of \mathcal{B} and Z at (a) $x/L_x = 0.0625$, (b) 0.4375 , (c) 0.9375 for case AZ1. The horizontal line indicates Z_{st}	125
6.8	Pdf of $(\mathcal{B} \dot{Q}^+ > 1.0)$ at $x/L_x = 0.0625, 0.1875, 0.3125, \dots, 0.9375$ (dark to light gray) for cases (a) AZ1, (b) AZ2, (c) BZ1.	126
6.9	Pdf of $(Z \mathcal{B} < -1.0)$ at $x/L_x = 0.0625, 0.1875, 0.3125, \dots, 0.9375$ (dark to light gray) for cases (a) AZ1, (b) AZ2, (c) BZ1. The dashed line indicates the stoichiometric mixture fraction. These pdfs are constructed for regions with $\dot{Q}^+ > 1.0$	127
6.10	Ignition delay time for the mixture considered. The vertical dashed lines indicate the stoichiometric mixture fraction for case AZ1-2 (black) and BZ1 (gray). These pdfs are constructed for regions with $\dot{Q}^+ > 1.0$	128
6.11	Pdf of $(Z \mathcal{B} \approx 0.0)$ at $x/L_x = 0.0625, 0.1875, 0.3125, \dots, 0.9375$ (dark to light gray) for cases (a) AZ1, (b) AZ2, (c) BZ1. The dashed line indicates the stoichiometric mixture fraction. These pdfs are constructed for regions with $\dot{Q}^+ > 1.0$	129
7.1	(a) Isosurfaces of unfiltered enstrophy (green) with isosurfaces of normalised heat release rate threshold at $\dot{Q}^+ = 2.5$ (red) and (b) isosurface of enstrophy filtered at $L = 30\eta$ (green) and at $L = 10\eta$ (red) for case AZ1. The iso-surface are threshold at a value of $\mu + \sigma$	132
7.2	Pdf of the energy transfer function between large scale $L = 30\eta$ to scale $S = 10\eta$, for case AZ1, computed at $t = 1.5\tau_f$	133
7.3	Normalised energy transfer function, $\hat{\Pi}_{V,b}^{L \rightarrow S}$, for case AZ1 (a) averaged over the entire domain and (b) conditionally averaged on the temperature progress variable c	134
7.4	Normalised energy transfer function, $\hat{\Pi}_{V,b}^{L \rightarrow S}$, for case AZ2 (a) averaged over the entire domain and (b) conditionally averaged on the temperature progress variable c	134
7.5	Normalised energy transfer function, $\hat{\Pi}_{V,b}^{L \rightarrow S}$, for case BZ1 (a) averaged over the entire domain and (b) conditionally averaged on the temperature progress variable c	135
7.6	Pdf of enstrophy production for vorticity at scale $L_\omega = 10\eta$ and strain rate at scale $L_s = 30\eta$ for case AZ1. The pdf is computed from the snapshot at $t = 1.5\tau_f$	135

7.7	Pdf of the magnitudes of direction cosines between vorticity at $L_\omega = 5\eta$ and principal strain rates at L_s for case AZ1 at $t = 1.5\tau_f$	136
7.8	Variation of probability of near perfect alignment of $\boldsymbol{\omega}$ with α versus \mathcal{L} for $L_\omega = 5\eta$ for case AZ1. Full line is for the unconditioned probability, dashed lines are for probability conditioned on the reaction rate.	137
7.9	Variation of probability of near perfect alignment of $\boldsymbol{\omega}$ with α versus \mathcal{L} for $L_\omega = 5\eta$ for cases AZ2 and BZ1. Full line is for the unconditioned probability, dashed lines are for probability conditioned on the reaction rate.	137
B.1	Lewis numbers in function of temperature for the species of the MS-58 mechanism.	165
B.2	Sensitivity of the autoignition delay time to the 10 most important reactions in the MS-58 mechanism.	168

List of tables

2.1	Oxidiser composition for the MILD mixture.	45
2.2	Initial scalar conditions for the MILD combustion DNS.	46
2.3	Initial turbulent and mixing conditions for the MILD combustion DNS. $\tau_t = l/u'$ is a turbulent time scale.	46
3.1	Characteristics of the (forced or decaying) homogeneous isotropic turbulence DNS database. l is the integral lengthscale, λ the Taylor microscale and η the Kolmogorov lengthscale.	53
3.2	DNS data attributes for the turbulent premixed flames.	54
5.1	Pearson linear correlation coefficients for the $\dot{Q}^*-S_\alpha^*$ scatter.	101
5.2	Volume fractions of regions having non-premixed, rich premixed, lean premixed and mixed-mode combustion at $t = 1.5\tau_f$. Their fractional contributions to the total heat release rate in the domain are also listed. .	112
6.1	Initial locations of the tracked particles $(x/L_x, y/L_y, z/L_z)$ highlighted in Fig. 6.2.	118
A.1	Parameters used to construct the initial progress variable field, \widehat{c}_Y	161
A.2	Parameters used to construct the initial mixture fraction field, \widehat{Z}	161
B.1	Lewis numbers used for each species in the MS-58 mechanism	164
B.2	Methane-air combustion mechanism used with OH* chemistry. Rate coefficients are in the form $k = AT^n \exp(-E/(RT))$, in moles, cc and cal. units. SMOOKE, KEE58 and KATHROTIA in the table denote the reactions from respectively Smooke & Giovangigli [1991], Bilger et al. [1990] and Kathrotia et al. [2012].	166

Nomenclature

Roman Symbols

\dot{Q}	Heat release rate
\dot{Q}^+	Normalised heat release rate
ℓ_c	Initial progress variable field lengthscale
ℓ_Z	Initial mixture fraction field lengthscale
\mathbf{q}	Heat flux vector
\mathbf{u}	Fluid velocity
\mathbf{u}_b^L	Velocity bandpass filtered at lengthscale L
$\mathbf{V}^{(c)}$	Correction velocity
\mathbf{V}_α	Diffusion velocity of species α
a_T	Tangential strain rate
c_p	Mass specific heat capacity of mixture at constant pressure
c_T	Progress variable based on temperature
c_Y	Progress variable based on a species mass fraction
$c_{p,\alpha}$	Mass specific heat capacity of species α at constant pressure
D_α	Diffusion coefficient of species α
E	Total energy
$F_b^{L \rightarrow S}$	Enstrophy flux function from scale L to S

Nomenclature

h_α	Total enthalphy of species α
$k_{b,m}$	Backward rate coefficient of the m -th reaction
$k_{f,m}$	Forward rate coefficient of the m -th reaction
l	Integral lengthscale
N_Z	Scalar dissipation rate of mixture fraction
p	Pressure
Q	Heating value
R^0	Universal gas constant
s_L	Laminar flame speed
S_{ij}	Strain-rate tensor
T	Temperature
T_p	Products temperature
T_r	Reactants temperature
T_{ign}	Mixture autoignition temperature
U_{in}	Average inflow velocity
W_α	Molar mass of species α
X_α	Mole fraction of species α
Y_α^c	<i>Incoming</i> non-reacting mass fraction of species α
Y_α	Mass fraction of species α
Z	Mixture fraction
Z_{MR}	Most reactive mixture fraction
Z_{st}	Stoichiometric mixture fraction
\mathcal{F}	Filamentarity
\mathcal{P}	Planarity

Greek Symbols

$\bar{\omega}_{\alpha,m}$	Molar production rate for species α in the m -th reaction
ω	Vorticity vector
δ_{th}	Laminar flame thickness
$\dot{\omega}_{\alpha}$	Reaction rate of species α
η	Kolmogorov lengthscale
κ	Flame stretch
λ	Taylor microscale
λ_{th}	Mixture thermal conductivity
τ	Viscous stress tensor
μ	Mixture dynamic viscosity
$\nu'_{\alpha,m}$	Reactant stoichiometric coefficient of species α of the m -th reaction
$\nu''_{\alpha,m}$	Product stoichiometric coefficient of species α of the m -th reaction
Ω	Enstrophy
ϕ	Equivalence ratio
$\Pi_{V,b}^{L \rightarrow S}$	Energy transfer function from scale L to S
ρ	Mixture density
τ_f	Flow-through time
τ_t	Turbulent time scale
τ_{ign}	Autoignition delay time

Other Symbols

Re_{λ}	Reynolds number based on u' and λ
Re_l	Reynolds number based on u' and l
Da	Damköhler number

Nomenclature

Ka Karlovitz number

Le Lewis number

Pr Prandtl number

Acronyms / Abbreviations

AJHC Adelaide Jet in Hot Coflow

CFD Computational Fluid Dynamics

CMC Conditional Moment Closure

CSE Conditional Source-term Estimation

DJHC Delft Jet in Hot Coflow

DNS Direct Numerical Simulation

EDC Eddy Dissipation Concept

EGR Exhaust Gas Recirculation

FI Flame index

HFDF Hot Fuel-Diluted Fuel

HODF Hot Oxidiser-Diluted Fuel

HODO Hot Oxidant-Diluted Oxidant

JHC Jet in Hot Coflow

LDV Laser Doppler Velocimetry

LES Large Eddy Simulation

LIF Laser Induced Fluorescence

MILD Moderate or Intense Low-oxygen Dilution

pdf Probability Density Function

PFR Plug Flow Reactor

PLIF Planar Laser Induced Fluorescence

PSR Perfectly Stirred Reactor

RANS Reynolds Averaged Navier-Stokes

WSR Well Stirred Reactor

Chapter 1

Introduction

1.1 Motivation

During the last century, energy consumption has been constantly rising and this increase is expected to continue in the future. Over that period, fossil fuels have been the main source of energy by which this increasing consumption has been met [EIA, 2013]. In the coming decades, despite the forecast growth of renewable energies, fossil fuels are still predicted to be the major source of energy worldwide. This is highlighted in Fig. 1.1 where forecasts predict that more than 75% of the energy consumption will still be provided for by fossil fuels. Thus, in this context, the improvement of combustion devices, in terms of energy efficiency and pollutants reduction, remains of the utmost importance.

To meet these two objectives, research is extensively carried out in developing novel combustion methods. Fuel lean combustion has been studied as a possibility. But it is sensitive to thermo-acoustic instability. To mitigate this effect, preheating of the reactant mixture through exhaust heat recovery systems can be used. This increases the

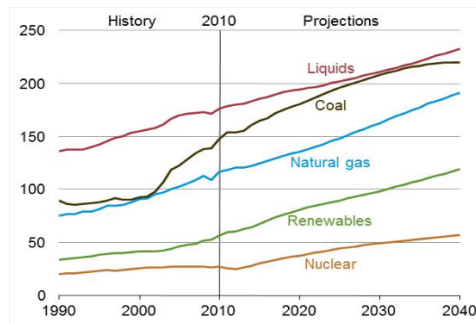


Fig. 1.1 World energy consumption by fuel type (quadrillion Btu in ordinate, year in abscissa) from EIA [2013].

Introduction

combustion efficiency as well as the combustion stability leading to quieter combustion. However, the peak temperatures are also increased leading to an increase in thermal NO_x production. This negative effect has limited the improvement of combustion efficiency by means of conventional combustion techniques.

A more promising alternative lies in Moderate or Intense Low-oxygen Dilution (MILD) combustion, also called *flameless* combustion, which can play a key-role in meeting these two objectives. It involves the preheating and dilution of reactants using products of combustion. This method increases the combustion efficiency and reduces pollutants and noise emissions compared to conventional combustion mechanisms. Most commonly, MILD combustion is defined as a combustion process where the reactants are preheated at a temperature T_r which is higher than the mixture autoignition temperature, T_{ign} , and where the maximum temperature rise, $\Delta T = T_p - T_r$, is smaller than T_{ign} , with T_p being the products temperature [Cavaliere & de Joannon, 2004]. The limited increase in temperature during the combustion process is achieved by the high dilution level with products and the low level of available oxygen for the combustion. The combustion is maintained and stabilised by the high reactants temperature. MILD combustion offers several advantages over other conventional combustion processes. First, the use of recovered exhaust heat increases the combustion efficiency. Secondly, the emission of NO_x is reduced as the peak temperatures in MILD combustion are significantly lower than in conventional combustion. Indeed, maximum temperatures in MILD methane-air combustion remain usually lower than 1900K [Cavaliere & de Joannon, 2004; Wünnig & Wünnig, 1997] and at these temperatures, the formation of NO_x takes several seconds compared to the milliseconds needed in conventional combustion where temperatures reach up to 2300K [Wünnig & Wünnig, 1997]. Another beneficial effect of this small temperature rise and high reactants temperature is the reduced combustion noise and instabilities [Katsuki & Hasegawa, 1998]. The high preheating temperature also allows for high-velocity combustion without the use of flame-holders or bluff bodies giving more freedom in the design of combustors [Cavaliere & de Joannon, 2004]. Finally, MILD combustion is relatively easy to implement in practical devices by exhaust gas recirculation (EGR) [Katsuki & Hasegawa, 1998; Wünnig & Wünnig, 1997]. It has already been used in furnaces [Woelk & Wünnig, 1993; Wünnig, 1991] but its use for gas turbines remains limited [Kulkarni et al., 2014; Nemitallah et al., 2018].

These advantages have spurred a growing interest in MILD combustion. However, the fundamental understanding of MILD combustion remains limited and research is still required to develop appropriate modelling frameworks for MILD combustion.

1.2 Background on MILD combustion

1.2.1 On the definitions of MILD combustion

In the past, several definitions of MILD combustion have been proposed [Cavaliere & de Joannon, 2004; Oberlack et al., 2000; Wüning & Wüning, 1997]. The original proposition by Oberlack et al. [2000] related MILD combustion processes to the behaviour of a stochastic homogeneous reactor. This definition was motivated by the initial experimental observations where homogeneous temperature fields were measured. In this context, MILD combustion was considered as the conditions where the ignition and extinction points no longer exist in the classical S-shaped curve and there is a monotonic shift from unburned to burned conditions.

Following the work of Oberlack et al. [2000], this can be shown formally by considering the conservation of fuel and temperature in a Perfectly Stirred Reactor (PSR), also called Well Stirred Reactor (WSR), evolving in time. These equations are:

$$m \frac{dY_F}{dt} = \dot{m}(Y_{F,r} - Y_F) - \dot{\omega}_F W_F V \quad (1.1)$$

$$m c_p \frac{dT}{dt} = \dot{m} c_p (T_r - T) + \dot{\omega}_F W_F Q V \quad (1.2)$$

where m is the mass inside the reactor with volume V and \dot{m} is the mass flow rate through the reactor. The mass fraction of the fuel in the incoming stream at a temperature T_r is $Y_{F,r}$ and its molecular weight is W_F . Q is the heating value of the fuel. The reaction rate is expressed using a single-step reaction, with an activation energy E , as

$$\dot{\omega}_F = B \left(\frac{\rho Y_F}{W_F} \right) \exp \left(-\frac{E}{R^0 T} \right) \quad (1.3)$$

for fuel-lean premixed combustion. The universal gas constant is R^0 . The residence time through the reactor is $t_r = m/\dot{m}$, which can be used to normalise the time, t . If one normalises Y_F using $Y_{F,r}$, T by T_r and recognising that $\rho = m/V$, the above two equations can be written as:

$$\frac{d\hat{Y}}{d\tau} = 1 - \hat{Y} - Da \hat{Y} \exp \left(-\frac{\hat{E}}{\hat{T}} \right) \quad (1.4)$$

$$\frac{d\hat{T}}{d\tau} = 1 - \hat{T} + \hat{Q} Da \hat{Y} \exp \left(-\frac{\hat{E}}{\hat{T}} \right) \quad (1.5)$$

where $Da = B t_r$, $\hat{Q} = Q Y_{F,r} / (c_p T_r)$, $\hat{E} = E / (R^0 T_r)$ and $\tau = t / t_r$. It can be shown that $\hat{Y} = (1 + \hat{Q} - \hat{T}) / \hat{Q}$ by multiplying the $d\hat{Y}/d\tau$ equation by \hat{Q} and adding it to the

Introduction

$d\hat{T}/d\tau$ equation and recognising that the steady state solution of the resulting equation is $(1 + \hat{Q}) = \hat{T} + \hat{Q}\hat{Y}$. By using this result, the above temperature equation can be written as

$$\frac{d\hat{T}}{d\tau} = 1 - \hat{T} + Da(1 + \hat{Q} - \hat{T}) \exp\left(-\frac{\hat{E}}{\hat{T}}\right) \quad (1.6)$$

which gives

$$1 - \hat{T}_s + Da(1 + \hat{Q} - \hat{T}_s) \exp\left(-\frac{\hat{E}}{\hat{T}_s}\right) = 0 \quad (1.7)$$

for steady state. The variation of \hat{T}_s with Da is shown in Fig. 1.2 for $\hat{Q} = 2.5$, for various values of \hat{E} . The ignition point is denoted as I and the extinction point is Ext. For the given value of \hat{Q} , the ignition and extinction (turning) points move towards one another as \hat{E} value decreases and for a particular value of \hat{E} , the distinction disappears and there is a monotonic variation from unburned to burned state, which is seen for $\hat{E} = 5$ in Fig. 1.2. The condition for the absence of turning points can be deduced from Eq. (1.7) using $dDa/d\hat{T}_s = 0$ and this condition is given by:

$$\hat{E} \leq 4 \left(\frac{1 + \hat{Q}}{\hat{Q}} \right) \quad (1.8)$$

This can be deduced to be

$$\hat{E} \leq 4 \left(1 + \frac{c_p T_r}{QY_{F,r}} \right) \approx 4 \left(1 + \frac{T_r}{\Delta T} \right) \quad (1.9)$$

The second part is obtained by approximating $(QY_{F,r})/(c_p T_r)$ by $(T - T_r)/T_r = \Delta T/T_r$.

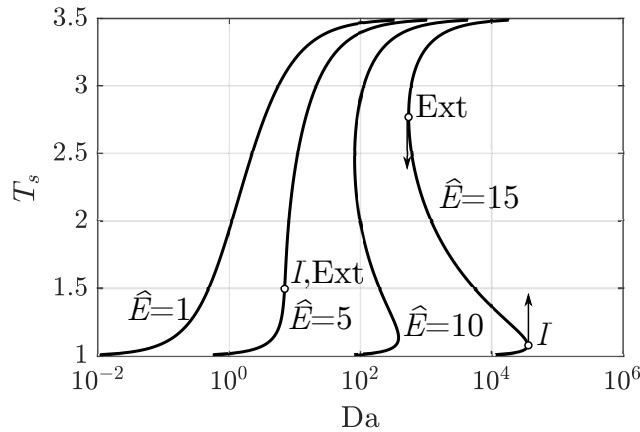


Fig. 1.2 S-shaped curves illustrating the conditions of premixed conventional and MILD combustion (as in [Oberlack et al., 2000]).

1.2 Background on MILD combustion

As mentioned earlier, another more commonly used definition was proposed by [Cavaliere & de Joannon \[2004\]](#) and according to which MILD combustion occurs when $T_r > T_{ign}$ and $\Delta T < T_{ign}$, where T_{ign} is the autoignition temperature for the mixture at a given thermo-chemical condition. This definition is widely used as it clearly differentiates MILD combustion from the other combustion types as shown in Fig. 1.3. In particular, MILD combustion differs from *feedback* (conventional) combustion as the former cannot be sustained without reactants preheating, and from *high temperature* combustion as it achieves a relatively low temperature rise.

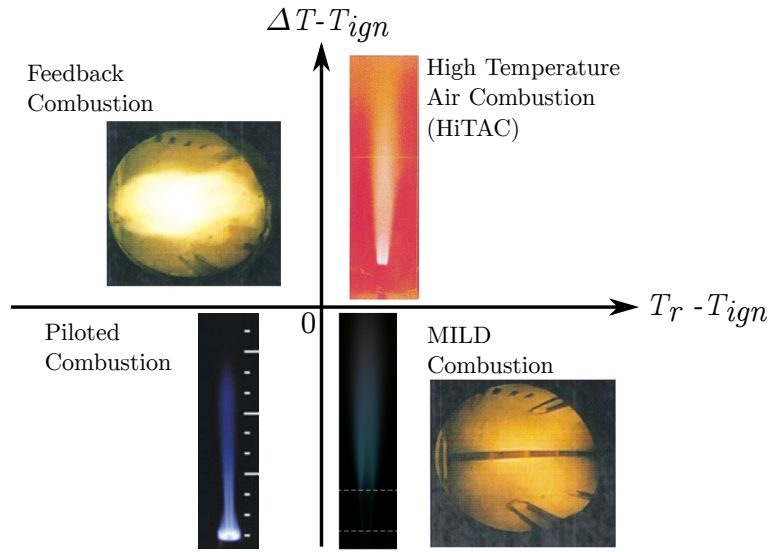


Fig. 1.3 Combustion types diagram with typical examples shown. Feedback combustion is from [de Joannon et al. \[2000\]](#). Piloted case is from [Dunn et al. \[2010\]](#), HiTAC case is from [Fujimori et al. \[1998\]](#) and MILD cases are from [Medwell et al. \[2007\]](#) and [de Joannon et al. \[2000\]](#).

It should be noted that the above two definitions could be applied for premixed combustion configurations because of the use of the residence time, t_r , inside the reactor. The mixing time, which is denoted by the scalar dissipation rate of the mixture fraction, $N_Z = D_Z |\nabla Z|^2$ where D_Z is the diffusivity of Z , plays an important role in non-premixed situation. Hence, the analysis of [Oberlack et al. \[2000\]](#) was reformulated by [Evans et al. \[2017c\]](#) using unsteady flamelets equations. That formulation, which was based on earlier work of [Pitsch & Fedotov \[2001\]](#), gave:

$$\frac{d\theta_{st}}{d\tau} + \frac{N_{Z,st}}{N_{Z,st}^0} \theta_{st} - \dot{\omega}(\theta_{st}) = 0 \quad (1.10)$$

Introduction

where τ is time normalised using $N_{Z,st}^0$ and $\theta_{st} = (T_{st} - T_{st,u})/\Delta T_{st}$. The reaction rate is

$$\dot{\omega}(\theta_{st}) = Da \exp(\beta_{ref} - \beta) \frac{(1 - \alpha)(1 - \theta_{st})^2}{[1 - \alpha(1 - \theta_{st})]\theta_{st}} \exp\left(-\frac{\alpha\beta(1 - \theta_{st})}{1 - \alpha(1 - \theta_{st})}\right) \quad (1.11)$$

It is to be noted that Eq. (1.10) is written for stoichiometric conditions, i.e. at $Z = Z_{st}$, in the mixture fraction space. The various symbols are defined as follows: $\beta = E_{eff}/(R^0 T_{st,b}) = T_a/T_{st,b}$, $\alpha = (T_{st,b} - T_{st,u})/T_{st,b} = \Delta T_{st}/T_{st,b}$, $Da = B/N_{Z,st}^0$. Under steady state conditions, Eq. (1.10) gives:

$$\frac{N_{Z,st}}{N_{Z,st}^0} \theta_{st} = \dot{\omega}(\theta_{st}) \quad (1.12)$$

The variation of θ_{st} with $\ln(N_{Z,st}/N_{Z,st}^0)$ is shown in Fig. 1.4 for $Da = 100$. As for the premixed case, here one also observes the S-shaped curve showing ignition and extinction (turning) points which disappear for particular combination of β and α . The turning points are obtained by using $dN_{Z,st}/d\theta_{st} = 0$ for Eq. (1.12) which gives:

$$(\beta^2 + 6\beta + 1)\alpha^2 - (6\beta - 2)\alpha + 1 < 0 \quad (1.13)$$

for monotonic variation from unburned to burned state (MILD combustion). This equation yields:

$$\frac{\Delta T}{T_r} < (1 + Q)f(\beta) \quad ; \quad f(\beta) = \frac{(6\beta - 2) \pm \sqrt{32\beta^2 - 48\beta}}{2(\beta^2 + 6\beta + 1)} \quad (1.14)$$

for MILD combustion.

The three conditions, Eq. (1.9), Eq. (1.14) and $\Delta T \leq T_{ign}$ are plotted in Fig. 1.5 for an example case with $T_{ign} = 1000\text{K}$ and $E_{eff} = 40 \text{ kcal/mol}$. Although this is a useful information, one must be mindful of the various approximations used for the above analysis. Just to spell them out, (i) a single-step reaction was assumed, (ii) the combustion was taken to be fuel-lean in the analysis of premixed system, (iii) adiabatic conditions were assumed, and (iv) the Lewis number was taken to be unity. The Lewis number could be seen as a second order effect for MILD combustion. The one-step reaction used includes the temperature sensitivity and finite rate chemistry effects but does not account for the presence of radicals and intermediates, which play a key-role in the thermochemical explosions required to stabilise MILD combustion as highlighted by [Wünning & Wünning \[1997\]](#). As noted by [Oberlack et al. \[2000\]](#), the analyses may be extended to include chain reactions but the analytical treatment is likely to be intractable. This would also

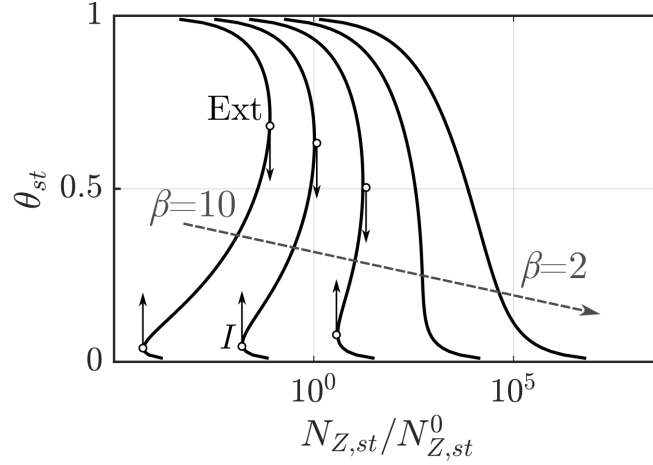


Fig. 1.4 S-shaped curves illustrating the conditions of conventional non-premixed and MILD combustion (as in [Evans et al., 2017c; Pitsch & Fedotov, 2001]).

be the case for non-adiabatic conditions. However, the numerical solutions with chain reactions and also for non-adiabatic conditions would give similar conclusions. More importantly, practical MILD combustion involves inhomogeneous mixtures containing unburned, partially and fully burned mixtures undergoing simultaneous mixing and chemical reactions and thus, it may not fit into one of the idealised cases investigated in past studies. Hence, further investigations are required to fully define MILD combustion.

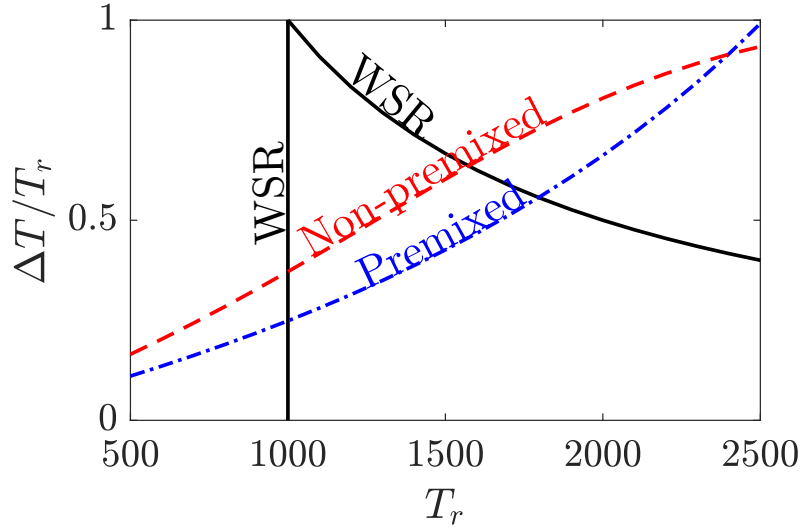


Fig. 1.5 Combustion regime map for MILD combustion according to the definitions of Cavaliere & de Joannon [2004] (in black), of Oberlack et al. [2000] (in dashed-dotted blue) and Evans et al. [2017c] (dashed red).

1.2.2 Experimental explorations

Early experimental work in MILD combustion mainly studied configurations involving a large amount of internal exhaust gas recirculation akin to furnaces [Katsuki & Hasegawa, 1998; Ozdemir & Peters, 2001; Plessing et al., 1998; Wüning & Wüning, 1997]. These works demonstrated the advantages of MILD combustion and provided experimental evidences for NO_x reduction with MILD combustion. In addition, various physical features of MILD combustion could be observed. In particular, Wüning & Wüning [1997] highlighted the absence of visible and audible appearance of combustion leading the authors to use the term *flameless* oxidation to name MILD combustion.

To understand this unique characteristic of “invisible” reaction zones, advanced laser diagnostics have been carried out in previous studies of a furnace-type burner operating under MILD combustion conditions, to measure instantaneous temperature and species fields [Dally et al., 2004; Ozdemir & Peters, 2001; Plessing et al., 1998]. Distributed reaction zones were observed under MILD conditions in comparison with conventional combustion cases in laser thermometry images. OH-LIPF and Rayleigh temperature measurements were also performed [Ozdemir & Peters, 2001; Plessing et al., 1998]. Here, homogeneous temperature fields were observed and the OH measurements showed a much lower intensity and lower gradients than in conventional premixed combustion. Furthermore, additional Laser Doppler Velocimetry (LDV) highlighted the existence of recirculation regions and their importance. These recirculation regions played an important role in mixing flue gases with reactants allowing to sustain the reactions. Furthermore, the reaction kinetics are slowed down and the burning intensity is reduced because of this recirculation. This combination led the authors to suggest that chemical kinetics time scales had become similar to typical flow time scales.

To more finely analyse the features of MILD combustion, other kinds of configuration were also proposed by Dally et al. [2002]; Duwig et al. [2012]; Oldenhof et al. [2010]; Sidey & Mastorakos [2015b] and Veríssimo et al. [2011]. Among these configurations, the Jet in Hot and diluted Coflow (JHC) of Adelaide [Dally et al., 2002] or Delft [Oldenhof et al., 2010] has become the most studied configuration with many subsequent works focusing on this configuration both experimentally and numerically. In this configuration, there is a high momentum central fuel jet issuing into a coflow of air mixed with combustion products. The hot products come from a secondary burner at an upstream position. A surrounding cold air can be used to cool the combustor walls, as in [Dally et al., 2002]. Because of the high momentum fuel jet, shear layers develop between the hot coflow and fuel. This induces mixing between the two streams leading to the ignition of the mixture which then stabilises further downstream. The main difference between the

1.2 Background on MILD combustion

Delft JHC, denoted DJHC, and the Adelaide JHC, denoted AJHC, is the possibility in the former to have a coflow that comes from partially premixed flames and not fully premixed flames like in the Adelaide JHC. It was suggested that this configuration could be representative of MILD combustion as it exhibits this mixing with products of combustion. The following paragraphs will summarize the physical observations obtained from these experiments and how these observations extend or not to other configurations.

As mentioned previously, MILD combustion occurs without visible reaction zones. As a result, advanced laser diagnostics were performed to identify these reaction zones. [Medwell et al. \[2007\]](#) performed CH_2O -PLIF (Planar Laser Induced Fluorescence) in a JHC configuration with $\text{CH}_4\text{-H}_2$ as fuel. Visual inspections of these CH_2O -PLIF images suggested the presence of spatially distributed reaction zones. Similar observations were made by [Duwig et al. \[2012\]](#) on another experimental set-up. However, OH-PLIF measurements obtained in both experiments suggested a different picture. These measurements showed the existence of a clear location of peak OH concentration with a clear gradient which indicates the presence of thin reaction zones. However, the intensity of the OH-PLIF were found to be much smaller and the general thickness of OH structures to be larger than in conventional flames. Furthermore, other OH-PLIF measurements performed by [Dally et al. \[2004\]](#) in a furnace-like configuration showed OH and temperature to be spatially distributed with a patchy appearance. However, a bimodal pdf was reported for the temperature which again suggests the existence of thin reaction zones. The shape and structure of the reaction zones in MILD combustion thus remain unknown as patchy and distributed reactions are reported but, at the same time, the existence of thin reaction zones is suggested by OH-PLIF measurements.

In addition, the identification of reaction zones in MILD combustion remains challenging. In particular, the use of only OH-PLIF to identify reactions and heat release rate in MILD combustion may be insufficient as there may be recirculating OH radicals coming from the exhaust gas which do not correlate with reacting regions. Along these lines, analysis of chemiluminescent OH, called OH^* , were also performed by [Veríssimo et al. \[2011\]](#) in a laboratory scale combustor. It was found that OH^* images showed that reaction zones were uniformly distributed over a large volume of the combustor compared to the OH-PLIF found in other experiments that showed thin regions of OH [[Medwell et al., 2007](#)]. Furthermore, [Sidey et al. \[2014\]](#) compared OH-PLIF with OH^* chemiluminescent images in a Jet in Hot Crossflow configuration. For the OH-PLIF, similarly to what was observed by [Medwell et al. \[2007\]](#), clear gradient of OH could be identified, suggesting the presence of thin reaction zones. However, discrepancies between the location of OH and OH^* could be observed. Indeed, mean measurements

Introduction

from OH-PLIF showed that OH radical was present in locations where they were not observed in the OH*-chemiluminescent pictures. This suggested that the presence of OH in MILD combustion does not necessarily coincide with the region of primary heat release. Oldenhof et al. [2013] also suggested that OH might not be an appropriate marker of reactions for MILD combustion. Indeed, in the DJHC, it was suggested that fuel decomposition was also taking place in fuel rich region where OH is not an adequate marker. As a result, OH may not cover all the region where first autoignition is taking place, and another marker like CH could prove more accurate.

The existence of thin gradient of OH in MILD combustion observed by Duwig et al. [2012]; Medwell et al. [2007] and Sidey et al. [2014] suggested the presence of thin reaction zones supporting the existence of flame propagation phenomena in MILD combustion. However, autoignition is also thought to be of importance given the high reactants temperature [Cavaliere & de Joannon, 2004]. The ignition process was studied using CH₂O-PLIF by Medwell et al. [2007, 2008] in a JHC configuration. It was observed that the heated coflow played a key role in sustaining the combustion by initiating the ignition of a mixture after localized extinction. This extinction was due to recirculation with the surrounding cold air. Oldenhof et al. [2010] used further UV-luminescence recordings to study the evolution of those ignition kernels in an experimental set-up similar to a JHC. In this work, an ignition kernel was identified as a region displaying enough luminescence. As these kernels evolve, they were then tracked from the UV-luminescence images. Contrarily to conventional lifted diffusion flames, it was found that ignition kernels were constantly produced by autoignition of the mixture. These kernels were then convected downstream, growing in size during the convection process. In a jet in hot crossflow, Sidey & Mastorakos [2015b] observed a similar mechanism with the formation and growth of ignition kernels. The importance of autoignition was also stressed by Abtahizadeh et al. [2013]. In this work, ignition kernels were appearing at the most reactive mixture fraction, Z_{MR} , on the lean side of the jet. Further downstream, these kernels were progressing towards stoichiometric and richer mixtures. Evans et al. [2017a,b] analysed the importance of the fuel blend and the coflow composition and temperature on this ignition and stabilisation mechanism by using natural gas and C₂H₄. The effect of the coflow temperature was also analysed and it was shown that natural gas yielded more diffuse flames with lower gradients and luminosity compared to C₂H₄ and were more sensitive to the coflow temperature and composition.

As mentioned previously, MILD combustion involves intense recirculation between the fuel stream and the diluted oxidiser. The chemical time scale is also relatively large due to the intense dilution. As a result, the interaction between turbulence and reaction zones

1.2 Background on MILD combustion

is generally significant compared to conventional combustion. In particular, [Medwell et al. \[2009\]](#) studied the effects of turbulence and strain on the reaction zones in MILD combustion. It was suggested that vortices could lead to a convolution and stretching of the reaction zones, and as a result, a spatial thinning of the reaction zone. In addition to this OH-"weakening", CH₂O-PLIF showed an increase in the level of their signals. Furthermore, an increase in the strain rate combined with the accompanying reduction of the reaction rate contributed to an additional transport of O₂ across the reaction zone which led to partial premixing. This behaviour was thought to lead to a stabilization of the reaction zones by increasing the formation of intermediate radicals. [Oldenhof et al. \[2011, 2013\]](#) also studied the turbulence–flame interaction in a JHC configuration using simultaneous PIV and OH-PLIF measurements. It was reported that the flow could be divided into a turbulent jet-influenced region and a quasi-laminar coflow-influenced region. The separation between these two regions was sharp and similar to a viscous superlayer. It was also observed that most reactions were residing in the quasi-laminar region. A correlation between regions of low vorticity/strain and strong OH signals was also measured. This was suggested to be because of the strong role of mixture fraction on the chemistry. Indeed, for the considered mixture, autoignition phenomena and most chemical reactions occur at relatively small mixture fraction, which thus yields a flame residing in the lean part of the mixing layer. As this lean mixture resides more in the quasi-laminar coflow, most reactions would occur in that same region.

It should be noted that most of the previous literature mentioned here concerns experimental studies focused on a Jet in Hot Coflow configuration because it allows for precise laser measurements of various flow and thermochemical quantities. However, in this configuration, other representative characteristics of MILD combustion present in practical burners with internal EGR, like the homogeneous temperature field and mild gradients of species, do not appear. Thus, recent experimental studies by [Sorrentino et al. \[2017, 2016\]](#) have been devoted to a MILD combustion burner with EGR using a strong swirl - called a cyclonic burner. This burner was used to study the effect of preheating temperature and dilution levels on the pollutant emissions.

Finally, recent research has also been devoted to extend MILD combustion to spray combustion. [Reddy et al. \[2015\]](#) developed a burner with a strong swirl able to operate under MILD combustion conditions with liquid spray. In the same configuration, [Sharma et al. \[2018\]](#) studied the effect of asymmetric fuel injection and observed that these extended the length of recirculation zones and thus yielded improved combustion stability and lower emission through improved mixing. The structure of reaction zones in spray MILD combustion in a JHC was studied by [Correia Rodrigues et al. \[2014\]](#) who showed

that the hot and diluted coflow had a strong influence on the spray flame structure. The peak temperature was found to be shifted towards leaner mixtures and the droplets vaporization rates were increased by the hot coflow temperature. This led to richer mixture close to the spray centerline yielding lower peak temperatures.

1.2.3 Investigations based on laminar model reactors

As discussed above from experiments, MILD combustion shows a large variety of intertwined phenomena. To isolate each effect, several authors have used simplified configurations to try to explain some of the fundamental features observed. In particular, the research groups of Prof. Cavaliere, Prof. de Joannon and Dr. Sabia from Naples have conducted extensive work in that direction using canonical laminar configurations such as the Well Stirred Reactor (WSR), counterflow flame and Plug Flow Reactor (PFR) both experimentally and computationally. The focus of their work has been to study the combustion behaviour, influence of dilution levels and diluent, the autoignition process and chemical pathways under MILD conditions. Their main findings are summarised below.

Well Stirred Reactor The use of a WSR configuration for MILD combustion was originally motivated by the homogeneous temperature fields with smaller gradients of species observed in initial experiments. Using this configuration for the MILD combustion of methane, [de Joannon et al. \[2000\]](#) showed that the flameless features of MILD combustion were compatible with a two-stage oxidation process by analysing the chemical pathways. The first stage corresponds to an oxidation in rich diluted conditions (oxygen starved environment) which is followed by further mixing of the radicals with oxygen ensuring the completion of the oxidation. The flameless feature of MILD combustion would come from the relatively low production of chemiluminescent species from this particular two-stage oxidation mechanism. The transient behaviour of this configuration was further studied by [de Joannon et al. \[2005, 2004\]](#) both numerically and experimentally. The existence of dynamic combustion modes, with temperature oscillations, was highlighted for inlet temperature and dilution levels typical of MILD combustion. This was caused by the competition between the oxidation and recombination pathways at the temperatures and dilution levels encountered in MILD combustion. Finally, [Sabia et al. \[2007\]](#) showed that adding hydrogen to the MILD mixture increased the range of stable conditions (in terms of inlet temperature and dilution levels) for MILD combustion by inhibiting these temperature oscillations. It should be noted that the previous studies were for non-adiabatic conditions. Thus, the temperature oscillations could have been amplified

by a coupling with the heat losses in addition to the kinetic competition. However, work by Sabia et al. [2015b] under adiabatic conditions still showed this dynamic behaviour.

The above observations from the studies on the WSR highlighted the importance of the various chemical pathways existing under MILD combustion. This highlights the importance of developing appropriate chemical kinetics for MILD combustion.

Counterflow flame The counterflow configuration was also used to study MILD combustion [de Joannon et al., 2007, 2012a, 2009, 2012b]. In particular, these various studies have covered the influence of the preheating and dilution of either fuel or oxidiser on MILD combustion. In this configuration, there are two opposing flows whose compositions and temperatures are varied to be representative of MILD combustion. From these studies, combustion behaviour maps were developed based on the shape of the heat release rate in mixture fraction space when varying the dilution level and temperature of the inflowing streams. de Joannon et al. [2007] considered the case where a mixture of $\text{CH}_4\text{-O}_2$ at various equivalence ratios was impinging against a flow of hot inert (N_2). In addition to a classical deflagrative regime (associated to classical mixture inside the flammability limits of the $\text{CH}_4\text{-O}_2$ mixture), the existence of a mode called Homogeneous Charged Diffusion Ignition (HCDI) was observed. This mode was appearing for high inert temperature and low temperature increase, ascribing it to the MILD combustion regime. Furthermore, this mode presented typical features of MILD combustion, namely a distribution of reactions over a wide range of mixture fraction and a smooth transition from HCDI to deflagrative regimes. de Joannon et al. [2009] considered a counterflow flame with, on one side, a stream of hot air and, on the other side, methane diluted with nitrogen at ambient temperature (Hot Oxidiser Diluted Fuel, HODF, condition). Compared to a conventional case without dilution, a large broadening of the reaction zone in mixture fraction space and thus also in physical space, was observed. Similar observations were made when considering air at ambient temperature opposing a stream of hot and diluted methane (Hot Fuel Diluted Fuel, HFDF, condition) [de Joannon et al., 2012b]. The final configuration considered is the Hot Oxidant Diluted Oxidant condition (HODO) where methane at ambient temperature opposes a hot and diluted oxidant [de Joannon et al., 2012a]. In all these configurations, the oxidation could only take place if the temperature of the preheated stream was high enough to promote autoignition. Furthermore, in those regions limited by the autoignition phenomena, the location of peak heat release rate was uncorrelated with the stoichiometric mixture fraction. Figure 1.6 shows typical temperature profiles (black) and heat release rate variations (gray) with mixture fraction, Z , for these three configurations HFDF, HODF and HODO for MILD conditions (dashed

Introduction

lines) and conventional conditions (full lines). In particular, the double peak of heat release rate, present in conventional high temperature combustion, disappears under MILD conditions. The absence of a pyrolytic region can also be observed at high dilution. These counterflow solutions were obtained using CANTERA [Goodwin et al., 2017] for a low strain-rate to ensure the existence of a fully burning solution, using the GRI3.0 mechanism.

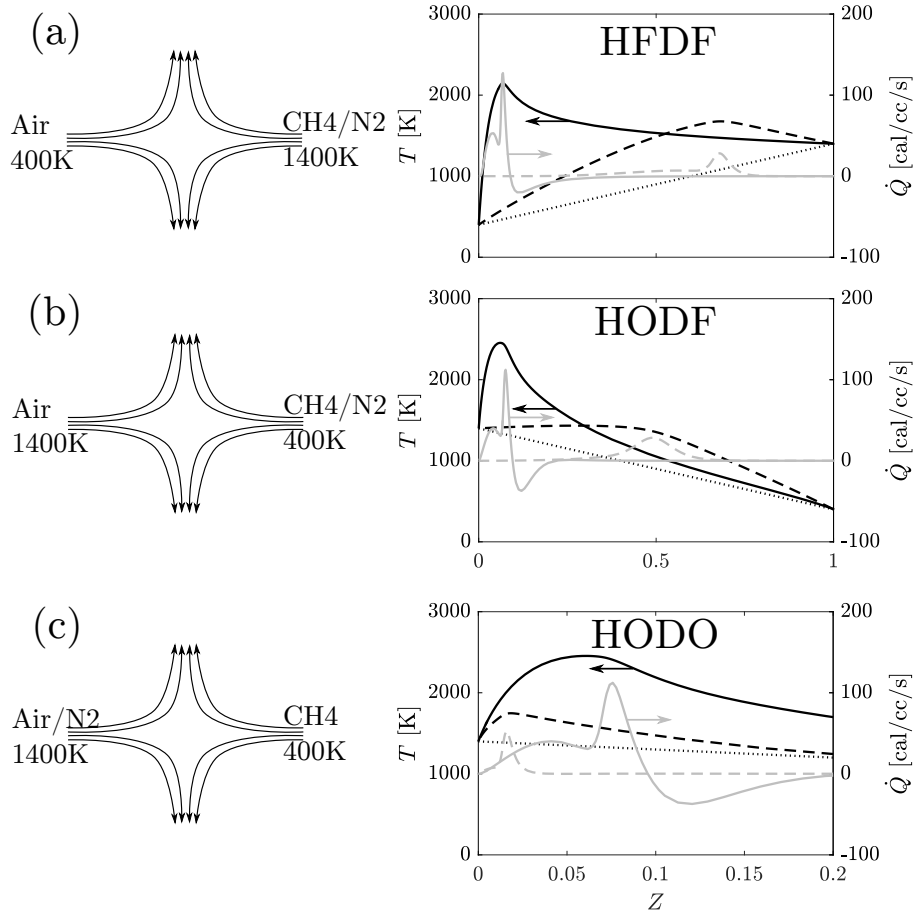


Fig. 1.6 Evolution of temperature (black) and heat release rate (gray) with mixture fraction for an undiluted case (full lines) and a MILD combustion case (5% in volume of fuel or air) (dashed lines) in the counterflow flame configuration associated. The temperature mixing line is plotted using a dotted line.

The transient evolutions of the HODF and HFDF configurations were further studied by Sorrentino et al. [2013]. This was done by performing 2D laminar simulations using FLUENT. Compared to the steady analysis performed in earlier studies, the range of conditions (in terms of dilution and preheated temperature) yielding MILD combustion

1.2 Background on MILD combustion

was found to be smaller. This meant that higher temperatures were needed to obtain autoignition.

Finally, the counterflow flame configuration was also used by Sidey & Mastorakos [2016] for the study of kerosene impinging against oxygen preheated and diluted with hot combustion product. Contrarily to the work discussed above, no large broadening of the reaction zones was observed and the existence of a clearly defined peak of heat release rate and OH radical was highlighted.

Plug Flow Reactor The tubular flow reactor or plug flow reactor (PFR) has also been used in past studies both experimentally and numerically [Sabia et al., 2014, 2013, 2015a, 2016]. The focus of these studies was on the ignition delay time for mixture under MILD conditions and chemical pathways analysis. Sabia et al. [2013] and Sabia et al. [2014] considered a mixture of oxygen with respectively CH_4 and C_3H_8 preheated and diluted with nitrogen. They showed that there was a significant slow down of the kinetic pathways during the ignition process. In addition, a comparison with traditional chemical kinetics suggested that existing chemical mechanisms may need to be revised to appropriately capture the competition between the various chemical pathways (oxidation/recombination) existing in MILD combustion. The use of CO_2 or H_2O instead of N_2 for the dilution was examined by Sabia et al. [2015a]. Compared to N_2 , these diluents decrease the system reactivity. Furthermore, the effect of these products on the autoignition time was found to be affected by the temperature: at low temperature, the presence of CO_2 and H_2O favoured reactions while at higher temperature, they inhibited them. The extension of this work to $\text{C}_1 - \text{C}_2$ fuel blend was performed by Sabia et al. [2016]. The addition of C_2 species decreased the autoignition time. It should be emphasized that for the studies above, a significant discrepancy was observed between the ignition delay times obtained from numerical calculations and experimental measurements, especially for fuel-rich regions. This suggests a strong need to develop chemical mechanisms adapted to MILD conditions.

Finally, Sidey et al. [2014] also considered the plug flow reactor but the dilution of the reactant mixture was obtained from either the major products of a laminar flame calculation or all the products. The presence of intermediate radicals was observed to decrease the ignition delay. It also supported that dilution significantly slows down chemical reactions.

Insights from laminar calculation All the studies discussed above have highlighted some fundamental features of MILD combustion. In particular, they have stressed the

Introduction

importance of the chemical kinetics in MILD combustion. It was observed both in the WSR and PFR configurations that there is a strong competition between oxidation and recombination pathways which could lead to dynamic behaviours. Furthermore, from the counterflow flame configuration, the shape of the heat release rate in MILD combustion was observed to be significantly different from conventional high temperature combustion. Indeed, no double peak nor pyrolysis regions were observed in MILD combustion. Finally, as mentioned previously, MILD combustion involves highly inhomogeneous mixture (burned, unburned, fuel, oxidiser and intermediates) and thus despite the insights provided, these laminar configurations represent large simplifications of the actual physics of practical MILD combustion.

1.2.4 Turbulent calculations

Many studies have been devoted to the numerical simulations of MILD combustion. More generally, computational fluid dynamics (CFD) has become a crucial tool in the study of turbulence and combustion thanks to the recent large increase in computational resources. In CFD, there exist three levels of simulation which can be classified based on the time and spatial scales resolved during simulations.

In the least precise level, called the Reynolds Averaged Navier-Stokes (RANS) simulations, only time-averaged quantities are resolved. In this context, the Reynolds averaged (or Favre averaged, if they are density weighted) balance equations are deduced by averaging the instantaneous Navier-Stokes equations, to be presented in chapter 2. As a result of the averaging process, additional terms appear in the equations, the Reynolds stress, turbulent flux terms and mean reaction rate. These require some form of modelling.

The next level of computational approach is called Large Eddy Simulation (LES). In this paradigm, LES explicitly captures large scale motions of turbulence while the effect of small scales (subgrid scales) requires modelling. The balance equations for LES are obtained by space-filtering the instantaneous Navier-Stokes equations. Similar modelling concepts as for RANS can be applied to LES. These, however, require some modifications as LES deals with subgrid scales effects while RANS models are concerned with variations around mean flows effects.

Finally, in the most precise level, called Direct Numerical Simulation (DNS), all the instantaneous fully compressible Navier-Stokes equations are solved without using any models for turbulence nor combustion. All scales of turbulence are explicitly resolved but DNS requires a large amount of computational resources which limits its use to simplified flow configurations with small domains (typically a domain of a few centimeters).

All three types of simulations, RANS, LES and DNS have been used in previous studies of MILD combustion and the next few sections summarise the insights obtained from these works.

RANS

Various modelling attempts have been carried out to simulate MILD combustion in a RANS context. These various approaches are summarised hereunder.

Flamelets based approach Coelho & Peters [2001] used an Eulerian Particle Flamelet model to simulate the configuration of Peters [2000]. Reasonable agreements with experimental results were obtained for the mean velocity. However, the predicted NO production was three times larger than what was measured. Dally et al. [2004] used the same model to study the effect of fuel mixture. The simulations could predict the general trends of temperature and NO production but peak temperatures were overpredicted in some cases by up to 100K. It should be noted that the use of flamelets based models is generally questionable for MILD combustion. Indeed, the flamelets model assumes that reactions occur in thin reaction layers, typically smaller than the Kolmogorov lengthscale. Consequently, the internal structure of the reaction zones is not affected by turbulence. However, as has been underlined in PLIF measurements [Dally et al., 2002] or laminar calculations [de Joannon et al., 2012b], MILD combustion is characterised by a broadening of the reaction zones. Thus, this underlying assumption may not be valid for MILD combustion. This has been further demonstrated in comparative studies by Christo & Dally [2005]; Rebola et al. [2013] and Shabanian et al. [2013] who compared the flamelets model to other modelling frameworks, like the Eddy Dissipation Concept (EDC) model or the transported PDF method. It was observed that the flamelets model consistently performed poorly when compared to the other models.

Eddy Dissipation Concept model The EDC model relies on the assumption that reactions occur in regions where the dissipation of turbulent kinetic energy happens, the so-called fine structures of turbulence [Magnussen, 1981]. These regions are then modelled as perfectly stirred reactors. The mass fraction of these fine structures and the residence time in these are estimated from an energy cascade model. This model has been used in many numerical studies of MILD combustion [Aminian et al., 2011; Christo & Dally, 2005; De et al., 2011; Evans et al., 2015; Frassoldati et al., 2010; Galletti et al., 2009; Lupant & Lybaert, 2015; Mardani et al., 2013]. It was shown to perform better than the flamelets model [Rebola et al., 2013; Shabanian et al., 2013]. Furthermore,

Introduction

Christo & Dally [2005] showed that the EDC model presented a reasonable agreement with experimental values as long as a detailed chemistry was included. This supported the observation of Sabia et al. [2013] that capturing the appropriate chemical pathways for MILD combustion was crucial. This ability of the EDC model to include finite rate chemistry was also stressed by Lupant & Lybaert [2015] and Parente et al. [2011] as a reason for the quality of the simulations obtained using this model. It was further observed that the accuracy of numerical results was extremely sensitive to the definition of the turbulence quantities at the boundaries. This emphasised the importance of turbulence in MILD combustion. Similar observations were reported by Mardani et al. [2013] who used the same model to study the effect of different chemical mechanisms and analyse the chemical pathways. Aminian et al. [2011] also drew similar conclusions with regards to the importance of the boundary turbulence definition, especially as it influences the development of the shear layers between the fuel jet, the hot coflow and the cold surrounding air.

This ability of the EDC to include finite rate chemistry and adjust the reaction rate was further studied by Aminian et al. [2012]. In that study, it was shown that a modification of the model constants, inducing longer residence times in the fine structures of turbulence or a larger volume fraction of those structures, improved the numerical results. The choice to modify the usual EDC constants was motivated by the fact that MILD combustion is characterised by more distributed reaction zones, lower gradients of species and temperature. This led to an improvement in the prediction of peak temperatures and species production, by lowering the values obtained from simulation, signifying a weakening of the reaction zones. A similar independent numerical analysis by De et al. [2011] for the JHC of Oldenhof et al. [2010] yielded similar conclusions on the importance of modifying the constants of the EDC model when simulating MILD combustion. This approach to providing improved EDC model constants has been further developed by Evans et al. [2015]; Mardani [2017] and Parente et al. [2016]. Evans et al. [2015] and Mardani [2017] performed a parametric study of the EDC model constants. Simulations performed with the optimized values yielded reasonable trends and result over the range of oxygen dilution levels considered. However, the peak OH value was overpredicted by a factor of two and the radial location of peak temperature was also overpredicted. In the methodology of Parente et al. [2016], the values of the EDC constants are estimated from the local values of Reynolds and Damköhler numbers. Improved results were found compared to the use of global optimal values for these coefficients. However, there still existed a clear overestimation of OH, especially for low oxygen levels, suggesting that a RANS-EDC simulation could not appropriately

capture the localized extinction happening at the very low oxygen level. [Li et al. \[2017\]](#) extended the work of [Parente et al. \[2016\]](#) by proposing to model reactions in the fine structures of turbulence in the EDC model using Plug Flow Reactor (PFR) equations. This helped improved the robustness of the calculations and offers the possibility of In-situ Adaptive Tabulation. [Aminian et al. \[2016\]](#) also extended the EDC model to include extinction effects. This was done by including a criterion on the mixing timescale of the fine structures of turbulence. Improved results were obtained when simulating the AJHC in the downstream regions where there is mixing with the surrounding cool air.

It should be noted that overall, the applicability of the EDC model for MILD combustion remains also questionable. Indeed, the assumption that reactions occur in the fine structures of turbulence may not be true in MILD combustion as reactions occur over larger regions. This can be partly remediated by modifying the constants of the EDC models. However, these modifications can appear somewhat arbitrary and more quantitative insights are needed to appropriately modify these constants.

Conditional Moment Closure (CMC) based model CMC models use conditional moments of reactive scalars to solve closure problems. It relies on the idea that fluctuations of reactive scalars are mainly linked with fluctuations of the mixture fraction. No assumption on the length scales of chemistry or turbulence is done and CMC methods should thus be able to simulate a wide range of combustion regimes without parameters tuning [[Klimenko & Bilger, 1999](#)]. This model was used by [Kim et al. \[2005\]](#) with Bilger’s mixture fraction as a conditioning variable. Generally, good agreements were obtained with the experimental measurements of [Dally et al. \[2002\]](#) except for the NO concentration that was underestimated. A similar model, the Conditional Source-term Estimation (CSE) model was used by [Labahn et al. \[2015\]](#). Two conditioning variables were used, the fuel mixture fraction and the oxygen mixture fraction. This model shares many features with the CMC model but in CSE, the conditional averages are obtained by inverting an integral equation while they are transported in the CMC model. Overall good agreements were obtained with experimental data from [Oldenhof et al. \[2010\]](#) for the temperature and velocity fields. The CSE model was also used to simulate a semi-industrial MILD furnace [[Labahn & Devaud, 2016](#)]. Good agreements for major species were obtained but discrepancies could still be observed for minor species, such as H_2 or CO.

Transported PDF model Transported PDF methods usually rely on the transport of the composition PDF [[Haworth, 2010](#)]. By solving this PDF, any thermochemical moments, among which the mean reaction rate, can be deduced. In this framework, the

Introduction

modelling shifts from the reaction rate to the modelling of the turbulent transport terms and the micromixing terms [Haworth, 2010]. This model was used in various studies for MILD combustion [Christo & Dally, 2004; De et al., 2013; Evans et al., 2015; Gordon et al., 2007; Lee et al., 2015].

The study by Christo & Dally [2004] showed that this method yielded better results than the EDC model (without the modification of the model constants). De et al. [2013] also used this model to simulate the configuration of Oldenhof et al. [2013]. The various micromixing models, Coalescence-Dispersion (CD), Interaction-by-Exchange-with-Mean (IEM) and Eulerian Minimum Spanning Tree (EMST), as well as two transported PDF approaches, the Lagrangian PDF (LPDF) and the Multi-environment Eulerian PDF (MEPDF) were compared. The ability of these transported PDF methods to appropriately capture the experimental trend was highlighted. It was also stressed that the results obtained from the MEPDF method were of comparable quality to the one obtained using the LPDF. The MEPDF method was also used by Lee et al. [2015] to simulate the configuration of Dally et al. [2002] and generally showed good agreements except in the lean side of the flame where the cold shrouded air may play a great role in extinguishing the flame. In that region, the peak temperature and CO mass fraction were greatly overestimated.

Other modelling frameworks A recent study by Chen et al. [2017] proposed to use the PSR model to simulate MILD combustion based on findings from Minamoto & Swaminathan [2014a, 2015]. This model was based on the framework of Ruan et al. [2014a] and Chen et al. [2015] where transport equations are solved for the Favre-averaged progress variable \tilde{c} , mixture fraction \tilde{Z} , their variances, $\widetilde{c''^2}$, $\widetilde{Z''^2}$ and their covariance $\widetilde{Z''c''}$. From these quantities, the joint PDF, $P(c, Z)$, is modelled using the copula method from which the mean reaction rate can be estimated as $\overline{\dot{\omega}_c} = \int_0^1 \int_0^1 \dot{\omega}_c(\xi, \zeta) P(\xi, \zeta) d\xi d\zeta$. And $\dot{\omega}_c(\xi, \eta)$ were obtained from tabulated PSR calculations. This model provided good results even when compared to results from Lee et al. [2015] despite its simplicity and lower computational cost.

Overall comparison Several authors have performed comparative studies between various existing models for MILD combustion. Dally et al. [2004] used the flamelets model and original EDC model and showed that the flamelets model was clearly insufficient for the simulation of MILD combustion. More comprehensive comparisons have been made by Shabanian et al. [2013] for ethylene and De & Dongre [2015] for methane combustion. It was found that EDC and transported PDF based methods generally

yielded better result than flamelets based ones. Furthermore, the quality of the results between transported PDF methods and EDC with modified constants were comparable to one another. This observation was also made by [Evans et al. \[2015\]](#). However, discrepancies between numerical and experimental results for the temperature and minor species profiles were still found for these models.

LES

It is generally accepted that results from LES are an improvement over RANS results. Indeed, LES explicitly solves the large scales of turbulence whereas models are used for the subgrid scale effects. Hence, LES can provide better predictions than RANS. This is of particular importance for MILD combustion as it has been largely reported that results were particularly sensitive to turbulence conditions [[Galletti et al., 2007](#)] and that the onset of reactions in MILD combustion was occurring in lean regions with low scalar dissipation rates [[Oldenhof et al., 2013](#)]. However, up to now, few studies of MILD combustion have been performed in a LES context. As such, the quality of the various models used is relatively difficult to assess. Nonetheless, this section will provide a succinct summary and will highlight the insights obtained.

[Kulkarni & Polifke \[2013\]](#) used the Eulerian Monte-Carlo (stochastic fields) method with tabulated chemistry from PSR calculation to simulate the configuration of [Oldenhof et al. \[2010\]](#). The velocity field was appropriately predicted and the lift-off height was reasonably well captured as well as its decreasing trend when increasing the Reynolds jet number. [Bhaya et al. \[2014\]](#) used the transported PDF method to simulate the same configuration. The velocity field was observed to be captured reasonably well. Further insights into the flow structure were provided. From the shear layer between the fuel jet and the hot coflow, Kelvin-Helmholtz instabilities were developing leading to the existence of Kelvin-Helmholtz toroidal structures further downstream. In these regions where these vortex rings were formed, recirculation was occurring and the ignition kernels started to ignite under the mixing between fuel and hot oxidizer. The evolution of these kernels was also captured in the simulation, and similarly to what was found in the experiments [[Oldenhof et al., 2010, 2011, 2013](#)], these kernels were convected downstream as they were growing in size. Furthermore, the apparition of multiple independent ignition kernels was observed during the simulation supporting the views expressed by [Oldenhof et al. \[2010\]](#) that MILD combustion was governed by multiple ignitions occurring continuously. The LES-CSE model was also used by [Labahn & Devaud \[2015\]](#) to simulate the same configuration. Qualitatively, the flame stabilization process, with the continuous formation of ignition kernels and their convection and growth, was also observed. Results

Introduction

in that studies showed a clear improvement over the previous RANS-CSE study by [Labahn et al. \[2015\]](#). However, this LES study was contradicting experimental results by predicting an increase in the lift-off height with increasing jet velocity. Furthermore, it should be noted that all these LES studies underpredicted the lift-off height suggesting that there was an overestimation of the reaction rate close to the jet exit.

A tabulated chemistry model was also used in a LES context by [Ihme & See \[2011\]](#); [Ihme et al. \[2012\]](#) to simulate the configuration of [Dally et al. \[2002\]](#). The Flamelets-Progress Variable (FPV) model was used. This model relies on the transport of a mixture fraction (defined between the fuel and oxidizer), an oxidizer split (quantifying the mixing with the shrouded air), their variances and the mean progress variable. The reaction rate is then obtained by use of tabulated chemistry from flamelets tables. Overall, a good agreement was observed between the numerical and experimental results. On the fuel-rich side, an overestimation of the CO species was observed and the temperature field was also overpredicted in the mixing region between the hot coflow and the shrouded air. The sensitivity of the burner to the scalar boundary conditions at the inlet was further stressed. Similarly, [Abtahizadeh et al. \[2017\]](#) used the Flamelet Generated Manifold (FGM) model based on igniting mixing layer with differential diffusion effects to simulate the DJHC. The flame stabilization mechanism was analysed. Similarly to other studies, it was suggested that the flame is stabilised by autoignition: multiple ignition kernels form, grow and are convected downstream. A similar FGM model based on counterflow flames was also developed by [Ma & Roekaerts \[2016a,b\]](#). It was used to simulate the spray flame configuration of [Correia Rodrigues et al. \[2014\]](#). Reasonable agreements for the droplets distribution and temperature profiles were obtained.

DNS

Previous sections have been devoted to the numerical studies of MILD combustion that relied on some form of modelling both in a RANS and LES context. By comparison, Direct Numerical Simulation (DNS) does not require any model and can thus directly provide physical insights into MILD combustion. However, DNS is largely limited to simplified configurations due to the high computational cost involved. To the author's best knowledge, only two different groups have performed DNS of MILD combustion and have focused on different aspects of MILD combustion.

In the studies by [van Oijen \[2013\]](#) (in 2D) and [Göktolga et al. \[2015\]](#) (in 3D), focus has been put on capturing the ignition of the mixing layer between the fuel and a hot coflow, thus trying to accurately simulate the micro-scale of an experimental setup like the JHC of [Dally et al. \[2002\]](#). The numerical configuration consisted of a rectangular

1.2 Background on MILD combustion

domain with fuel in the middle layer surrounded by a hot and diluted oxidizer. This layer in the middle is flowing in a direction while the coflow is flowing in the opposite direction, resulting in a shear layer between fuel and oxidizer. The main findings from these DNS were about the ignition. It was observed that autoignition was occurring along the iso-surface of most reactive mixture fraction, Z_{MR} , with various ignition delay times depending on the local temperature and scalar dissipation rate, rather than by some ignition kernels developing into propagating flames. Furthermore, the importance of real 3D turbulence over the simplified 2D configuration of van Oijen [2013] was emphasised as 3D turbulence could account for small scale structures that induced more variations in the species distribution. Based on these DNS data, Göktolga et al. [2017] proposed a Multistage FGM-based model. The particularity of this model was to use two different progress variables to describe MILD combustion, one based on a precursor of autoignition and the other based on the production of combustion products. It was observed in an *a priori* assessment of the 2D simulation that this model could reasonably well capture the evolution of heat release and species production.

In contrast, the studies by Minamoto et al. [2013]; Minamoto & Swaminathan [2014a,b, 2015]; Minamoto et al. [2014a,b] simulated the physics corresponding to MILD combustion where internal exhaust gas recirculation is taking place, as in the furnace-like configuration of Peters [2000]. These studies considered premixed MILD combustion. It was observed by Minamoto et al. [2014b] that there existed regions of strong chemical reactions similar to flamelets. However, compared to conventional premixed combustion, these regions were spread over a much larger portion of the domain and strongly interacted with each other leading to an apparent thickening and spreading of the reaction zones. Furthermore, these interactions were increasing in frequency with an increase of the turbulence level or of the dilution level. As a result, clearly non bimodal PDF were observed for the progress variable leading to the conclusion that flamelets-based models were inadequate for MILD combustion. This was further confirmed by Minamoto & Swaminathan [2014b] where it was found that the tangential scalar gradient in MILD combustion was not negligible with regards to the normal gradient, further supporting a non-flamelets behaviour. A closer study of the reaction zones using Minkowski functionals analysis showed that their most probable shape was pancake-like and not sheet-like, which is the case in turbulent premixed combustion [Minamoto et al., 2014a]. This shape emerged because of the combination of autoignition phenomena, flame propagation and the spatial variation of the mixture containing at the same time unburnt, burnt and reacting mixture. The study of chemical markers for MILD combustion was also performed by Minamoto & Swaminathan [2014b]. It showed that the use of the LIF-signal from OH and CH₂O,

or HCO could be adequate for the detection of heat release in MILD combustion, but may prove insufficient to study the actual characteristics of MILD combustion and the structure of reaction zones. From these DNS results, modelling attempts have also been made in RANS and LES contexts [Minamoto & Swaminathan, 2015; Minamoto et al., 2014a]. *A priori* assessment of a PSR model with a presumed β -pdf was shown to be a suitable candidate for MILD combustion. This model was also validated in the *a posteriori* study of Chen et al. [2017].

From these studies using DNS, various insights into MILD combustion have been obtained. However, they should be nuanced. On one hand, the DNS from Göktolga et al. [2015] only focused on the autoignition process and, features of MILD combustion such as a more homogeneous temperature field and the spatial distribution of reactions were not observed. On the other hand, the DNS of Minamoto [2013] considered a fully premixed configuration which does not represent the majority of MILD combustion applications. Thus, it still remains to verify whether the results obtained from this latter study can be extended to a non-premixed configuration.

1.3 Outstanding issues and modelling challenges

From the studies summarised in the previous section, it is clear that several aspects of MILD combustion still remain to be researched and understood.

The first aspect concerns the fundamental definition of MILD combustion. Indeed, three different definitions of MILD combustion have been proposed and while the one proposed by Cavaliere & de Joannon [2004] has become the *de facto* conventional definition, its applicability to non-premixed system remains ambiguous. The more recent definition by Evans et al. [2017c] constitutes an attempt at improving this. It uses a one dimensional counterflow flame as a representative model of ignition in MILD combustion. This new definition cast doubts on several works on MILD combustion as it considered that various experiments conducted in the past were not actually in the MILD combustion regime (see Fig. 2 of Evans et al. [2017c]). However, all these definitions rely on large simplifications of MILD combustion and are thus unable to account for some key-aspects of MILD combustion like the presence of intermediates and radicals in the stabilisation of MILD combustion. This has, however, been shown to be a key feature of MILD combustion [Wünning & Wünning, 1997].

In addition to this difficulty to appropriately define what represents MILD combustion, several physical aspects of MILD combustion remain unclear. First, the structure of the reaction zones remains largely unknown. Indeed, experiments have yielded contradicting

1.3 Outstanding issues and modelling challenges

views with some highlighting the existence of thin reaction zones [Medwell et al., 2007; Sidey & Mastorakos, 2015b] while more distributed reactions were also observed by Dally et al. [2002] and in the laminar calculations of de Joannon et al. [2012a, 2009, 2012b]. Additional DNS calculations showed that this observation could be due to the frequent interactions of flamelets-like structures [Minamoto & Swaminathan, 2014b]. Thus, the actual structure of the reaction zones remains largely unknown and there is uncertainty as to which assumptions can be made when trying to model them. This put in question the use of flamelets-based or EDC-based models for the simulation of MILD combustion.

The identification of reaction zones in MILD combustion has also been shown to be challenging with a possible non-correlation between usual markers like OH and heat release [Sidey & Mastorakos, 2015b]. This was supported by numerical studies from Evans et al. [2015]. DNS of Minamoto & Swaminathan [2014b] suggested that the use of only one species would be insufficient and suggested the use of $\text{OH} \times \text{CH}_2\text{O}$ as a potential substitute. Whether this is also valid for non-premixed configuration remains to be determined.

The mechanism by which MILD combustion stabilised has also been a subject of research. In the JHC configuration, the general picture that emerged from experimental [Oldenhof et al., 2010; Sidey et al., 2014] and numerical [Bhaya et al., 2014] studies was that ignition kernels were constantly produced near the flame base. These kernels are then convected downstream and grow in size stabilising the flame. This mechanism was also supported by the DNS from Göktolga et al. [2015] who observed the autoignition of these kernels in regions corresponding to the most reactive mixture fraction. Thus, there appears to be a coexistence between ignition and propagating flames phenomena in MILD combustion.

The importance of turbulence on MILD combustion has also been noted in many different studies. For example, the presence of ignition kernels were observed to be favoured in regions of low scalar dissipation rate [Göktolga et al., 2015; Oldenhof et al., 2010]. Further studies [Oldenhof et al., 2011, 2013] showed the importance of the entrainment flows and how the flame was stabilising with regards to the mixing layer between the fuel stream and the hot oxidizer. How to appropriately reproduce this relation in MILD combustion models remains to be understood.

The kinetic pathways in MILD combustion have also been observed to be different from usual kinetics [de Joannon et al., 2000; Sabia et al., 2014, 2013, 2016, 2015b]. Adapted chemical kinetics may thus be necessary for MILD combustion. This is of particular importance in MILD combustion as autoignition is thought to be of particular importance and thus capturing the appropriate oxidation paths is crucial.

Considering all these uncertainties about the physics of MILD combustion on the characteristics of the reaction zones, its stabilization and chemical kinetics, results obtained from numerical simulations should be taken with caution. Indeed, the validity of the assumptions underlying the various models is still unknown for MILD combustion.

1.4 Aims and objectives

The present work aims to provide some physical insights into non-premixed MILD combustion using numerical simulations further to those gained by [Minamoto \[2013\]](#). As mentioned previously, there exist three different paradigms in computational fluid dynamics: RANS, LES and DNS. Given the relative novelty of MILD combustion, its unique features and the limited understanding of MILD combustion, the use of any existing models is questionable and results obtained with LES or RANS can only be used cautiously. Accordingly, this thesis work will use DNS to simulate MILD combustion with mixture fraction variations to obtain these physical insights.

However, before tackling the analysis and study of MILD combustion, a few initial questions need to be answered. Indeed, a major limitation of DNS for turbulent reacting flows is the relatively low level of turbulence, and thus low turbulence Reynolds numbers, achievable. In this context, and considering that turbulence is understood to play a major role in MILD combustion [[Galletti et al., 2007](#); [Plessing et al., 1998](#)], studying the effects of turbulence in these low turbulence simulations may raise some questions. Hence, some initial analysis will be conducted on pure turbulence to study whether the mechanisms of turbulence, in particular the vortex stretching mechanism and the energy transfer, show the same dynamical features at low and high Reynolds numbers. Subsequently, this analysis is extended to turbulent premixed flames to provide further understanding on how chemical reactions influence the presence and intensity of vortical structures and the way by which flames are strained. These investigations on turbulent premixed flames would provide a basis of comparison for the analysis of turbulence-chemistry interaction in MILD combustion. Thus, the first part of this thesis work will aim to answer the following questions:

1. In non-reacting flows, are the dynamical features of turbulence similar at low and high Reynolds numbers? If that is the case, then performing DNS of reacting flows at low or moderate Reynolds numbers should already provide useful physical insights as the interaction of scales would be representative of cases at high Reynolds numbers.

2. In turbulent premixed flames, what is the relevant scales of eddies most influencing the flame structure and does heat release influence the interaction of turbulent structures among different scales?

In a second part, the DNS and the analysis of MILD combustion will be carried out and the objective is to answer the following questions arising from the literature review discussed earlier:

3. What is the role of radicals in the inception of MILD combustion? Given that in internal EGR MILD combustor, a large amount of radicals are recirculating with the inflowing fuel, these may play an important role in the onset of MILD combustion.
4. What are the structures of MILD combustion reactions zones and in particular, do thin regions exist and which process leads to their thickening? Furthermore, given the presence of recirculating radicals like OH, which species are appropriate to identify these reaction zones? Finally, in these regions, what are the modes of combustion involved?
5. What are the physical mechanisms of MILD combustion? Specifically, what is the balance between autoignition and flame-propagation? Given the high reactants temperature, autoignition is likely to play a significant role, but as mentioned in the review discussed earlier, thin reaction zones have also been observed.
6. How are different turbulent scales interacting in MILD combustion? In MILD combustion, it was suggested that chemical reactions and turbulence were occurring over similar scales and thus the interaction between reaction zones and turbulent structures could be significant.

These questions are tackled in this thesis using DNS data. DNS is used here because of the physical insights that can be obtained from them as they resolve all scales of turbulence and chemistry. The first part of this thesis will rely on the analysis of DNS data of homogeneous isotropic turbulence and premixed flames. For the study of MILD combustion, a methodology to conduct DNS of MILD combustion with mixture fraction variation is developed and the DNS data generated are then analysed to answer the questions listed above.

1.5 Thesis structure

The structure of this thesis is as follows. Chapter 2 describes the governing equations and the methodology used to perform the DNS of MILD combustion with mixture fraction variations. The turbulence and thermochemical characteristics of the DNS data of MILD combustion generated here is also detailed.

Chapter 3 discusses the first part of this thesis work. In particular, the analysis of non-reacting turbulence and turbulent premixed flames, answering the points 1 and 2 of the above list, is presented. In particular, a multiscale analysis method, called the bandpass filtering method, is presented and applied to DNS of homogeneous isotropic turbulence to study the vortex stretching mechanism and the scale-locality of the energy cascade at various Reynolds numbers. Subsequently, the same method is applied to DNS of statistically planar turbulent premixed flames propagating in homogeneous turbulence. This latter analysis is focused on the vortex stretching mechanism and on identifying the scales of eddies imparting the most strain on the flame.

The analysis of the DNS of MILD combustion generated in this thesis work starts in chapter 4 where the inception of MILD combustion is studied. In particular, the role of radicals on the onset of MILD combustion is analysed and the implication for previously proposed definitions of MILD combustion is discussed.

In chapter 5, the structure of the reaction zones in MILD combustion, which is the subject of the point 4 above, is analysed to provide some fundamental insights. The use of typical species for the identification of reaction zones is also discussed. Furthermore, given the existence of mixture fraction variations, the modes of combustion, from non-premixed to premixed, are studied.

The mechanism of MILD combustion and its stabilisation are investigated in chapter 6. In particular, the balance between ignition and propagative flame processes is analysed and described using a flux analysis of the species transport equation.

Chapter 7 presents a multiscale analysis of the energy cascade and vortex stretching in MILD combustion using the bandpass filtering method and evaluate the effect of the volumetric heat release on these mechanisms.

The main findings of this thesis work are summarized in chapter 8 along with directions for future work.

Chapter 2

Direct Numerical Simulation

This chapter describes the governing equations for turbulent reacting flows. The DNS methodology used for the simulation of MILD combustion is also presented, with details on the configurations and conditions of the DNS cases of MILD combustion run for this thesis.

2.1 Governing equations

The instantaneous governing equations for a fully compressible reacting flow consist of [Cant, 2013; Poinso & Veynante, 2011]

- Mass conservation equation:

$$\frac{\partial \rho}{\partial t} + \nabla \cdot (\rho \mathbf{u}) = 0 \quad (2.1)$$

where ρ denotes the mixture density and \mathbf{u} is the velocity vector.

- Navier-Stokes momentum equations:

$$\frac{\partial(\rho \mathbf{u})}{\partial t} + \nabla \cdot (\rho \mathbf{u} \otimes \mathbf{u}) = -\nabla p + \nabla \cdot \boldsymbol{\tau} \quad (2.2)$$

where $\boldsymbol{\tau}$ is the viscous stress tensor:

$$\boldsymbol{\tau} = \mu \left(\nabla \mathbf{u} + (\nabla \mathbf{u})^T \right) - \frac{2}{3} \mu (\nabla \cdot \mathbf{u}) \mathbf{I} \quad (2.3)$$

μ is the mixture dynamic viscosity, \mathbf{I} the identity matrix and T denotes the transpose operation.

Direct Numerical Simulation

- Species mass fractions conservation equations:

$$\frac{\partial \rho Y_\alpha}{\partial t} + \nabla \cdot (\rho \mathbf{u} Y_\alpha) = \dot{\omega}_\alpha - \nabla \cdot (\rho \mathbf{V}_\alpha Y_\alpha) \quad (2.4)$$

where Y_α is the mass fraction of species α with a diffusion velocity \mathbf{V}_α and chemical reaction rate $\dot{\omega}_\alpha$. The following compatibility conditions apply on Y_α , \mathbf{V}_α and $\dot{\omega}_\alpha$:

$$\sum_{\alpha=1}^N Y_\alpha = 1 \quad \sum_{\alpha=1}^N Y_\alpha \mathbf{V}_\alpha = 0 \quad \sum_{\alpha=1}^N \dot{\omega}_\alpha = 0 \quad (2.5)$$

with N being the number of species involved in the description of the combustion chemical kinetics.

- Internal energy equation:

$$\frac{\partial E}{\partial t} + \nabla \cdot (\rho \mathbf{u} E) = -\nabla \cdot (p \mathbf{u}) - \nabla \cdot \mathbf{q} + \nabla \cdot (\boldsymbol{\tau} \cdot \mathbf{u}) \quad (2.6)$$

where \mathbf{q} is the heat flux vector and E , the stagnation internal energy. These are defined as:

$$\mathbf{q} = -\lambda_{th} \nabla T + \sum_{\alpha=1}^N \rho \mathbf{V}_\alpha h_\alpha \quad (2.7)$$

$$E = \sum_{\alpha=1}^N Y_\alpha h_\alpha - \frac{p}{\rho} + \frac{1}{2} \mathbf{u} \cdot \mathbf{u} \quad (2.8)$$

where λ_{th} is the mixture thermal conductivity.

The enthalpy of species α is defined as:

$$h_\alpha = \int_{T_0}^T c_{p,\alpha} dT + \Delta h_{f,\alpha}^0 \quad (2.9)$$

where $c_{p,\alpha}$ is the mass specific heat capacity of species α at constant pressure and $\Delta h_{f,\alpha}^0$ is the species formation enthalpy at the reference temperature T_0 .

- Thermal equation of state for the mixture:

$$p = \rho R^0 T \sum_{\alpha=1}^N \frac{Y_\alpha}{W_\alpha} \quad (2.10)$$

R^0 is the universal gas constant and W_α is the molar mass of the species α .

2.1.1 Thermodynamic and transport quantities

For a semi-perfect gas, the molar specific heat capacity at constant pressure, $\bar{c}_{p,\alpha}$ depends on temperature. This dependency is modelled using a polynomial of the form [Cant, 2013]:

$$\frac{c_{p,\alpha}}{R^0} = \sum_{j=1}^J a_{\alpha,j}^{(l)} T^{j-1}, \quad (2.11)$$

In the present work, polynomials of degree 5 are used. The coefficients $a_{\alpha,j}^{(l)}$ are different depending on the species and the temperature interval. They are obtained from the CHEMKIN database [ReactionDesign, 2015].

The molecular transport terms are represented using the relation [Smooke & Giovangigli, 1991]

$$\frac{\lambda_{th}}{c_p} = A_\lambda \left(\frac{T}{T_0} \right)^r \quad (2.12)$$

where $c_p = \sum Y_\alpha c_{p,\alpha}$ is the mixture specific heat capacity at constant pressure. A_λ , r and T_0 are constants. The mixture dynamic viscosity, μ , is then given by

$$\mu = \frac{\lambda_{th}}{c_p} Pr \quad (2.13)$$

where $Pr = 0.7$ is the mixture Prandtl number which is assumed to be a constant. The diffusive mass flux for species α is represented using Fick's law:

$$\rho \mathbf{V}_\alpha Y_\alpha = -\rho D_\alpha \nabla Y_\alpha \quad (2.14)$$

where the diffusion coefficient D_α for each species is given by

$$D_\alpha = \frac{\lambda_{th}}{\rho c_p Le_\alpha} \quad (2.15)$$

Le_α is the Lewis number of the species α and is assumed to be constant, but takes different values for different species.

The use of constant Lewis numbers does not guarantee that the continuity equation will be recovered by summing all the species mass fraction equations. Instead, this yields

$$\frac{\partial}{\partial t} \rho + \nabla \cdot (\rho \mathbf{u}) = \sum_{\alpha=1}^N \nabla \cdot (\rho D_\alpha \nabla Y_\alpha) \quad (2.16)$$

where the compatibility conditions have been applied. By comparison to the continuity equation, the quantity on the right hand side is an error term. It can be removed by

Direct Numerical Simulation

adding a correction to the diffusion velocity [Ern & Giovangigli, 1994]:

$$\rho \mathbf{V}_\alpha Y_\alpha = -\rho D_\alpha \nabla Y_\alpha + \rho \mathbf{V}^{(c)} Y_\alpha \quad (2.17)$$

where the correction velocity $\mathbf{V}^{(c)}$ is given by:

$$\rho \mathbf{V}^{(c)} = \sum_{\alpha=1}^N \rho D_\alpha \nabla Y_\alpha \quad (2.18)$$

2.1.2 Reaction rate

For a reaction mechanism involving M steps, the chemical reaction rate, $\dot{\omega}_\alpha$, for the species α , is evaluated using:

$$\dot{\omega}_\alpha = W_\alpha \sum_{m=1}^M \bar{\dot{\omega}}_{\alpha,m} \quad (2.19)$$

where $\bar{\dot{\omega}}_{\alpha,m}$ is the molar production rate of species α in the step m .

In this mechanism, forward and backward reaction steps are expressed as

$$\sum_{\alpha=1}^N \nu'_{\alpha,m} \mathcal{M}_\alpha \rightleftharpoons \sum_{\alpha=1}^N \nu''_{\alpha,m} \mathcal{M}_\alpha \quad (2.20)$$

where the molar production rate for a species, $\bar{\dot{\omega}}_{\alpha,m}$, is given by

$$\bar{\dot{\omega}}_{\alpha,m} = (\nu''_{\alpha,m} - \nu'_{\alpha,m}) \left[k_{f,m}(T) \prod_{\beta=1}^N c_\beta^{\nu'_{\beta,m}} - k_{b,m}(T) \prod_{\beta=1}^N c_\beta^{\nu''_{\beta,m}} \right]. \quad (2.21)$$

The forward and backward coefficients $k_{f,m}$ and $k_{b,m}$ are evaluated using an Arrhenius expression of the form:

$$k_m(T) = A_m T^{n_m} \exp\left(-\frac{E_m}{R^0 T}\right) \quad (2.22)$$

In the above expression, usually, only the forward rate coefficients are provided while the backward rate coefficients are evaluated using the equilibrium constant for concentrations [Cant, 2013].

For a reaction step, m , involving third bodies:

$$\sum_{\alpha=1}^N \nu'_{\alpha,m} \mathcal{M}_\alpha + M \rightarrow \sum_{\alpha=1}^N \nu''_{\alpha,m} \mathcal{M}_\alpha + M \quad (2.23)$$

the molar production rate is evaluated with the following formula

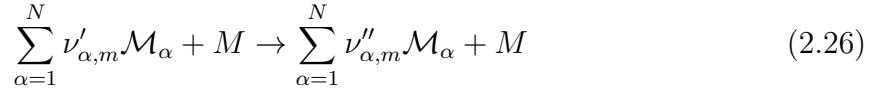
$$\bar{\omega}_{\alpha,m} = \left(\nu''_{\alpha,m} - \nu'_{\alpha,m} \right) k_m(T) c_M \prod_{\beta=1}^N c_{\beta}^{\nu'_{\beta,m}}. \quad (2.24)$$

The molar concentration of the third body, M , is given by

$$c_M = \sum_{\alpha=1}^N \eta_{\alpha,M} c_{\alpha} \quad (2.25)$$

where $\eta_{\alpha,M}$ are the third-body efficiencies for the species M and c_{α} is the molar concentration of species α .

Certain reaction steps may have a dependency with pressure. In the low-pressure limits, they would require a third body collision to provide the energy necessary for the reaction, i.e. they are of the type



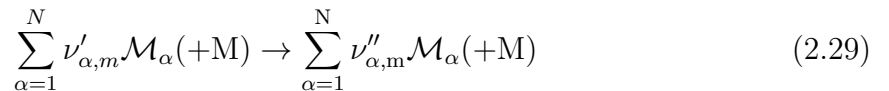
In the high pressure limits, the third-body collisions are not necessary, and the reaction step can thus be represented by



For intermediate pressure, the dependency of the reaction with the pressure has to be taken into account. The Lindemann form is used for that purpose [[Lindemann, 1922](#)]

$$k_{L,m} = \frac{k_{\infty}}{1 + k_{\text{fall}}/c_M} \quad (2.28)$$

where k_{∞} is the high pressure limit constant, $k_{\text{fall}} = k_{\infty}/k_0$ is the fall-off rate coefficient, k_0 is the low pressure limit rate constant, c_M the third body concentration. Reactions falling into that pressure regime, called the fall-off region, will be indicated with (+M) rather than a +M following the convention used in CHEMKIN:



2.2 Non-premixed MILD combustion

This section describes the methodology used to perform the DNS of MILD combustion. The numerical code used is SENG2 [Cant, 2013]. It is a fully compressible code that solves the continuity, momentum, internal energy and species mass fractions equations, presented in section 2.1, for turbulent reacting flows. The spatial derivatives are discretized using a tenth order central difference scheme that reduces gradually to a fourth order scheme near the boundaries. The time integration is performed using a third order Runge-Kutta scheme. In this section, the methodology, configuration and conditions used for the simulation of MILD combustion are explained.

2.2.1 Numerical flow configuration

MILD combustion of mixtures having spatio-temporal variations of mixture fraction with recirculated exhaust gases is of interest in the present thesis work. However, typical MILD combustion systems are of a few tens of centimeters in size involving EGR or either spatially or temporally staged fuel injection techniques. DNS of such system is not feasible at this time because of the heavy computational cost involved and thus a simplified two-stage approach is used here following earlier studies [Minamoto et al., 2014b]. The first stage mimics the mixing of fuel, air and exhaust gases yielding inhomogeneous mixture field which subsequently undergoes combustion in the second stage. This two-stage process is illustrated schematically in Fig. 2.1. The left box titled “Preprocessing” represents the first stage elaborated in section 2.2.2. The symbol \dot{Q}_{out} represents the cooling of exhaust gases.

The computational domain for MILD combustion (second stage) is a cuboid with periodic boundary conditions in the y and z directions. Reflecting inflow and non-reflecting outflow are specified for the x -direction using the Navier-Stokes characteristics boundary condition (NSCBC) approach [Poinsot, 1992]. Spatially and temporally varying mixture of vitiated air and fuel (generated in the first stage) is fed at an average velocity of U_{in} through the inlet located at $x = 0$ of the computational domain. The turbulent velocity, \mathbf{u} , species mass fractions, Y_i , of the partially premixed mixture and temperature, T , of the inflowing mixture are specified as

$$\mathbf{u}(x = 0, y, z, t) = \hat{\mathbf{u}}(\underline{x}(t), y, z) \quad (2.30)$$

$$Y_i(x = 0, y, z, t) = \hat{Y}_i(\underline{x}(t), y, z) \quad (2.31)$$

$$T(x = 0, y, z, t) = \hat{T}(\underline{x}(t), y, z) \quad (2.32)$$

where $\hat{\mathbf{u}}$, \hat{Y}_i and \hat{T} are the turbulent velocity, species mass fractions and temperature obtained during the (first) preprocessing stage to be explained in section 2.2.2. The x -location of the scanning plane, $\underline{x}(t)$, moves with a velocity of $U_{in} = 20$ m/s inside the preprocessed field.

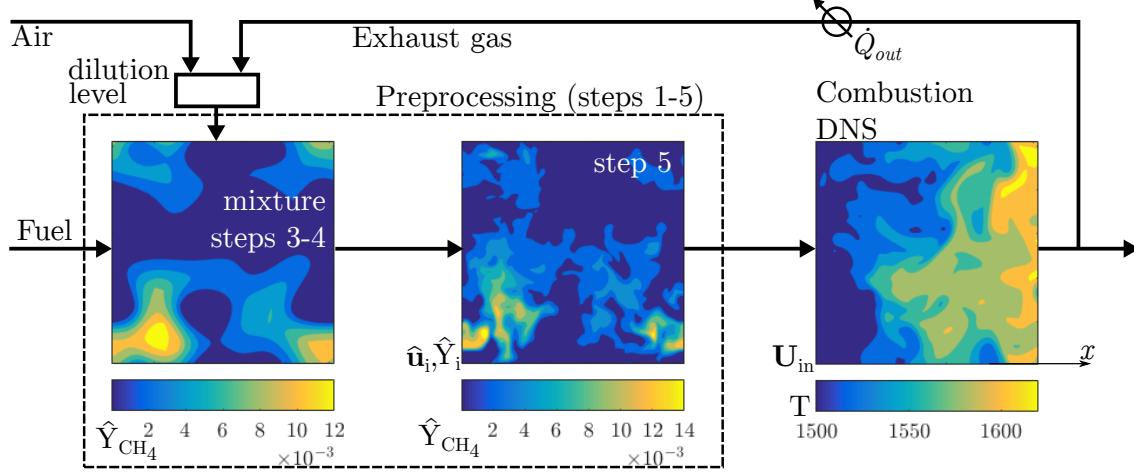


Fig. 2.1 Schematic illustration of DNS steps followed for MILD combustion of inhomogeneous reactant mixture field obtained with internal recirculation of exhaust gases. Steps 1-5 are discussed in section 2.2.2.

2.2.2 Generation of initial and inflow fields

The flow and mass fraction fields for the combustion DNS are generated by extending the methodology described by Minamoto et al. [2013]; Minamoto & Swaminathan [2014b]; Minamoto et al. [2014b]. This preprocessing step mimics the mixing of vitiated air with fuel (first stage of the two-stage approach) before autoignition occurs. Earlier studies [Minamoto et al., 2013; Minamoto & Swaminathan, 2014b; Minamoto et al., 2014b] considered premixed MILD combustion and thus there was no variation of mixture fraction. Since the influence of mixture fraction variation on the MILD reaction zones structure is of interest for this thesis, appropriate modifications are introduced to generate fields which are representative of non-premixed MILD combustion system. The steps described below are followed to obtain the desired fields of $\hat{\mathbf{u}}$ and \hat{Y}_i .

Step 1: A turbulence field is generated first by conducting a DNS of freely decaying, homogeneous isotropic turbulence inside a periodic cube. The initial turbulence field is specified using a prescribed turbulent kinetic energy spectrum as described by Rogallo [1981]. Here, the Batchelor-Townsend spectrum [Batchelor & Townsend,

Direct Numerical Simulation

1948] is used with the following two controlling parameters, $c_0 = 14000$ and $k_0 = 1.6$. Additional information on this turbulent energy spectrum can be found in appendix A. This simulation is run until the turbulence is fully developed, which is recognised when the velocity derivative skewness reaches a value of about -0.5 .

Step 2: One-dimensional freely propagating premixed laminar flames for a wide range of mixture fractions (or equivalence ratios) are simulated with CANTERA using the same kinetic mechanism to be employed for the combustion DNS. The reactants considered are a mixture of methane and diluted-air (without intermediate species) with desired dilution levels (specified in section 2.2.4). Based on the earlier studies [Minamoto et al., 2013; Minamoto & Swaminathan, 2014b; Minamoto et al., 2014b], the reactant temperature is set at $T_r = 1500$ K, which is higher than the reference autoignition temperature. This step yields a database of one-dimensional laminar premixed flames having thermochemical conditions of interest and these flames are parametrised using the mixture fraction (or equivalence ratio) and progress variable. Such database is illustrated in Fig. 2.2 for some representative species mass fractions.

Step 3: Following the method described by Eswaran & Pope [1988b], two scalar fields bounded between 0 and 1 are generated by specifying scalar-energy spectrum functions having prescribed length scales, ℓ_c and ℓ_Z , and means, $\langle c \rangle$ and $\langle Z \rangle$. These two fields are taken to be the initial reaction progress variable, \widehat{c}_Y , and mixture fraction, \widehat{Z} , fields. The progress variable is defined as

$$\widehat{c}_Y = \frac{Y_{\text{CH}_4} - Y_{\text{CH}_4,p}}{Y_{\text{CH}_4,r} - Y_{\text{CH}_4,p}}, \quad (2.33)$$

where the subscripts r and p in the methane mass fraction, Y_{CH_4} , denote respectively the reactant and product mixtures of a laminar flame computed in Step 2. The mixture fraction is defined using Bilger's definition [Bilger et al., 1990]:

$$\widehat{Z} = \frac{\beta - \beta_{ox}}{\beta_f - \beta_{ox}} \quad (2.34)$$

where the subscripts f and ox denote fuel and vitiated air streams respectively (see Fig. 2.1), and $\beta = 2Y_C/W_C + 0.5Y_H/W_H - Y_O/W_O$ with the elemental mass fractions and atomic masses for the elements carbon, hydrogen and oxygen. Typical variations of these two fields generated are shown in Fig. 2.3 for the mid x - y plane of the computational domain and additional details on the methodology are provided

2.2 Non-premixed MILD combustion

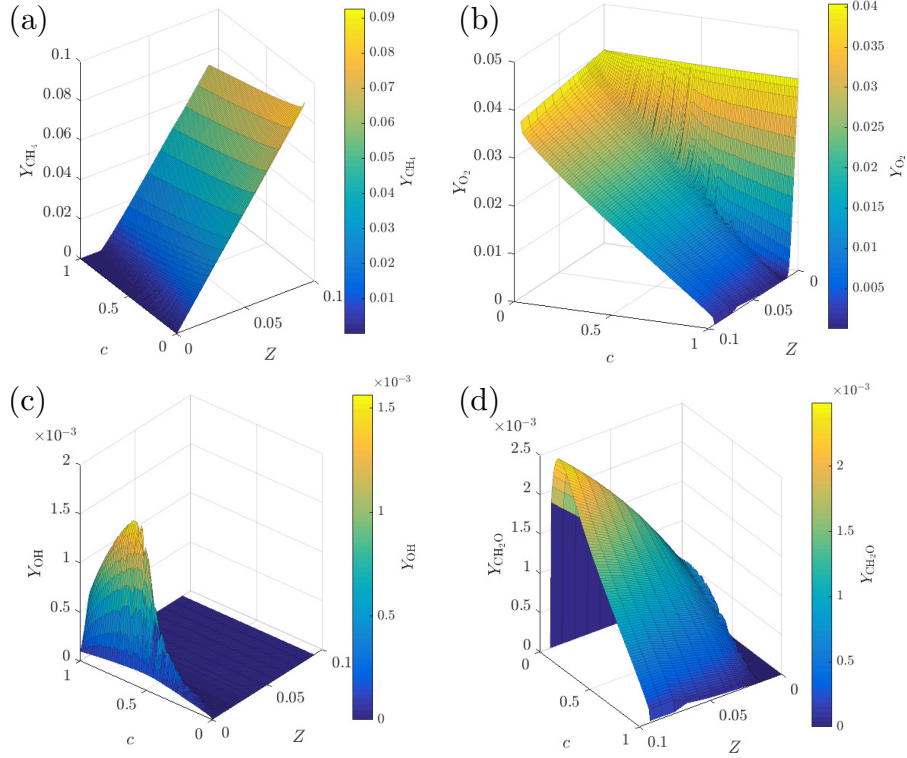


Fig. 2.2 Species mass fractions of MILD premixed flames parametrized on Z and c used for the MILD combustion DNS pre-processing stage (step 2).

in appendix A. As expected $\widehat{c_Y}$ presents variations bounded between 0 and 1 by construction with a prescribed lengthscale. On the other hand, \widehat{Z} has a smaller range of variation with a typically larger lengthscale. The probability density functions (pdfs) of these two fields are also shown in this figure. The pdfs of $\widehat{c_Y}$ for the various cases show a clearly bimodal behaviour for the choices of $\langle c \rangle$ and ℓ_c . On the other hand, the pdfs of \widehat{Z} vary according to the case considered. For cases AZ1 and BZ1, the pdfs have a peak value centred around the specified mean value of Z while for case AZ2, the pdf does not present a peak value. It should be noted that there are no pocket of pure fuel in the present domain as a result of the small value for $\langle Z \rangle$ and the limited variations for ℓ_Z . Further details about the various cases considered are provided at the end of this section and in section 2.2.4.

Step 4: The species mass fractions obtained in Step 2 are used to initialise the scalar mass fraction fields depending on the local values of \widehat{Z} and $\widehat{c_Y}$. If the local value of \widehat{Z} is beyond the flammability limits then the mixing line solution in the mixture fraction space is used to obtain the local species mass fraction values. The temperature

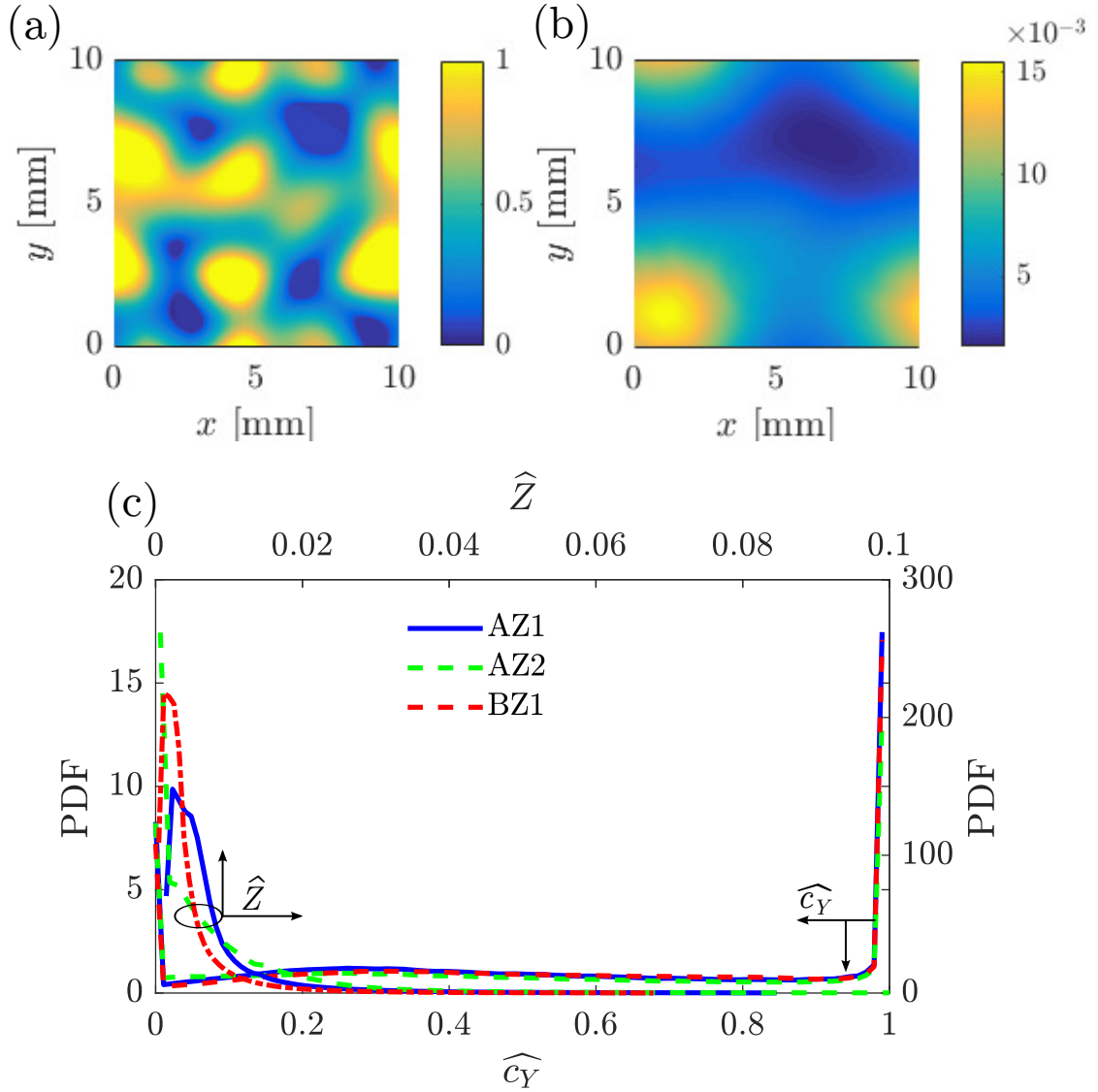


Fig. 2.3 Representative spatial variation of (a) $\widehat{c_Y}$ and (b) \widehat{Z} , obtained at the end of Step 3 for case AZ1. The results are shown for the mid x - y plane. The pdfs of $\widehat{c_Y}$ and \widehat{Z} for the sample from the entire domain are shown in (c) for all cases.

is set to 1500 K. The scalar field obtained thus has partially premixed mixture (varying equivalence ratio) containing reactants, partially burnt mixtures and products. These conditions would be quite similar to those in the recirculation zones of a MILD combustion burner investigated experimentally, for example the one in [Ozdemir & Peters, 2001]. The fluctuations in the scalar mass fraction fields obtained in this step do not have any correlation with the turbulence field obtained

in Step 1. This lack of correlation may lead to some non-physical transients, which are overcome using the method described in the next step.

Step 5: The scalars and the turbulence from Step 1 are allowed to interact and evolve inside the periodic domain without any chemical reactions for a duration of about one large eddy timescale, l/u' where l and u' are the integral length scale and root-mean-square (rms) value of the turbulence field. Based on past studies, the duration of this simulation was kept deliberately below the ignition delay time to avoid occurrence of combustion but sufficiently long for the interactions between the scalar and velocity fields to have developed in a meaningful way. Indeed, past DNS studies of scalar mixing using the same methodology to generate initial scalar fields [Eswaran & Pope, 1988b; Ruetsch & Maxey, 1991; Yeung & Pope, 1993] have shown that such durations already allow for these correlations to develop. The scalar fields obtained at the end of this step are shown in Figs. 2.4, 2.5 and 2.6. These are shown for the 3 cases run in the present work. The characteristics of each case are further discussed in section 2.2.4. It is clear that unburnt ($\widehat{c_Y} = 0$), partially burnt (intermediate values of $\widehat{c_Y}$), and fully burnt ($\widehat{c_Y} = 1$) mixtures are present. Furthermore, the equivalence ratio, $\widehat{\phi} = \widehat{Z} (1 - \widehat{Z}_{st}) / (\widehat{Z}_{st} (1 - \widehat{Z}))$, ranges from 0 to 10 inside the computational domain. Intermediate species and radicals are also present as seen in Figs. 2.4d, 2.5d and 2.6d. These fields serve as the initial and inflowing fields for the combustion DNS.

A desired level of dilution is obtained by changing the reactant mixture used for the laminar calculations in Step 2. The length scales ℓ_c and ℓ_Z denote typical eddy sizes for the progress variable and mixture fraction fields respectively and they will influence the spatio-temporal evolution of mixing and reactions. The chemical (flame) length scales are usually smaller than the mixing length scale and so the case of $\ell_c > \ell_Z$ is excluded. Hence, three cases, which are discussed in section 2.2.4, are considered here. The first two cases, noted AZ1 and AZ2, have almost the same dilution level but different ℓ_c/ℓ_Z values. The third case, called BZ1, has the same length scale ratio as the first case but substantially higher dilution level. The PDFs of $\widehat{c_Y}$ and \widehat{Z} for the initial and inflowing fields of these three cases are shown in Fig. 2.7. The maximum \widehat{Z} observed in the domain is about 0.1 which corresponds to $\widehat{\phi} \approx 11$ for cases AZ1 and AZ2 and $\widehat{\phi} \approx 19$ for case BZ1, but the pdf for $\widehat{Z} > 0.04$ is small and thus is not shown in Fig. 2.7. The value of $\widehat{Z} = 0.04$ corresponds to $\widehat{\phi} = 4.1$ for cases AZ1 and AZ2, and $\widehat{\phi} = 7.1$ for case BZ1, implying a substantial variation in equivalence ratio. Compared to the initial pdfs of \widehat{Z} shown in Fig. 2.3, the pdfs of \widehat{Z} after the mixing in Step 5 have not changed much since this mixing simulation time is kept to be about one eddy turnover time and the peak of

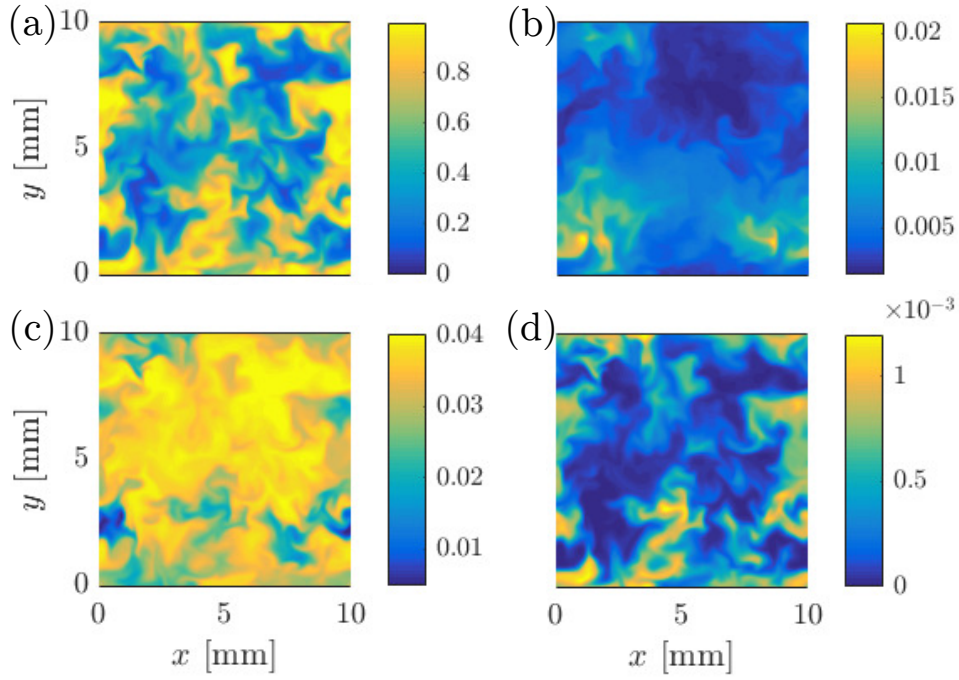


Fig. 2.4 Spatial variation of (a) \widehat{c}_Y , (b) \widehat{Z} , (c) \widehat{Y}_{O_2} and (d) \widehat{Y}_{OH} in the mid x - z plane at the end of Step 5 for case AZ1.

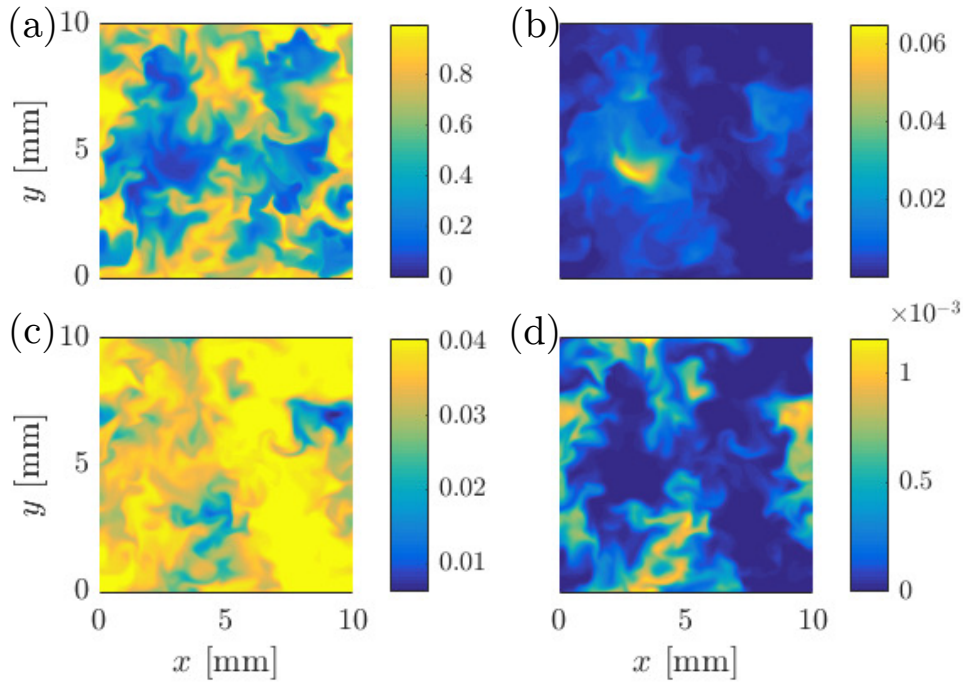


Fig. 2.5 Spatial variation of (a) \widehat{c}_Y , (b) \widehat{Z} , (c) \widehat{Y}_{O_2} and (d) \widehat{Y}_{OH} in the mid x - z plane at the end of Step 5 for case AZ2.

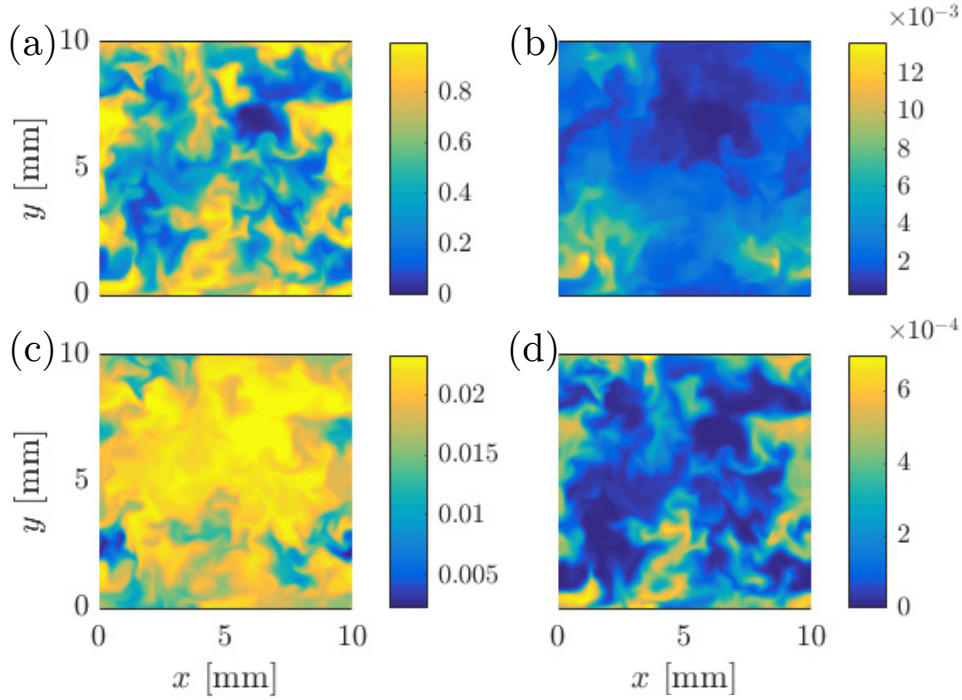


Fig. 2.6 Spatial variation of (a) \widehat{c}_Y , (b) \widehat{Z} , (c) \widehat{Y}_{O_2} and (d) \widehat{Y}_{OH} in the mid x - z plane at the end of Step 5 for case BZ1.

the Z pdf is already close to $\langle Z \rangle$. On the other hand, the pdfs of \widehat{c}_Y present much more variation showing the presence of unburnt, intermediate and burnt mixtures. The mixing process has also created high probability for intermediate values of c . Finally, the large variations of Z in the inflowing mixture yields a large variation in the reactivity of the mixture with various ignition delay times. This is shown in Fig. 2.8 where the pdf of ignition delay time computed from laminar calculations in a 0D adiabatic homogeneous reactor with CANTERA is shown for the inflowing mixture. It should be noted that those laminar calculations consider the unburnt mixture and thus the presence of radicals is not accounted for in these calculations. This particular aspect of MILD combustion will be further elaborated in chapters 4 and 6.

2.2.3 Combustion mechanism

The fuel considered for this study is methane as in previous studies [Minamoto et al., 2013; Minamoto & Swaminathan, 2014b; Minamoto et al., 2014b] with similar turbulence and dilution conditions. This helps us to contrast the difference between premixed and non-premixed turbulent MILD combustion. The skeletal mechanism of Smooke & Giovangigli [1991] is selected following earlier studies. Since the chemiluminescent

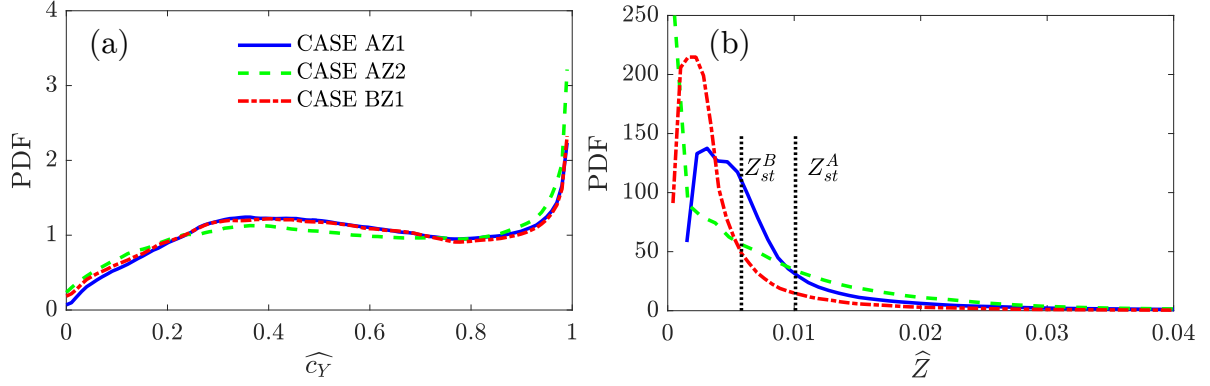


Fig. 2.7 Pdf of (a) \hat{c}_Y and (b) \hat{Z} for the initial and inflowing mixture fields (after Step 5) used for combustion DNS.

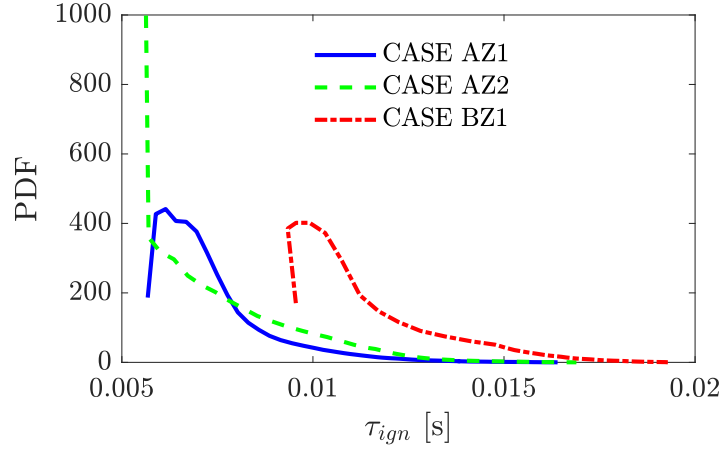


Fig. 2.8 Pdf of τ_{ign} for the initial and inflowing mixture field (after Step 5) used for combustion DNS.

species such as OH^* and CH^* are also of interest from the perspective of experimental investigation [Evans et al., 2015; Sidey & Mastorakos, 2015b], the Smooke & Giovangigli mechanism is modified to include precursor species required for OH^* chemistry taken from Kathrotia et al. [2012]. The elementary reactions required for the precursor species are taken from Bilger et al. [1990]. The kinetic mechanism assembled thus involves 19 species and 58 reactions in total and this mechanism is listed in appendix B along with sources for the respective rate constants. This modified mechanism is referred as MS-58 and that from Bilger et al. [1990] is called KEE-58 in the discussion below.

Figures 2.9, 2.10 and 2.11 compare the measured and computed laminar flame speeds and ignition delay times. The laminar flame speeds are computed using CANTERA with 4 different chemical mechanism, viz., GRI-3, Smooke & Giovangigli, MS-58 and KEE-58

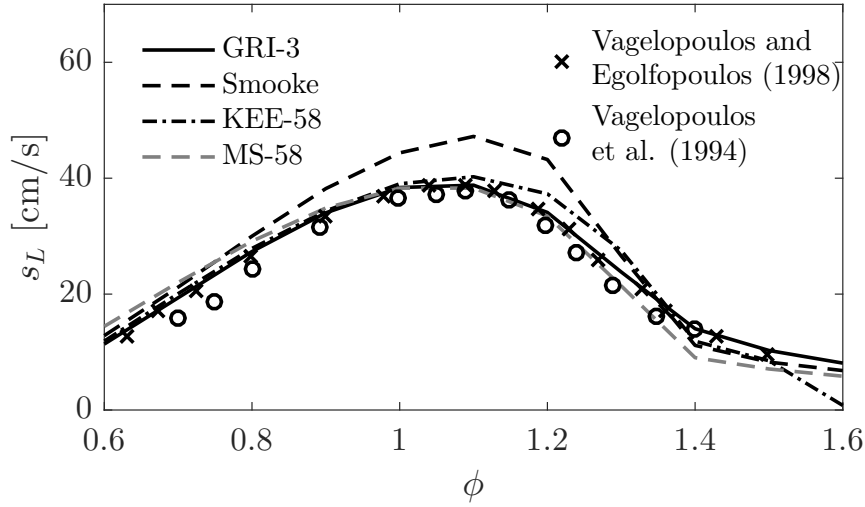


Fig. 2.9 Comparison of computed and measured laminar flame speeds at standard conditions. Experimental data are taken from Vagelopoulos & Egolfopoulos [1998]; Vagelopoulos et al. [1994].

using the following expression [Poinso & Veynante, 2011]:

$$s_L = -\frac{1}{\rho_u Y_{\text{CH}_4}} \int_{-\infty}^{+\infty} \dot{\omega}_{\text{CH}_4} dx \quad (2.35)$$

The experimental results are taken from Vagelopoulos & Egolfopoulos [1998]; Vagelopoulos et al. [1994]. It is clear that the MS-58 mechanism assembled using reactions from Smooke & Giovangigli [1991] and Bilger et al. [1990] predicts the laminar flame speed, s_L , variation with equivalence ratio, ϕ , for methane-air mixture very well. These results are comparable to GRI-3 values and MS-58 slightly under-predicts s_L for $\phi \geq 1.4$.

The computed ignition delay times for methane-air mixture at 1 and 4 atm and various equivalence ratios over a wide range of temperatures are compared to measurements in Figs. 2.10 and 2.11. These were computed with CANTERA by simulating the ignition process in an adiabatic zero-dimensional reactor. As one would expect, the GRI-3 mechanism estimates the ignition delay time accurately and, Smooke & Giovangigli and MS-58 mechanisms overestimate the ignition delay time for both pressures but the level of overestimation, in comparison to GRI-3, remains almost constant over the temperature range. The KEE-58 mechanism substantially overestimates the ignition delay time as shown in Fig. 2.11 for the case at 4 atm. At 1 atm, it performs better than the other two mechanisms for relatively high temperature, but substantially over predicts the ignition delay time for the temperature of interest here, $T = 1500\text{K}$.

Direct Numerical Simulation

It seems that the mechanism MS-58 is very good for flame propagation, quite good for ignition delay time estimates and also includes OH^* precursors, and thus it is adequate to address the objectives of this study. However, the over estimate of the ignition delay time must be borne in mind while investigating the simulation results. As expected, the reactions involving OH^* do not affect these estimates while allowing us to track OH^* in the DNS. It is also worth remarking here that CH^* and other chemiluminescent species are not included because C_2 and higher species acting as precursors for them are not available in the MS-58 mechanism. The accuracy for the ignition delay times can be improved by including C_2 chemistry. However, including a comprehensive mechanism such as GRI-3 with C_2 and higher species is prohibitively expensive for DNS at this time. Also, there is no chemical mechanism with OH^* precursor which is suitable for DNS and so MS-58 mechanism is assembled for this study.

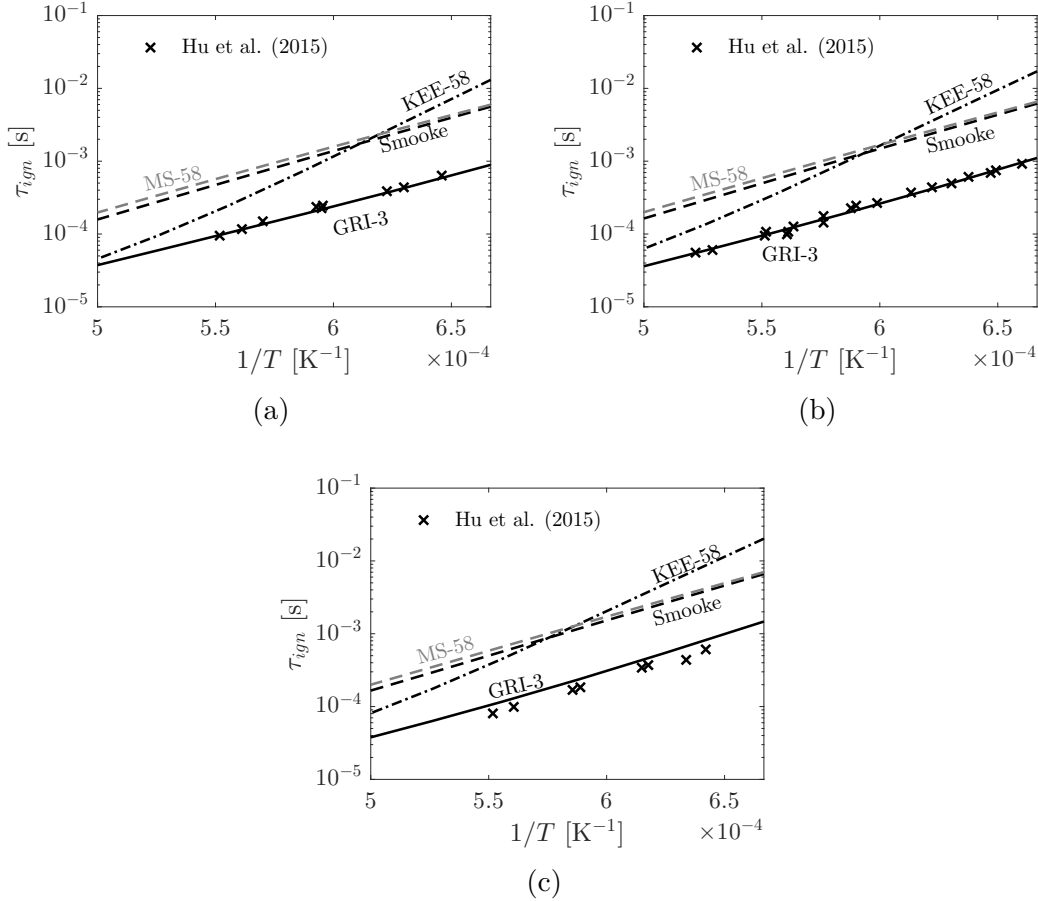


Fig. 2.10 Ignition delay time for CH_4 -air mixture at atmospheric pressure and for (a) $\phi = 0.5$, (b) $\phi = 1.0$ and (c) $\phi = 2.0$. Experimental data are from [Hu et al. \[2015\]](#).

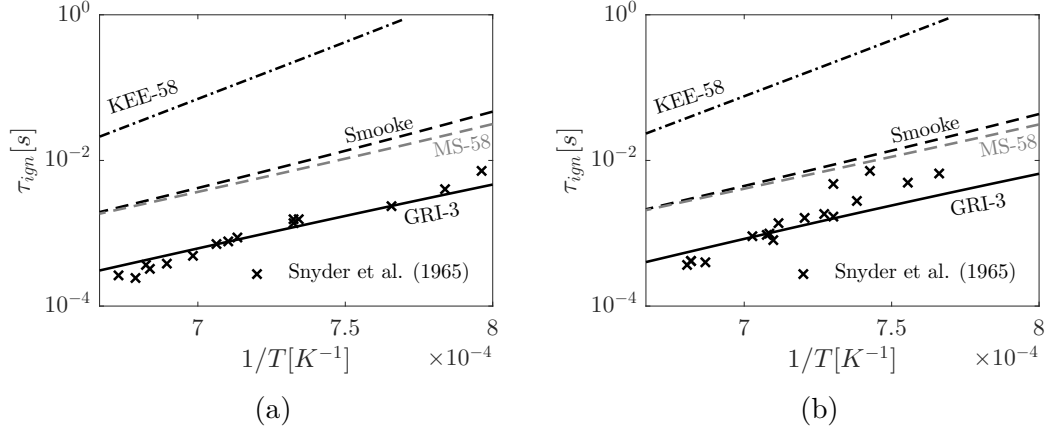


Fig. 2.11 Ignition delay time for CH_4 -air mixture at 4 atm and for (a) $\phi = 0.5$ and (b) $\phi = 1.0$. Experimental data are from Snyder et al. [1965].

2.2.4 MILD combustion conditions

Two dilution levels are considered, the reference case has 3.5% oxygen by volume in the oxidiser mixture, which is the same as for the Case B of Minamoto et al. [2014b] in terms of dilution conditions. The earlier study considered the premixed case but this study is with non-premixed counterpart which includes spatio-temporally varying mixture fraction. The oxygen level is reduced to 2% by volume for the case BZ1. The mole fractions of major species in the diluted oxidiser mixture for these two conditions are listed in Table 2.1. The sum of the mole fractions must be equal to 1 and so the rest of the mixture is N_2 .

Table 2.1 Oxidiser composition for the MILD mixture.

Case	$X_{\text{O}_2,ox}$	$X_{\text{H}_2\text{O},ox}$	$X_{\text{CO}_2,ox}$
AZ1-2	0.035	0.134	0.067
BZ1	0.020	0.146	0.073

The turbulence and thermochemical conditions for the combustion DNS are summarized in Tables 2.2 and 2.3. The values in those tables are for the initial conditions of the reacting DNS of MILD combustion (at the end of step 5, as described in section 2.2.2). The turbulence conditions used here are similar to the Case B of Minamoto et al. [2014b] and are the same for all cases. The turbulence field obtained at the end of Step 5 has an rms value of $u' \approx 16.66$ m/s, for the velocity fluctuations and an integral length scale of $l \approx 1.42$ mm. This gives a turbulence Reynolds number of $Re_t \approx 96$ and Taylor micro-scale Reynolds number of $Re_\lambda \approx 34.73$. There are about 7 integral

Direct Numerical Simulation

eddies inside the computational domain of size $L_x = L_y = L_z = 10$ mm. Since there are spatial variations of mixture fraction and progress variable (unburnt and burnt mixtures) fields, the ratio of their integral length scales is an important parameter. The influence of this parameter is also investigated by changing the value of ℓ_c/ℓ_Z from 0.77 to about 1 while keeping the dilution level the same. This case is denoted as AZ2 in Table 2.2. The condition of $\ell_c/\ell_Z > 1$ is seen to be unphysical because the thickness of either a propagating flame or an ignition kernel at a reactant temperature of about 1500 K is expected to be thinner than a representative mixture fraction length scale resulting from turbulent mixing of fuel and vitiated air.

Table 2.2 Initial scalar conditions for the MILD combustion DNS.

Case	l/ℓ_Z	$\langle X_{O_2} \rangle$	$X_{O_2}^{\max}$	ℓ_c/ℓ_Z	$\langle Z \rangle$	Z_{st}	σ_Z	$\langle c \rangle$	σ_c
AZ1	0.60	0.0270	0.035	0.77	0.008	0.010	0.0084	0.56	0.26
AZ2	0.79	0.0285	0.035	0.99	0.008	0.010	0.0105	0.56	0.28
BZ1	0.60	0.0160	0.020	0.77	0.0046	0.0058	0.0057	0.56	0.26

Table 2.3 Initial turbulent and mixing conditions for the MILD combustion DNS. $\tau_t = l/u'$ is a turbulent time scale.

Case	u' [m/s]	l [mm]	λ [mm]	$\tau_t/\langle \tau_{ign} \rangle$	$\tau_t/\langle \delta_{th}/s_L \rangle$	$\langle N_Z \rangle$ [s ⁻¹]	σ_{N_Z} [s ⁻¹]
AZ1	16.66	1.42	0.51	0.0109	0.1876	0.0303	0.1678
AZ2	16.66	1.42	0.51	0.0109	0.1876	0.0826	0.3615
BZ1	16.66	1.42	0.51	0.0073	0.0798	0.0142	0.0087

From Table 2.2, it can be observed that all cases correspond, on average, to a lean condition with an equivalence ratio of approximately 0.8. The variance of the mixture fraction in case AZ2 is higher than for case AZ1 as that case was initialised with a smaller ℓ_Z which allows for more variations of Z . Furthermore, the maximum O_2 concentrations found in the computational domain for all cases correspond to the concentration from the oxidiser composition (see Table 2.1) meaning that pure oxidiser (vitiated air) is present in the domain. All cases share similar statistics, $\langle c \rangle$ and σ_c , for the progress variable field which is to be expected because similar initial c field was used. An average value of c equal to 0.56 signifies the presence of both burnt and unburnt mixture. Table 2.3 highlights the ratio between the turbulent timescale and the chemical timescales for the average mixture ($\phi = 0.8$) and it is seen that the turbulent timescale is smaller than the chemical ones. Some mixing characteristics, the mean scalar dissipation rate of mixture fraction $\langle N_Z \rangle$ and its standard deviation σ_{N_Z} , are also provided. These indicate that case AZ2 has a stronger mixing field than the other cases. This is to be expected as that

case has initially the smallest ℓ_Z . Thus, there are the most variations of Z in that case compared to the others.

The computational domain is discretised using $512 \times 512 \times 512$ uniform grid points which ensures that there are about 30 grid points inside the smallest chemical thickness for the mechanism MS-58 used here. This thickness is related to OH^* species reaction rate. The timestep used is 1 ns which is smaller than the shortest chemical timescale imposed by OH^* chemistry.

Each of these simulations has been run for about 1.5 flow-through time, which is defined as $\tau_f = L_x/U_{in}$. Statistics were collected after the first flow-through time to ensure that the transients from the initial conditions had left the domain before data sampling. These simulations have been run on ARCHER, a Cray XC30 system, and each simulation took about 550 hours on a wall-clock using 4096 cores.

2.2.5 On the choice of laminar configuration

Previously, in section 2.2.2 describing the methodology used to obtain the initial and inflowing fields, for Step 2, the choice was made to use a laminar premixed flame to construct the initial scalar fields. However, it can be argued that a PSR or counterflow flames could be alternative choices. As such, a comparison was performed between these various laminar configurations to assess whether they would have a high influence on the initial conditions.

Figure 2.12 compares the species mass fractions distributions, $Y_i(Z, c)$, obtained from premixed and PSR configurations for the AZ1-2 mixture conditions used in the DNS (see Table 2.1). There are very minor differences in the variations of major and minor species and thus the DNS solution would not be influenced by the choice of the canonical configuration used to get the initial field. The major and minor species variations with Z in a fully burning non-premixed combustion established in a counterflow configuration using the DNS mixture are shown in Fig. 2.13. The solutions from premixed and PSR configurations for the minimum and maximum values observed in these configurations are also shown using respectively crosses and circles. It is observed that the counterflow flame solution shown for a strain rate of 50 s^{-1} lies between the minimum and maximum of the premixed flame solution, mostly towards the reacting situation except for CH_2O which is a radical.

Thus, the variations of Y_i with Z and c are observed to be very similar for premixed, PSR and counterflow non-premixed configurations under fully reacting conditions. Furthermore, Z and c vary in the local normal direction across the reaction zone and thus the reaction zone structure in Z - c space does not depend on the flow configuration. From

these observations, it is thus clear that the choice of the canonical configuration will not greatly affect the DNS solution.

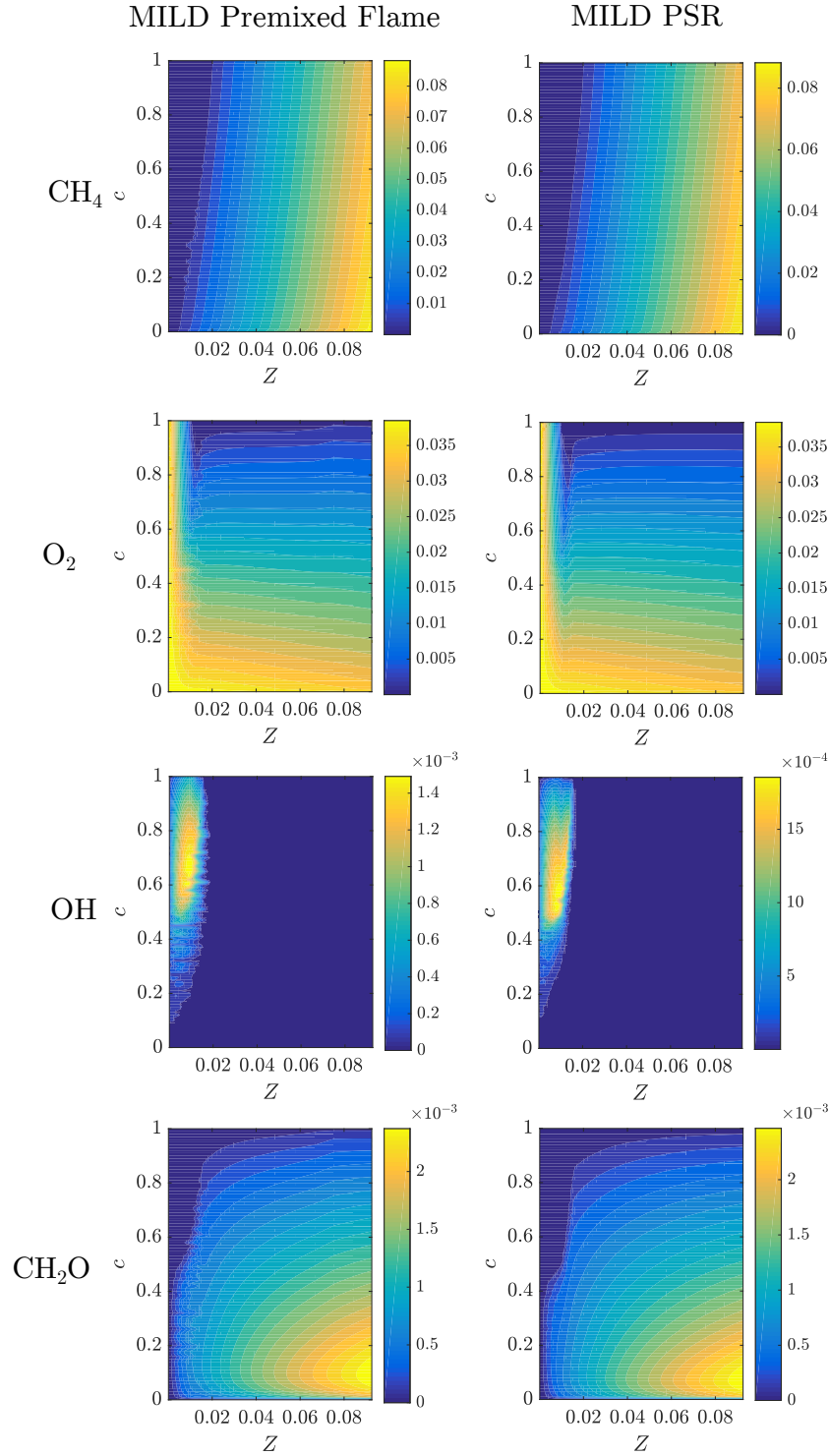


Fig. 2.12 Species mass fractions distribution for MILD premixed flames or MILD PSR.

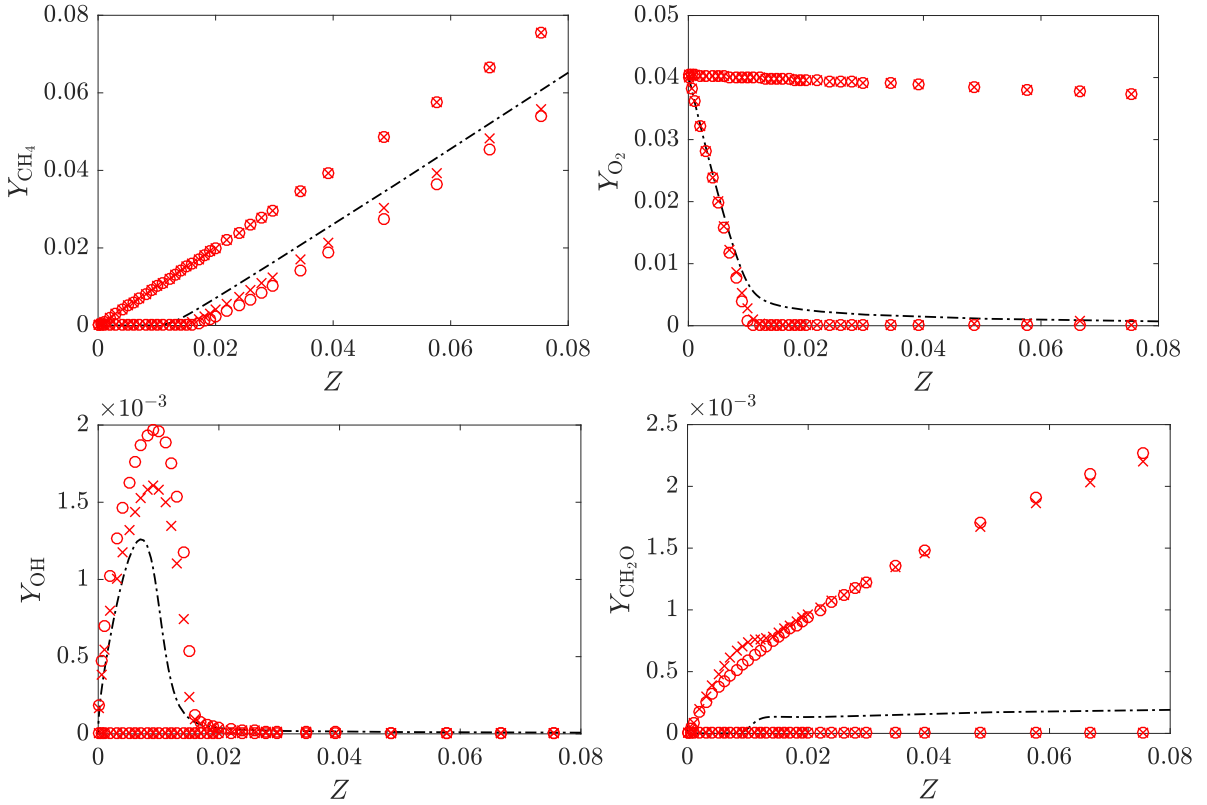


Fig. 2.13 Species mass fractions for a counterflow flame (dashed-dotted) with minimum and maximum of the associated premixed flame (cross) or PSR (circle).

2.3 Summary

In this chapter, the governing equations for turbulent reacting flows have been introduced and the methodology used to conduct DNS of MILD combustion with mixture fraction variations has been described. The turbulence and thermochemical conditions for each case considered have been presented. The data obtained using this methodology will be analysed to address the objectives listed in section 1.4. However, before embarking on that analysis, the next chapter will study the interactions of scales in turbulence and premixed flames to answer the two initial objectives.

Chapter 3

Multiscale Analysis of Turbulence and Premixed Flames

3.1 Background and objectives

As suggested by [Duwig et al. \[2012\]](#); [Galletti et al. \[2007\]](#); [Minamoto et al. \[2014b\]](#) and [Plessing et al. \[1998\]](#), the turbulence-chemistry interaction is of great importance in the understanding, and thus modelling, of MILD combustion. Indeed, there exists a strong coupling between turbulence and chemistry, both occurring over similar time scales which makes this analysis more complex than in conventional cases. One of the key mechanism of turbulence is the vortex stretching mechanism by which eddies are formed over multiple length scales. In this work, it is proposed to analyse how this mechanism and the energy cascade is affected in MILD combustion as the development of vortical structures will be greatly influenced by the presence of chemical reactions. Conversely, the presence of reactions and the mixing process will be affected by the turbulence field. However, DNS of reacting flows are subject to computational restrictions that limit the range of turbulent scales present in the numerical domain and thus limiting the conclusions that can be drawn from a study of turbulence-reaction zones interactions. As such, the present chapter presents some analysis in turbulence and conventional premixed flames to support the analysis subsequently applied to the DNS of MILD combustion and to provide some comparison basis.

First, as the computational cost to simulate reacting flows is much higher than for non-reacting flows, limitations exist on the turbulence field and turbulence scales that can be solved by DNS. In particular, one aspect is the relatively low Reynolds number achievable. Indeed, Taylor-microscale Reynolds number, Re_λ , of reacting flows DNS would typically be of the order of magnitude of about 100 while in non-reacting cases, it

can attain values up to about 1000 in recent simulations [Ishihara et al., 2013]. Thus, the question arises as to whether turbulence-flame interaction studies using simulations with those low Re_λ are meaningful. As a first step towards answering that question, the present chapter will first study the mechanism of development of turbulence, namely the vortex stretching mechanism and the energy cascade. This can be studied by analysing the alignment statistics between vorticity at a given scale and the strain-rate coming from another scale. To do so, a multiscale decomposition technique, the bandpass filtering method of Leung et al. [2012] is used. The influence of the Reynolds number on that statistics is also analysed to draw conclusions concerning the use of low Reynolds numbers turbulence fields in the simulation of turbulent reacting flows.

In a second stage, this chapter will present a multiscale analysis of flame-turbulence interactions in conventional premixed flames. Indeed, the understanding of flame-turbulence interactions remains relatively limited and the present chapter proposes to use this multiscale decomposition method to identify the scales of turbulence imparting the most strain on a flame. Obtaining these informations in the context of turbulent premixed combustion should help indicate how to perform a similar analysis in MILD combustion. Furthermore, this should give indications as to which scales of turbulence may be relevant for MILD combustion compared to conventional premixed flames.

This chapter first presents the DNS data used for this analysis. The multiscale analysis method, called the bandpass filtering method, is then described. The results obtained by applying this technique to turbulence to study the energy cascade and vortex stretching mechanism are presented, followed by the analysis of turbulence-flame interactions in premixed combustion. Finally, a summary and implications for DNS of MILD combustion are discussed.

3.2 DNS data used

3.2.1 Homogeneous isotropic turbulence

To study the interaction of scales in turbulence, various DNS of homogeneous isotropic turbulence are considered. Elaborate details on these datasets can be found in the relevant references. These datasets, from Donzis et al. [2008]; Ishihara et al. [2013]; Kobayashi et al. [2011] and Tanahashi et al. [1999], cover Re_λ from 37 to 1131 (or integral length scale Reynolds number, Re_l , from 97 to 36,345) as listed in Table 3.1. These datasets cover the widest range of Reynolds number currently available and are from a variety of research groups. The computational domain for each dataset is a triply periodic cube

of length 2π with N grid points in each direction. Two cases at $Re_\lambda = 140$ and 1131 have forced turbulence while all the others have freely decaying turbulence. The case at $Re_\lambda = 140$ uses stochastic forcing at large scale, applied on wave numbers smaller than $K_c = 2\sqrt{2}$ [Donzis et al., 2008; Eswaran & Pope, 1988a]. For the case at $Re_\lambda = 1131$, the forcing is performed in wave-number space as $\hat{\mathbf{f}}(\mathbf{k}) = c\hat{\mathbf{u}}(\mathbf{k})$ where $\hat{\mathbf{f}}$ is the Fourier transform of the forcing and c is a non-zero coefficient independent of k and is equal to a parameter, noted Γ , for $k < K_C$ and 0 otherwise. The value of Γ was adapted at each time step so as to maintain the total kinetic energy inside the domain. The value of K_c was taken to be 2.5 for the $Re_\lambda = 1131$ case [Ishihara et al., 2013]. It should be noted that these forcing schemes mainly affect structures of turbulence of a scale of about $2\pi/K_c$ and have a decreasing influence as one considers smaller and smaller scales. This scale of $2\pi/K_c$ corresponds to approximately 190η or 4900η respectively for the case at $Re_\lambda = 140$ and $Re_\lambda = 1131$, where η is the Kolmogorov lengthscale. Thus for the range of scales considered here, which are smaller than the integral lengthscale, the influence of the forcing scheme should be limited.

The analysis which will be presented in section 3.4 is performed on snapshots of the data taken once the turbulence is fully developed, as judged by the velocity derivative skewness approaching -0.5 . Since only instantaneous snapshots are available for analysis, the temporal aspects of the energy cascade is not studied here. Characteristics of each case required for this study are summarised in Table 3.1 and more detail on these datasets can be found in the relevant references.

Table 3.1 Characteristics of the (forced or decaying) homogeneous isotropic turbulence DNS database. l is the integral lengthscale, λ the Taylor microscale and η the Kolmogorov lengthscale.

Re_λ	N	l/η	λ/η	Forced or Decaying	Reference
37.1	128	31	11.8	D	[Tanahashi et al., 1999]
64.9	128	55	17.1	D	[Tanahashi et al., 1999]
97.1	256	100	20.9	D	[Tanahashi et al., 1999]
140	256	101	28.0	F	[Donzis et al., 2008]
141.1	400	200	24.0	D	[Tanahashi et al., 1999]
222.7	640	494	29.3	D	[Kobayashi et al., 2011]
393.8	1536	1146	39.0	D	Unpublished (from Tokyo Tech)
1131	4096	2137	66.5	F	[Ishihara et al., 2013]

3.2.2 Turbulent premixed flames

Five sets of turbulent premixed flame DNS data from [Gao et al. \[2014\]](#); [Minamoto et al. \[2014a\]](#) and [Rutland & Cant \[1994\]](#) will be analysed in section 3.5 to study flame-turbulence interactions in a conventional premixed combustion context. These simulations are of a statistically planar premixed flame propagating into homogeneous isotropic turbulence in the reactant mixture. The various characteristics of these data are listed in Table 3.2. The turbulent Reynolds number, Re_l , is based on the integral length scale l and the root mean square of turbulent velocity fluctuation u' entering the computational domain. The laminar burning velocity is s_L and the thermal thickness is δ_{th} . The Damköhler number is $Da = l s_L / (\delta_{th} u')$ and the Karlovitz number is $Ka = (u'/s_L)^{3/2} (\delta_{th}/l)^{1/2}$.

Table 3.2 DNS data attributes for the turbulent premixed flames.

u'/s_L	l/δ_{th}	Re_l	Da	Ka	Ref.
1.41	6.16	56.7	4.37	0.67	[Rutland & Cant, 1994]
2.19	2.11	38.5	0.97	2.22	[Minamoto et al., 2014a]
7.5	2.45	47.0	0.33	13.2	[Gao et al., 2014]
9.0	4.31	100.0	0.48	13.0	[Gao et al., 2014]
11.25	3.75	110.0	0.33	19.5	[Gao et al., 2014]

The combustion conditions of these five flames span from corrugated-flamelets to the thin reaction zones in the regime diagram of [Peters \[2000\]](#) as shown in Fig. 3.1. The flame of [Rutland & Cant \[1994\]](#) is in the corrugated-flamelets regime and that of [Minamoto et al. \[2014a\]](#) is in the lower part of the thin reaction zones regime. The cases from [Gao et al. \[2014\]](#), first described by [Chakraborty et al. \[2011\]](#), are in the upper part of the thin reaction zones regime. A single-step chemistry is used for the DNS of [Rutland & Cant \[1994\]](#) and [Gao et al. \[2014\]](#), which is sufficient for the future analysis of this data because the focus will be on kinematic aspects of turbulence-flame interaction. The skeletal mechanism of Smooke [\[Smooke & Giovangigli, 1991\]](#) was used by [Minamoto et al. \[2014a\]](#) and thus the analysis of this data will give first glimpses on the influence of chemistry on the present findings. All cases are stoichiometric flames except the case from [Minamoto et al. \[2014a\]](#) which is a lean methane/air flame with an equivalence ratio, ϕ , of 0.8. Elaborate information on these datasets is available in the references cited above.

These data have already been used in previous studies [\[Minamoto & Swaminathan, 2014b; Swaminathan & Grout, 2006\]](#) to investigate velocity and scalar gradients in premixed flames and thus the numerical resolution used for those simulations is good to

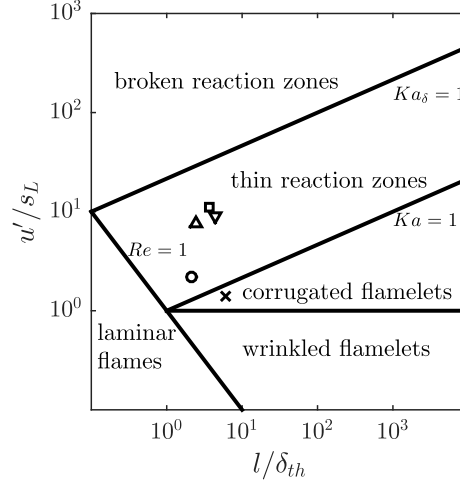


Fig. 3.1 Combustion regime diagram showing conditions of flames in [Rutland & Cant, 1994] \times , [Minamoto et al., 2014a] \circ , [Gao et al., 2014] \triangle , ∇ , \square .

address the objectives of this study. It should be further noted that for the data from Gao et al. [2014], the mesh size is such that the grid spacing is either smaller or equal to the Kolmogorov length scale which is enough to resolve the scales of turbulence under study here.

3.3 Bandpass filtering method

In past studies of turbulence, several methodologies have been proposed to extract its hierarchy of scales. For example, Farge [1992] proposed to use the wavelets decomposition method. This was later extended by Bermejo-Moreno & Pullin [2008]; Bermejo-Moreno et al. [2009] to the use of curvelets. While these studies have shed some lights on the multiscale geometrical decomposition of enstrophy and dissipation, these methods are complicated and are yet to lead to a clear conclusion on the hierarchy of turbulence. On the other hand, methods based on filtering in Fourier space have shown to be both practical and straightforward to apply [Goto et al., 2017; Leung et al., 2012] and are thus used here.

In particular, the bandpass filtering method described by Leung et al. [2012] is used for the multiscale analysis of the different DNS datasets. This procedure allows one to educe structures of a particular lengthscale L . It is summarized hereunder.

Let us first consider a low-pass filtered velocity field $\mathbf{u}^L(\mathbf{x})$:

$$\mathbf{u}^L = \int \mathbf{u}(\mathbf{x} - \mathbf{r}) G(L, r) d\mathbf{r} \quad (3.1)$$

where L is the length scale at which the velocity field is filtered, $G(L, r)$ is the low-pass filter and $r = |\mathbf{r}|$.

Here, low-pass is interpreted in the frequency sense and thus \mathbf{u}^L contains information about scales greater than L . As a result, the derivative of \mathbf{u}^L with regards to L , $\partial \mathbf{u}^L / \partial L$, should contain information about scales centred around L . The bandpass filtered velocity field can then be defined as

$$\mathbf{u}_b^L = -\frac{\alpha L}{\sqrt{L}} \frac{\partial \mathbf{u}^L}{\partial L} \quad (3.2)$$

where α is a constant depending on the low-pass filter chosen.

Applying the Fourier transform, the following relations are deduced from the previous equation

$$\hat{\mathbf{u}}^L = T(\kappa) \hat{\mathbf{u}}(\mathbf{k}) \quad (3.3)$$

where \mathbf{k} is the wavenumber vector, $\kappa = kL/2$ with $k = |\mathbf{k}|$ and $T(\kappa)$ is the transfer function of the filter. And the transform of the bandpass filtered velocity field is

$$\hat{\mathbf{u}}_b^L = -\frac{\alpha \kappa}{\sqrt{L}} \frac{dT}{d\kappa} \hat{\mathbf{u}}(\mathbf{k}) \quad (3.4)$$

The spectrum of the bandpass filtered velocity field can be deduced

$$E_b^L(L, k) = \frac{\alpha^2 \kappa^2}{L} \left(\frac{dT}{d\kappa} \right)^2 E(k) \quad (3.5)$$

where $E(k)$ and E_b^L are respectively the energy spectra of the unfiltered and bandpass filtered velocity fields.

The coefficient α is chosen so that the following condition is satisfied

$$\int_0^\infty E_b^L(L, k) dL = E(k) \quad (3.6)$$

In all subsequent analysis, the low-pass filter considered is the Gaussian filter:

$$G(L, r) = \frac{1}{\pi^{3/2} L^3} \exp\left(-\frac{r^2}{L^2}\right), \quad \int G(L, r) d\mathbf{r} = 1 \quad (3.7)$$

In this case, Eq. (3.4) reads

$$\hat{\mathbf{u}}_b^L = \frac{\alpha}{\sqrt{L}} 2\kappa^2 \exp(-\kappa^2) \hat{\mathbf{u}}(\mathbf{k}) \quad (3.8)$$

and $\alpha = \sqrt{2}$. An inverse Fourier transform can then be applied to obtain the bandpass filtered velocity field, \mathbf{u}_b^L , and one can use that bandpass filtered velocity field to deduce typical turbulence quantities such as the vorticity, strain rate tensor, Reynolds stresses or flames quantities such as the tangential strain rate.

3.4 Energy cascade in turbulence

A key description of turbulence relies on the existence of a hierarchy of eddies of different scales whose morphology and spatial clustering depend on the turbulence Reynolds number. Many views have been proposed in the past to describe the interactions of these eddies and how the energy cascades through these scales from the large energy-containing eddies to the small dissipative structures. In particular, the Richardson/Kolmogorov energy cascade [Kolmogorov, 1941; Richardson, 1922] conjectured that kinetic energy introduced at large scales is progressively transferred to smaller and smaller scales through the inertial range, eventually reaching the Kolmogorov scale where it is dissipated by fluid viscosity. The key assumption of this conjecture is the scale locality of the cascade, the idea by which eddies mainly interact with and transfer energy to eddies of neighbouring (smaller) sizes.

Historically, turbulence and turbulent structures have often been described in spectral space and their wave numbers become a surrogate for their physical scales. In this formalism, the locality of the energy cascade is understood as the proximity between interacting wave numbers. From this perspective, various closure models relying on this notion of cascade for turbulence were developed based on algebraic expressions for the spectral kinetic energy transfer function [Heisenberg, 1948; Obukhov, 1941; Pao, 1965] with reasonable success. Furthermore, the locality of the energy cascade in wave number space was assessed by studying the interactions between triads of wave numbers and their contribution to the energy flux. It was shown that the energy transfer was dominated by local wave number triad interactions [Aluie & Eyink, 2009; Brasseur & Wei, 1994; Domaradzki & Carati, 2007; Eyink & Aluie, 2009]. Approaches analogous to the analysis of the spectral energy transport equation had also been performed in physical space using the two-point velocity correlation transport equation and the Karman-Howarth equation [Davidson, 2015]. In this context, the family of closures proposed are the

quasi-normal-type schemes which assume that for the fourth-order velocity correlations terms, the joint-pdf of the velocity field measured at two points is Gaussian. This then allows to close the Karman-Howarth equation and these closures are reviewed by [Lesieur \[2008\]](#). However, there is an inherent arbitrary nature to the approximations used and the heuristic modifications required to correct these models. Thus, there is no consensus on the locality of these scale interactions in physical space. Indeed, some studies have both supported this assumption [[Cardesa et al., 2015, 2017](#); [Domaradzki et al., 1993](#); [Goto et al., 2017](#)] while others have shown that energy could be transferred directly from large scales to much smaller ones [[Lumley, 1992](#); [Tsinober, 2009](#); [Yeung & Brasseur, 1991](#)]. Clear evidence for this real space scale-locality of the energy cascade is scant.

Nonetheless, from the physical space perspective, since Taylor’s work [[Taylor, 1938](#); [Taylor & Green, 1937](#)], it has often been suggested that the mode of energy transfer across the scales is through vortex stretching, in which vortical structures of a given scale are stretched and intensified by larger vortices, leading to the transfer of energy from the larger to the smaller eddies with the smallest eddies having a worm-like shape, an idea that dates back to [Burgers \[1948\]](#). In particular, the rate of generation of enstrophy, $\Omega = |\boldsymbol{\omega}|^2/2$, by vortex stretching, $\psi = \omega_i \omega_j S_{ij}$, is often taken as a proxy for energy transfer in real scale space [[Betchov, 1956](#); [Cocke, 1969](#)].

Despite the relatively wide acceptance of this classical picture interweaving energy cascade and vortex stretching, rigorous evidence supporting this association remains elusive and additional investigations are required to support the vortex stretching picture and its locality in scale space. Indeed, past Direct Numerical Simulations (DNS) [[Ashurst et al., 1987](#); [She et al., 1991](#); [Vincent & Meneguzzi, 1994](#); [Yoshimatsu et al., 2015](#)] and experiments [[Mullin & Dahm, 2006](#); [Su & Dahm, 1996](#)] show that the vorticity aligns preferentially with the intermediate strain rate, β , which suggests the formation of vortex sheets rather than vortex tubes [[Betchov, 1956](#)]. By contrast, one would expect $\boldsymbol{\omega}$ to preferentially align with the most extensional strain rate, α , if the vortices being stretched are tube-like (worms) [[Betchov, 1956](#)]. This apparent disconnect stems from the influence of *local* (in physical space) straining associated with the self-induced strain fields of vortices [[Jiménez, 1992](#); [Moffatt et al., 1994](#)]. Indeed, when these effects are excluded and only *non-local* straining in physical space retained, it is found that $\boldsymbol{\omega}$ is indeed aligned, on average, with α [[Hamlington et al., 2008a,b](#); [Leung et al., 2012](#)]. The effects of self-straining can be filtered out by using a bandpass filter to educe vorticity and straining structures of different scales and examine their mutual interactions. This shows that, for modest values of Taylor microscale Reynolds numbers, Re_λ , a vortex of a given size is stretched primarily by the α strain from structures that are 3 to 5 times

larger than the vortical structure [Leung et al., 2012]. These results were obtained for homogeneous isotropic turbulence and similar results supporting the scale-locality of the energy cascade and the vortex stretching in shear flows were reported in [Elsinga & Marusic, 2016; Lozano-Durán et al., 2016; Wei et al., 2014]. By contrast, if one does only consider the alignment between vorticity and straining structures at the same scale, and thus not excluding the self-straining effect, the preferential alignment of $\boldsymbol{\omega}$ with $\boldsymbol{\beta}$ is retained [Leung et al., 2012; Tordella et al., 2014].

The relatively low Re_λ of 107 [Hamlington et al., 2008b] and 141 [Leung et al., 2012] in the previous studies raises questions as to the validity of their findings for higher Reynolds numbers, particularly as it is often suggested that high Re_λ turbulence presents dynamical features that differ from lower Reynolds number turbulence. For example, Ishihara et al. [2013] examined data at $Re_\lambda = 1131$ and highlighted the appearance of thin shear layers consisting of clusters of thin intense vortex tubes. They suggested that the spatial structure of turbulence undergoes a transition as Re_λ approaches 1000, with larger values of Re_λ favouring the clustering of vortex worms into slabs or sheets. This clustering is less apparent at lower Re_λ . Thus, a definitive theory of the energy cascade, applicable across all Re_λ , remains elusive.

The objectives of the study here are (i) to revisit the classical cartoon of the energy cascade using DNS data presented in section 3.2.1, to investigate its locality in scale space, through a clear analysis of the energy and enstrophy transfers, and vortex stretching mechanism between various scales; (ii) to investigate whether or not the nature of the cascade changes with Re_λ and in particular whether the results observed by Leung et al. [2012] for $Re_\lambda = 141$ are valid for smaller and larger Reynolds numbers and (iii) to study the morphology of the straining and strained structures. These objectives are addressed by analysing DNS data for Re_λ ranging from 37 to 1131. Each dataset is analysed using the bandpass filtering method [Leung et al., 2012] which allows one to focus on structures of a chosen length scale, L . The morphological features of these structures are then analysed using Minkowski functionals. The present work will thus mainly focus on the scale-locality of the energy cascade using quantities in real space rather than in wave number space and not on the spatial locality of the energy/enstrophy transfer.

3.4.1 Scale decomposition and interactions analysis

To analyse the scale-by-scale transfer and interaction, following earlier works [Davidson et al., 2008; Frisch, 1995], one can decompose the velocity, \mathbf{u} , and vorticity, $\boldsymbol{\omega}$, into *large* and *small* scales such that $\mathbf{u} = \mathbf{u}^{\mathbb{L}} + \mathbf{u}^{\mathbb{S}}$ and $\boldsymbol{\omega} = \boldsymbol{\omega}^{\mathbb{L}} + \boldsymbol{\omega}^{\mathbb{S}}$, where the superscripts \mathbb{L} and \mathbb{S} denote the contribution of structures respectively larger and smaller than a specified

scale r . Such decomposition is not unique and depends on the low-pass filter used to yield $\boldsymbol{\omega}^{\mathbb{L}}$ and $\boldsymbol{u}^{\mathbb{L}}$. This aspect will be tackled subsequently.

Nonetheless, using this formalism, an energy equation for the large and small scales can be deduced by taking the dot product of $\boldsymbol{u}^{\mathbb{L}}$ and $\boldsymbol{u}^{\mathbb{S}}$ with the Navier-Stokes equations and ensemble averaging the resulting equations [Davidson et al., 2008; Frisch, 1995]. This gives

$$\frac{\partial}{\partial t} \left\langle \frac{1}{2} (\boldsymbol{u}^{\mathbb{L}})^2 \right\rangle = -\Pi_V - \nu \left\langle (\boldsymbol{\omega}^{\mathbb{L}})^2 \right\rangle \quad (3.9)$$

$$\frac{\partial}{\partial t} \left\langle \frac{1}{2} (\boldsymbol{u}^{\mathbb{S}})^2 \right\rangle = \Pi_V - \nu \left\langle (\boldsymbol{\omega}^{\mathbb{S}})^2 \right\rangle \quad (3.10)$$

for the energy in scales \mathbb{L} and \mathbb{S} respectively. The symbol Π_V is defined as:

$$\Pi_V(r) = \left\langle S_{ij}^{\mathbb{L}} \tau_{ij}^{\mathbb{S}} - S_{ij}^{\mathbb{S}} \tau_{ij}^{\mathbb{L}} \right\rangle \quad (3.11)$$

with S_{ij} the symmetric strain-rate tensor, $\tau_{ij}^{\mathbb{L}} = -u_i^{\mathbb{L}} u_j^{\mathbb{L}}$ and $\tau_{ij}^{\mathbb{S}} = -u_i^{\mathbb{S}} u_j^{\mathbb{S}}$ are the Reynolds stresses at large and small scales. In the present formalism, as $\Pi_V(r)$ appears in both equations with an opposite sign, it can be interpreted as the flux of energy from larger to smaller scales across the scale r .

In a similar manner, by taking the dot product of $\boldsymbol{\omega}^{\mathbb{L}}$ or $\boldsymbol{\omega}^{\mathbb{S}}$ with the vorticity equation, one can obtain the enstrophy equations for the large and small structures [Davidson et al., 2008]:

$$\frac{\partial}{\partial t} \left\langle \frac{1}{2} (\boldsymbol{\omega}^{\mathbb{L}})^2 \right\rangle = -F(r) + G^{\mathbb{L}}(r) - \nu \left\langle (\nabla \times \boldsymbol{\omega}^{\mathbb{L}})^2 \right\rangle \quad (3.12)$$

$$\frac{\partial}{\partial t} \left\langle \frac{1}{2} (\boldsymbol{\omega}^{\mathbb{S}})^2 \right\rangle = F(r) + G^{\mathbb{S}}(r) - \nu \left\langle (\nabla \times \boldsymbol{\omega}^{\mathbb{S}})^2 \right\rangle \quad (3.13)$$

with

$$F(r) = \left\langle \boldsymbol{\omega}^{\mathbb{L}} \cdot (\boldsymbol{u} \cdot \nabla \boldsymbol{\omega}^{\mathbb{S}}) \right\rangle = - \left\langle \boldsymbol{\omega}^{\mathbb{S}} \cdot (\boldsymbol{u} \cdot \nabla \boldsymbol{\omega}^{\mathbb{L}}) \right\rangle \quad (3.14)$$

$$G^{\mathbb{L}}(r) = \left\langle \boldsymbol{\omega}^{\mathbb{L}} \cdot (\boldsymbol{\omega} \cdot \nabla \boldsymbol{u}) \right\rangle = \left\langle \omega_i^{\mathbb{L}} \omega_j S_{ij} \right\rangle \quad (3.15)$$

$$G^{\mathbb{S}}(r) = \left\langle \boldsymbol{\omega}^{\mathbb{S}} \cdot (\boldsymbol{\omega} \cdot \nabla \boldsymbol{u}) \right\rangle = \left\langle \omega_i^{\mathbb{S}} \omega_j S_{ij} \right\rangle \quad (3.16)$$

Here, $G^{\mathbb{L}}(r)$ and $G^{\mathbb{S}}(r)$ represent the generation of enstrophy via vortex stretching at large and small scales respectively and $F(r)$ is the transfer or flux of enstrophy across the scale r , from larger to smaller scales.

From this formalism, the transfer of energy and enstrophy from scales \mathbb{L} to \mathbb{S} across the scale r can be analysed by studying the flux functions, Π_V for the energy and F for the enstrophy as has been done by Davidson et al. [2008]. However, the interest of the present work is to investigate the interactions between a given scale L and various smaller scales S to identify the range of scales interacting with structures at scale L and thus assess the locality of the energy/enstrophy transfer. This is achieved by using the bandpass filtering method proposed by Leung et al. [2012].

Indeed, by using the bandpass filtered velocity field at a scale L , as described in section 3.3, one can compute the fields of vorticity, strain-rate and Reynolds stresses for that particular scale L as:

$$\boldsymbol{\omega}_b^L = \nabla \times \mathbf{u}_b^L, \quad S_{ij,b}^L = \frac{1}{2} \left(\frac{\partial u_{b,i}^L}{\partial x_j} + \frac{\partial u_{b,j}^L}{\partial x_i} \right), \quad \tau_{ij,b}^L = -u_{b,i}^L u_{b,j}^L \quad (3.17)$$

By using this technique, one can educe these “large” and “small” scales separately, and not necessarily across a given scale r . The bandpass filtered velocity at some specified scales L and S , with $L > S$, can be used in Eqs. (3.11) and (3.14) to directly compute the transfer of energy or enstrophy from structures of scale L to those of scale S , i.e.,

$$\Pi_{V,b}^{L \rightarrow S} = \langle S_{ij,b}^L \tau_{ij,b}^S - S_{ij,b}^S \tau_{ij,b}^L \rangle \quad (3.18)$$

$$F_b^{L \rightarrow S} = \langle \boldsymbol{\omega}_b^L \cdot (\mathbf{u} \cdot \nabla \boldsymbol{\omega}_b^S) \rangle \quad (3.19)$$

where the subscript b indicates the use of bandpass filtered fields.

Furthermore, to analyse the vortex stretching mechanism, one can analyse the interplay between the vorticity at scale L_ω and the strain rate at L_s . Indeed, the rate of generation of enstrophy at scale L_ω due to straining structures at scale L_s can be expressed as:

$$\psi = \omega_i^{L_\omega} \omega_j^{L_\omega} S_{ij}^{L_s} = |\boldsymbol{\omega}^{L_\omega}|^2 \left(\alpha^{L_s} \cos^2 \theta_\alpha + \beta^{L_s} \cos^2 \theta_\beta + \gamma^{L_s} \cos^2 \theta_\gamma \right) \quad (3.20)$$

where α^{L_s} , β^{L_s} and γ^{L_s} are the principal components of $S_{ij}^{L_s}$ with $\alpha^{L_s} > \beta^{L_s} > \gamma^{L_s}$ and θ_i are the corresponding angles between the vorticity vector and these principal components. Thus, to analyse the vortex stretching mechanism, one can analyse the

alignment statistics as measured by the pdf of $\cos(\theta_i)$ between vortical structures at a lengthscale L_w and straining structures at a larger lengthscale L_s .

The analysis presented above has been applied on the 8 DNS cases of homogeneous isotropic turbulence with Re_λ ranging from 37 to 1131, presented in section 3.2.1.

3.4.2 Morphology descriptor

The Minkowski functionals are used to perform an objective analysis of the morphology of turbulent structures educed at various scales using the bandpass filtering methodology. These Galilean invariants are commonly used in cosmology, for example by Mecke et al. [1994], and describe the morphology of a given three dimensional structure. The four functionals for a three dimensional structure are given by [Sahni et al., 1998]:

$$V_0 = V, \quad V_1 = \frac{A}{6}, \quad V_2 = \frac{1}{3\pi} \int_A \frac{\mathcal{K}_1 + \mathcal{K}_2}{2} dA, \quad V_3 = \frac{1}{2\pi} \int_A \mathcal{K}_1 \mathcal{K}_2 dA \quad (3.21)$$

V is the volume enclosed by the three dimensional object with a surface area, A . The principal curvatures at a given point on this surface are \mathcal{K}_1 and \mathcal{K}_2 . Using these Minkowski functionals, one can then define the *shapefinders* - length, ℓ , width, w , and thickness, t , ordered as $t < w < \ell$ and computed using

$$t = \frac{V_0}{2V_1}, \quad w = \frac{2V_1}{\pi V_2}, \quad \ell = \frac{3V_2}{2V_3} \quad (3.22)$$

It should be noted that particular care is taken with V_3 as holes could be present in the structure, thus yielding $V_3 \leq 0$. In those cases, ℓ is defined as $\ell = 3V_2/(4(G+1))$ where $G = 1 - V_3/2$ is the genus of the structure. The genus of the structure is the number of cuts that can be made along a simple curve on the object without splitting it [Sheth & Sahni, 2005]. From these three characteristics lengthscales, two quantities called planarity, \mathcal{P} , and filamentarity, \mathcal{F} , can be defined [Sahni et al., 1998]:

$$\mathcal{P} = \frac{w - t}{w + t}, \quad \mathcal{F} = \frac{\ell - w}{\ell + w} \quad (3.23)$$

These two dimensionless quantities are bounded between 0 and 1 and can then be used to classify the considered three dimensional object in terms of simple shapes, such as a blob or sphere $(\mathcal{P}, \mathcal{F}) = (0, 0)$, very long tube $(0, 1)$, thin sheet $(1, 0)$ and very long ribbon $(1, 1)$ as noted by Leung et al. [2012].

This procedure has been applied on vortical and straining structures educed at various lengthscales as will be detailed in section 3.4.3.

3.4.3 Morphology of the turbulent vortices

The turbulent velocity fields have been obtained at various scales by using the bandpass filter with length scale, L , varying from 5η to up to 1300η depending on the dataset. From these fields, the strained (enstrophy) and straining structures can be deduced using Eq. (3.17). Figure 3.2 shows examples of the strained and straining structures for $Re_\lambda = 140$ and 1131 . The length scales L_s and L_ω are respectively 24η and 5η for Figs. 3.2a and 3.2c. These lengthscales are $L_s = 75\eta$ and $L_\omega = 24\eta$ for Fig. 3.2b, and they are $L_s = 750\eta$ and $L_\omega = 150\eta$ for Fig. 3.2d. These specific combinations of L_s and L_ω are chosen based on the suggestions of Leung et al. [2012] which showed that most stretching imparted on strained structures was coming from straining structures 3 to 5 times larger. The isosurfaces are thresholded at a value of $\mu + 2\sigma$, where μ is the mean and σ is the standard deviation. This threshold was chosen following the work of Leung et al. [2012] to focus on regions with intense vorticity or strain rate. Despite the variations in the volume of these structures, it is observed that their general morphology is not significantly modified by varying the threshold, as also observed by Leung et al. [2012]. Indeed other thresholds of $\mu + \sigma$ and $\mu + 3\sigma$ yielded similar results (not shown here for brevity). The enstrophy and straining structures are more space filling in the larger Re_λ case, irrespective of their scales. This was assessed by computing the volume fraction occupied by these structures at various Reynolds numbers. For example, when comparing the enstrophy structures of Fig. 1a to 1c, they occupy respectively 2.97% and 10.4% for cases $Re_\lambda = 140$ and $Re_\lambda = 1131$. Similarly, the straining structures of Fig. 1a for $Re_\lambda = 140$ only occupy 4.3% of the volume compared to 24.64% for $Re_\lambda = 1131$ shown in Fig. 1c. Furthermore, the enstrophy structures are predominantly tube and blob-like with large strain fields at their periphery, as in the Burgers vortex model. This is illustrated in Fig. 3.3 where a single enstrophy structure has been isolated from Fig. 3.2c along with its neighbouring straining structures.

The shapefinders, \mathcal{P} and \mathcal{F} , for the strained and straining structures seen in Fig. 3.2 are plotted in Fig. 3.4. The results are shown as contours of joint probability density function of \mathcal{P} and \mathcal{F} for the strained structures and as scatter plots for the straining structures. This particular choice is due to the small number of straining structures at larger scales preventing the computation of a smooth pdf. For example, there are only 18 straining structures observed in Fig. 3.2b for $L_s = 75\eta$ and their \mathcal{P} and \mathcal{F} are shown as a scatter plot in Fig. 3.4b. The ranges of \mathcal{P} and \mathcal{F} observed in Fig. 3.4 suggest that the deduced structures seen in Fig. 3.2 are mostly blob-like (low \mathcal{P} and low \mathcal{F}) or tube-like (low \mathcal{P} and medium or high \mathcal{F}) even for the largest Re_λ and $L_\omega = 150\eta$ considered here. More specifically, the straining structures tend to have a blob-like aspect

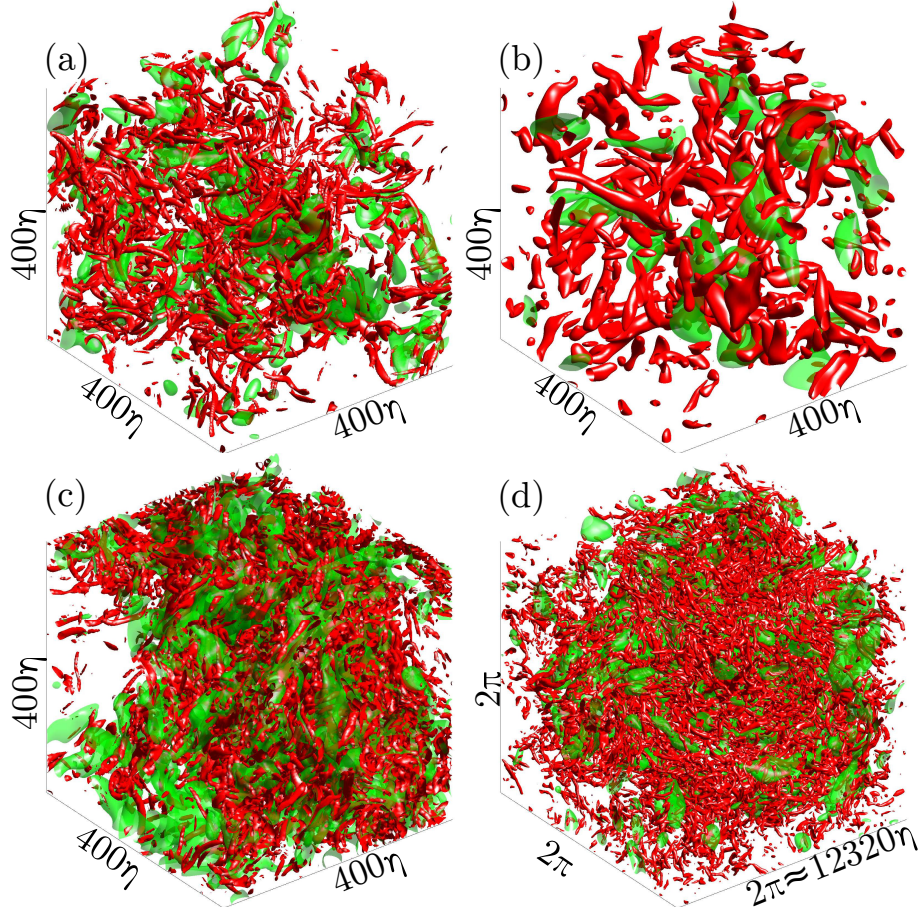


Fig. 3.2 Iso-surfaces of enstrophy (red) and straining (green) structures with a threshold value of $\mu + 2\sigma$, where μ is the mean and σ is the rms. Panels (a) & (b) are for $Re_\lambda = 140$ and (c) & (d) are for $Re_\lambda = 1131$. In (a) and (c) $L_s = 24\eta$ and $L_\omega = 5\eta$, in (b) $L_s = 75\eta$ and $L_\omega = 24\eta$ and in (d) $L_s = 750\eta$ and $L_\omega = 150\eta$.

ratio for all lengthscales considered here, while the small scale vortices with $L_\omega = 5\eta$ present a tube-like morphology (see Figs. 3.4a and 3.4c). However, as L_ω increases, the enstrophy structures starts to show blob-like morphology as observed by the shift in the position of the joint-pdf towards lower value of \mathcal{F} (compare Fig. 3.4a to 3.4b, and Fig. 3.4c to 3.4d). Similar observations about the difference in the shapes of the vortical and straining structures were also made by Leung et al. [2012] using bandpass filters and by Moisy & Jiménez [2004] based on the fractal dimensions for the intense vortical and straining structures.

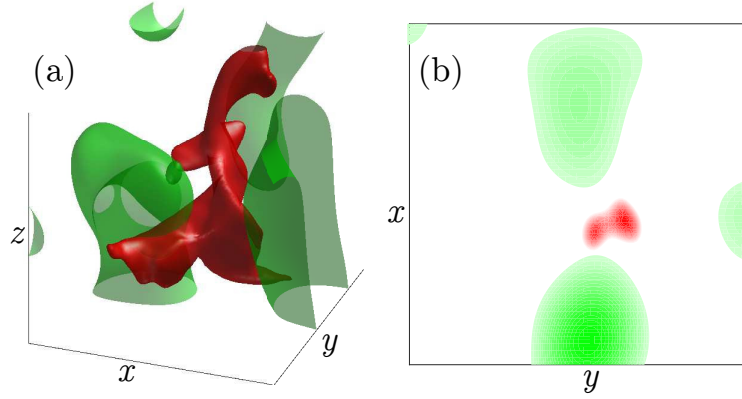


Fig. 3.3 (a) Isolated single iso-surface of enstrophy (red) and dissipation (green) structures with a threshold value of $\mu + 2\sigma$ extracted from the case $Re = 1131$. (b) The associated mid x - y plane distribution.

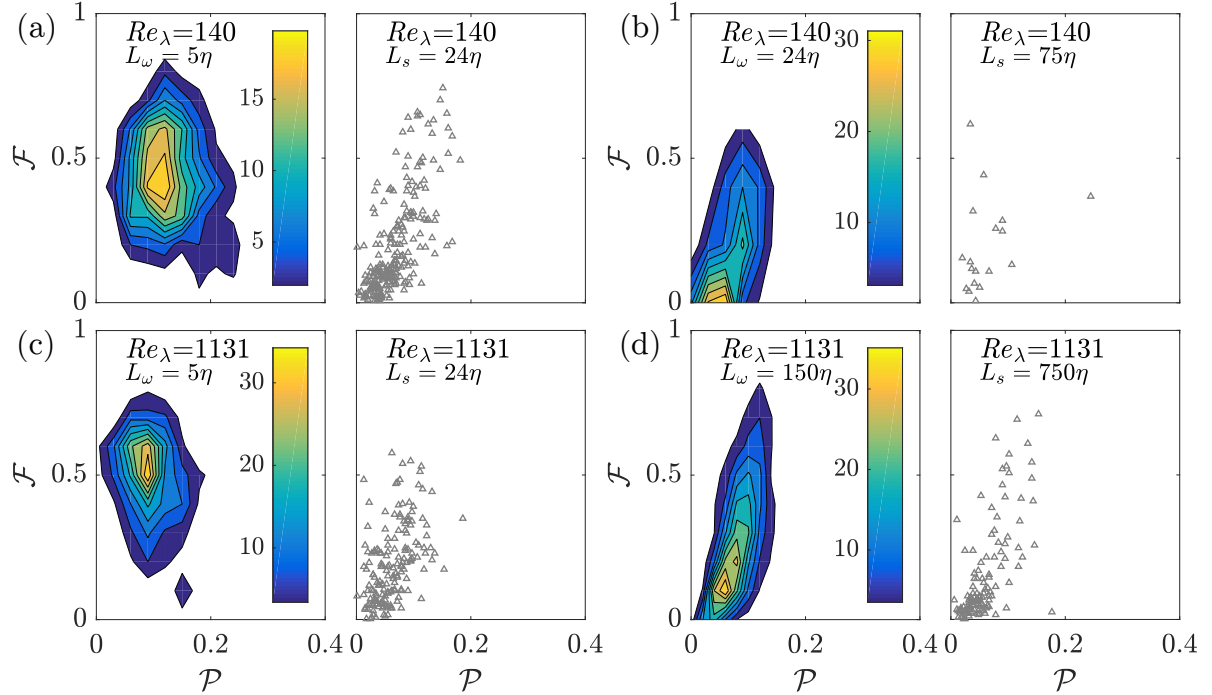


Fig. 3.4 Joint-pdf of planarity, \mathcal{P} , and filamentarity, \mathcal{F} , of the strained (or enstrophy) structures seen in Fig. 3.2.

3.4.4 Energy and enstrophy transfer

The normalised energy transfer function, $\hat{\Pi}_{V,b}^{L \rightarrow S} = \Pi_{V,b}^{L \rightarrow S} / \max(\Pi_{V,b}^{L \rightarrow S})$, is shown in Fig. 3.5 where it is plotted for three different Reynolds numbers $Re_\lambda = 97.1, 222.7$ and 1131 . For each case, a large scale, L , is picked first and the small scale S is varied to determine which small scale receives the most energy from the structures of size L . This can be

repeated for various values of L to analyse if the range of scale interactions evolves across scales of turbulence in a particular fashion or not.

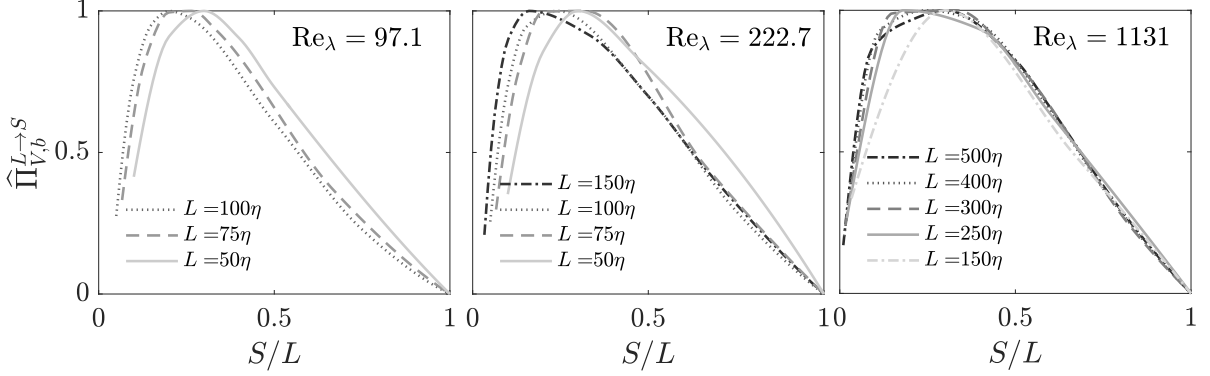
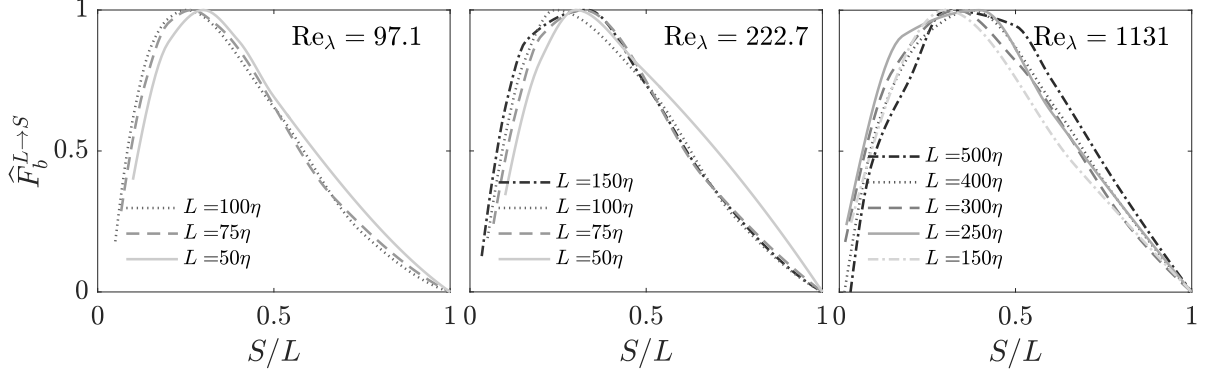


Fig. 3.5 Normalised energy transfer function, $\hat{\Pi}_{V,b}^{L \rightarrow S}$, for various cases.

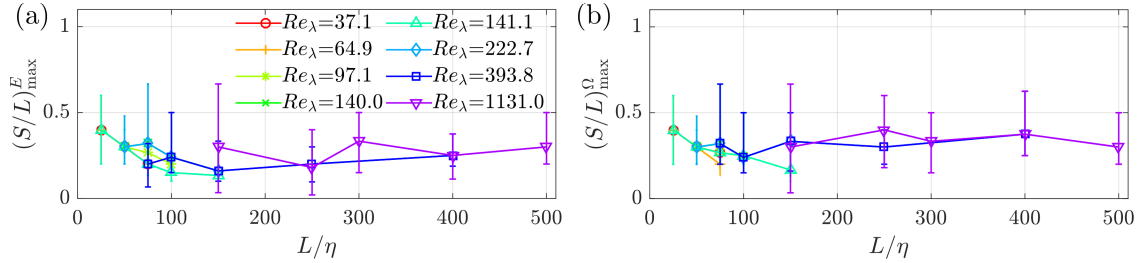
It is observed that $\hat{\Pi}_{V,b}^{L \rightarrow S}$ peaks for values of S/L around 0.3 for all values of L . This indicates that structures at scale L mostly transfer energy to structures having a size of about $\sim 0.3L$. Furthermore, the normalising quantity, $\max(\Pi_{V,b}^{L \rightarrow S})$, increases with decreasing L , for the range of L studied here, and increases with increasing Re_λ . As this analysis is performed for various L , the results in Fig. 3.5 show that there exists a locality in the energy transfer for the range of scales across the turbulence spectrum. This strongly supports the energy cascade picture which portrays that the energy is transferred from one scale to its neighbouring smaller scale. Furthermore, this result is observed to be insensitive for all the Reynolds numbers considered here suggesting that the energy cascade picture is robust and does not change with Re_λ .

A similar analysis is performed for the enstrophy flux between two scales, L and S . The normalised value of the enstrophy flux, $\hat{F}_b^{L \rightarrow S} = F_b^{L \rightarrow S} / \max(F_b^{L \rightarrow S})$, is shown in Fig. 3.6 for the same cases considered for the energy transfer in Fig. 3.5. The behaviour of $\hat{F}_b^{L \rightarrow S}$ is very similar to that for the energy transfer. The enstrophy of scale L is mostly transferred to scales of about $0.3L$ for all L considered and $\max(F_b^{L \rightarrow S})$ has the same behaviour as $\max(\Pi_{V,b}^{L \rightarrow S})$ with variations of Re_λ and L . This similar behaviour between $\hat{F}_b^{L \rightarrow S}$ and $\hat{\Pi}_{V,b}^{L \rightarrow S}$ hints at a close relation between the energy and enstrophy transfers and the enstrophy still cascades from large to small scales just like the energy [Davidson et al., 2008].

To further quantify the locality of this energy and enstrophy flux, one can plot the value of the ratio S/L yielding the highest energy or enstrophy transfer for various L and Re_λ considered. These ratios, denoted as $(S/L)_{\max}^E$ for the energy transfer and $(S/L)_{\max}^\Omega$ for the enstrophy flux, are shown in Fig 3.7 with the uncertainty associated


 Fig. 3.6 Normalised enstrophy flux, $\hat{F}_b^{L \rightarrow S}$, for various cases.

with the location of the peak. This uncertainty comes from the limited combination of the ratios (S/L) computed for this study. Indeed, to estimate $(S/L)_{\max}^{\Omega}$ and $(S/L)_{\max}^E$, first a large scale, L , is chosen and then a finite number of small scales, S , are considered subsequently to compute the energy/enstrophy transfer and to determine for which S the energy/enstrophy transfer is maximum for the chosen L . From this set of ratios (S/L) , $(S/L)_{\max}^{\Omega}$ and $(S/L)_{\max}^E$ are determined. Thus, the uncertainty of the maximum corresponds to the interval between the two consecutive (S/L) bracketing the peaks seen in Figs. 3.5 and 3.6. This interval width is shown as vertical bars in Fig. 3.7.


 Fig. 3.7 Ratio (a) $(S/L)_{\max}^E$ and (b) $(S/L)_{\max}^{\Omega}$ yielding the maximum energy or enstrophy transfer from eddies of a scale L to a scale S .

It is observed that for all cases, the values of $(S/L)_{\max}^{\Omega}$ and $(S/L)_{\max}^E$ lie between 0.25 and 0.4. This provides strong support for the scale-by-scale energy or enstrophy cascade throughout the range of scales of turbulence and more importantly, for all Reynolds numbers considered. The results shown in Figs. 3.5 and 3.6 have also been compared for the decaying and forced cases with Re_λ of about 140 and no significant differences were observed (not shown) implying that the forcing of the turbulence at sufficiently large scale does not influence the energy or enstrophy flux through the scales. Furthermore, the similar behaviour of the results for both large and small scales in the cases with

$Re_\lambda = 140$ and $Re_\lambda = 1131$ suggests that the forcing scheme does not influence the results unduly.

3.4.5 Vorticity - strain rate alignment

As noted by Eq. (3.20), the generation of enstrophy through vortex stretching mechanism is dictated by the alignment between the vorticity vector and the principal strain rates.

The probability density function of $|\cos \theta|$ between vorticity at 5η and the principal strain rates at various L_s is shown in Fig. 3.8 for four Reynolds numbers. This alignment pdf is shown for both the α and β strain rates. The vorticity is observed to align preferentially with the most extensional strain, α , when $L_s > L_\omega$ and the alignment with the β strain rate increases progressively as $L_s/L_\omega \rightarrow 1$, as observed by Leung et al. [2012] for $Re_\lambda = 141$. Statistics similar to unfiltered alignment characteristics reported by Ashurst et al. [1987], i.e. alignment with the β strain rate, are observed for $L_s \approx L_\omega$. This statistics with unfiltered field computed for the case $Re_\lambda = 1131$ is shown for comparison in the frame for $L_s = 5\eta$ of Fig. 3.8 using gray lines.

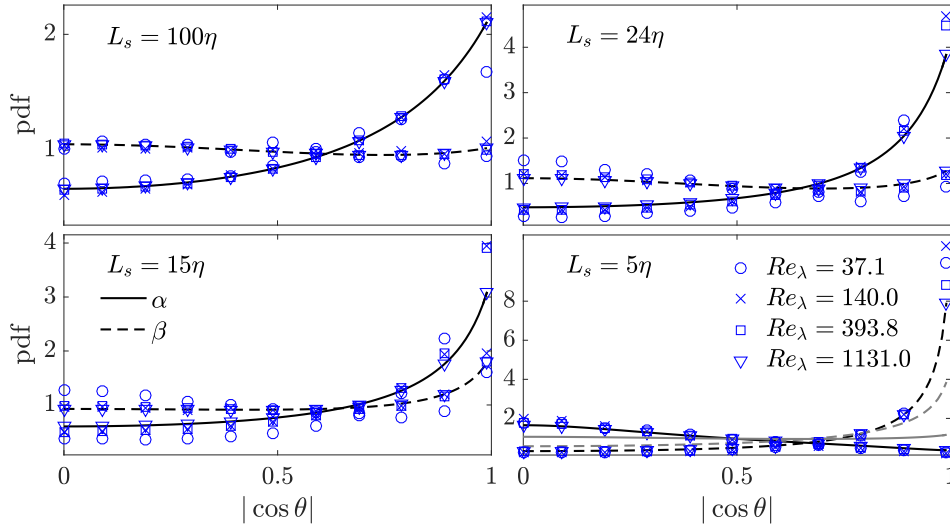


Fig. 3.8 Pdf of alignment between the vorticity filtered at scale $L_\omega = 5\eta$ and the principal directions of the strain filtered at scales L_s . Solid line α and dashed line β . The gray lines are for the case $Re_\lambda = 1131$ computed using unfiltered fields.

One can also quantify the size of larger structures primarily responsible for stretching a vortex of size L_ω by studying the probability, P , of the alignment with the α strain rate. As discussed by Leung et al. [2012], this can be obtained by simply integrating the results in Fig. 3.8 for $\xi_1 \leq |\cos \theta_\alpha| \leq 1$ and the variation of this probability with $\mathcal{L} = L_s/L_\omega$ is shown in Fig. 3.9, with $\xi_1 = 0.99$, for the range of Reynolds numbers in Table 3.1.

3.4 Energy cascade in turbulence

Figures 3.9a and 3.9b show this quantity respectively for $L_\omega = 5\eta$ and $L_\omega = 45\eta$ with L_s ranging from 5η to 1300η depending on the dataset under analysis. (The additional case of $L_\omega = 150\eta$ is included for $Re_\lambda = 1131$ in Fig. 3.9a). Evidently, for all cases considered, the probability peaks for $3 \leq \mathcal{L} \leq 5$, implying that the vortical structures of scale L_ω are stretched mostly by structures that are about 3 or 5 times larger, as noted by Leung et al. [2012]. Although the results shown in Fig. 3.9 are for $\xi_1 = 0.99$, they are observed to be insensitive to the choice of the ξ_1 value. These results support the hypothesis that the enstrophy structures are predominantly stretched by the extensional strain from larger eddies, corroborating the idea that the most effective vortex stretching is incremental in scale-space. More importantly, it is seen that this observation holds for all values of Re_λ investigated here and even for relatively large enstrophy structures at large Re (see curve corresponding to $Re_\lambda = 1131$ with $L_\omega = 150\eta$ in Fig. 3.9a). This observation is also consistent with the ratios of scales for the maximum energy or enstrophy transfer, $(S/L)_{\max}^E$ or $(S/L)_{\max}^\Omega$, shown in Fig 3.7.

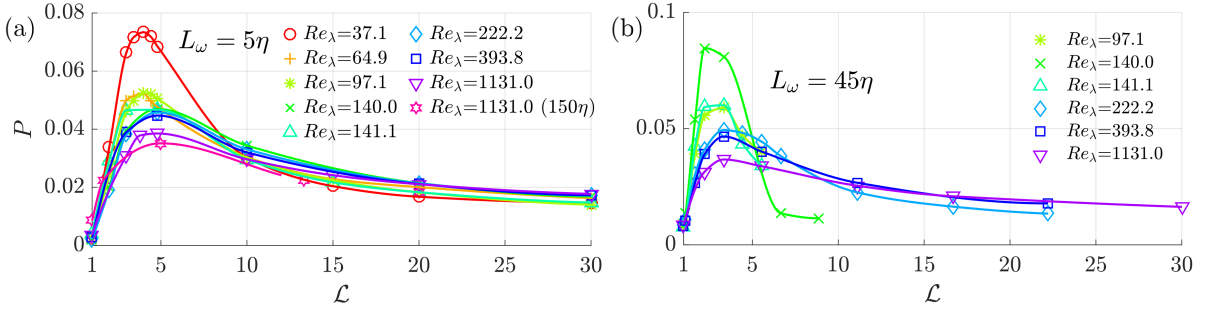


Fig. 3.9 Variation of probability of near perfect alignment of ω with α versus \mathcal{L} with (a) $L_\omega = 5\eta$ and (b) $L_\omega = 45\eta$.

The value of \mathcal{L} associated with the peak probability for near perfect alignment between ω and α , noted as \mathcal{L}^* , is plotted against Re_λ in Fig. 3.10 where various values of L_ω , ranging from 5 to 100η , are considered for the strained structures. It is clear that this length scale ratio is between 3 and 5 and is more or less independent of Re_λ , at least for the range considered in this study and independent of the choice of L_ω . This provides further evidence of a scale-by-scale energy transfer. The results for larger L_ω , for example 45η , do not extend to lower Re_λ because the larger straining scales required for the analysis become larger than the size of the computation domain. Furthermore, in light grayscale, the range of ratios $(L/S)_{\max}^E$ for each Re_λ case observed in Fig. 3.7 is also plotted. This ratio also lies in the same range as \mathcal{L}^* which clearly shows that all these phenomena related to the energy cascade picture are local in scale and more or

less independent of the Reynolds number. This provides support and evidence for the universality of the energy cascade picture, even at modest values of Re_λ .

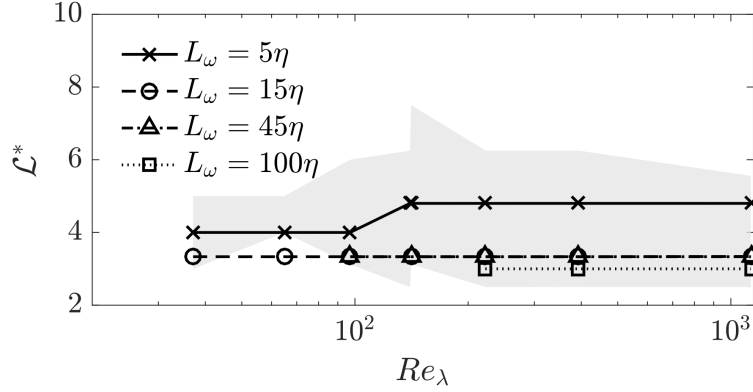


Fig. 3.10 Ratio $\mathcal{L}^* = L_s/L_\omega$ yielding the highest probability for perfect alignment of ω with the α strain rate (lines). The shaded region shows the minimum and maximum values of $(L/S)_{\max}^E$ yielding the highest energy transfer for the associated Re_λ .

Furthermore, the importance of the alignment of vorticity with the α -strain, and thus the actual vortex stretching, for the enstrophy production can be highlighted by estimating the contribution of each principal strain to the total enstrophy production. Indeed, the contributions of α , β and γ to the volume averaged enstrophy production $\langle \psi \rangle = \langle \omega_i S_{ij} \omega_j \rangle = \langle \psi_\alpha \rangle + \langle \psi_\beta \rangle + \langle \psi_\gamma \rangle$ is known to be in the ratio of $\langle \psi_\gamma \rangle : \langle \psi_\beta \rangle : \langle \psi_\alpha \rangle = -1 : 1.41 : 2.06$. For a vortex of scale L_ω , these contributions from strain rates of various sizes of eddies can be estimated using

$$\begin{aligned} \langle \psi^{L_\omega} \rangle &= |\omega^{L_\omega}|^2 \int_1^\infty \left(\alpha^{\mathcal{L}} \cos^2 \theta_\alpha + \beta^{\mathcal{L}} \cos^2 \theta_\beta + \gamma^{\mathcal{L}} \cos^2 \theta_\gamma \right) d\mathcal{L} \\ &= \langle \psi_\alpha^{L_\omega} \rangle + \langle \psi_\beta^{L_\omega} \rangle + \langle \psi_\gamma^{L_\omega} \rangle \end{aligned} \quad (3.24)$$

The ratio $\langle \psi_\gamma^{L_\omega} \rangle : \langle \psi_\beta^{L_\omega} \rangle : \langle \psi_\alpha^{L_\omega} \rangle = -1 : 0.46 : 3.44$ is observed for $L_\omega = 5\eta$ and $Re_\lambda = 140$. If one considers $L_\omega = 24\eta$ then this ratio becomes $-1 : 0.49 : 4.93$. For $Re_\lambda = 1131$, this ratio is $-1 : 0.32 : 2.51$ when $L_\omega = 5\eta$ and $-1 : 0.36 : 2.67$ when $L_\omega = 150\eta$. The α strain rate thus clearly dominates over the β strain for all the filtered fields. Hence, the main mechanism of enstrophy production is through the axial vortex stretching as suggested by the original energy cascade picture [Betchov, 1956; Richardson, 1922; Taylor & Green, 1937].

3.4.6 Summary

In summary, the validity of the Richardson/Kolmogorov energy cascade picture has been investigated using real space quantities by employing DNS data having Re_λ varying from about 37 to 1131. Through the detailed study of the energy and enstrophy fluxes, it has been confirmed that there is a scale-locality in the energy and enstrophy transfer across the cascade. In particular, it was observed that turbulent structures of a scale L mostly transfer energy/enstrophy to smaller structures of a size $\sim 0.3L$. Furthermore, as it is generally thought that the energy/enstrophy transfer is made through vortex stretching, this mechanism was studied by considering the alignment statistics between vorticity at a scale L_ω and straining structures at a scale L_s . It was confirmed that vortical structures of a length scale L_ω are mostly stretched by structures 3 to 5 times larger than L_ω for the range of Re_λ considered. This was noted by [Leung et al. \[2012\]](#) for $Re_\lambda = 141$, but it is seen here that this result extends to Re_λ as high as 1131 and as low as 37. In particular, the statistics of near perfect alignment between the filtered vorticity and filtered strain rate fields shows a clear maximum for a ratio of L_s/L_ω between 3 and 5. Considering the similarity between all these findings, a close link between the vortex stretching mechanism, energy transfer and enstrophy flux can be summarised. At a given scale L_ω , vortical structures are mostly stretched by structures of a scale $\sim 3L_\omega$. This gives rise to a transfer of energy from this large scale $\sim 3L_\omega$ to this scale L_ω . Subsequently, at this scale L_ω , enstrophy is being generated locally but this enstrophy is directly transferred to a smaller scale $\sim 0.3L_\omega$ through vortex stretching at smaller scales. And this process continues down the energy cascade until the Kolmogorov and dissipative scales. Furthermore, the statistics found are qualitatively the same for all the Reynolds numbers investigated here and choice of L_ω . This suggests the existence of a similar vortex stretching mechanism across a wide range of values of Re_λ and turbulence scales, and provides a strong support for the classical picture of the energy cascade and its locality. The morphology of these vortical structures has also been studied using the Minkowski functionals and were characterised as being tube-like, supporting the vortex-worm structures proposed by [Burgers \[1948\]](#). Thus, it is quite clear that the classical mechanism for the energy cascade prevails even at Re_λ as low as about 40 or as high as 1131. Thus, this indicates that DNS at these low Reynolds numbers still show dynamical features similar to those present at higher Re_λ .

This is of particular importance for the DNS of turbulent reacting flows like those conducted in the present work, as the Reynolds number is limited for reacting flows. Indeed, this result implies that those low Re_λ turbulent flows DNS still present the same

scales interactions as in higher Re_λ turbulence. Thus, meaningful results can still be obtained when analysing scales interactions in these low Re_λ DNS.

3.5 Interactions of scales in turbulent premixed flames

In the previous section, the interactions among various scales of turbulence has been studied to shed light on the energy cascade. In reacting flows, there is an additional interaction between the turbulence field and the reaction zones, which has been conjectured to be important in MILD combustion. As an initial step towards studying that effect in MILD combustion, this interaction is studied here in conventional turbulent premixed flames.

Most of practical combustion occurs in turbulent flows involving a strong nonlinear coupling between turbulence and chemical processes, and the flame is wrinkled and strained by turbulent eddies [Bray & Cant, 1991; Hamlington et al., 2011; Peters, 2000; Poinsoot & Veynante, 2011]. The flame wrinkling and straining are caused respectively by vorticity and strain-dominated structures in turbulence [Steinberg & Driscoll, 2009, 2010]. The heat release from combustion changes fluid properties such as density and viscosity and they in turn affect the turbulence. Hence, the turbulence-flame interaction is a two-way coupling. The premixed combustion is a small scale phenomenon having the laminar flame thermal thickness and burning velocity as its representative scales while the turbulence involves a spectrum of scales ranging from energy containing, integral, to viscous, Kolmogorov, scales. One can query if the whole spectrum of these scales imparts influences on the flame physics or only a certain part of this spectrum influences the flame predominantly. This classical question has been raised in many earlier studies and it has been suggested that the Gibson scale may be an appropriate cut-off scale [Peters, 2000], and Kolmogorov scale are too weak to wrinkle or strain the flame [Poinsoot et al., 1991; Roberts et al., 1993].

A key modelling quantity resulting from the turbulence-flame interaction is the flame stretch, κ , which is a measure for the change of elemental flame area, δA , given by [Candel & Poinsoot, 1990]:

$$\begin{aligned} \kappa &= \frac{1}{\delta A} \frac{d\delta A}{dt} = (\delta_{ij} - n_i n_j) S_{ij} + s_d \frac{\partial n_i}{\partial x_i} \\ &= a_T + s_d K_m \end{aligned} \quad (3.25)$$

where δ_{ij} is the Kronecker delta, n_i is the component in spatial direction x_i of the flame normal vector $\mathbf{n} = -\nabla c/|\nabla c|$ with c as a reaction progress variable based on fuel mass

3.5 Interactions of scales in turbulent premixed flames

fraction, $s_d = (Dc/Dt)/|\nabla c|$ is the displacement speed as defined by Peters [2000], and $S_{ij} = 0.5(\partial u_i/\partial x_j + \partial u_j/\partial x_i)$ is the strain tensor with u_i being the turbulent velocity component in the direction i . The tangential strain rate, a_T , and the curvature, K_m , coming from flame wrinkling are defined by Eq. (3.25). The flame stretch is typically taken as a source for flame surface area in the context of Flame Surface Density (FSD) formulation [Hawkes & Cant, 2001; Veynante & Vervisch, 2002] and there is a possibility for the surface averaged stretch to be negative [Chakraborty et al., 2007; Dopazo et al., 2015; Ruan et al., 2014b]. The stretch is used to obtain the flame wrinkling in LES for the thickened flame model [Charlette et al., 2002; Colin et al., 2000] and is also required to determine the local flame propagation speed in the G equation approach [Pitsch, 2006]. Various approaches such as strained flamelets and efficiency function have been proposed in the past for both RANS [Kolla & Swaminathan, 2010; Meneveau & Poinso, 1991] and LES [Charlette et al., 2002; Colin et al., 2000; Knudsen et al., 2013] calculations of premixed combustion, and these approaches work well for RANS calculations. Since most of the dynamic scales are resolved in LES, the inclusion of the flame stretch induced by subgrid eddies may not be required in these approaches because these eddies may be too weak to stretch the flame.

These formulations mentioned above were proposed based on a general picture that large scales stretch the flame while small scales merely broaden the preheat zone. Nevertheless, this is only a conjecture which is yet to be validated. The Kolmogorov scales were noted to have lower efficiency for flame stretching [Poinso et al., 1991; Roberts et al., 1993] but another study [Lipatnikov et al., 2014] suggested that this scale produced the highest stretch. Taylor timescale was also suggested to be an appropriate scaling factor for the tangential strain rate [Nada et al., 2004; Yenerdag et al., 2015]. These qualitative arguments were based on tests using flows such as counter rotating vortices or a weak homogeneous turbulence (with low intensity) interacting with a premixed flame. The hydrogen-air flames of Nada et al. [2004]; Yenerdag et al. [2015] include thermo-diffusive instabilities which will affect the flame-turbulence interaction. The efficiency function [Meneveau & Poinso, 1991] approach was developed using premixed flame interacting with two-dimensional counter rotating vortices, which was developed further for LES [Charlette et al., 2002; Colin et al., 2000]. However, turbulent flows involve non-linear interaction of spectrum of scales (or eddies) having complex morphology and topology which could challenge the presumption that the stretch efficiency can be taken to be well described by an ensemble of interactions between pairs of counter-rotating vortices. Indeed, measurements of Steinberg & Driscoll [2009, 2010] showed that the flame stretching produced by turbulent flows is not described well by this canonical flow.

Furthermore, previous DNS studies devoted to the analysis of stretch or tangential strain rate in low Ka [Chakraborty, 2007; Chakraborty & Cant, 2005] or high Ka [Wang et al., 2016, 2017] flames did not decompose the effects of the various scales of turbulence on these quantities.

Thus, there are contradictory views and these qualitative analysis raise two questions (1) what is the smallest turbulence scale imparting significant flame stretch? and (2) what is its implication for the modelling of the filtered reaction rate in LES? The vortical structures are produced by the vortex stretching mechanism in turbulence and hence the influence of turbulence-flame interaction on this mechanism is also of interest.

3.5.1 Instantaneous features

The five sets of statistically planar turbulent premixed flame DNS data, from Gao et al. [2014]; Minamoto et al. [2014a]; Rutland & Cant [1994] and presented in section 3.2.2, are analysed here. These simulations are of statistically planar premixed flames propagating into homogeneous turbulence in the reactant mixture flowing from left to right as illustrated in Fig. 3.11, which will be discussed in detail later. The various characteristics of these data have been presented in details in section 3.2.2 and Table 3.2.

The compensated turbulent kinetic energy spectrum $\Pi_k(k) = E(k)k^{5/3}\epsilon^{-2/3}$, where ϵ is the turbulent kinetic energy dissipation rate, is presented in Fig. 3.12 for the unfiltered and three bandpass filtered velocity fields for the highest u'/s_L case in Table 3.2. The filtered fields have $L = 15\eta$, 10η and 5η and the peak energy is at $\sqrt{5}/L$ [Leung et al., 2012]. As expected, the energy in the filtered field is centred around the chosen length scale and the energies of larger and smaller eddies are attenuated. The spectrum of the unfiltered field is the envelop of the peaks in the filtered spectra. The compensated energy spectrum, Π_c , of the scalar, c , is also shown in Fig. 3.12, which has the peak at $k\delta_{th} \approx 0.49(k\eta = k\delta_{th}Ka^{-1/2} \approx 0.11)$. These results are similar for the other flames in Table 3.2. It should be noted that only a small inertial range is observed on the unfiltered spectrum as a result of the limited range of scales and Reynolds numbers of the present data. However, this does not affect the conclusion of this study as the flame scale is very much smaller than the scales of the inertial range. Furthermore, what really matters for the multiscale analysis is the presence of some scales and their relative range.

Typical spatial distribution of the filtered structures are shown in Fig. 3.11 with contours of normalized progress variable reaction rate, $\dot{\omega}^+$ which is threshold at $\dot{\omega}^+ = 1$ for its iso-surface shown in Fig. 3.11. The reaction rate is normalised using $\rho_u s_L/\delta_{th}$, where ρ_u is the reactant density. The strain rate, $S_{ij}^{L_s}$, structures have a scale $L_s = 14.6\eta \approx 3.3\delta_{th}$ and the vortical structures identified using enstrophy, $\Omega^{L_\omega} = 0.5|\boldsymbol{\omega}^{L_\omega}|^2$ where $\boldsymbol{\omega}^{L_\omega}$ is the

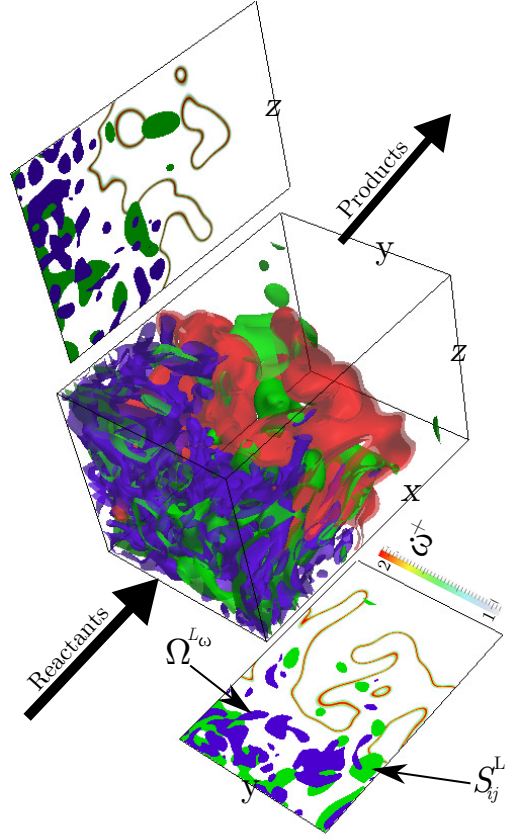


Fig. 3.11 Reaction rate of c with bandpass filtered strain rate $S_{ij}^{L_s}$, at $L_s \approx 3.3\delta_{th}$ and enstrophy Ω^{L_ω} , at $L_\omega = \delta_{th}$, fields for $u'/s_L = 11.25$ case in Table 3.2, x - z and x - y cuts are shown.

vorticity vector, having $L_\omega = 4.4\eta \approx \delta_{th}$. Turbulent structures presented in Fig. 3.11 are threshold at their respective mean plus half standard deviation value. It can be observed in the plane cuts in Fig. 3.11 that downstream of the flame, less and sparser structures of Ω^{L_ω} and $S_{ij}^{L_s}$ are found suggesting that the flame dampens the turbulence. Furthermore, variations in the distribution and sizes of these structures are observed suggesting that their effects on the flame will be different [Hamlington et al., 2011; Lipatnikov et al., 2014; Treurniet et al., 2006]. Indeed, strain rate structures can be found in both upstream and downstream of the flame front, even in its neighbourhood, whereas the enstrophy structures representing small scales are present predominantly in far upstream of the flame. This implies that small scales structures may have a reduced influence on the flame. This will be discussed in further detail later in section 3.5.3. Furthermore, it is important to analyse the effect of the flame on the vortex stretching mechanism which produces these small scales.

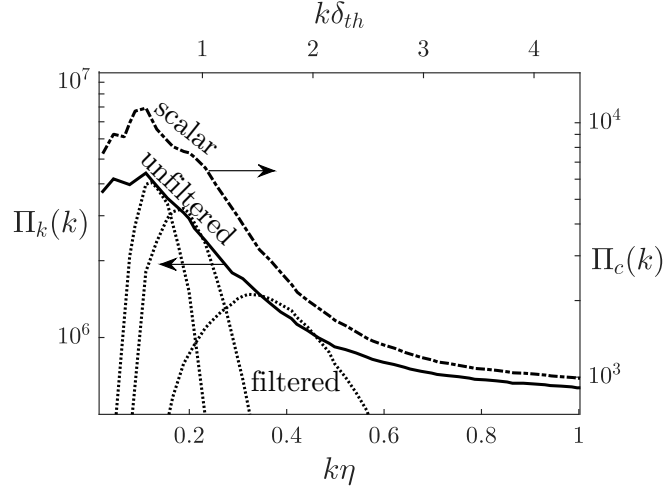


Fig. 3.12 Compensated energy spectrum for unfiltered and filtered at $L = 15\eta$, 10η and 5η (left to right) velocity fields and unfiltered progress variable.

3.5.2 Vorticity-strain rate analysis

In the present section, the vortex stretching mechanism is analysed to study how it may be influenced by the presence of heat release and chemical reactions. Similarly to what has been done in turbulence in section 3.4, the analysis is performed by studying the alignment statistics between the strain rate at a give length scale and the vorticity at a different scale. The pdf of $|\cos \theta_i|$ for α and β strain rates for the bandpass filtered fields of premixed flame with $u'/s_L = 11.25$ is shown in Fig. 3.13 for $L_\omega = \delta_{th}$ and $0.5\delta_{th} \leq L_s \leq 10\delta_{th}$. These pdfs are extracted from the entire computational domain. Similar to the non-reacting flow results by Leung et al. [2012], a preferential alignment of ω is found with α from eddies larger than the vortical structure and the alignment with β is approached when $L_s \leq L_\omega$. This alignment with β was also observed when considering unfiltered fields in a high Ka jet flame [Wang et al., 2016]. The probability, P , for $0.98 \leq |\cos \theta_\alpha| \leq 1$ as a function of $\mathcal{L} = L_s/L_\omega$ is shown in Fig. 3.14 for all the flames in Table 3.2 to quantify the eddy scale imparting the most stretching on vortical structures of scale L_ω . The peak occurs for \mathcal{L} between 3 and 4 for the flames, implying that the vortical structure is stretched mostly by structures 3 to 4 times bigger than itself, which was also observed in section 3.4 and by Leung et al. [2012].

In order to assess the role of reactions on this alignment statistics more effectively, the alignment pdfs conditioned on the reaction rate can be investigated. This is done through the joint-pdf of $\psi = |\cos \theta_\alpha|$ and $\dot{\omega}^+$, noted as $p_{\psi, \dot{\omega}^+}$, and computing P conditioned on $\dot{\omega}^+$ for the various \mathcal{L} using $P|\dot{\omega}^+ = \int_{0.98}^1 p_{\psi, \dot{\omega}^+} d\psi / p_{\dot{\omega}^+}$ with $p_{\dot{\omega}^+}$ as the marginal pdf. Figure 3.15 shows this result. It can be observed that the reaction rate does not have a strong

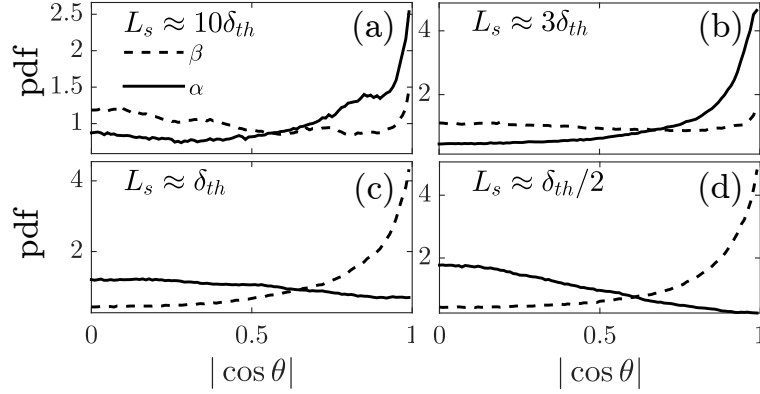


Fig. 3.13 Pdf of the magnitudes of direction cosines between vorticity at $L_\omega = \delta_{th}$ and principal strain rates at L_s in the case with $u'/s_L = 11.25$.

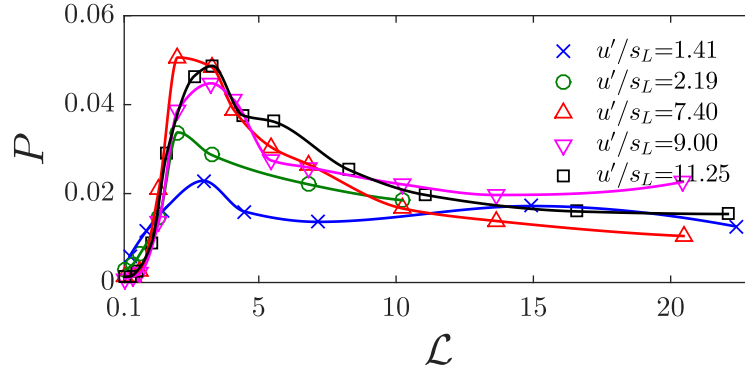


Fig. 3.14 Probability of perfect alignment between the vorticity at L_ω and α strain rate at $L_s = \mathcal{L}L_\omega$.

influence on the behaviour previously mentioned as the maximum probability P is found for $3 \leq \mathcal{L} \leq 5$ for all reaction rates.

The similarity between the present reacting and non-reacting results (from [Leung et al., 2012] and those shown in section 3.4) suggests that the mechanism of vortex stretching and the role of relative eddy sizes on this mechanism are not unduly influenced by the presence of chemical reactions and heat release. Hence, the vortex stretching mechanism is expected to play a key role in turbulent flows. Other mechanisms such as baroclinic torque for enstrophy production [Hamlington et al., 2011; Lipatnikov et al., 2014; Treurniet et al., 2006] are not considered because the main focus is on the eddy-interaction and vortex stretching mechanism in reacting turbulence.

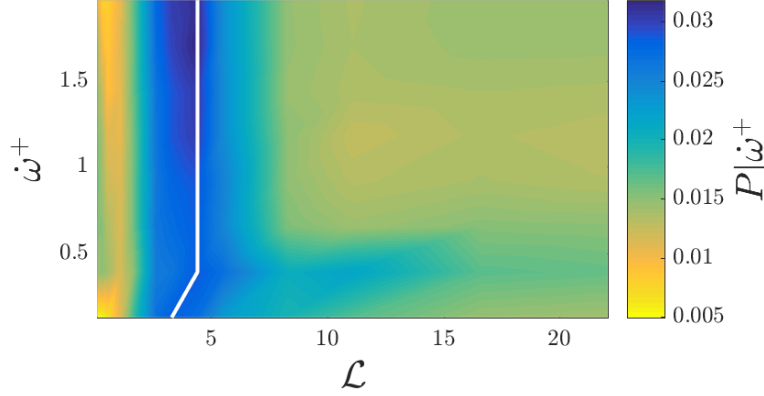


Fig. 3.15 Probability of perfect alignment between the vorticity at L_ω and α strain rate at $L_s = \mathcal{L}L_\omega$ conditioned on ω^+ with the maximum probability shown (white line) for case with initial $u'/s_L = 11.25$.

3.5.3 Multiscale analysis of tangential strain-rate

The bandpass filtering technique can also be used to calculate the tangential strain imparted by eddies of scale L_s through $a_T^{L_s} = (\delta_{ij} - n_i n_j) S_{ij}^{L_s}$ and its surface averaged value is

$$\psi(L_s^+) = \langle |\nabla c| a_T^{L_s^+} \rangle / \langle |\nabla c| \rangle, \quad (3.26)$$

where $L_s^+ = L_s/\delta_{th}$ and $\psi_{\text{int}} = \int_0^\infty \psi dL_s^+$ gives the surface averaged contribution coming from all eddies in the flow. Figure 3.16a shows the variation of fractional contribution, $\hat{\psi} = \psi/\psi_{\text{int}}$, with L_s^+ . The peak contribution is for $5 \leq L_s^+ \leq 8$ in the corrugated flame with $u'/s_L = 1.41$. The flame with $u'/s_L = 2.19$ and a skeletal mechanism also has peak $\hat{\psi}$ from similar sized eddies of $6 \leq L_s^+ \leq 10$ suggesting that the chemical mechanism does not play a significant role in the kinematic aspect of flame-turbulence interaction. There are no data for eddies larger than $13\delta_{th}$ for the flame with $u'/s_L = 2.19$ because larger structures are bigger than the computational domain, however, the decreasing trend is seen already. Furthermore, the length scale ratio, ℓ/δ_{th} , does not seem to influence this behaviour unduly when u'/s_L is similar. The peak value is shifted towards L_s^+ of about 2 to 3 for flames with higher turbulence intensity. Furthermore there is a sharp decrease in contributions from eddies of smaller size whereas the decrease is slower for larger scales up to $L_s^+ \simeq 17$. This suggests that eddies in the range $3 \leq L_s^+ \leq 17$ have substantial effect on flame straining. This is confirmed further by the cumulative integral $\psi^* = \int_0^{L_s^+} \hat{\psi} dL_s^+$ plotted in Fig. 3.16b. There is less than 20% contribution from eddies smaller than $3\delta_{th}$ and less than 10% for eddies larger than $17\delta_{th}$.

3.5 Interactions of scales in turbulent premixed flames

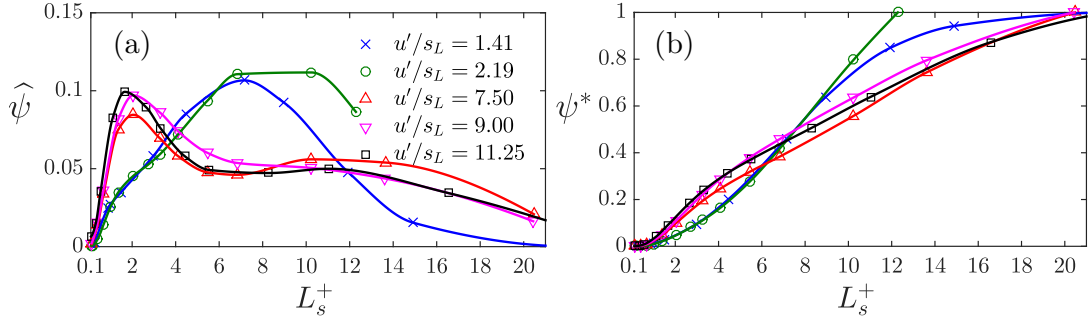


Fig. 3.16 (a) Surface averaged tangential strain rate from eddies of scale L_s^+ normalised by total contribution and (b) its cumulative integral.

Roberts et al. [1993] defined a cutoff scale, l_R , given by

$$(l_R/\delta_{th}) = 2.0 (u'/s_L)^{-3/4} (\ell/\delta_{th})^{1/4}, \quad (3.27)$$

and eddies smaller than l_R are thought to have nearly no impact on flame wrinkling and straining. Also, Gibson scale $l_G = s_L^3/\epsilon$, where ϵ is the turbulent kinetic energy dissipation rate, was suggested to be the smallest eddy size that can interact effectively with flames [Peters, 2009]. These cutoff scales, normalised by δ_{th} , are compared in Fig. 3.17 for the five flames along with length scales corresponding to $\psi^* = 0.1$ and peak $\hat{\psi}$. These two scales are l_{10}^+ and l_p^+ respectively, and l_{10}^+ implies that eddies smaller than l_{10}^+ contribute 10% or smaller to the total tangential strain rate experienced by the flame. The l_p^+ is about 10 for $u'/s_L = 2.19$ and it approaches l_{10}^+ as u'/s_L increases. The results in Fig. 3.17 suggest that the range of eddies having weak influence in straining the flame is larger than that originally thought.

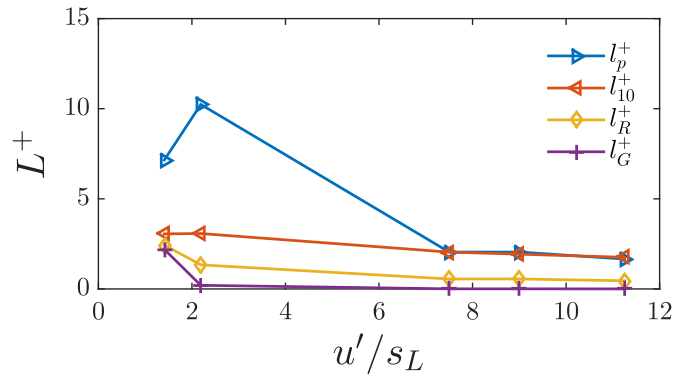


Fig. 3.17 Comparison of various cutoff scales.

This result has wider implications for LES combustion modelling. Indeed, this analysis has shown that eddies of sizes larger than $2\delta_{th}$ imparted the most influence on the flame and it may not be required to resolve scales smaller than this in LES. The bandpass filter used is efficient in cutting scales smaller than the specified one and cuts larger scales less sharply. As a consequence the values found here for l_p^+ and l_{10}^+ are conservative because $a_T^{L_s^+}$ includes contributions from eddies of sizes L_s^+ and slightly larger. This suggests that LES numerical grid resolving turbulence down to l_p^+ or l_{10}^+ would capture the flame stretching quite well and it may not be necessary to use a refined model for this aspect. This is of practical importance because LES meshes typically resolve reacting turbulence down to a size of the order of δ_{th} [Pitsch, 2006]. This finding is consistent with the inner cut-off scale estimates based on fractal analysis found in several previous studies in the context of FSD [Chakraborty & Klein, 2008; Knikker et al., 2004] and scalar dissipation rate [Gao et al., 2014] closures.

3.5.4 Summary

From this analysis of DNS of turbulent premixed flames, it is observed that vortical structures of scale L_ω are stretched by larger eddies with the maximum stretching from eddies of scale about $4L_\omega$. This is similar to non-reacting turbulence, which suggests that the premixed flame has negligible influence on the vortex stretching mechanism. The influence of eddy on turbulence-flame interaction has also been investigated using surface averaged tangential strain rate imparted by the eddy. It is shown that eddies smaller than $2\delta_{th}$ contribute less than 10% of the total tangential strain rate and eddies larger than $17\delta_{th}$ contribute less than 10%. This has implication for the subgrid modelling for LES of premixed combustion. Indeed, these results suggest that resolving turbulence scales down to few multiples of δ_{th} would be enough to capture most of the flame straining caused by turbulence. These will be captured by the LES equations and additional modelling may not be required for subgrid scale flame stretching.

3.6 Implications for MILD combustion

In this chapter, analysis of turbulence and turbulent premixed flames have been performed. In a first step, the scale locality of the energy cascade has been confirmed through a study of the energy/enstrophy transfer across scales of turbulence and by analysing the vortex stretching mechanism. More importantly, it was observed that the classical picture of the energy cascade, whereby energy is transferred from large scales to a neighbouring

3.6 Implications for MILD combustion

smaller scale, showed no significant difference between turbulence at low or high Reynolds numbers. This has strong implications for the DNS of MILD combustion here. Indeed, this suggests that the interactions of scales in the turbulence field of the DNS of MILD combustion will possess similar features as those that would be present in DNS at larger Reynolds numbers. Hence, this supports the future analysis of scales interactions to be discussed in chapter 7.

In a second stage, it was observed that the vortex stretching mechanism was not unduly affected by heat release in premixed flames. A question that arises is whether this would still be the case for MILD combustion where reactions are volumetrically distributed and not confined to thin reaction zones. This will be discussed in chapter 7.

Chapter 4

Inception of MILD combustion

This chapter starts the analysis of the DNS of MILD combustion generated in this thesis work and focuses on the inception of MILD combustion. In particular, the role of radicals on this inception is analysed and the implications of the results obtained on existing definitions of MILD combustion are discussed.

4.1 Motivation

As discussed in section 1.2.1, various definitions have been proposed, in the past, to characterise MILD combustion using classical combustion theories involving a single step irreversible reaction. In particular, the theoretical analysis of Oberlack et al. [2000] for premixed and Evans et al. [2017c]; Pitsch & Fedotov [2001] for non-premixed MILD combustion were detailed there. One aspect that needs to be stressed is that both single reaction with no intermediate [Oberlack et al., 2000; Pitsch & Fedotov, 2001] and complex chemical kinetics [Evans et al., 2017c] were used for their analysis, but overall, similar S-curve characteristics were deduced.

It is, however, important to note that there were no intermediate species present in the high temperature oxidiser stream (made of H_2O , CO_2 , O_2 and N_2) for the opposed flow non-premixed flame of Evans et al. [2017c] while they may play an important role in the inception of MILD combustion. Indeed, Fig. 4.1 shows the variations of product composition from the equivalent laminar premixed flames with T . These are computed using CANTERA considering a premixed flame with an oxidiser at 1100 K with $X_{\text{O}_2} = 0.03$, $X_{\text{CO}_2} = 0.03$, $X_{\text{H}_2\text{O}} = 0.1$ and $X_{\text{N}_2} = 0.84$ and C_2H_4 as fuel for various equivalence ratios as in the studies of Evans et al. [2017c]; Medwell et al. [2008]. It is quite clear that these products contain a non-negligible amount of intermediate species. Hence, in the oxidiser stream of a MILD combustor with internal EGR, one needs to

allow for these intermediates to be present in the oxidiser stream, which would be akin to typical MILD combustion involving EGR. However, if one allows the intermediates in the oxidiser stream of the opposed-flow then the classical flame solution to obtain S-curves may not exist and thus the laminar configuration used in this previous definition of MILD combustion may not be entirely adequate as it cannot account for the effects of the radicals present in MILD mixture. As will be discussed in chapter 5, this is because MILD combustion has shown to have premixed and non-premixed flames, and auto-ignition events entangled in space and time. Thus, there are distinctive features along with conventional flames in MILD combustion and hence, one needs to be cautious while defining it.

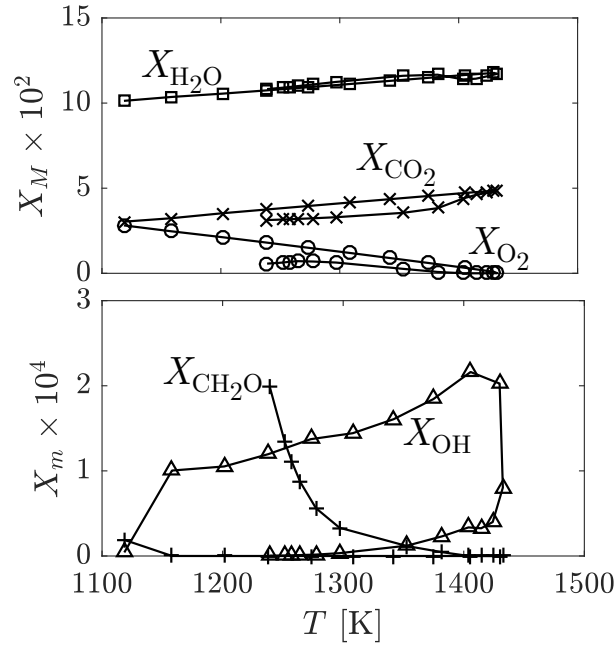


Fig. 4.1 Variations of major, X_M , and minor, X_m , species mole fractions with T for $0.1 \leq \phi \leq 5$ using the same oxidiser and fuel compositions, as in [Evans et al., 2017c; Medwell et al., 2008].

The objective here is to analyse these definitions, specifically the classical S-curve for non-premixed situations, using the DNS data of MILD combustion generated in the present thesis work and subsequently assess if the definition based on laminar counterflow configuration [Evans et al., 2017c] is suitable or not. Specifically, the role of chemically active radicals, i.e. radicals such as CH_2O , OH or H , playing key-roles in the inception of MILD combustion, is studied.

4.2 Role of radicals on MILD combustion inception

As noted in section 1.2.1, the scalar dissipation rate (SDR), N_Z , is an important quantity in the ignition process of non-premixed systems and is thus studied in more details here. In Fig. 4.2, iso-surfaces of $\dot{Q}^+ = \dot{Q}\delta_{th}/(\rho_r s_L c_p(T_p - T_r))$ is shown for all cases where they are coloured by $\log(N_Z)$ with the temperature field shown in the bottom and side surfaces. The normalisation is done using the thermo-chemical quantities, appearing in the above expression, for the local mixture fraction. One can also use these quantities for Z_{st} in the normalisation but this would mask regions with relatively low heat release rate per unit volume, for example lean regions. It is observed that the reaction zones are extremely convoluted and multiply connected which will inevitably results in reaction zones interactions. This aspect of the reaction zones will be further discussed in the next chapter.

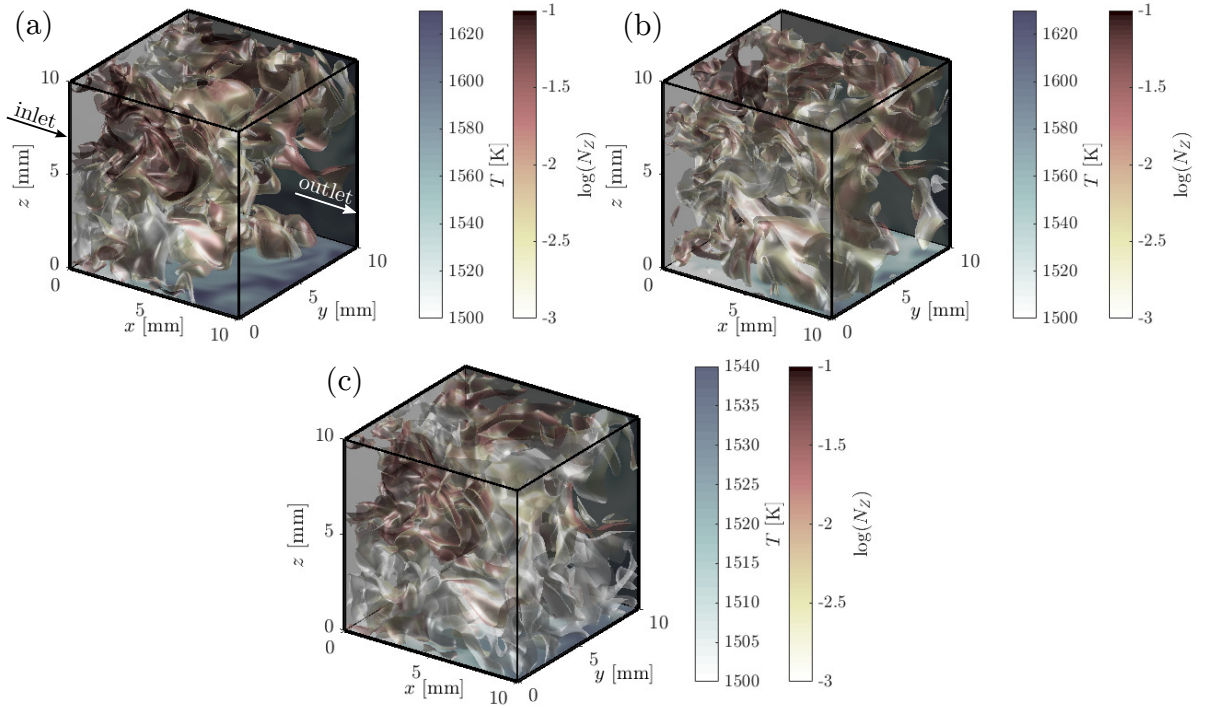


Fig. 4.2 Typical iso-surfaces of normalised heat release rate $\dot{Q}^+ = 2.0$ at $t = 1.5\tau_f$ for cases (a) AZ1, (b) AZ2 and (c) BZ1, coloured by $\log(N_Z)$. The temperature field is shown on the bottom and side surfaces.

It is also observed that N_Z varies over several orders of magnitude and it is also apparent that reactions (and ignition) occur in regions of high (compared to the mean) SDR. To more finely analyse the effect of SDR, from these DNS data, the S-curve, similar to those presented in Fig. 1.4, can be constructed by extracting N_Z and $\theta =$

Inception of MILD combustion

$(T - T_r)/(T_{\max} - T_r)$. There are two ways to plot this result, one is to consider the entire domain and construct:

$$\langle N_Z | \theta \rangle = \int N_Z p(N_Z | \theta) dN_Z. \quad (4.1)$$

The other way is to consider the conditionally averaged quantities along the stoichiometric mixture fraction and this is given by:

$$\langle N_Z | \theta_{st}, Z = Z_{st} \rangle = \int N_Z p(N_Z | \theta_{st}, Z_{st}) dN_Z \quad (4.2)$$

The conditional probability density function of N_Z conditioned on θ is $p(N_Z | \theta)$. The doubly conditioned pdf of N_Z on θ and $Z = Z_{st}$ is $p(N_Z | \theta, Z_{st})$. These pdfs are constructed using samples collected over the entire sampling time. In the expression for θ , $T_r = 1500$ K is the unburnt temperature and T_{\max} is the maximum temperature either for stoichiometric mixture or for the entire domain depending on if Eq. (4.2) or (4.1) is used.

The results are plotted in Fig. 4.3 for all cases, where N_Z for each case is normalised by $N_{Z,st}^0$ defined as $\langle N_Z | \theta = 0, Z_{st} \rangle$ computed for case AZ1. The DNS results show a

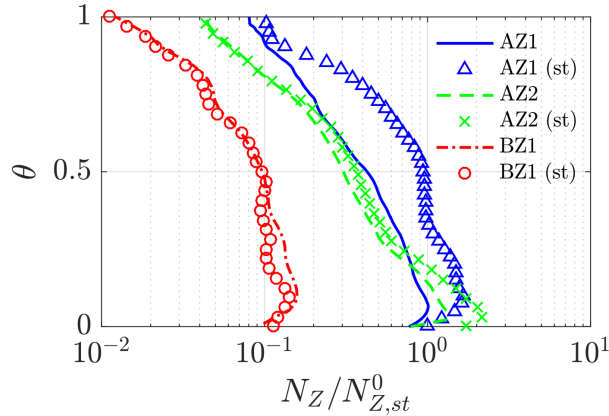


Fig. 4.3 Variation of normalised temperature with SDR. This variation for Z_{st} is also shown.

different behaviour compared to the laminar cases depicted in Fig. 1.4. Specifically, θ increases with $N_Z / N_{Z,st}^0$ near $\theta = 0$, which is the opposite of the behaviour in Fig. 1.4. For larger θ , the increase in θ is accompanied by a decrease in N_Z which is similar to the classical S-curve. These observations hold for both stoichiometric (symbols) or entire (lines) mixtures as shown in Fig. 4.3. The difference between the entire and stoichiometric mixtures in case AZ1 is because of the difference in the mixture fraction distribution and its lengthscale which leads to different SDR for these mixtures but both the entire and stoichiometric mixtures exhibit this particular behaviour during inception. Furthermore, this behaviour was also observed when considering the pdf constructed

4.2 Role of radicals on MILD combustion inception

from just an instantaneous snapshot (not shown here) and thus the observations made using Fig. 4.3 hold both statistically and instantaneously for MILD combustion. This contrasting behaviour near $\theta = 0$ (inception of combustion) is quite intriguing and is explored further below.

Figure 4.4 depicts regions of heat release rate normalised using the maximum value in the mid x - y plane shown. The top 80% is shown to highlight regions with large heat release rate and the white regions have $\hat{Q} < 0.2$. The dashed black lines show contours of $\hat{N}_Z = N_Z / \max(N_Z) = 0.2$. Here and in the following discussion, quantities with a hat imply that they are normalised using the maximum value observed in the plane chosen for the analysis. This threshold value of 0.2 is used to focus on regions of high SDR and large heat release rate. It is quite clear that the regions with large heat release rate and \hat{N}_Z values overlap, which is specifically so in the upstream part of the computational domain. This behaviour gives the lower branch (with both θ and $N_Z/N_{Z,st}^0$ increasing) of the DNS S-curve shown in Fig. 4.3. Although a single plane at a particular time is shown in Fig. 4.4 for case AZ1, similar situations were also found for cases AZ2 and BZ1 (not shown here) and the result in Fig. 4.3 demonstrates that such a behaviour occurs in other planes and at other times since the data collected over the entire sampling period is used for Fig. 4.3.

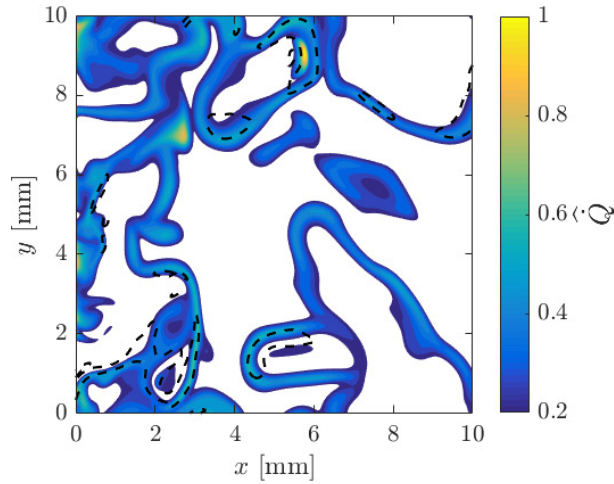


Fig. 4.4 Typical variation of \hat{Q} in the mid x - y plane for case AZ1 at $t = \tau_f$. Dashed black lines enclose regions with $\hat{N}_Z > 0.2$.

The reason behind this increase in θ with an increase in N_Z during the inception stems from the nature of MILD combustion with internal EGR. Indeed, the mixture for MILD combustion with internal EGR contains fuel, air and combustion products with chemically active radicals as established in Fig. 4.1. The radicals such as CH_2O , OH

Inception of MILD combustion

and H, play a key role in initiating the combustion reactions. This is demonstrated in Fig. 4.5 showing CH_2O and OH mass fractions fields normalised using their respective maximum values observed in the plane shown. The radicals present in the recirculated hot gases give non-zero (indeed quite high) values of $\hat{Y}_{\text{CH}_2\text{O}}$ and \hat{Y}_{OH} , which are of interest to understand the inception of MILD combustion. The relatively larger values seen in Fig. 4.5 for the middle and downstream parts of the domain are because of the combustion occurring in the domain. A closer scrutiny of the results in Fig. 4.5 shows that the high SDR are occurring in regions with overlapping \hat{Y}_{OH} and $\hat{Y}_{\text{CH}_2\text{O}}$. This is particularly so in the upstream 30% of the computational domain, where the MILD combustion begins. Hence, it is quite clear that the radicals play a vital role in the inception of MILD combustion which gives a quite different behaviour for the lower branch of the S-curve compared to the classical curve as seen in Fig. 4.3.

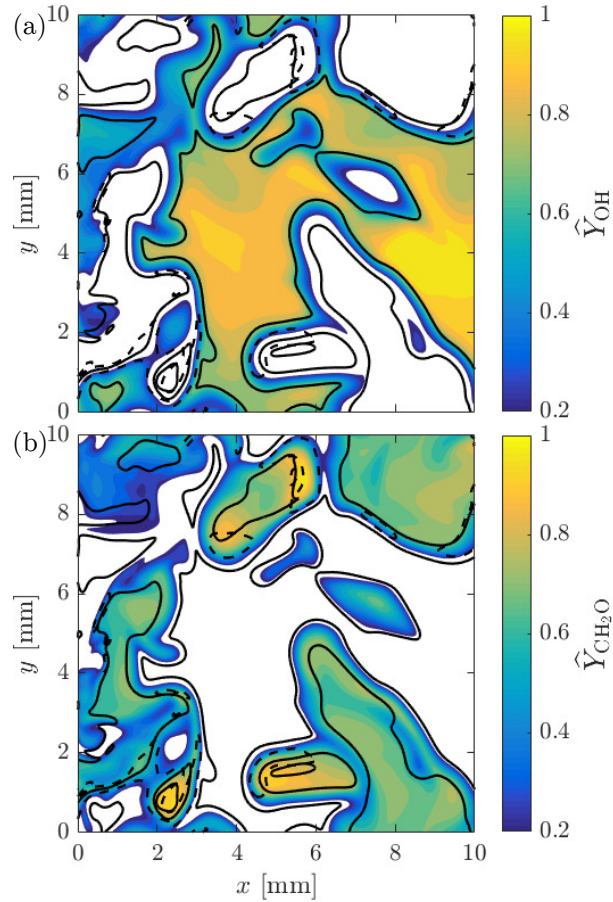


Fig. 4.5 Variation of (a) \hat{Y}_{OH} and (b) $\hat{Y}_{\text{CH}_2\text{O}}$ in the mid x - y plane for case AZ1 at $t = \tau_f$. Isolines of $\hat{Q} = 0.2$ (full black lines) and $\hat{N}_Z = 0.2$ (dashed) are also shown.

4.2 Role of radicals on MILD combustion inception

The role of these radicals on the inception of MILD combustion, OH in particular, is further explored by considering a quantity $\Delta Y_{\text{OH}} = Y_{\text{OH}} - Y_{\text{OH}}^c$, where Y_{OH}^c is the local value of the *incoming* OH mass fraction where there is no combustion. This quantity is obtained by performing a DNS with the same initial and inflowing fields (species and velocities) as the present MILD combustion DNS but by removing all the chemical reactions. One, then, obtains the purely convective-diffusive evolution for the species inside the computational domain with the same turbulence field. Since the temperature rise in the MILD combustion DNS is moderate, only few tens of Kelvin, the velocity fields in this and the convective-diffusive cases remain similar, especially in regions close to the inlet. A comparison of the species mass fractions from the combustion DNS to those from the convective-diffusive case allows one to understand the local influence of combustion on these species, at a given time and location. Hence, $\Delta Y_{\text{OH}} > 0$ implies that OH is produced locally by combustion since the local Y_{OH} is larger than Y_{OH}^c . The values of ΔY_{OH} normalised by its maximum value in the plane shown is plotted in Fig. 4.6 and it is seen that close to the inlet, the normalised value, $\widehat{\Delta Y}_{\text{OH}}$, is mostly negative. This indicates that the incoming OH is consumed by chemical reactions, i.e. $Y_{\text{OH}} < Y_{\text{OH}}^c$. Thus, the OH in the incoming recirculated exhaust gases is consumed and acts as a precursor for initiating ignition and heat release – inception of MILD combustion.

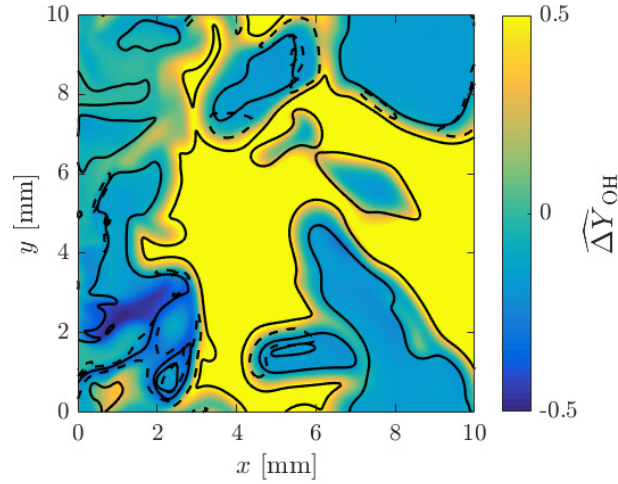


Fig. 4.6 Variation of $\widehat{\Delta Y}_{\text{OH}}$ in the mid x - y plane for case AZ1 at $t = \tau_f$. Isolines of $\widehat{Q} = 0.2$ (full black lines) and $\widehat{N}_Z = 0.2$ (dashed) are also shown.

The importance of the incoming radicals is even more apparent if one cross-plots ΔY_{OH} with normalised temperature θ . This is shown in Fig. 4.7 as a scatter plot for regions with $\widehat{N}_Z = N_Z / \max(N_Z) \geq 0.2$ with $\max(N_Z)$ as the maximum for the chosen timestep. The samples are collected from the upstream portion of the domain, $0 \leq x/L_x \leq L_2 = 0.05$,

Inception of MILD combustion

since the focus is on the inception of MILD combustion. It is clear that there is a strong correlation between the temperature increase and the consumption of incoming OH. This further indicates that the inflowing radicals, here OH, play a key-role in the inception of MILD combustion, which is absent in the classical S-curve. This result was observed not to be strongly sensitive to L_2 up to $L_2 \approx 0.1$. Furthermore, this result was also observed not to be unduly influenced by the choice of the threshold for \widehat{N}_Z (not shown here). Similar behaviours are observed for the cases AZ2 and BZ1. Furthermore, while the results are shown here only for OH, a sensitivity analysis of the autoignition delay time with regards to the reaction steps of the MS-58 mechanism, shown in Fig. B.2 of appendix B, highlights that the other radicals, such as H, O or CH₂O, have an importance similar to the one of OH on the ignition process. Thus, analysing those would yield similar results to those shown here for OH.

These results imply that the MILD combustion inception is driven by chemical kinetics initiated by the radicals present. As a result of this, close to the inlet boundary of the domain, an increase in N_Z implies increased small-scale mixing between neighbouring mixtures containing differing levels of radicals. This increased mixing promotes reactivity leading to an increase in θ .

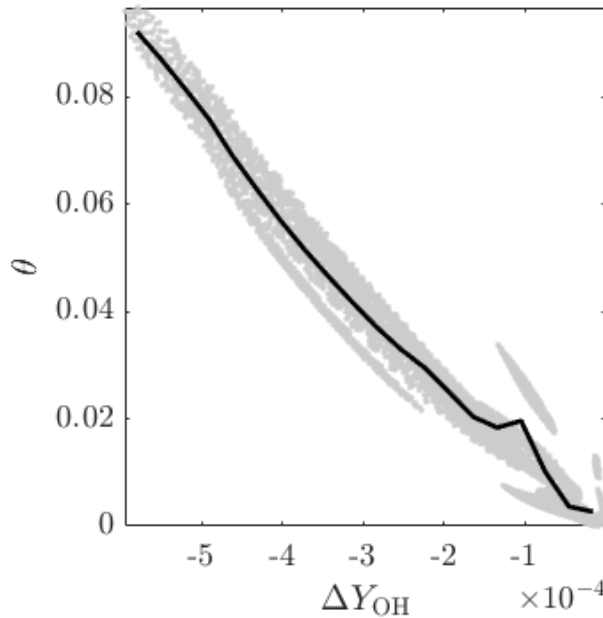


Fig. 4.7 Variation of ΔY_{OH} with θ for points with $\widehat{N}_Z > 0.2$ and axial locations $0 \leq x/L_x \leq 0.05$ for case AZ1 at $t = \tau_f$. The corresponding conditional average $\langle \theta | \Delta Y_{OH} \rangle$ is plotted as full black line.

From the analysis presented here using DNS of MILD combustion with internal EGR, it is clear that the past definitions of MILD combustion deduced using one-step chemistry in simplified configurations present various shortcomings. In particular, while the present DNS also show a smooth ignition and a progressive increase in temperature, these definitions do not include the important role played by chemically active radicals in the inception of MILD combustion while over-emphasizing the importance of N_Z . Indeed, a one-step chemistry solely characterised by an activation energy cannot account for the presence of radicals on the reaction. However, these radicals in the incoming stream play a major role in initiating and sustaining combustion as has been noted by Wüning & Wüning [1997]. Furthermore, the preferential diffusion has been shown to be important in the past [Göktolga et al., 2015] and thus the unity Lewis number assumed in the earlier analysis may have to be revisited for MILD combustion.

4.3 Summary

In this chapter, it was shown that the S-curve deduced from the DNS data presents a unique and contrasting behaviour in the inception phase (lower branch) compared to the classical case. Indeed, there is an increase in θ with an increase in SDR which is the opposite of the classical S-curve. The classical behaviour of θ increasing with decreasing SDR is observed for higher values of θ . The contrasting behaviour in the inception phase is because of the chemically active radicals present in the incoming stream. These results highlight a need to revisit the definitions of MILD combustion specifically when there is internal EGR or vitiated air stream which are quite typical of MILD combustion applications. Indeed, previous definitions of MILD combustion [Evans et al., 2017c; Oberlack et al., 2000] do not show this behaviour as they do not account for the effect of radicals and intermediate species. It should, however, be noted that the definition proposed by Cavaliere & de Joannon [2004] seems to be adequate, as it does not make any assumptions as to how the temperature rise occurs and only uses the initial and final temperatures.

Chapter 5

Reaction Zones Structure and Combustion Modes in MILD Combustion

In the previous chapter, the role of radicals on MILD combustion inception has been studied. From this inception, reaction zones in MILD combustion develop into structures which have extremely convoluted shapes and thus, they will have a unique behaviour. The objective of this chapter is to analyse the structure of these reaction zones and to shed light on the modes of combustion occurring in MILD combustion. The potential use of some particular species to identify these reaction zones for MILD combustion is also discussed.

5.1 General combustion features and evolution

Figure 5.1 shows the volume rendered temperature field from the DNS of conventional turbulent combustion (case with $u'/s_L = 2.19$ of Table 3.2) and the case AZ1 of the present work. These are numerical equivalents to line of sight photographs from experiments. In conventional premixed combustion, the existence of a flame front is still clearly observed which supports the presence of a strong gradient of temperature across the flame. On the other hand, MILD combustion shows a homogeneous temperature field with no visible flame front. This supports the experimental observations by [de Joannon et al. \[2000\]](#) and [Ozdemir & Peters \[2001\]](#).

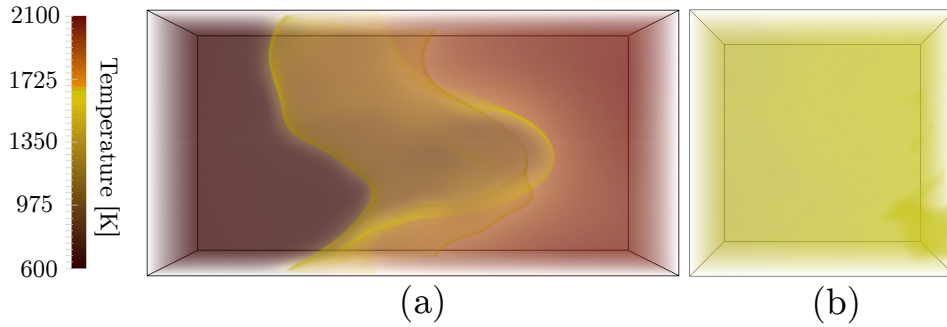


Fig. 5.1 Comparison of volume rendered temperature field at $t = 1.5\tau_f$ of (a) conventional turbulent premixed combustion (case with $u'/s_L = 2.19$ of Table 3.2) and (b) non-premixed MILD combustion (case AZ1 from the present work, see Table 2.2).

The overall influence of combustion can be investigated using the variations of averaged, in the y - z plane and in time, quantities such as temperature and various scalar mass fractions values with x . These averages, noted $\langle \cdot \rangle_x$, are presented in Fig. 5.2.

Analysis of these quantities shows that the averaged temperature increases progressively from 1500 K to about 1600 K for cases AZ1 and AZ2, and 1550 K for case BZ1 and the reactant species such as fuel and oxygen mass fractions decrease with x while the product mass fractions increase gradually. Intermediate species like OH or CH_2O show a small decrease from their inlet values because of their consumption to initiate combustion reactions and then increases as they are produced by combustion (not shown here for conciseness). These are all conventional behaviours.

5.2 Features of the instantaneous reaction rate

The typical iso-surface of normalised heat release rate, $\dot{Q}^+ = \dot{Q}\delta_{th}/(\rho_r s_L c_p (T_p - T_r))$ is shown in Fig. 5.3 for $\dot{Q}^+ = 2.0$ for all cases. For case AZ1 in Fig. 5.3a, it can be observed that reactions occur over a very large portion of the computational domain with an extremely convoluted aspect. This increases the possibility for interactions of reaction zones and clearly differentiates MILD combustion from conventional combustion where a clear flame front with localised heat release rate is usually present. Furthermore, reactions occur near the entrance of the computational domain, shown by the presence of the iso-surfaces there (see Fig. 5.4a). This is due to the elevated temperature and the presence of radicals that initiate reactions as discussed in the previous chapter. The variation of this iso-surface in case AZ2, shown in Fig. 5.3b, is similar to that shown in Fig. 5.3. However, case BZ1 shows increased volumetrically distributed reaction with

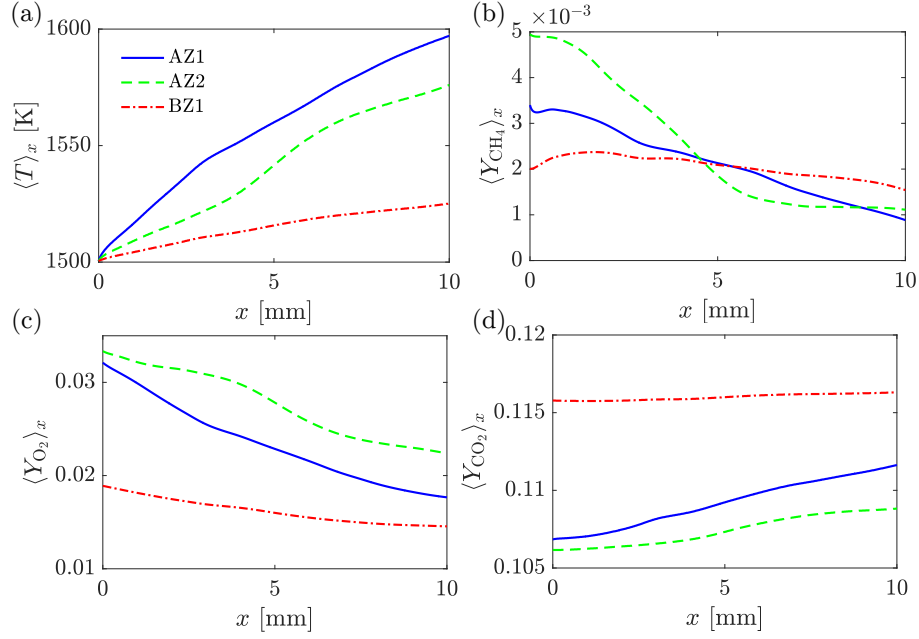


Fig. 5.2 Mean axial profiles of (a) temperature, (b) Y_{CH_4} , (c) Y_{O_2} and (d) Y_{CO_2} for all cases.

broader reaction zones, as seen in Fig. 5.3c. The variations of this iso-surface is similar when considering different time instants and are thus not shown here.

For a close analysis of these reaction zones, 2D slices in the mid x - y plane are shown in Fig. 5.4 for the three cases. One observes both thin and thick heat releasing zones in Figs. 5.4a and 5.4b. The thickening of the reaction zones originates from interactions of reaction zones yielding larger regions of chemical activity and heat release. These regions can then occupy large patches in the computational domain. The typical thickness of these reaction zones present a large variation as pictured in Figs. 5.4a and 5.4b.

Furthermore, for cases AZ1 and AZ2 with $X_{\text{O}_2}^{\text{max}}$ of about 3.5%, most reactions occur in the first half of the domain with less reactions occurring in the downstream regions while case BZ1 with $X_{\text{O}_2}^{\text{max}}$ of about 2% shows chemical activity throughout the domain. In addition, the degree of convolution of the reaction zones between cases AZ1 and AZ2 appears to be similar despite the different initial mixture fraction lengthscales (see Table 2.2). Comparing the cases AZ1 and BZ1, shown respectively in Fig. 5.4a and 5.4c, the case BZ1 has much thicker reaction zones nearly over the entire computational domain and no region could be identified as a thin reaction zone as seen for AZ1 and AZ2. This finding is in agreement with those observed in premixed MILD combustion investigations [Minamoto et al., 2014b] suggesting that a higher dilution level led to thicker reaction zones with more frequent interactions of reaction zones.

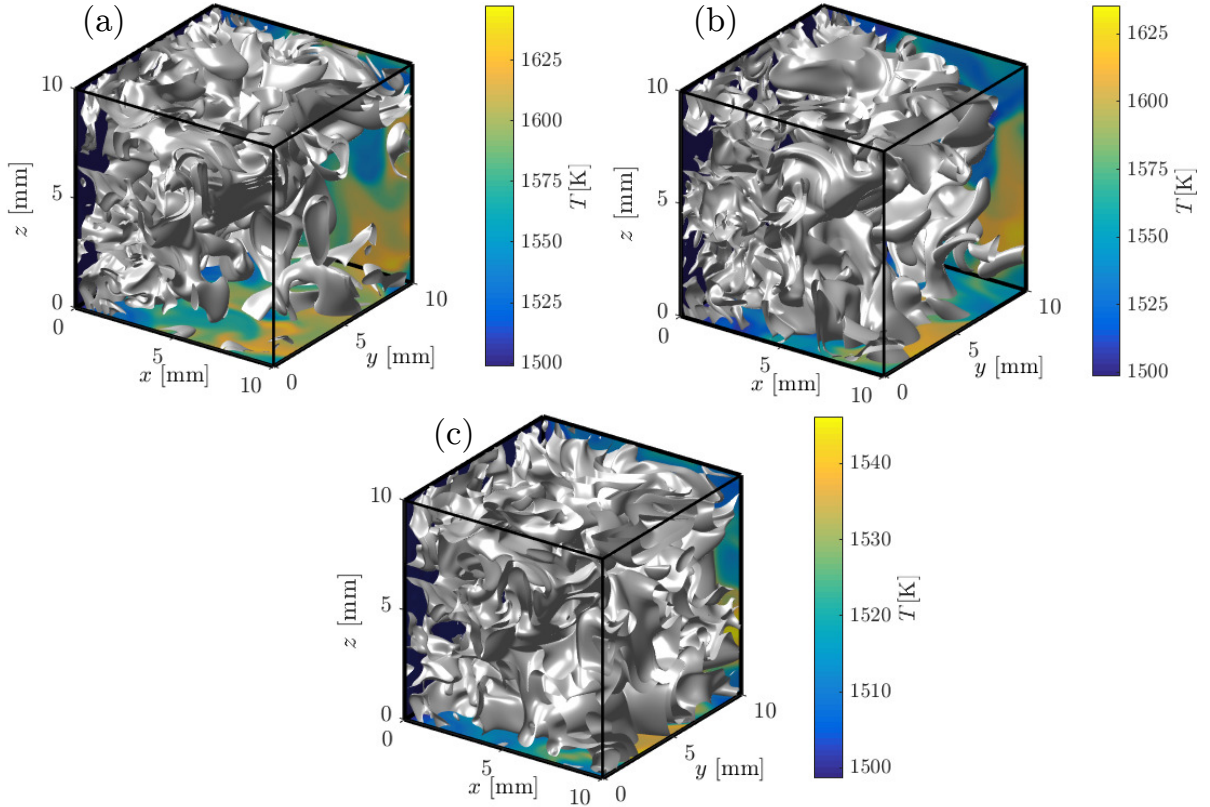


Fig. 5.3 Typical iso-surface of normalised heat release rate $\dot{Q}^+ = 2.0$, at $t = 1.5\tau_f$ for cases (a) AZ1, (b) AZ2 and (c) BZ1. The temperature field is shown on the bottom and side surfaces.

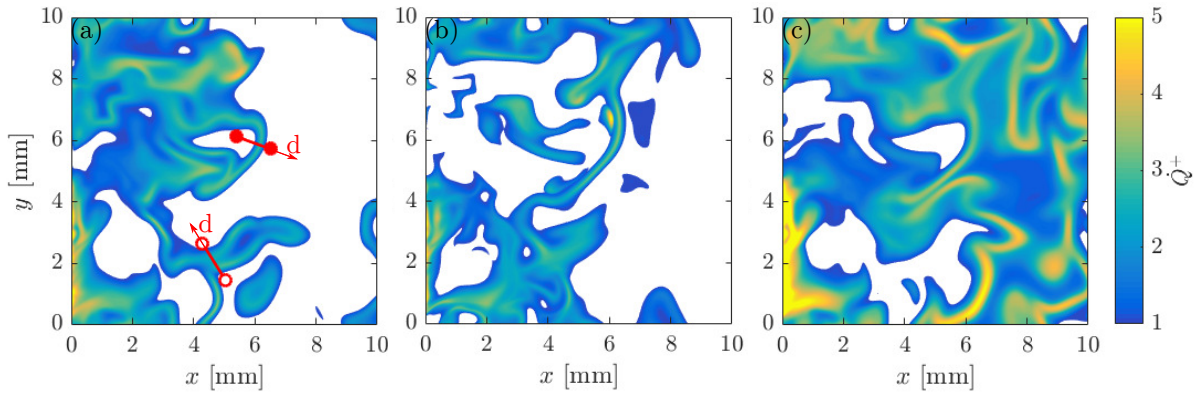


Fig. 5.4 Variation of \dot{Q}^+ in the mid x - y plane for cases (a) AZ1, (b) AZ2 and (c) BZ1 at $t = 1.5\tau_f$.

The evolution of species in these reaction zones is studied in Fig. 5.5 to investigate the physical space structure of these zones. The spatial evolutions of \dot{Q}^* , Y_{OH}^* , $Y_{O_2}^*$, Y_{OH}^* ,

$Y_{\text{CH}_4}^*$ and c_T at the locations marked in Fig. 5.4a are shown. The * superscript denotes quantities normalised by the maximum value in the plane. The distance d in Fig. 5.5 is along the local normal $n = -\nabla c_T / |\nabla c_T|$ and $d = 0$ corresponds to the point along n with peak heat release rate per unit volume. The variations of the above quantities with d are shown for a non-interacting reaction zone (marked using filled circles in Fig. 5.4a) and an interacting one (open circles) in Figs. 5.5b and 5.5d respectively. Figures 5.5a and 5.5c show these variations for the same locations at an earlier time, $t = 1.46\tau_f$. For the non-interacting zone (Figs. 5.5a and 5.5b), a clear localised heat release profile with a progressive increase of c_T is observed and this variation is typical of a flame. The variations of normalised methane and oxygen mass fractions shown in the figure suggest that this reaction zone is of premixed type. However, there is a substantial variation of mixture fraction across this reaction zone ($0.49 \leq \phi \leq 1.15$) and this variation is well within the flammability limits for the conditions analysed here. The propagation of this reaction zone is tracked through detailed interrogation of the time evolution of \dot{Q}^+ shown in Fig. 5.4. This analysis and the results in Fig. 5.5 show that there is a propagation of this flame in the downstream direction (compare Figs. 5.5a and 5.5b).

Figures 5.5c and 5.5d show the variation of the normalised quantities with d for the second location (open circles) in Fig. 5.4a, where reaction zones interact. Figure 5.5c is shown for $t = 1.46\tau_f$ depicting two distinct peaks for the heat release rate. The variations of other quantities shown clearly suggest the presence of two distinct flames, which start to interact as they are propagating towards each other. This interaction leads to a broader peak for the heat release rate as seen in Fig. 5.5d shown for $t = 1.5\tau_f$. This is confirmed further by the variation of OH along n showing a clear discrepancy with the variation of heat release as observed in earlier studies on interactions of laminar flames [Echekki et al., 1996]. Conversely, OH^* seems to adequately follow the variation of heat release. This suggests that OH may not be a suitable surrogate to identify reaction zones in non-premixed MILD combustion as also observed for premixed MILD combustion [Minamoto & Swaminathan, 2014b].

Thus the question arises as to which species can be used to identify reaction zones in MILD combustion which is the subject of the next section.

5.3 Markers of heat release rate

Generally, the use of PLIF signal of some species, like OH, CH_2O or HCO, is quite common to identify regions of heat release in conventional turbulent combustion. However, in the context of non-premixed MILD combustion, the adequacy of these species still needs to

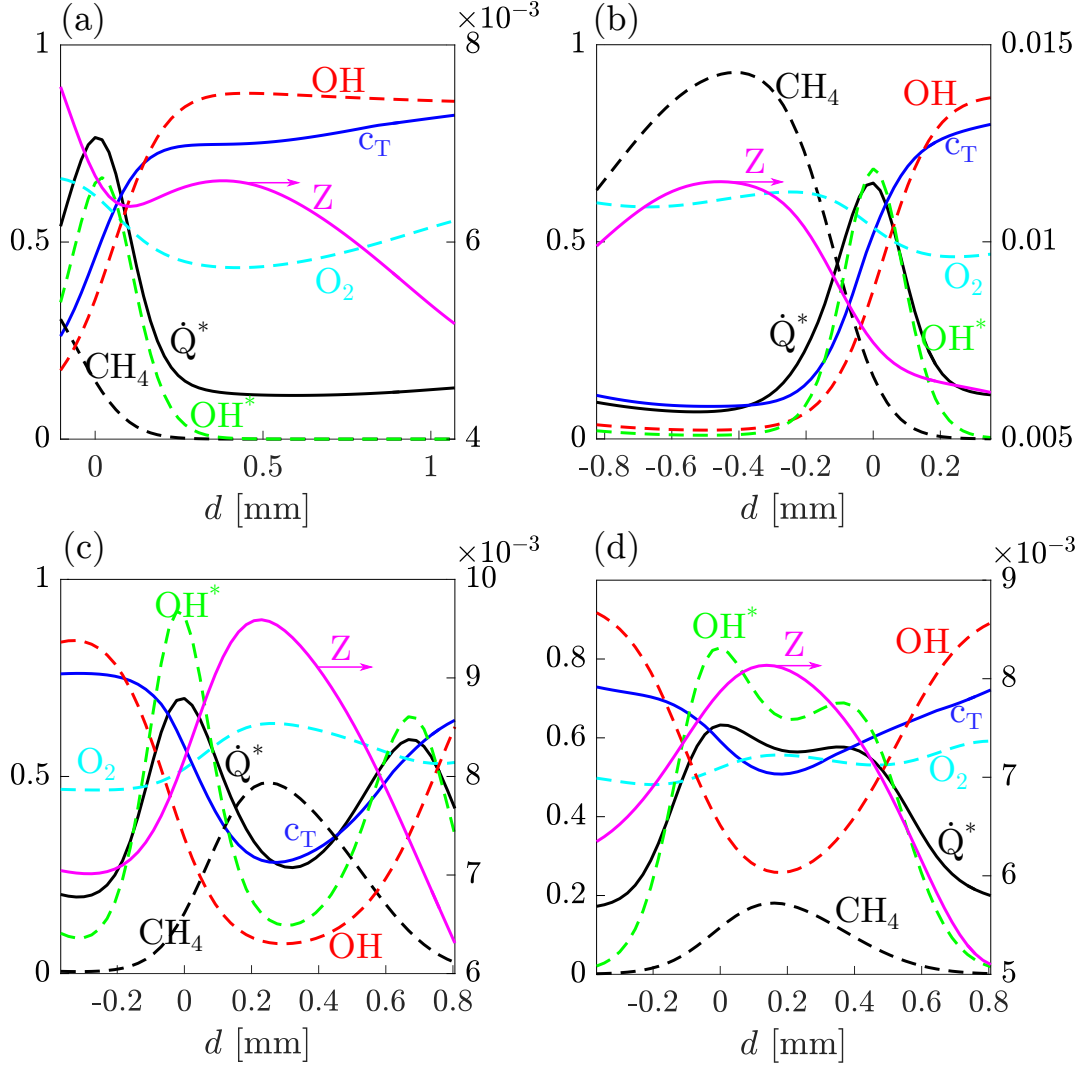


Fig. 5.5 Variation of \dot{Q}^* , $Y_{CH_4}^*$, $Y_{O_2}^*$, Y_{OH}^* , $Y_{OH^*}^*$ and c_T with normal distance d marked in Fig. 5.4a for locations marked using (a-b) filled and (c-d) open circles. The location corresponding to peak \dot{Q}^* is $d = 0$. (a) and (c) are for $t = 1.46\tau_f$ and (b) and (d) are for $t = 1.5\tau_f$.

be assessed as MILD combustion has a large dilution and a highly non-uniform mixture which may contain radicals. Thus, the aim here is to assess which species can be an appropriate marker of heat release rate for MILD combustion. From DNS data, it is indeed possible to reconstruct the LIF signals of conventional species used in PLIF, like

CH₂O, OH and HCO, using [Minamoto & Swaminathan, 2014b]:

$$S_{\text{CH}_2\text{O}} \propto [\text{CH}_2\text{O}]T^{1-\beta}, \quad 2.2 \leq \beta \leq 3.0 \quad (5.1)$$

$$S_{\text{OH}} \propto [\text{OH}]T^{1-\beta}, \quad -2.0 \leq \beta \leq 1.0 \quad (5.2)$$

$$S_{\text{HCO}} \propto [\text{HCO}]T^{1-\beta}, \quad 1.0 \leq \beta \leq 1.5 \quad (5.3)$$

where the brackets, $[\alpha]$, denote the molar concentration of the species α . The range of coefficients β in the previous expression have been reported in previous studies [Najm et al., 1998a,b; Paul & Najm, 1998]. For the present work, similarly to the values chosen by Minamoto & Swaminathan [2014b], they are taken as respectively 2.6, 0 and 1.25 for the LIF signals of CH₂O, OH and HCO. It should be noted that using a different values of β does not unduly change the result presented here.

Furthermore, it is quite conventional in experiments to consider the product of the OH and CH₂O PLIF signals together. Thus, typical reconstructed PLIF signals in the mid x - y plane are shown for case AZ1 at $t = 1.5\tau_f$ in Fig. 5.6 for respectively the original DNS signal of heat release rate, S_{OH}^* , $S_{\text{OH}}^* \times S_{\text{CH}_2\text{O}}^*$ and S_{HCO}^* . Here, the $*$ denotes a normalisation by the global maximum. It is readily observed that both S_{HCO}^* and $S_{\text{OH}}^* \times S_{\text{CH}_2\text{O}}^*$ provide a reasonable agreement with the original signal as they reproduce most features of the reaction zones from DNS. However, it is clear that S_{OH}^* does not capture these appropriately. Specifically, there is still a large amount of OH downstream where no reaction is taking place anymore while in the upstream OH is nearly not present while reactions are taking place. This could be explained by the fact that as shown in chapter 4, OH is consumed in the early stage of the domain for the inception of MILD combustion while in the latter stage OH is present in the products of combustion.

This can be better analysed by plotting the scatter plot of heat release rate and PLIF signals. The sample for this scatter are obtained from the mid x - y plane shown in Fig. 5.6. The scatter is coloured with the axial locations and is presented in Fig. 5.7 for case AZ1. As noted earlier, S_{OH}^* does not show a good correlation to identify reaction zones as seen in Fig. 5.7b, contrarily to S_{HCO}^* and $S_{\text{OH}}^* \times S_{\text{CH}_2\text{O}}^*$, respectively shown in Fig. 5.7c and d. Indeed, S_{OH}^* is present in regions where there is nearly no heat release while the two other markers show a good correlation. In particular, it is observed that S_{OH}^* overestimates the heat release rate close to the inlet and downstream close to the outlet. The first is due to the inflowing OH while the latter is due to the OH present in the combustion products. In the other parts of the domain, S_{OH}^* underestimates the heat release rate as it is consumed for the inception of MILD combustion and is thus not well correlated with the peak heat release rate. In Fig. 5.7a, an additional comparison with

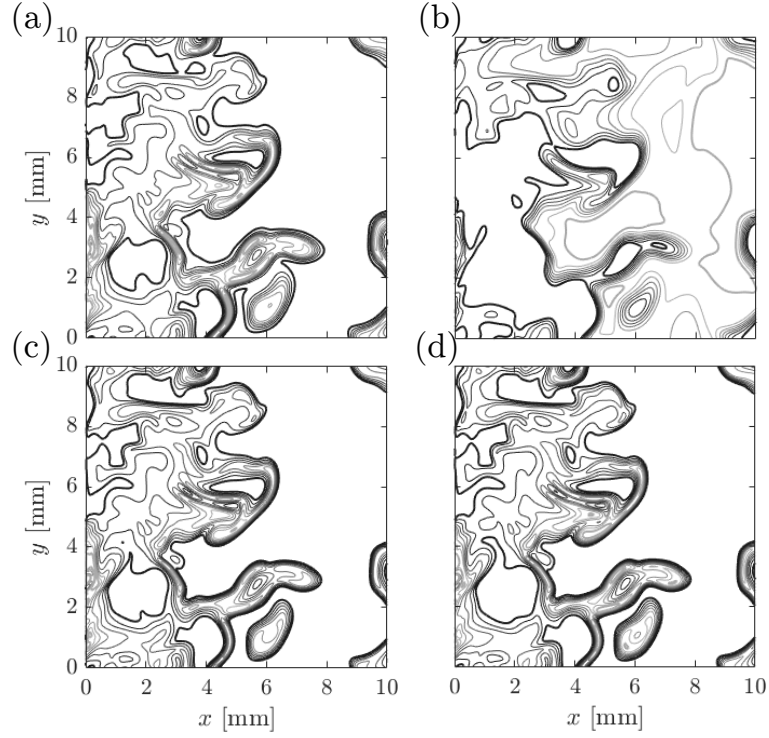


Fig. 5.6 Contours of (a) \dot{Q}^* , (b) S_{OH}^* , (c) S_{HCO}^* and (d) $S_{OH}^* \times S_{CH_2O}^*$ in the mid x - y plane for case AZ1 (dark to light gray lines are for isocontours at 0.1, 0.2, ..., 0.9).

OH^* is made. OH^* is not a species which can be used for PLIF signal but nonetheless, this comparison allows one to see that OH^* presents a much better correlation with heat release rate than OH . This further supports the discussion made in the previous section, in Fig. 5.5, that OH is not an appropriate marker for MILD combustion as it is present in many regions which are not reacting. Similar observations can be made for the cases AZ2 and BZ1 shown respectively in Figs. 5.8 and 5.9. To further quantify the adequacy of these markers, their corresponding correlation coefficients are summarized in Table 5.1 which again highlights that OH^* , HCO and $OH \times CH_2O$ are appropriate markers.

The observation made here using OH^* for heat release rate is inline with common expectations and observations in earlier studies [Panoutsos et al., 2009; Zhou et al., 2015], but it is in contrast to those reported in the study of Sidey & Mastorakos [2015a].

Finally, it should be noted that the LIF signals of other species such as CO [Barlow et al., 2015], H [Nikolaou & Swaminathan, 2014] or CH [Tanahashi et al., 2005] can also be measured experimentally. However, it is not the objective of this present study to make an exhaustive assessment of these markers and the present section already highlights the difficulty of using conventional single species markers for the identification

5.4 Structure of reaction zones in mixture fraction space

of reaction zones in MILD combustion and this thus suggest that particular care must be taken when identifying the reaction zones in MILD combustion.

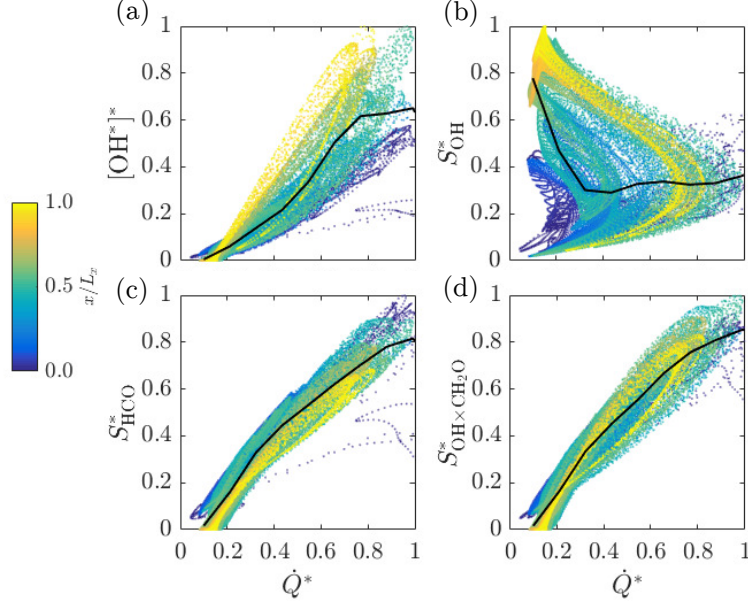


Fig. 5.7 Variations of (a) $[\text{OH}^*]^*$, (b) S_{OH}^* , (c) S_{HCO}^* and (d) $S_{\text{OH}}^* \times S_{\text{CH}_2\text{O}}^*$ with \dot{Q}^* for case AZ1 in the mid x - y plane. Points are coloured by their streamwise locations. Black lines are the conditional averages.

Table 5.1 Pearson linear correlation coefficients for the \dot{Q}^* - S_α^* scatter.

Case	$[\text{OH}^*]^*$	S_{OH}^*	S_{HCO}^*	$S_{\text{OH}}^* \times S_{\text{CH}_2\text{O}}^*$
AZ1	0.9153	-0.4835	0.9447	0.9543
AZ2	0.9431	0.0134	0.9511	0.9557
BZ1	0.9458	0.2023	0.9529	0.9555

5.4 Structure of reaction zones in mixture fraction space

One of the main objectives of this study is to analyse the effects of spatial and temporal variations of the mixture fraction on MILD combustion. The variations of typical quantities such as temperature, heat release rate, major and minor species with mixture fraction are shown in Figs. 5.10 to 5.14 for case AZ1. The results are shown for two streamwise (x) locations and two instances which are marked in the respective figures.

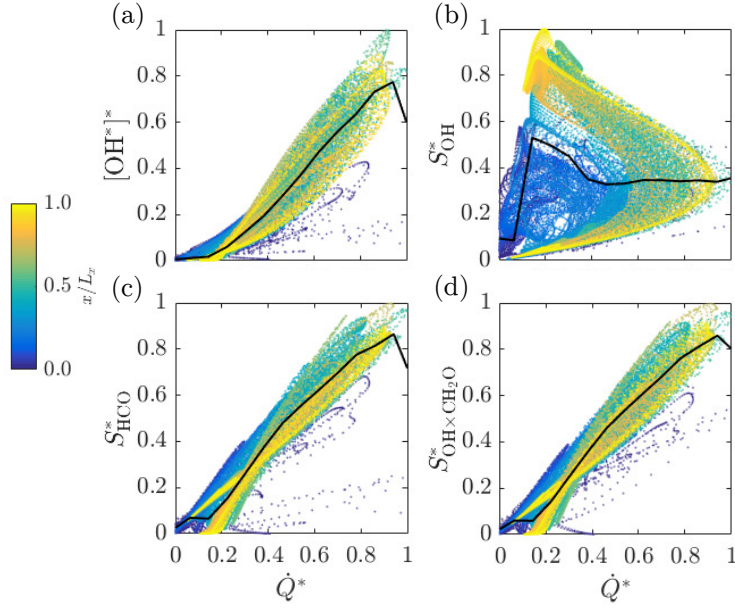


Fig. 5.8 Variations of (a) $[\text{OH}^*]^*$, (b) S_{OH}^* , (c) S_{HCO}^* and (d) $S_{\text{OH}}^* \times S_{\text{CH}_2\text{O}}^*$ with \dot{Q}^* for case AZ2 in the mid x - y plane. Points are coloured by their streamwise locations. Black lines are the conditional averages.

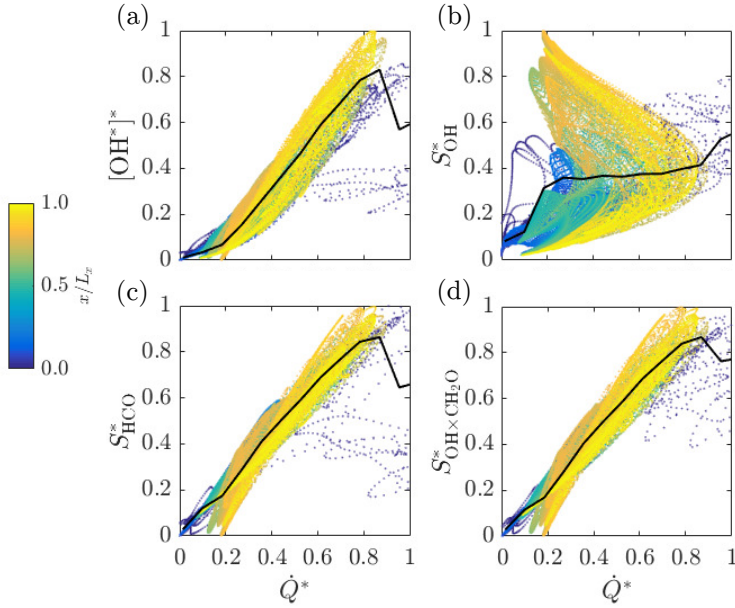


Fig. 5.9 Variations of (a) $[\text{OH}^*]^*$, (b) S_{OH}^* , (c) S_{HCO}^* and (d) $S_{\text{OH}}^* \times S_{\text{CH}_2\text{O}}^*$ with \dot{Q}^* for case BZ1 in the mid x - y plane. Points are coloured by their streamwise locations. Black lines are the conditional averages.

The conditional averages for the quantities are shown using lines with symbols with an error bar of width representing their 2 standard deviation σ from the conditional mean

5.4 Structure of reaction zones in mixture fraction space

value. The dash-dotted lines represent the variation in a laminar counterflow flame with a very low (50s^{-1}) strain rate computed using CANTERA. This laminar flame has pure fuel as one stream and the vitiated air (see Table 2.1) used for case AZ1 as the other stream. This strain rate has been chosen to ensure a fully reacting solution. The choice of this value is, however, not critical for MILD combustion as there are no extinction events because of the reactant stream at high temperature which contains intermediates and radicals.

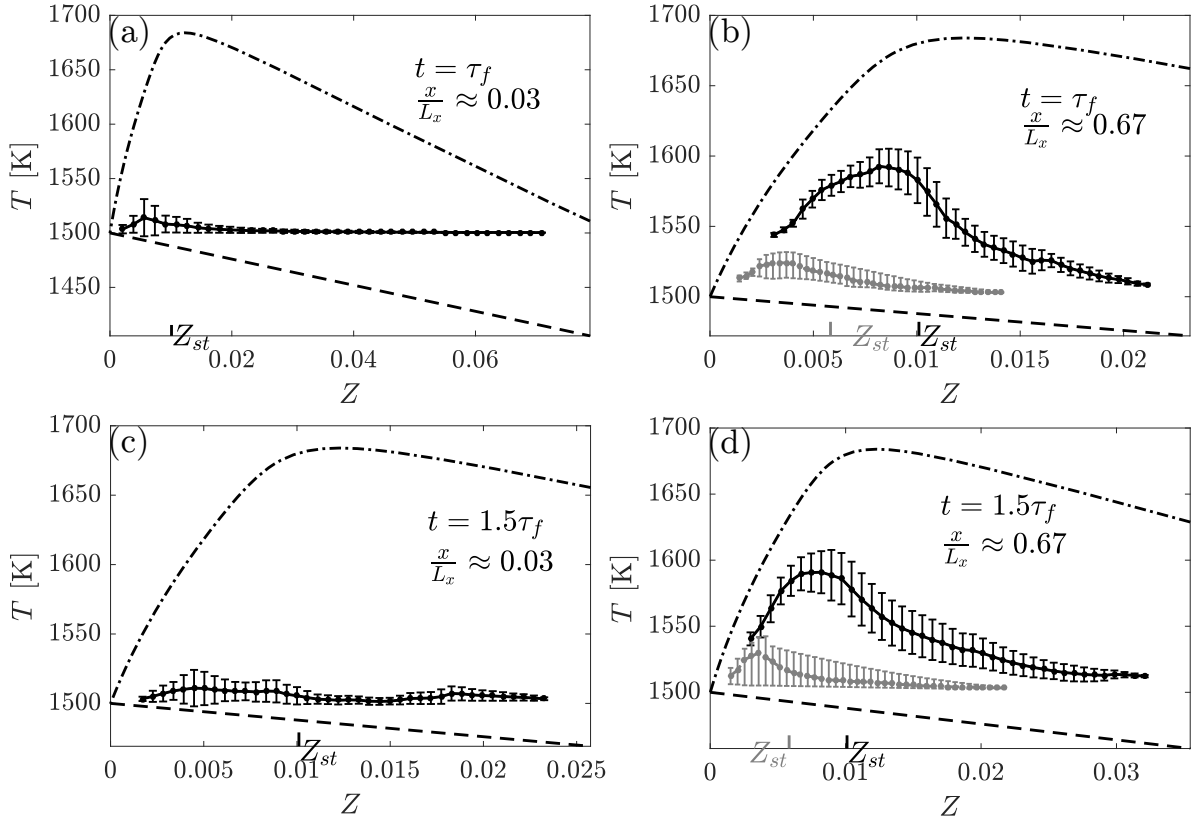


Fig. 5.10 Variations of conditionally averaged temperature, T , with Z for case AZ1 (black) and BZ1 (gray). Counterflow flame results are shown using dash-dotted. Mixing line is shown as dashed line. The results are shown for two instances at two streamwise locations as marked above.

The mixing line for the oxidiser at 1500K and the fuel at 300K is also shown as dashed line in Fig. 5.10 which shows the variation of T with Z . The time variation of the incoming mixture fraction is observed by comparing Figs. 5.10a and 5.10c. The maximum Z seen at $t = 1.5\tau_f$ is nearly 30% of the value at $t = \tau_f$. For the location close to the inlet, most mixture is at about 1500 K represented by the conditionally averaged temperature irrespective of the time of analysis, see Figs. 5.10a and 5.10c.

However, there is a relatively larger scatter for the lean mixture because of its lower ignition delay compared to rich ones [Göktolga et al., 2015] allowing some of these lean mixtures to have already reacted. As one moves downstream (Figs. 5.10b and 5.10d), the conditionally averaged temperature increases for all mixtures due to heat release. The peak temperature in the turbulent case is observed to occur for lean mixture and not for a slightly rich mixture as in the counterflow flame. This is due to interactions (mixing) between the various mixture fractions present in the flow. The stoichiometric and slightly rich mixtures which are hotter diffuse heat towards the leaner (slightly cooler) mixture. As a result, the conditional averaged temperature of these hotter mixtures decreases while the one of the leaner mixtures increases. This yields a peak in temperature located around the average mixture fraction inflowing in the domain (of $Z \approx 0.008$ for case AZ1). Furthermore, there are ignition fronts as one shall see shortly.

The peak of conditional and also unconditional temperature in the turbulent case is smaller than the temperature observed for the counterflow flame because the inflowing mixture at 1500 K in the DNS contains pockets of burnt and unburnt mixtures with the same equivalence ratio (see Fig. 2.4) which is not the case for the steady counterflow flame shown in Fig. 5.10. The spatial variation of the conditional temperature at $t = \tau_f$ can be understood by comparing Figs 5.10a and 5.10b. The time evolution at a given location can be observed by comparing the results shown in the top and bottom rows of Fig. 5.10. The spatio-temporal variation of the mixture fraction can also be observed in these figures. The range of Z decreased nearly by half from about 0.06 to 0.03 when comparing Figs. 5.10a to 5.10d. This change is because of turbulent mixing of the inhomogeneous incoming Z field and when this mixing is complete the mixture fraction will be equal to the mean value of 0.008 for the case AZ1 (see Table 2.2).

Figure 5.10d can be interpreted as the state of the mixture used for Fig. 5.10a after it has reacted and been convected downstream by the mean flow velocity of approximately U_{in} . The x/L_x values given in the figure suggests that $\Delta x/U_{in} = 0.64\tau_f$ which is approximately equal to the time difference between Figs. 5.10a and 5.10d. Figures 5.10b and 5.10d also show the evolution of conditionally averaged T for case BZ1. Similar observations can also be made for this case.

The temperature evolution shown in Fig. 5.10 clearly suggests that there are ignition fronts moving in space and time. This front evolution in space can be seen clearly in Fig. 5.11 showing the evolution of conditional temperature in the mixture fraction space for five streamwise locations. One can clearly see the propagation of ignition front in space. If one plots this variation at a given location for various instances then one

5.4 Structure of reaction zones in mixture fraction space

observes a similar behaviour (see Figs. 5.10b and 5.10d for example). The mixtures ignited at an earlier location and time yield propagating flames subsequently.

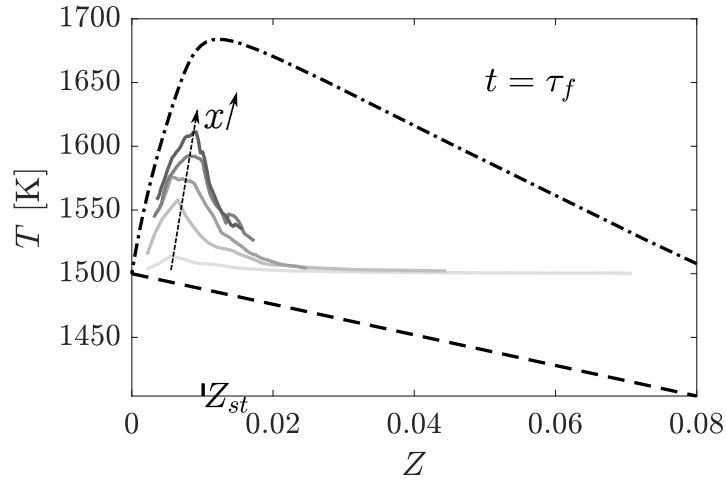


Fig. 5.11 Variations of conditionally averaged temperature, T , with Z in case AZ1 for five streamwise locations $x/L_x \approx 0.03, 0.27, 0.50, 0.73$ and 0.97 . Counterflow flame result is shown using dash-dotted line. Mixing line is shown in dashed line.

Figure 5.12 shows the variations of \dot{Q} with Z . It is observed that the maximum heat release rate occurs for a slightly lean mixture for both the counterflow flame and turbulent case, and not for a slightly rich mixture as observed for a conventional flame. This behaviour is seen for all locations and times in the turbulent case. Furthermore, the conditional average of \dot{Q} in the turbulent case is higher than the laminar counterflow flame. This is because the turbulent case contains mixture of different thermo-chemical state for a given mixture fraction value, leading to a large fluctuation in \dot{Q} as shown by the vertical bars (representing the conditional rms values). It is also to be noted that the incoming mixture contains intermediates and radicals, which is not so for the counterflow case.

Further insights into these structures can be gathered by studying the mixture fraction space variations of major and minor species. This variation for major species, CH_4 and O_2 , is shown in Fig. 5.13. The mass fraction of CH_4 follows closely the laminar case for the lean mixture, i.e., $Z < Z_{st} = 0.01$ for the locations and instances shown in the figure. For other mixture fraction values, the mass fractions are substantially larger compared to the fully reacting laminar case. This behaviour is typical of ignition phenomena. For example, if one compares the temperature, \dot{Q} and these mass fraction values from Figs. 5.10a, 5.12a and 5.13a respectively for $Z = 0.03$ then one can see that this mixture has not ignited yet. The results in these figures show that this specific mixture has not

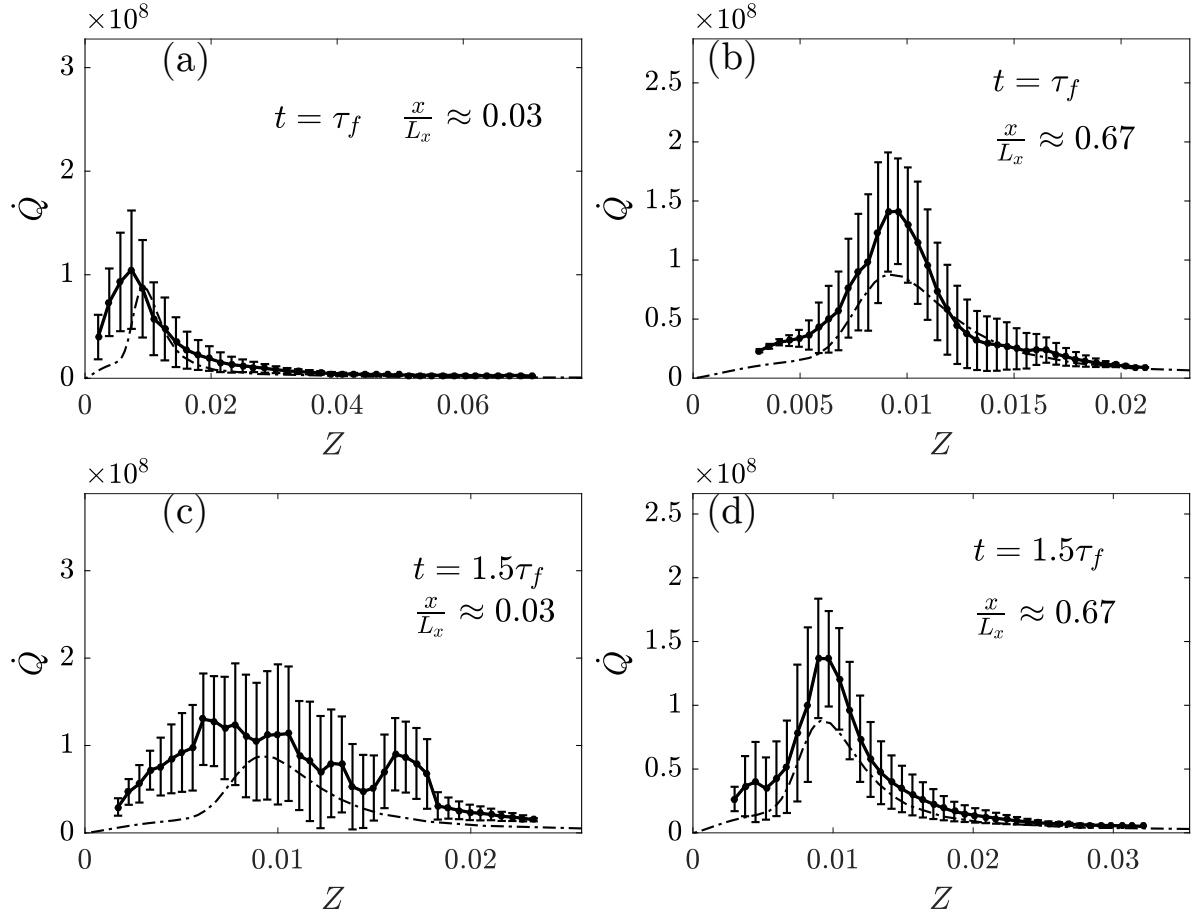


Fig. 5.12 Variations of conditionally averaged \dot{Q} [W/m^3] with Z for case AZ1. Counterflow flame result is shown using dash-dotted line.

reacted even at $x/L_x \approx 0.67$. This is because this mixture at this specific location has emerged from a richer mixture through turbulent mixing which would drive the mean Z value towards $\langle Z \rangle = 0.008$. This physics is reflected by the abrupt ending of the various curves in Fig. 5.11 at some intermediate values of Z .

The variations of minor species for the same locations and times are shown in Fig. 5.14. It is clear that these species variations do not follow those in counterflow configuration. For $x/L_x \approx 0.03$, which is close to the inlet, the reactions are just beginning to occur through ignition by consuming the incoming OH (see Fig. 2.4) and thus OH levels are substantially lower compared to the laminar case. The formaldehyde level is higher because it is also present in the incoming mixture. This gives substantially larger level even for unreacted mixture fraction value of $Z \geq 0.004$. As the ignition front moves through the mixture fraction space, OH and CH_2O mass fractions move towards counterflow flame values. The substantially larger values seen for $Z \geq 0.01$ is because the

5.4 Structure of reaction zones in mixture fraction space

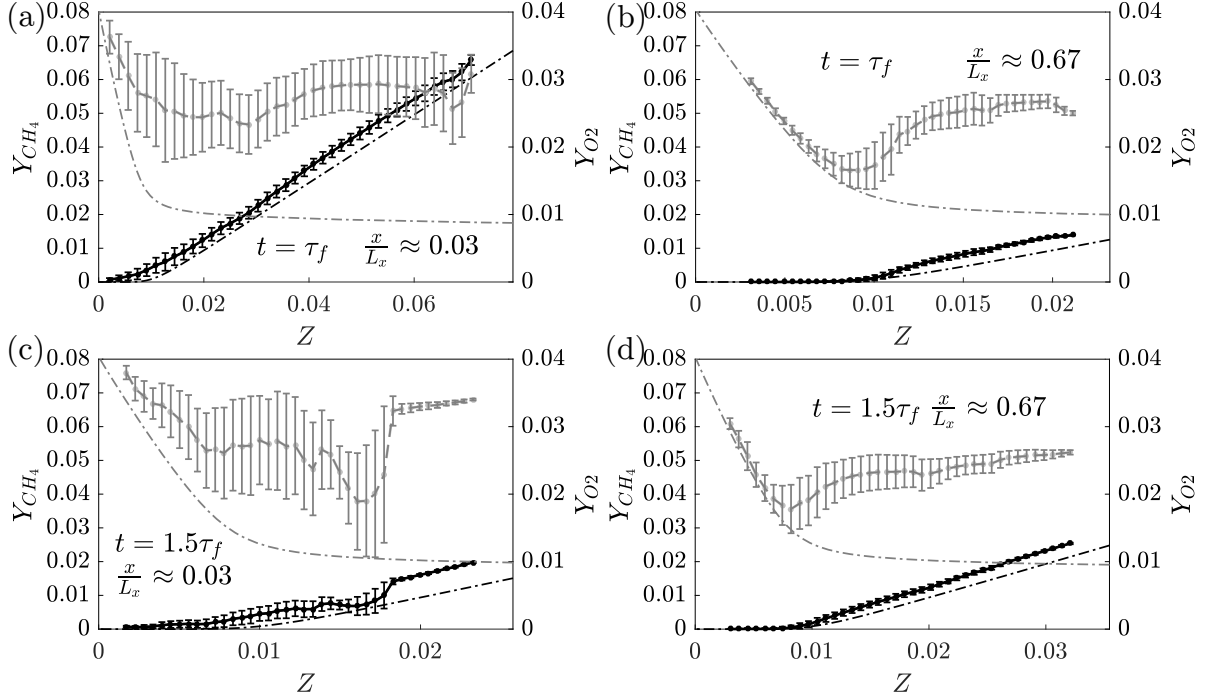


Fig. 5.13 Variations of conditionally averaged Y_{CH_4} (black) and Y_{O_2} (gray) with Z for case AZ1. Counterflow flame results are shown using dash-dotted lines.

ignition front has not moved to these mixtures yet. Thus, these variations are consistent with ignition front behaviour seen in earlier figures. For cases AZ2 and BZ1, the mixture fraction space variations of species and their spatio-temporal evolution are observed to be similar to those shown here for AZ1. For example see the variations of conditionally averaged temperature with Z shown in Fig. 5.10 for the case BZ1.

However, it is worth to note that the effects of ℓ_c/ℓ_Z and the dilution will be felt in the physical space but not in the mixture fraction space. The physical space structure shown in Figs. 5.4 and 5.5, and the mixture fraction space evolution shown in Figs. 5.10 to 5.14 suggest that non-premixed MILD combustion involves ignition fronts, propagating premixed and non-premixed reaction zones. The latter two aspects are analysed further in the next section. The presence of ignition fronts and propagating premixed flames was also observed for premixed MILD combustion [Minamoto et al., 2014a]. Their relative roles, contributions, and mutual influences are subject matters for chapter 6.

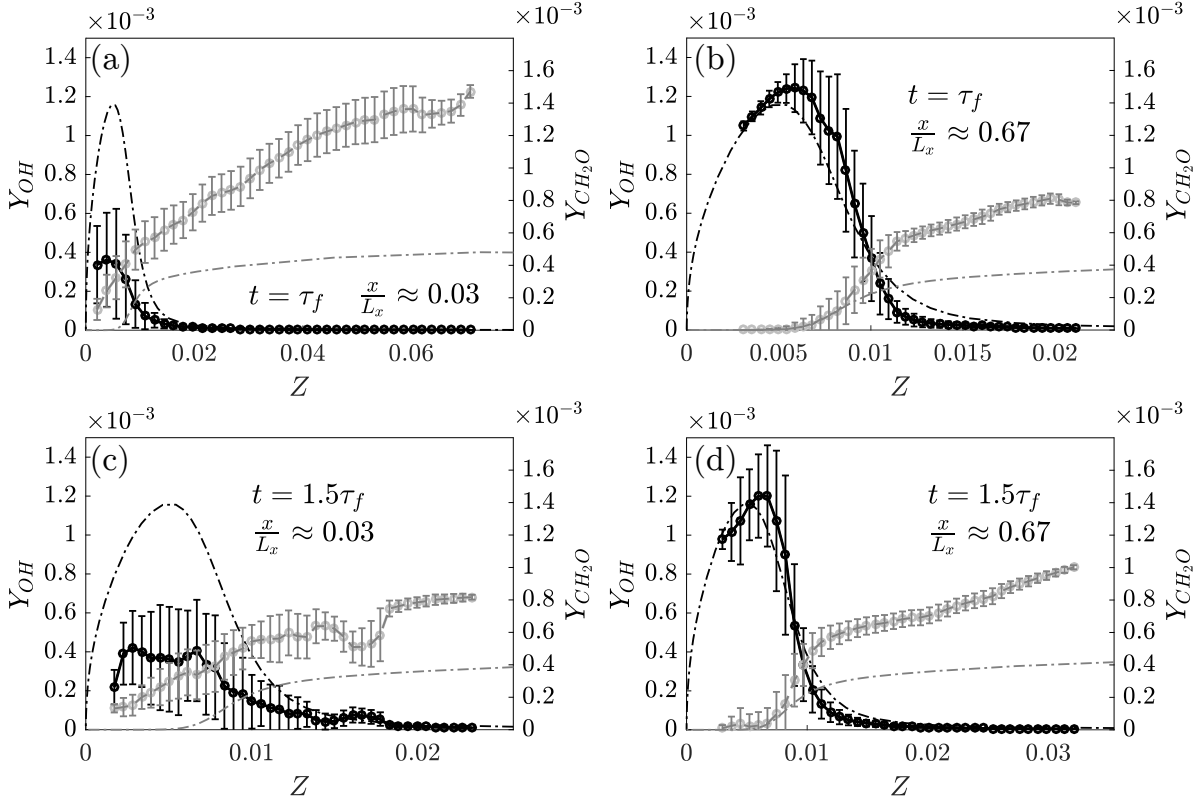


Fig. 5.14 Variations of conditionally averaged Y_{OH} (black) and Y_{CH_2O} (gray) with Z for case AZ1. Counterflow flame results are shown using dash-dotted lines.

5.5 Premixed and non-premixed behaviours of reaction zones

Since the mixture temperature is higher than the ignition temperature for methane, autoignition events occur which can subsequently lead to either premixed or non-premixed combustion depending on the local mixture condition. The premixed characteristics arise because both oxidizer and fuel are present in the incoming partially premixed mixture. The spatio-temporal variation of mixture fraction yields non-premixed combustion features. This dual behaviour can be investigated using the flame index introduced by Yamashita et al. [1996] which was modified by Briones et al. [2006]. The modified flame index, FI, is given by:

$$FI = \frac{Z - Z_{st}}{2|Z - Z_{st}|} \left(1 + \frac{\nabla Y_{CH_4} \cdot \nabla Y_{O_2}}{|\nabla Y_{CH_4}| |\nabla Y_{O_2}|} \right). \quad (5.4)$$

This FI provides information about the gradient (molecular mixing) direction and thus the combustion mode when computed in heat releasing regions. It takes a value close to

5.5 Premixed and non-premixed behaviours of reaction zones

0 for non-premixed combustion, a value close to -1 for lean and $+1$ for rich premixed combustion. The spatial variation of FI in regions with substantial heat release rate per unit volume ($\dot{Q}^+ \geq 1$) is shown in Fig. 5.15 for all three cases. This result is shown in the mid x - y plane of the computational domain.

This figure shows islands of non-premixed combustion surrounded by regions of premixed combustion (few regions showing these characteristics are marked in the insets of Fig. 5.15). The regions of non-premixed combustion originate from the flux of fuel coming from a neighbouring richer mixture and the flux of oxygen coming from an adjacent leaner mixture. As a result of this, the gradients of fuel and oxygen mass fractions have opposite directions giving $FI = 0$ (see Eq. (5.4)). This situation is illustrated in the insets of Figs. 5.15a to 5.15c where there is a richer mixture on one side and a leaner mixture on the other side. For the inset of Fig. 5.15a, despite a clear localised peak of heat release rate, similar to those found in premixed flame, a further analysis to be presented later in Fig. 5.17 shows that this heat release still comes from non-premixed mode of combustion. The inset in Fig. 5.15b shows a non-premixed island which has just started to react as indicated by the relatively low \dot{Q}^* and low c_T (the superscript $*$ implies that the value is normalised using the respective maximum value seen in the corresponding x - y plane shown). As it has just begin to ignite, the levels of OH and OH * are low.

Furthermore, by comparing the case AZ1 to AZ2, it is observed that the proportion of non-premixed combustion is higher in the case AZ2. This is linked to the relatively larger value of ℓ_c/ℓ_Z for the case AZ2 compared to the case AZ1 (see Table 2.2). This creates steeper gradients of mixture fraction in case AZ2 leading to stronger and more frequent fluxes of CH $_4$ and O $_2$ coming from opposite directions. The flux of CH $_4$ comes from richer and that of O $_2$ from leaner mixtures.

The results depicted in Fig. 5.15 show the complex nature of MILD combustion and the coexistence of premixed and non-premixed modes. It is to be noted that FI does not help to identify autoignition. The preponderance of these modes and their relative contribution can be investigated by studying the pdf of FI, $p(\psi)$. This pdf constructed using 40 bins is shown in Fig. 5.16 for the three cases. The result is shown for $t = 1.5\tau_f$ and it is similar for other times. Note that the y -axis is shown in logarithmic scale to clearly see the pdf variation for intermediate values of FI. Let us remind ourselves here that $FI = -1$ corresponds to lean premixed while $+1$ corresponds to rich premixed and 0 implies non-premixed combustion modes. It is quite clear that the lean premixed mode is dominant in all three cases. The rich premixed mode is the next dominant mode in the case AZ1, which is reduced in the cases AZ2 and BZ1. This drop in the case BZ1 is because of high dilution level. The stronger mixture fraction gradient, resulting from

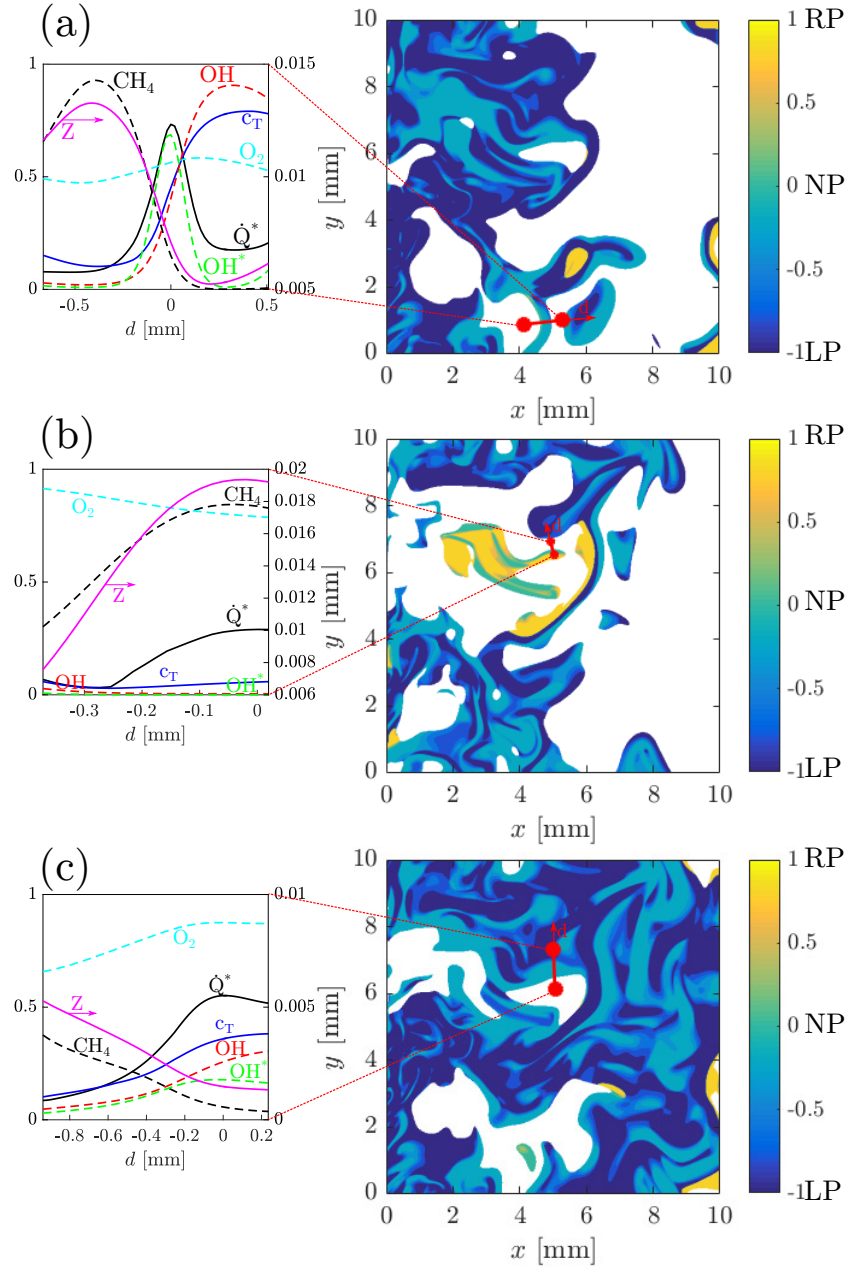
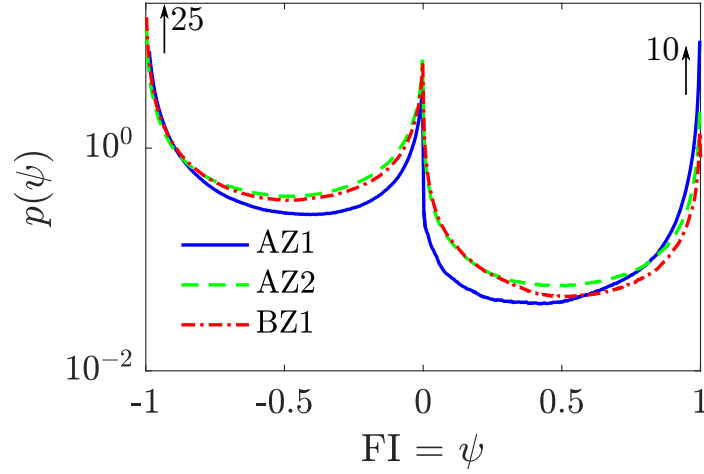


Fig. 5.15 Flame Index shown in regions with $\dot{Q}^+ \geq 1.0$ for cases (a) AZ1, (b) AZ2, (c) BZ1 at $t = 1.5\tau_f$. The results are shown in the mid x - y plane.

smaller ℓ_Z , in AZ2 compared to AZ1 decreases the rich premixed mode. However, the non-premixed mode increases in AZ2 and BZ1 compared to AZ1. Even the mixed mode, having $0.1 \leq |\text{FI}| \leq 0.8$, increases in these two cases. These changes can be quantified by calculating the fraction of the computational volume with these combustion modes.


 Fig. 5.16 Pdf of the flame index for all cases at $t = 1.5\tau_f$.

These fractions can be obtained by simply using:

$$\mathcal{V}_{NP} = \int_{-\xi_1}^{\xi_1} p(\psi) d\psi \quad \mathcal{V}_{LP} = \int_{-1}^{-\xi_2} p(\psi) d\psi \quad \mathcal{V}_{RP} = \int_{\xi_2}^1 p(\psi) d\psi \quad (5.5)$$

for non-premixed, lean premixed and rich premixed combustion modes respectively while the fraction of the mixed mode is computed using $\mathcal{V}_{MM} = 1 - (\mathcal{V}_{NP} + \mathcal{V}_{LP} + \mathcal{V}_{RP})$. The fractions obtained thus are summarised in Table 5.2. The symbol ψ is the sampling space variable for FI and, $\xi_1 = 0.1$ and $\xi_2 = 0.8$. These limits are chosen carefully after extensive testing on the sensitivity of the respective integrals to these parameters. It is clear from those values that premixed combustion is predominant with the lean condition being the main contributor in the present configuration. This is to be expected since all cases have lean mixture with $\phi = 0.8$ on average. Furthermore, in the configuration considered here, fuel and oxidiser are introduced as a partially premixed mixture which naturally yields a dominant premixed combustion mode. However, the volume fraction having non-premixed combustion is non-negligible, which increases substantially for the most diluted case BZ1. As noted earlier, the increased mixture fraction gradient resulting from larger ℓ_c/ℓ_Z in case AZ2 yields larger \mathcal{V}_{NP} . Nearly 70 to 80% of the domain experiences these classical modes of combustion and the remaining 20 to 30% has mixed mode combustion, i.e., with $0.1 \leq |\text{FI}| \leq 0.8$.

The pdf of FI constructed using planar data for various streamwise (x) locations has also been studied for all cases. These pdfs are similar to that shown in Fig. 5.16 and it is observed that the three combustion modes exist at all locations but with varying level of their relative importance. In the early stage of the domain, the lean premixed

Reaction Zones Structure and Combustion Modes in MILD Combustion

mode is dominant with nearly non-existent rich premixed and non-premixed modes. This originates from the early ignition of lean mixtures. Further downstream, non-premixed mode starts to appear with the flux of O_2 coming from the excess oxygen in the burnt lean mixtures and CH_4 coming from unreacted or partially reacted rich mixtures. Rich premixed mode also appears only in the downstream regions as the ignition delay time for rich mixtures is larger than for lean ones.

Table 5.2 Volume fractions of regions having non-premixed, rich premixed, lean premixed and mixed-mode combustion at $t = 1.5\tau_f$. Their fractional contributions to the total heat release rate in the domain are also listed.

Case	\mathcal{V}_{NP}	\mathcal{V}_{RP}	\mathcal{V}_{LP}	\mathcal{V}_{MM}	\mathcal{Q}_{NP}	\mathcal{Q}_{RP}	\mathcal{Q}_{LP}	\mathcal{Q}_{MM}
AZ1	0.13	0.13	0.52	0.22	0.114	0.134	0.504	0.248
AZ2	0.28	0.07	0.37	0.28	0.230	0.027	0.499	0.244
BZ1	0.26	0.05	0.44	0.25	0.206	0.026	0.533	0.235

Following the analysis of non-premixed combustion by [Bilger \[1979\]](#), the heat release rate per unit volume in non-premixed mode can be written as:

$$\dot{Q}_{NP} \approx \rho D_Z (\nabla Z \cdot \nabla Z) \frac{\partial^2 h^s}{\partial Z^2} = \rho N_Z \frac{\partial^2 h^s}{\partial Z^2} \quad (5.6)$$

where h^s is the sensible enthalpy of the mixture, through the use of mixture fraction theory. Similar non-premixed contribution was shown to exist by [Bray et al. \[2005\]](#) using Z and c to investigate partially premixed combustion. This contribution can be estimated directly using the DNS data. Denoting the total heat release rate per unit volume at a given point as $\dot{Q}_{tot} = \sum_i \dot{\omega}_i \Delta h_{f,i}^0$, where $\Delta h_{f,i}^0$ is the enthalpy of formation of species i , one expects that $\dot{Q}_{NP}/\dot{Q}_{tot}$ should be close to unity in regions with $FI \approx 0$. This is simply another way to verify that the combustion in those regions is through non-premixed mode or not. The spatial variation of this ratio in the mid x - y plane for the case AZ1 is shown in Fig. 5.17. The colour map shows this ratio and the contour lines of $|FI| = 0.1$ are used to mark regions with $|FI| < 0.1$. This inequality is used to include the contributions coming from the slightly longer negative tail in the pdf of FI shown in Fig. 5.16. A good agreement between the regions having $FI \approx 0$ and $\dot{Q}_{NP}/\dot{Q}_{tot} \approx 1$ is observed confirming the non-premixed nature of combustion in these regions (see Fig. 5.15 for FI).

The fractional contribution, \mathcal{Q} , of these various modes of combustion to the total heat release rate for the entire domain is given in Table 5.2. These fractions are obtained by computing the ratio of the heat release rate per unit volume, \dot{Q}_{tot} , integrated over these regions to the heat release rate integrated over the entire computational domain. It

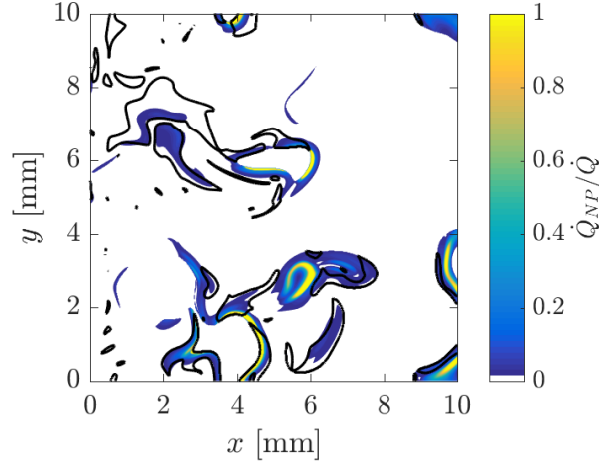


Fig. 5.17 Ratio $\dot{Q}_{NP}/\dot{Q}_{tot}$ presented in regions where $\dot{Q}^+ \geq 1$ with isoline of $|FI| = 0.1$ at $t = 1.5\tau_f$. The regions bounded by these contours has $|FI| < 0.1$.

is observed that nearly 50% comes from lean premixed combustion and the contribution from rich premixed mode drops below 3% as dilution or ℓ_c/ℓ_Z is increased. However, the non-premixed contribution still amounts to a non-negligible portion of the total heat release rate. The contribution from mixed mode is about 25%.

5.6 Summary

A close scrutiny of the DNS results in the present chapter offered the following insights. The chemical reactions of MILD mixtures occur over a wider region of the computational domain unlike the conventional combustion typically showing chemical reactions confined to narrower regions. As noted in earlier studies [Minamoto et al., 2013, 2014a,b], the MILD reaction zones are observed to have their salient features, such as strongly convoluted zones with frequent interactions while retaining conventional flame characteristics. It was further observed that OH, a conventional marker of reaction zones, did not correlate well with regions of heat release in MILD combustion. This was explained by the fact that they are consumed during the inception. Hence, there is nearly no OH in the initial reacting regions. OH was also found to be present in non-reacting regions like in the downstream as product of combustion. By contrast, its equivalent chemiluminescent species, OH^* , was well correlated with the reaction zones as it is a species which is only

present in heat releasing regions. HCO and the product of $\text{OH} \times \text{CH}_2\text{O}$ were also found to be good markers for MILD combustion.

Furthermore, the mixture fraction variation were also observed to introduce further complexities in the structure of reaction zones. Spatial and temporal ignition fronts are observed, leaner mixtures with shorter ignition delay times are observed to ignite first and these kernels evolved into propagating premixed flames. These flames remained as lean or become rich premixed flames depending on the mixture fraction value along their propagation paths produced by turbulent mixing of Z field. The rich mixtures are observed to ignite later at downstream locations of the computational domain. These features are observed clearly by analysing the spatio-temporal evolution of the reactions zones and their structures in the physical and mixture fraction spaces. More importantly, the presence of non-premixed combustion mode is also observed through an analysis of flame index, FI, defined in Eq. (5.4). A value of -1 and 1 for FI implies lean and rich premixed combustion respectively and $\text{FI} = 0$ means non-premixed combustion as noted in [Briones et al., 2006]. The flame index does not distinguish ignition fronts. The presence of non-premixed mode was not observed in the previous MILD combustion DNS studies [Minamoto et al., 2013, 2014a,b] as the mixture fraction variations were excluded. The non-premixed mode combustion results from the fluxes of methane and oxygen coming from neighbouring pockets of richer and leaner mixtures and the premixed and non-premixed zones are observed to coexist along with ignition fronts. The fractions of computational volume having lean and rich premixed, and non-premixed combustion modes are computed using the pdf of flame index and the corresponding fractional contributions of heat release rate are calculated. The results suggest that nearly 50% of the contribution to the total heat release rate comes from the lean premixed mode. The contribution from rich premixed mode drops from about 13% in the reference case AZ1 to about 3% in the diluted case BZ1 when the mean oxygen mole fraction in the inflowing mixture is reduced from 2.7% to 1.6% (see Table 2.2). Whereas the non-premixed contribution increases substantially and this increase is also observed when the integral length scale of the mixture fraction field is reduced as noted in Table 3. However, the sum of these three fractional contributions to the total heat release rate is noted to be about 75% only and the remaining 25% is found to come from regions with $0.1 \leq |\text{FI}| \leq 0.8$. To conclude, non-premixed turbulent MILD combustion is a complex process with spatial and temporal ignitions fronts, propagating flames that are strongly convoluted and interacting, non-premixed combustion and interactions among these.

Chapter 6

Autoignition and Flame Propagation in Non-Premixed MILD Combustion

As mentioned in the review of MILD combustion in section [1.2](#) and observed in the previous chapter, MILD combustion involves high reactants temperature which suggests the importance of autoignition while at the same time propagating and interacting reaction zones are also present. Thus, there is a coexistence between these phenomena in MILD combustion and the objective of the present chapter is to investigate this balance and assess which of the two phenomena may be predominant.

6.1 Balance of reaction and convection/diffusion effects

MILD combustion involves a mixture of fuel and hot diluted oxidiser in unburnt, burnt and partially burnt states. This range of mixture states is produced by imperfect mixing and reactions of fuel with the oxidiser stream. This produces a large fluctuation in the local mixture fraction, reaction progress variable and mass fractions of radicals and intermediates. This will have a strong impact on the development of local combustion mode - autoignition or flames. Furthermore, the local turbulence conditions will also have a large influence on this aspect. The preponderance of and the interplay between these phenomena in MILD combustion is studied using a flux-balance analysis which allows to delineate regions dominated by autoignition (reaction) and flames.

The transport equation for the mass fraction of species α is given by

$$\frac{\partial \rho Y_\alpha}{\partial t} + \underbrace{\frac{\partial \rho u_j Y_\alpha}{\partial x_j}}_{\mathcal{C}: \text{ conv.}} = \underbrace{\frac{\partial}{\partial x_j} \left(\rho D_\alpha \frac{\partial Y_\alpha}{\partial x_j} \right)}_{\mathcal{D}: \text{ diff.}} + \underbrace{\dot{\omega}_\alpha}_{\mathcal{R}: \text{ react.}} \quad (6.1)$$

where u_j is the velocity in direction j , D_α is the molecular diffusivity of the species α and $\dot{\omega}_\alpha$ is its reaction rate. Turbulent combustion can thus be interpreted as a balance between convection, diffusion and chemical reactions. Following work by [Minamoto et al. \[2014a\]](#), this balance can be studied by analysing \mathcal{B} , defined as:

$$\mathcal{B} \equiv |\mathcal{C} - \mathcal{D}| - |\mathcal{R}| \quad (6.2)$$

The species transport equation can then be approximated as $\partial \rho Y_\alpha / \partial t + \mathcal{B} = 0$. Equation (6.2) suggests that regions described by $\mathcal{B} < 0$ are dominated by the reaction source. These regions are taken to be similar to what happens inside a Perfectly Stirred Reactor (PSR) and thus ignition dominated regions. Conversely, in a steady laminar flame, there is a balance among convection, diffusion and reaction terms and thus $\mathcal{B} = 0$. However, the large velocity fluctuations can lead to flame displacements, which translates into large \mathcal{C} . Hence, in the presence of turbulence, regions with unsteady flames are characterised with $\mathcal{B} > 0$. The mass fraction of H_2O is used for the flux analysis for \mathcal{B} and investigations using Y_{CH_4} and other species yielded results similar to those discussed below.

Figure 6.1 shows the variations of \mathcal{B} in regions with $\dot{Q}^+ \geq 1$ for the three cases, listed in Table 2.2, where $\dot{Q}^+ = \dot{Q}_{th} / (\rho_r s_{LP} (T_p - T_r))$ is the normalised heat release rate per unit volume. It is observed that reaction zones in all cases are spread over a substantial portion of the domain and this spread seems to increase with dilution level as seen in Fig. 6.1. However, the cases AZ1 and AZ2 suggest the existence of thin reaction zones. The preponderance of autoignition ($\mathcal{B} < 0$) region is clear for the case BZ1.

6.2 Lagrangian evolution

To further analyse this mixed ignition-flame behaviour, the evolution of \mathcal{B} can be tracked using Lagrangian particles to study how a given fluid parcel evolves through the domain and for example how it undergoes ignition or how from an ignition kernel it develops into a propagating flame. These particles are seeded at $t = \tau_f$ in the flow at four different axial plane locations, $x = 0$, $L_x/4$, $L_x/3$ and $L_x/2$, and their spatial locations are tracked

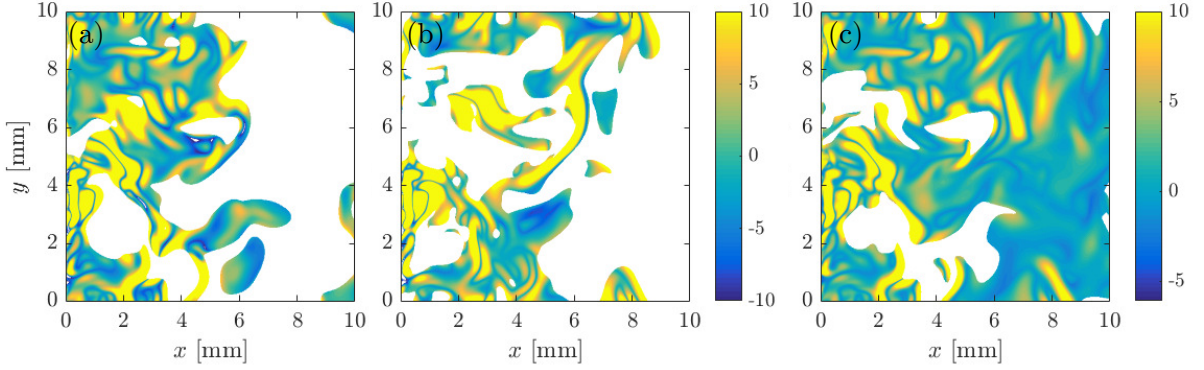


Fig. 6.1 Typical spatial variations of \mathcal{B} field shown in regions with \dot{Q}^+ , normalised heat release rate, larger than 1.0 at $t = 1.5\tau$ for cases (a) AZ1, (b) AZ2 and (c) BZ1.

in time as $\underline{x}(t + \Delta t) \approx \underline{x}(t) + \underline{u}(t)\Delta t$ where $\Delta t = 4.5\mu s$ is the time difference between two saved snapshots of the DNS. This is performed for the entire sampling duration, i.e. for $\tau_f \leq t \leq 1.5\tau_f$. In each of these four planes, a particle is injected at every in-plane grid points, thus yielding 512×512 particles per plane, which are then tracked in time. Their behaviours and the evolution of key quantities along their paths are carefully analysed here.

It should be noted that one could have used the DNS timestep of $\delta t = 1$ ns instead of Δt . A comparison of the particle locations obtained using $\Delta t = 1$ ns (by rerunning the DNS for a short period) with those obtained using $\Delta t = 4.5 \mu s$ showed an average relative difference of about 0.02% for the particle location and various quantities analysed. Thus, a value of $\Delta t = 4.5 \mu s$ was used for the analysis reported here. This choice avoids rerunning the entire DNS with particles and the very small difference for the location (0.02%) observed is because the velocity field is not unduly influenced by the local heat release rate. However, the state of the fluid mixture at the location $\underline{x}(t + \Delta t)$ for time $(t + \Delta t)$ was computed using δt in the DNS and thus it has evolved under the influence of convection, diffusion and reaction. Figure 6.2 shows a few typical trajectories for all cases and those highlighted using arrows are investigated further in Figs. 6.4 to 6.6. There are similarities in the various trajectories shown for the three cases because they have been initialised using the same turbulence field, since the heat release rate is small, it does not have a strong influence on the velocity field. However, it can be seen that the evolution of \mathcal{B} along these trajectories are quite different from one case to another, suggesting the importance of the thermo-physical properties of the mixture used for the simulations. To emphasize the three-dimensional motion of the particles, the projection of their trajectories in the x - y and x - z planes are presented in Fig. 6.3 for the case AZ1.

Autoignition and Flame Propagation in Non-Premixed MILD Combustion

It is readily observed that the individual trajectories are quite different due to the intense turbulence field. Furthermore, the value of \mathcal{B} varies widely along these trajectories and it is thus expected that these fluid parcels may undergo ignition and/or flame propagation and may present highly different behaviours. Out of these trajectories, a few particles exhibiting representatives evolutions, annotated in Fig. 6.3 and also shown by arrows in Fig. 6.2, are selected for further analysis. The starting locations of the highlighted particles of Fig. 6.2 are listed in Table 6.1.

Table 6.1 Initial locations of the tracked particles ($x/L_x, y/L_y, z/L_z$) highlighted in Fig. 6.2.

	AZ1	AZ2	BZ1
a	(0.250, 0.225, 0.008)	(0.250, 0.008, 0.002)	(0.250, 0.241, 0.969)
b	(0.500, 0.006, 0.583)	(0.333, 0.288, 0.816)	(0.000, 0.231, 0.315)
c	(0.333, 0.245, 0.796)		

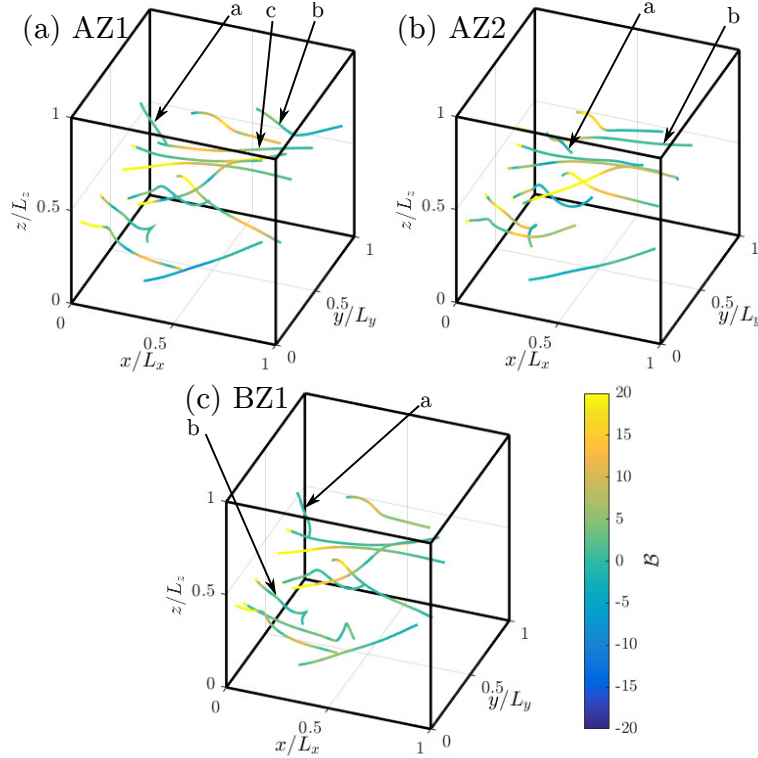


Fig. 6.2 Typical trajectories of Lagrangian particles tracked for $\tau_f \leq t \leq 1.5\tau_f$ for all cases. Lines are coloured with the value of \mathcal{B} along the trajectory. Arrows indicate trajectories which will be further studied.

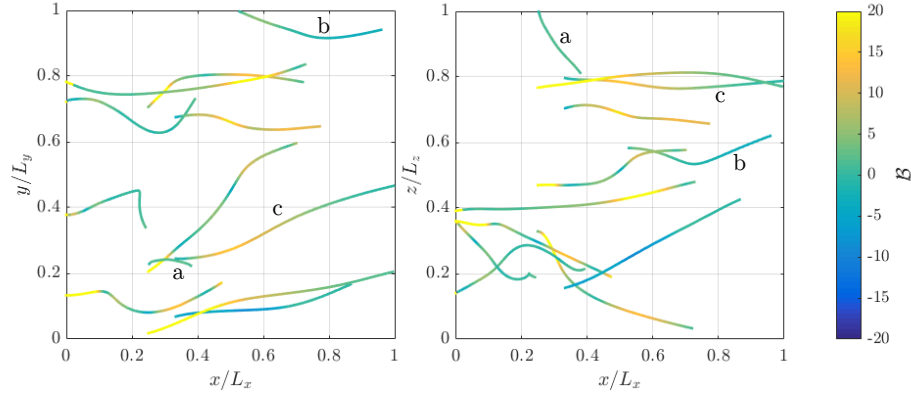


Fig. 6.3 Projection on the x - y and x - z planes of the trajectories of Fig. 6.2a. Lines are coloured with the value of \mathcal{B} along the trajectory. Annotated trajectories are further discussed in Fig. 6.4.

Figure 6.4 shows the spatial evolutions of \dot{Q} , Y_{CH_4} , $|\nabla Z|$, $|\nabla c_T|$ and $\Delta T = T - T_r$, normalised by their respective maximum along the chosen trajectory, along with the variations of \mathcal{B} and ϕ for the three trajectories highlighted in Figs. 6.2 and 6.3. The normalised quantities are denoted with a "*" superscript. It should be noted that these are plotted as a function of only x , the streamwise direction, but the particles are also moving in the transverse, y and z , directions as shown in Figs. 6.2 and 6.3. Furthermore, as their starting axial locations are different, the range of x on each frame is different. The quantities shown are for the period starting from $t = \tau_f$ to $1.5\tau_f$. The starting location of the tracking corresponds to the left side of the x -axis while the end is on the right. Furthermore, \mathcal{B} is only computed in regions where $\dot{Q}^+ > 1$ (and plotted as solid black line) to focus on the study of \mathcal{B} in reacting regions. Otherwise, \mathcal{B} is plotted as dotted line having a value of 0.

These specific particles were chosen because they illustrate the statistical evolution of \mathcal{B} to be discussed later in section 6.3. Figure 6.4a shows the evolution of an ignition kernel towards a propagating flame-structure. Indeed, \mathcal{B} starts as negative, indicating the preponderance of reaction and an ignition-like behaviour and then increases towards zero which is representative of a steady flame. In addition, the ignition occurs in a lean region ($\phi < 1$) close to the inlet, as $x/L_x \approx 0.25$. This is due to the high reactivity of lean mixture and their relatively small ignition delay time [Göktolga et al., 2015] (also see Fig. 6.10 to be discussed later). Further downstream, this ignition kernel propagates through a slightly richer mixture developing into a flame as $\mathcal{B} \rightarrow 0$. The quantity $|\nabla c_T|$ is high at the beginning because the particle corresponds to an ignition spot: locally, the value of c_T for the particle is relatively larger than its surrounding with unburned

mixture ($c_T \approx 0$). Also, the mixture fraction distribution in regions surrounding this ignition kernel yields large $|\nabla Z|$. The ignition occurring at this location with high $|\nabla Z|$ is contrary to conventional combustion situation and this occurs because of the presence of radicals as noted in chapter 4. As the parcel is convected downstream, its surrounding mixture having relatively uniform c_T also starts to react and thus $|\nabla c_T|$ decreases. The evolution of $|\nabla Z|$ gives an indication of the small scale mixing evolution. It is seen that there are two instances of large $|\nabla Z|$ and the second local maximum of $|\nabla Z|$ is interesting, which results from the particle mixing with a richer mixture (as ϕ increases). This provides the fuel required to sustain the chemical reactions, which is seen from the variation of Y_{CH_4} and \dot{Q} shown in Fig. 6.4a. There is a progressive increase in temperature throughout this process due to chemical reactions occurring in the fluid parcel. The variations shown in Fig. 6.4a depicting the history of the chosen fluid parcel illustrate the ignition of a lean mixture in the upstream developing into a propagating flame downstream.

Figure 6.4b illustrates another behaviour in MILD combustion, namely the ignition of a rich mixture in the downstream region. The rich mixture is nearly not reacting in the early stage, as indicated by the low heat release rate, despite the presence of both CH_4 (and O_2 , not shown here for clarity of Fig. 6.4). This is due to the low reactivity and large ignition delay time of this rich mixture (to be discussed in detail later in Fig. 6.10). However, this rich parcel undergoes mixing in the early parts of the domain as indicated by the relatively large and nearly constant value of $|\nabla Z|$, slow drop in Y_{CH_4} , slow increase in ΔT but no change in \dot{Q}^* . This decreases the equivalence ratio and gradually heats up the parcel (as ΔT increases slowly), leading to its ignition, as observed by the large increase of \dot{Q}^* and the decrease of Y_{CH_4} further downstream. Thus, \mathcal{B} starts to become negative as seen in Fig. 6.4b. The large value of $|\nabla c_T|$ in the downstream indicates that the particle is surrounded by burned mixture while it begins to react. The rate of change of $|\nabla c_T|$ changes sharply once the fluid parcel ignites ($x/L_x = 0.83$).

Figure 6.4c presents the evolution of a rich flame-like structure. This parcel, from a flame around stoichiometry ($\mathcal{B} \approx 0$, $\phi \approx 1$, with decreasing \dot{Q}), propagates towards an unburnt rich mixture (increasing value of Y_{CH_4}). The high $|\nabla c_T|$ value indicates that the mixture around the tracked parcel have a different c_T , smaller here verified separately, and $|\nabla Z|$ is large too indicating the flux of mixture fraction and thus mixing. This is also confirmed by the small decrease in ΔT which indicates that the original parcel has mixed with cooler mixture. This mixing is also emphasized by the large increase in CH_4 . As a result of this mixing which is driven predominantly by the convective effect, \mathcal{B} increases to large values and the flame continues to propagate towards richer mixture.

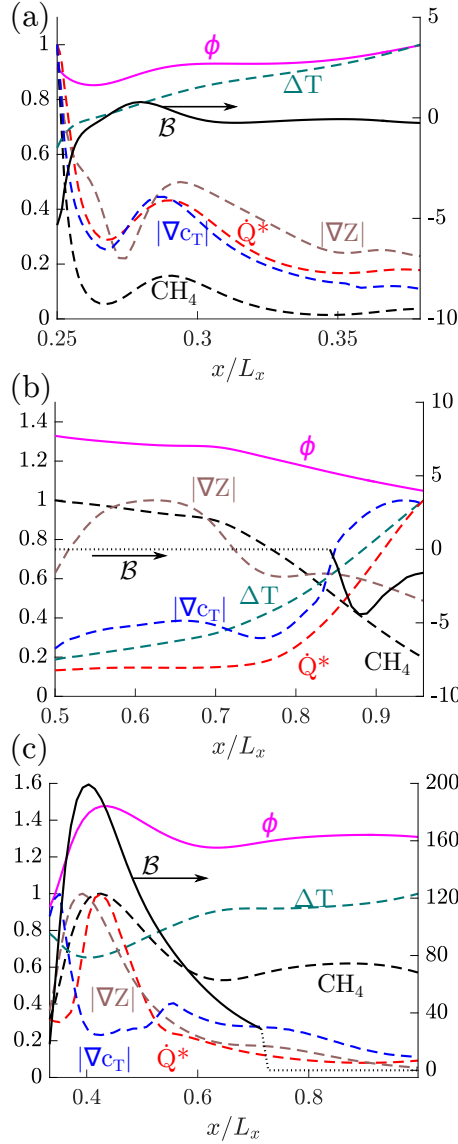


Fig. 6.4 Evolutions of \dot{Q}^* , ϕ , $Y_{\text{CH}_4}^*$, $Y_{\text{O}_2}^*$, $|\nabla Z|^*$, $|\nabla c_T|^*$, ΔT^* , (left axis) and \mathcal{B} (right axis) along the trajectory of three particles for case AZ1.

Comparing these three evolutions, an important aspect to highlight is in their stream-wise locations. Indeed, the ignition of the lean parcel, and its subsequent evolution towards a propagating flame, shown in Fig. 6.4a occurs in the early part of the domain ($x/L_x \approx 0.25$) while the ignition of the rich parcel occurs much more downstream ($x/L_x \approx 0.9$). This large difference is explained by the large difference in their ignition delay times (which will be shown later in Fig. 6.10). Finally, for each parcel, it should be observed that the temperature increase is extremely progressive which is a

key characteristics of MILD combustion where there is no sharp or sudden increase of temperature.

The three previous behaviours illustrate several key characteristics for the case AZ1 which will be re-emphasized in the next subsection. Mainly, that lean mixtures show an autoigniting behaviour then stabilize towards a flame while rich mixtures either are autoigniting in the downstream or are undergoing reaction through the propagation of an initially lean flame propagating towards a rich mixture. The existence of flames observed in the present study can already be contrasted to the observation made in the DNS of an autoigniting mixing layer [Göktolga et al., 2015] where the main process observed was the auto-ignition of mixture along the iso-surface of most reactive mixture fraction. A stronger flame in the initial stages can become relatively weaker because of large fuel flux coming from mixing with surrounding richer mixtures.

For case AZ2, the predominant behaviour observed corresponds to ignition-like events which is in contrast to the case AZ1 discussed above. This is illustrated in Fig. 6.5 which shows the evolutions of various quantities for the particles tracked (see Fig. 6.2b) for the case AZ2. In particular, Fig. 6.5a shows the ignition of a very lean mixture ($\phi \approx 0.17$). However, unlike the lean parcel in the case AZ1 shown in Fig. 6.4a, this parcel in the case AZ2 has nearly no CH_4 and thus it is convected downstream mixing with richer mixtures which makes it ignitable. The sharp rise in $|\nabla c_T|$ is because of this ignition. A particular behaviour is also observed with a double peak of \mathcal{B} . Indeed, after ignition takes place (the first negative peak of \mathcal{B}), that parcel evolves towards $\mathcal{B} = 0$ but instead of stabilising there, \mathcal{B} becomes negative again indicating a second ignition-like event. This is further emphasised by the existence of a double peak for the heat release rate. This occurs while the igniting parcels encounters a large mixture fraction stratification (as indicated by the large $|\nabla Z|$ and progressive increase in ϕ). This kind of sequential ignition is due to the stratification in the mixture fraction and is also found in PCCI combustion with stratified mixture [Luong et al., 2017]. In contrast, in Fig. 6.4a for the case AZ1, there is no such sequential ignition because the mixture stratification is relatively small making it closer to HCCI conditions where the development of ignition towards deflagration is more likely [Luong et al., 2017]. Figure 6.5b shows the converse ignition behaviour of a rich mixture which is similar to that observed in Fig. 6.4b. It should be noted that a careful analysis showed that these ignition-like events are much more probable in the case AZ2 compared to the case AZ1. This will be further discussed in section 6.3 on a statistical basis.

Figure 6.6 shows the evolution of two typical parcels for the case BZ1. In both cases, \mathcal{B} starts negative indicating an ignition-like behaviour before increasing towards

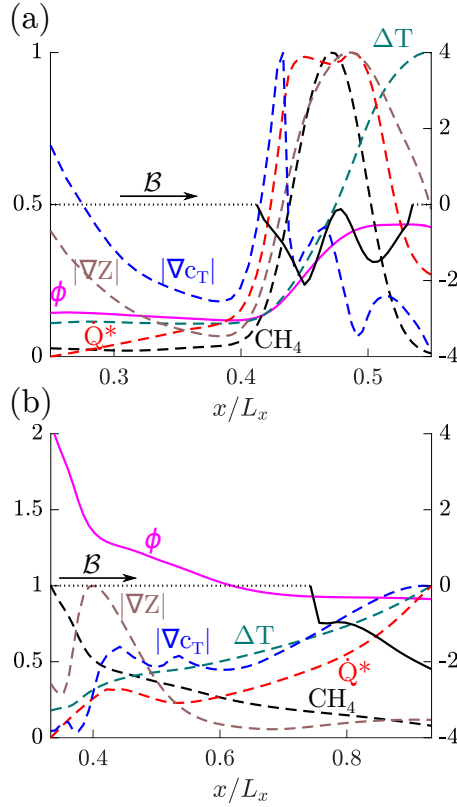


Fig. 6.5 Evolutions of \dot{Q}^* , ϕ , $Y_{\text{CH}_4}^*$, $Y_{\text{O}_2}^*$, $|\nabla Z|^*$, $|\nabla c_T|^*$, ΔT^* (left axis) and \mathcal{B} (right axis) along the trajectory of three particles for case AZ2.

positive or zero values as the parcels move downstream. It should however be noted that Fig. 6.6b shows a more flame-like behaviour with a nearly constant heat release rate while Fig. 6.6a shows a decrease in heat release rate after ignition because reactions are slowing down. This particular behaviour is explained by the difference in mixture fraction between the two parcels. Indeed, a lean reacting parcel propagates towards a richer mixture having a relatively lower reactivity in Fig. 6.6a. Conversely, a lean parcel propagates in a mixture with nearly constant mixture fraction in Fig. 6.6b. The large and sharp variations around $x/L_x = 0.4$ in Fig. 6.6b are due to the projection of the trajectory on the x axis. This parcel is inside a recirculating flow and has a nearly zero streamwise velocity (as it is moving in the y and z directions as observed in Fig. 6.2c).

Given the variety of combustion behaviours observed in Figs. 6.4 to 6.6, the question that arises is which of these modes is the most preponderant in MILD combustion or how these modes are balanced?

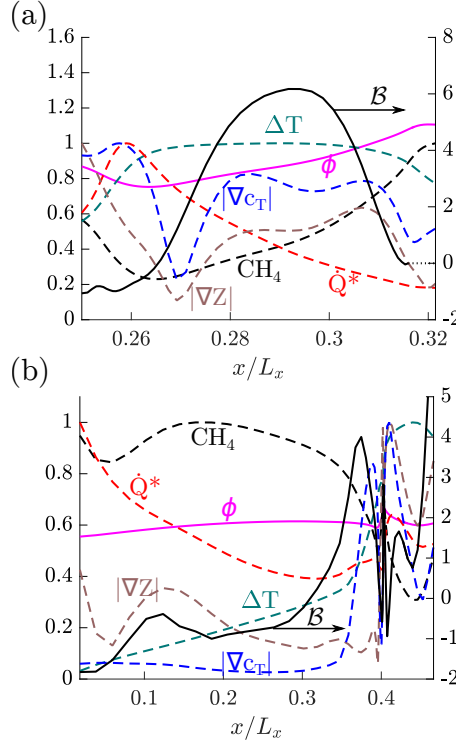


Fig. 6.6 Evolutions of \dot{Q}^* , ϕ , $Y_{\text{CH}_4}^*$, $Y_{\text{O}_2}^*$, $|\nabla Z|^*$, $|\nabla c_T|^*$, ΔT^* , (left axis) and \mathcal{B} (right axis) along the trajectory of three particles for case BZ1.

6.3 Statistical behaviour

The discussion in the previous section depicts the rich variety of combustion modes existing in MILD combustion and the spatial distribution of \mathcal{B} depicted in Fig. 6.1 suggests a strong interplay and entanglement between reaction dominated regions ($\mathcal{B} < 0$) and propagating flame regions ($\mathcal{B} \geq 0$). The relative importance of reaction and flame dominated regions and its correlation with the mixture fraction Z can be investigated in a statistical sense by studying the joint probability density function of \mathcal{B} and Z at various axial locations. The pdfs presented in this study are constructed using the data collected over the entire sampling time and about 1200 bins for \mathcal{B} and 400 bins for Z and only data from regions with $\dot{Q}^+ > 1$ so that only reacting regions are considered. This joint-pdf is shown for case AZ1 in Fig. 6.7 for various axial locations. It is observed that negatives values of \mathcal{B} are mostly present in lean mixture while very rich mixture have strictly positive \mathcal{B} . Furthermore as one moves downstream, the range of Z decreases due to turbulent mixing and the probability of high values of \mathcal{B} decreases. The latter is caused by the turbulence decay along the domain (thus decreasing convective effects).

To further understand the various effects, appropriately conditioned pdfs for all cases are studied.

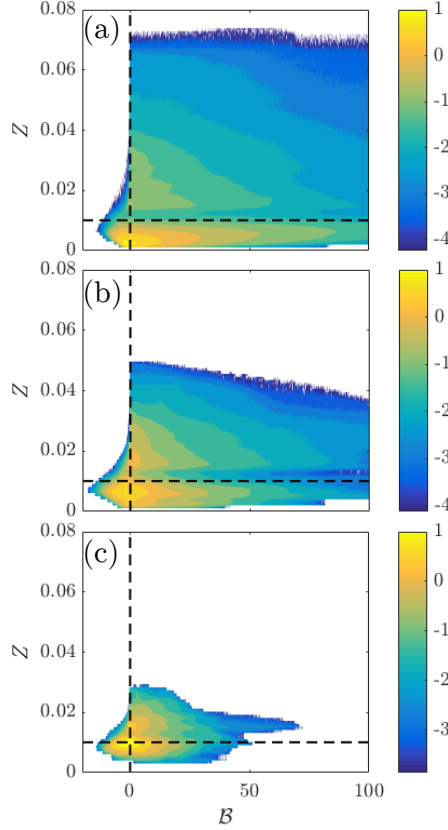


Fig. 6.7 Logarithm of the joint-pdf of \mathcal{B} and Z at (a) $x/L_x = 0.0625$, (b) 0.4375 , (c) 0.9375 for case AZ1. The horizontal line indicates Z_{st} .

Figure 6.8 shows the pdf of \mathcal{B} conditioned on the large heat release rate for all three cases, computed at various axial locations. For the case AZ1 in Fig. 6.8a, it is observed that close to the inlet, reaction-dominated regions are preponderant as shown by the pdf peaking for $\mathcal{B} < 0$. As one moves downstream, the pdf peak shifts towards $\mathcal{B} = 0$ indicating a balance among convection, diffusion and reaction terms which characterises propagating flame phenomena. However, a negative tail is still observed in the downstream locations which suggests that ignition-like reaction zones remain present. This confirms the interweaved ignition and flame propagation behaviour observed in Fig. 6.1. The case AZ2 shows a somewhat different behaviour in Fig. 6.8b. In this case, the pdf shows a clear shift of the peak towards negative values of \mathcal{B} which indicates an increase in reaction dominated regions. The case BZ1 shows a behaviour similar to the case AZ1 with a peak slightly negative at first and slowly shifting towards 0 as one moves downstream. The range of variations in the latter case in the negative regions is however

smaller than for the two other cases. This is due to the lower level of oxygen which yields less reactive mixture and thus lower peak values of $\dot{\omega}_\alpha$ while the turbulence field is the same as for the two other cases. Hence, while the magnitude of convective-diffusive effects remains similar across all cases, the magnitude of the reaction term in case BZ1 is lower which leads to, on average, larger positive value of \mathcal{B} .

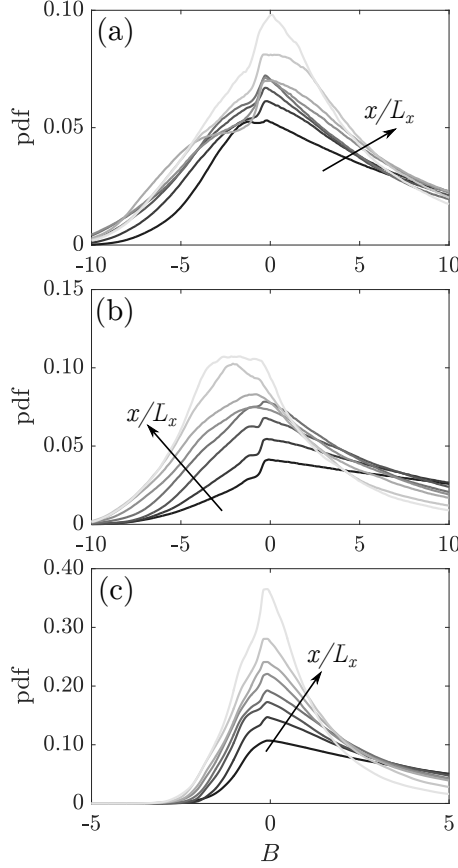


Fig. 6.8 Pdf of $(\mathcal{B}|\dot{Q}^+ > 1.0)$ at $x/L_x = 0.0625, 0.1875, 0.3125, \dots, 0.9375$ (dark to light gray) for cases (a) AZ1, (b) AZ2, (c) BZ1.

The difference of behaviours between the case AZ2 and the two other cases indicates a dependency on the length scale ratio ℓ_c/ℓ_Z for the observed phenomena in MILD combustion. Indeed, having $\ell_c/\ell_Z < 1$, the cases AZ1 and BZ1 have relatively smooth gradient of Z as ℓ_Z is large. As a result, an ignition spot will evolve in regions of similar equivalence ratio thus allowing for a "flame-front" like structure to develop. On the contrary, case AZ2 has smaller ℓ_Z , as listed in Table 2.2 leading to a more stratified mixture. The presence of stronger gradients of $|\nabla Z|$ prevents such a development and favours sequential autoignition of the mixture. Furthermore, as there is a wider range of mixture fractions, the range of timescale for the ignition delay will be larger resulting in

ignition occurring both in upstream and downstream locations inside the computational domain depending on the local mixture and turbulent conditions. Finally, due to the higher variations in the mixture fraction field, mixing may be required between leaner and richer (beyond the flammable) mixtures to yield a burnable mixture which will thus only ignite in the downstream regions, explaining the dominance of ignition further downstream. Such behaviour was observed in Fig. 6.5, for example.

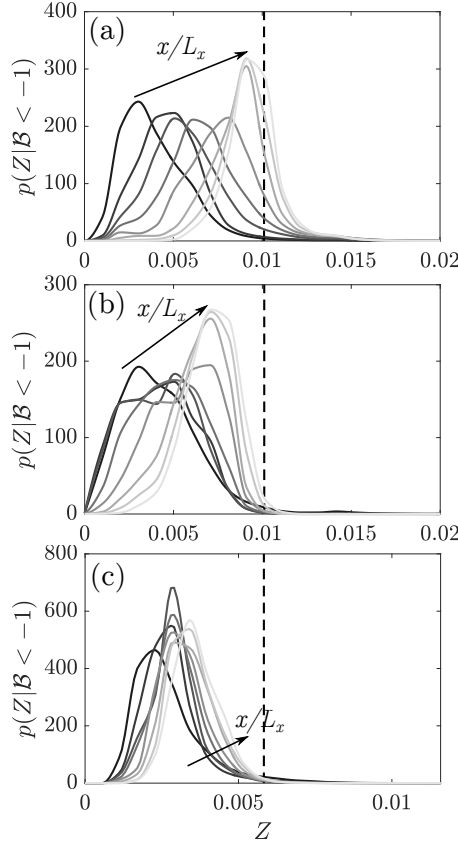


Fig. 6.9 Pdf of $(Z|\mathcal{B} < -1.0)$ at $x/L_x = 0.0625, 0.1875, 0.3125, \dots, 0.9375$ (dark to light gray) for cases (a) AZ1, (b) AZ2, (c) BZ1. The dashed line indicates the stoichiometric mixture fraction. These pdfs are constructed for regions with $\dot{Q}^+ > 1.0$.

It is possible to further characterize the reaction dominated regions by analysing the mixture fraction distribution in these regions. Figure 6.9 shows the pdf of mixture fraction Z in regions with $\mathcal{B} < -1$ for various axial locations. It can be readily observed that upstream, close to the inlet, the pdf peaks for a really lean mixture fraction, close to the most reactive mixture fraction. As one moves downstream, this peak shifts towards richer mixture fractions confirming the existence of sequential autoignition. The shift from leaner to richer mixture can be explained by the increase in ignition delay times between these mixtures as shown in Fig. 6.10. These ignition delay times were obtained

using CANTERA and by considering a constant volume homogeneous reactor containing an appropriate mixture initially at $T_r = 1500\text{K}$.

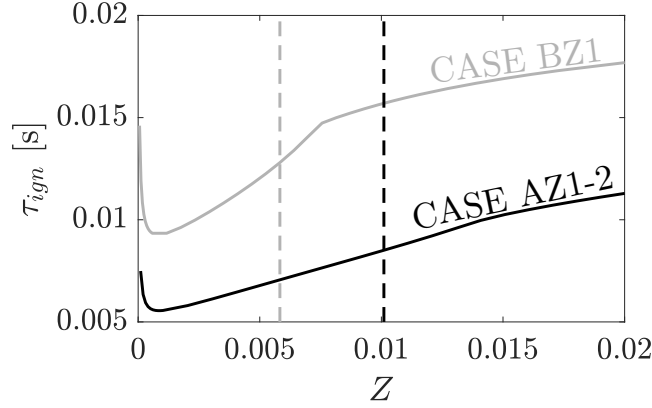


Fig. 6.10 Ignition delay time for the mixture considered. The vertical dashed lines indicate the stoichiometric mixture fraction for case AZ1-2 (black) and BZ1 (gray). These pdfs are constructed for regions with $\dot{Q}^+ > 1.0$.

A similar analysis is performed to characterise the mixture in steady flame-dominated regions where $\mathcal{B} \approx 0$ in Fig. 6.11. For case AZ1, it is observed that the mixtures in these regions evolve from lean to stoichiometric values indicating that as one moves downstream either flames start to appear in richer regions (from the apparition of richer ignition kernels as seen in Fig. 6.11) or that the existing leaner flames start to propagate in richer mixture. Furthermore, rich flames also exist in the downstream as indicated by the local peak of the pdf for richer mixture. It should however be noted that these rich flames do not originate from the ignition of a rich kernel developing into a flame but rather from the propagation of a lean flame into those rich mixture as the pdf of rich mixture with $\mathcal{B} < -1$ is nearly zero as seen in Fig. 6.9a. This particular behaviour was also observed in the Lagrangian particles analysis studied in Fig. 6.4a. Similar observations can be made for case BZ1, shown in Fig. 6.11c. However, a different picture emerges from case AZ2. It is observed in Fig. 6.11b that there already exist rich flames in the early stage of the domain. These rich flames originate from the propagation of lean flames towards richer mixture and not from the ignition of rich kernels developing into flame-like structures as there is no rich regions with $\mathcal{B} < 0$. However due to the small ℓ_Z , there exist rich mixtures directly next to leaner mixtures and thus a lean flame can propagate in richer mixture compared to the cases AZ1 and BZ1 where ℓ_Z is larger.

It should also be noted that for case AZ2, there are no rich flame appearing in downstream locations, contrarily to the other two cases. This is due to the actual

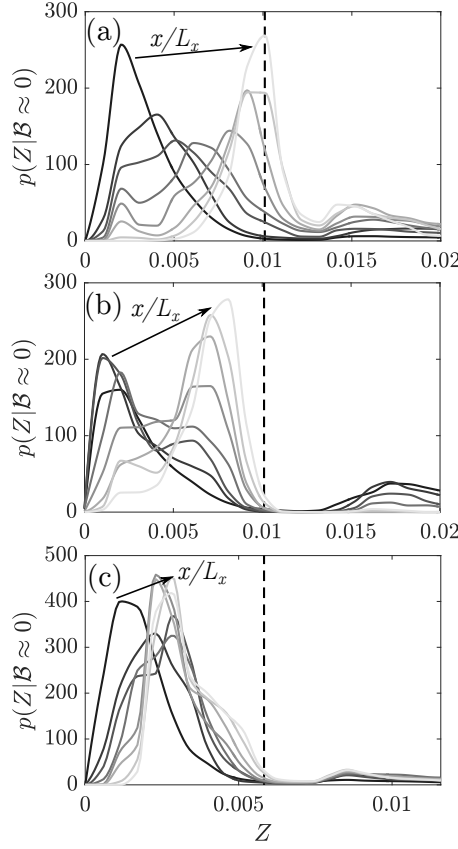


Fig. 6.11 Pdf of $(Z|\mathcal{B} \approx 0.0)$ at $x/L_x = 0.0625, 0.1875, 0.3125, \dots, 0.9375$ (dark to light gray) for cases (a) AZ1, (b) AZ2, (c) BZ1. The dashed line indicates the stoichiometric mixture fraction. These pdfs are constructed for regions with $\dot{Q}^+ > 1.0$.

turbulent mixing effect. In those downstream regions, the mixture fraction distribution does not show the presence of rich mixture. Indeed, as ℓ_Z is smaller in the case AZ2, the mixing timescale required to diffuse and mix the rich regions is smaller. Hence, the absence of rich flames in the downstream for the case AZ2 originates from the fact that these rich mixtures mix with leaner ones and do not react as rich mixtures.

Finally, in the discussion above, the specific effect of "back-support" was not analysed. Back-support refers to situation where excess heat and radicals from the reaction zones can feed the mixture in front of the propagating flame. This could indeed play an additional role in the mechanisms of MILD combustion. However, while such effects are important in stratified flames [Masri, 2015; Richardson et al., 2010], in the present MILD combustion conditions, there is already an excess of enthalpy due to the large reactants temperature and a large pool of radicals coming from the EGR that can initiate and sustain the reactions. Thus, extracting the specific effect of "back-support" in MILD combustion would require a finer analysis than the one performed here.

6.4 Summary

In this chapter, the co-existence of autoignition and flame-propagation phenomena is highlighted as observed by [Minamoto et al. \[2014a\]](#) for premixed MILD combustion. This is observed using the various fluxes in the species transport equation and this analysis shows the balance and entanglement of both of these phenomena. However, ignition is predominant in the early stage of the domain and are associated with lean mixture as these have a lower ignition delay time. As one moves downstream, the evolution of MILD combustion is dependent on the typical lengthscale of the mixture fraction field, ℓ_Z . Indeed, for larger ℓ_Z (yielding $\ell_c/\ell_Z < 1$), flame-like structures start to be preponderant because the earlier ignition kernels develop into flames. However, when $\ell_Z \sim \ell_c$, it is observed that reaction-dominated regions (ignition) stays predominant. Furthermore, the co-existence of lean and rich flame-like reaction zones is also observed.

The picture that emerges from the present analysis is as follows. In the regions of the domain close to the inlet, MILD combustion is dominated by ignition-like kernels which are located mainly in lean mixtures as these mixtures are more reactive (i.e. have a lower ignition delay time). Then, depending on the mixture fraction length scale, these kernels develop into flame-like structures which then propagate into either lean or rich mixtures. In addition to this, ignition of richer mixtures occurs in the downstream locations. Hence, MILD combustion is extremely rich in terms of physical phenomena and this diversity needs to be included in the modelling of MILD combustion.

Chapter 7

Multiscale Analysis in MILD Combustion

In chapter 3, the bandpass filtering method, a methodology to conduct multiscale analysis and study scales interactions, was presented. Furthermore, homogeneous isotropic turbulence was studied and the energy cascade and vortex stretching mechanism were found to be local in terms of scales interactions. A similar analysis in turbulent premixed flames showed that the vortex stretching mechanism was relatively unaffected by the presence of the flame and also exhibited this scale-locality. However, other studies have shown that strong heat release and reaction may have an effect on the features of turbulence through the apparition of a peak in the turbulence kinetic energy spectra [Kolla et al., 2014] or with, on average, a reverse energy transfer from small to large scales [O'Brien et al., 2017].

The objective of this chapter is to use the analysis methodology presented in chapter 3, the bandpass filtering method and the energy transfer decomposition, to assess whether the energy cascade is affected and whether a reverse energy cascade is observed under MILD combustion conditions where heat release rate is volumetrically distributed.

7.1 Energy cascade and vortex stretching

Figure 7.1a shows the isosurface of enstrophy threshold at its mean plus one standard deviation value alongside the isosurface of normalised reaction rate $\dot{Q}^+ = 2.5$ for case AZ1 at $t = 1.5\tau_f$. In this figure, it is seen that the enstrophy structures are mainly located upstream of the domain and disappear under turbulent decay in the downstream regions. Furthermore, a strong entanglement and overlap is observed between the enstrophy

structures and the reaction zones which raises the question as to whether the heat release in these regions has an effect on the development of the turbulent structures.

To study this, similarly to the analysis conducted in chapter 3, the velocity field in the DNS of MILD combustion is bandpass filtered to analyse the interactions of scales. Typical enstrophy structures at scale $L = l \approx 30\eta$, where l is the integral lengthscale, and $L = 10\eta$ are shown in Fig. 7.1b for case AZ1. It is seen that small scales turbulent structures (in red) are mostly clustered in the upstream regions while larger ones (in green) are present over the entire domain. This is expected as small scales turbulent structures decay faster than large ones which can be convected further downstream by the inflowing velocity.

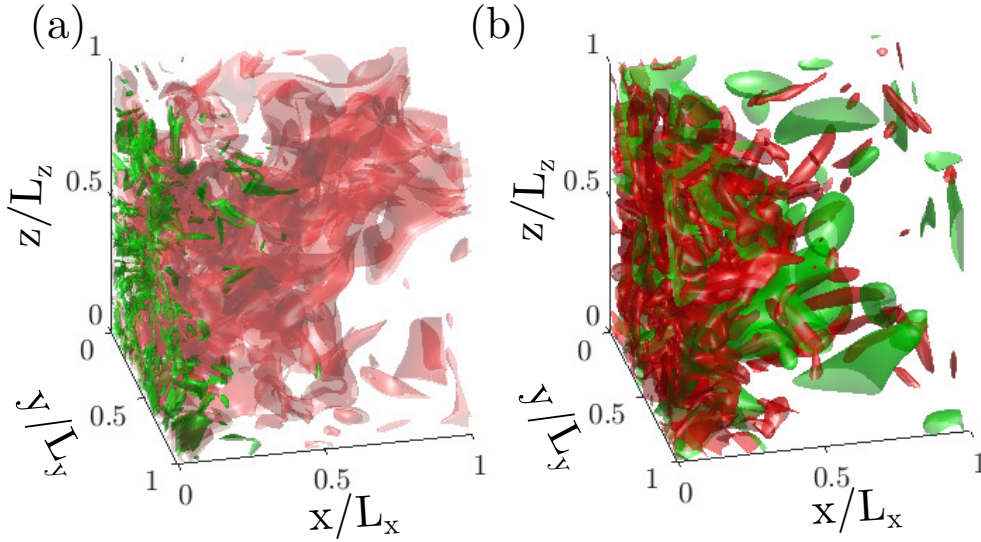


Fig. 7.1 (a) Isosurfaces of unfiltered enstrophy (green) with isosurfaces of normalised heat release rate threshold at $\dot{Q}^+ = 2.5$ (red) and (b) isosurface of enstrophy filtered at $L = 30\eta$ (green) and at $L = 10\eta$ (red) for case AZ1. The iso-surface are threshold at a value of $\mu + \sigma$.

7.1.1 Energy transfer

From the bandpass filtered quantities, similarly to the analysis presented in chapter 3, it is possible to compute the energy transfer between different scales. The pdf of the energy transfer normalised by its maximum (see Eq. (3.18)) is presented in Fig. 7.2 for a large scale $L = 30\eta$ and a small scale $S = 10\eta$. The pdf is constructed from an instantaneous snapshot of the DNS, by computing the energy transfer at every nodes in the computational domain and binning them appropriately. It is observed that the energy transfer function takes both positive and negative values suggesting that, instantaneously,

7.1 Energy cascade and vortex stretching

there is a two-way transfer between large and small scales. It should however be noted that the mean value of the energy transfer is positive, with a value of 0.031, indicating that on average the energy still cascades from large to small scales. Similar results have been observed by Aoyama et al. [2005] in homogeneous isotropic turbulence indicating that the heat release in MILD combustion may not have a strong influence on the dynamics of the energy cascade.

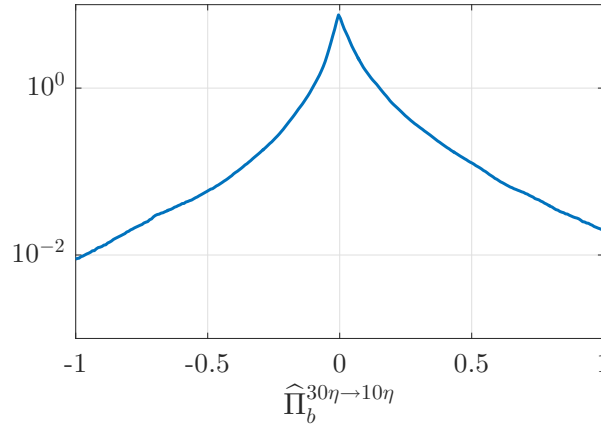


Fig. 7.2 Pdf of the energy transfer function between large scale $L = 30\eta$ to scale $S = 10\eta$, for case AZ1, computed at $t = 1.5\tau_f$.

Figure 7.3 shows the normalised scale-by-scale energy transfer in an average sense, i.e. after performing the ensemble averaging operation in Eq. (3.18), for two large scales, $L = l$ (the integral lengthscale) and $L = 2l/3$. It is observed that the results are similar to those presented in Fig. 3.5 for homogeneous isotropic turbulence with a peak of energy transfer observed for a value of S/L of 0.3 to 0.5. This suggests that the energy transfer is not unduly affected by the heat release in MILD combustion. This becomes even clearer when analysing Fig. 7.3b where the averaging is conditioned on the value of the progress variable based on temperature. Indeed, for all considered values of c , the peak remains located around similar values of S/L . Hence, this suggests that despite the volumetric heat release rate present in MILD combustion, the energy still cascades from large to slightly smaller scales and no reverse energy cascade is observed in an average sense.

Cases AZ2 and BZ1, respectively shown in Figs. 7.4 and 7.5, exhibit similar behaviour to case AZ1. This is expected as all cases shows relatively low heat release rate and were initialised with the same turbulence field. Hence, the interaction of scales of turbulence should remain similar for all cases.

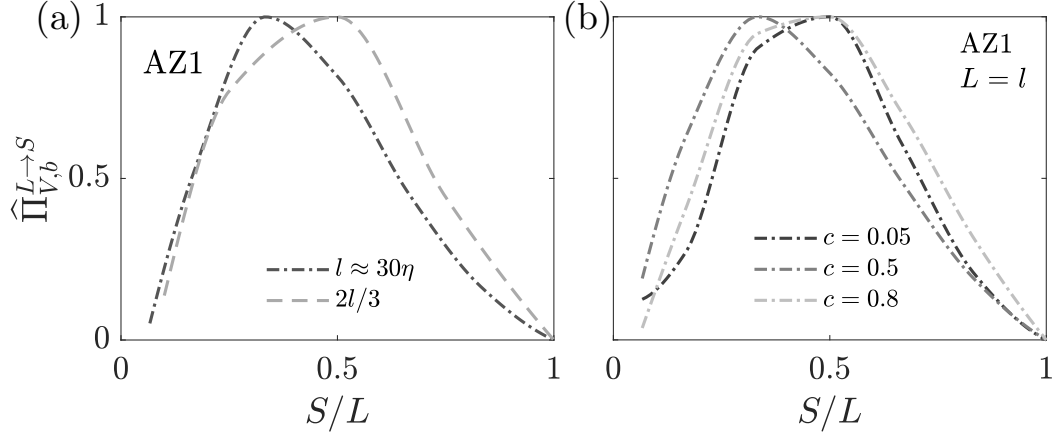


Fig. 7.3 Normalised energy transfer function, $\hat{\Pi}_{V,b}^{L \rightarrow S}$, for case AZ1 (a) averaged over the entire domain and (b) conditionally averaged on the temperature progress variable c .

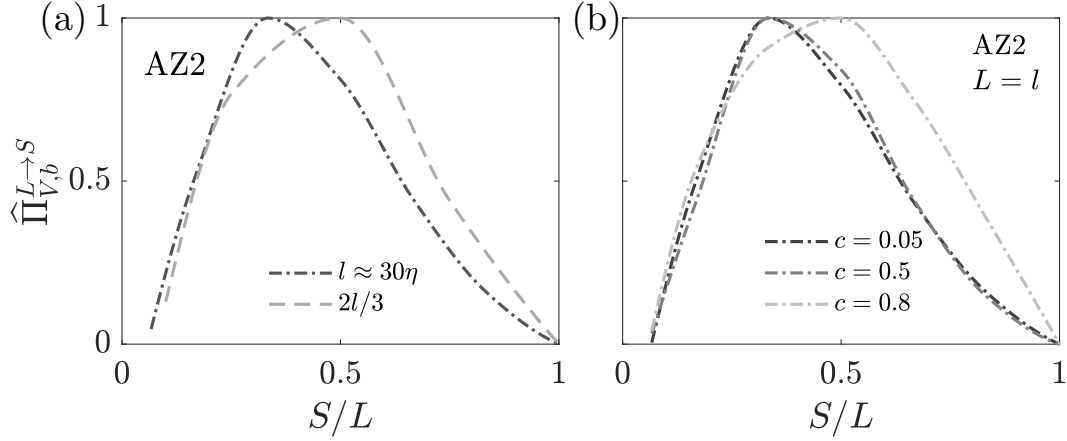


Fig. 7.4 Normalised energy transfer function, $\hat{\Pi}_{V,b}^{L \rightarrow S}$, for case AZ2 (a) averaged over the entire domain and (b) conditionally averaged on the temperature progress variable c .

7.1.2 Vortex stretching

Using a similar methodology to section 3.4.5, the vortex stretching mechanism can be analysed through the enstrophy production term between scale L_ω and scale $L_s = \mathcal{L}L_\omega$, and the probability of perfect alignment between the vorticity at scale L_ω and the extensional strain rate at scale L_s .

Figure 7.6 shows the pdf of the normalised enstrophy production term, $\omega_i^{L_\omega} \widehat{S_{ij}^{L_s}} \omega_j^{L_\omega}$, for $L_\omega = 10\eta$ and $L_s = 30\eta$ for case AZ1. The enstrophy production is normalised by its global maximum. It is observed that the pdf has a shape quite similar to the pdf of energy transfer shown in Fig. 7.2 supporting the existence of a close link between enstrophy production and energy transfer [Betchov, 1956; Cocke, 1969]. Similarly to the

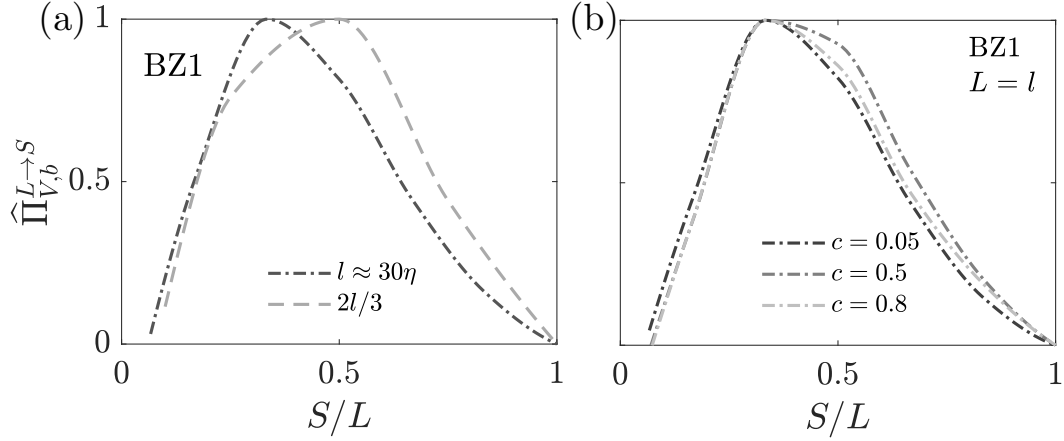


Fig. 7.5 Normalised energy transfer function, $\hat{\Pi}_{V,b}^{L \rightarrow S}$, for case BZ1 (a) averaged over the entire domain and (b) conditionally averaged on the temperature progress variable c .

energy transfer, negative values of enstrophy production can be found but, overall, the average enstrophy production is positive, with a value of 0.051. This again indicates that the general direction of enstrophy is to be produced at small scales by the straining from larger scales.

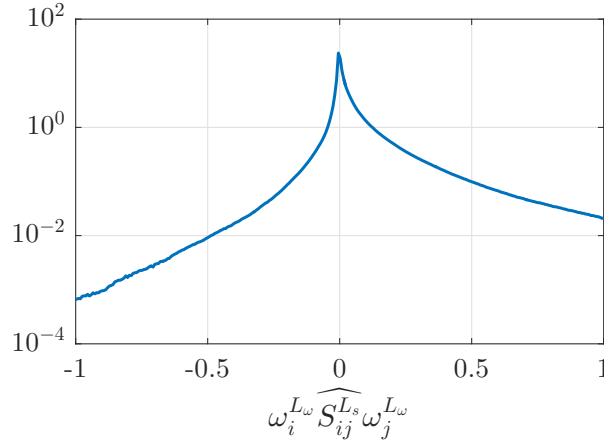


Fig. 7.6 Pdf of enstrophy production for vorticity at scale $L_\omega = 10\eta$ and strain rate at scale $L_s = 30\eta$ for case AZ1. The pdf is computed from the snapshot at $t = 1.5\tau_f$.

To further study the interactions between vortical structures at small scales and the straining structures at larger scales, the pdfs of $|\cos \theta_i|$ for the α and β strain rates are computed for the vorticity at scale $L_\omega = 5\eta$ and straining structures at larger scales. This is shown for case AZ1 in Fig. 7.7. Similar results as those shown in Fig. 3.8 for homogeneous isotropic turbulence and Fig. 3.13 for premixed flames are observed.

Specifically, there is a preferential alignment with the α strain-rate when $L_s > L_\omega$ while, when $L_s = L_\omega$, the vortical structures align with the β strain-rate.

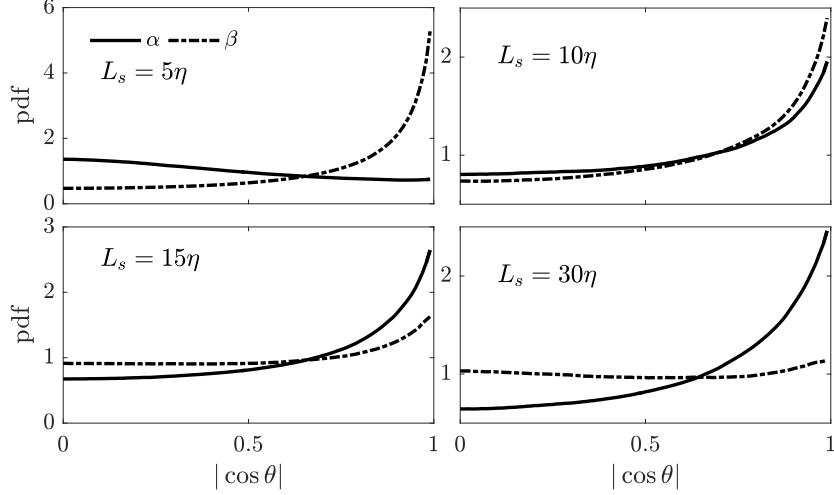


Fig. 7.7 Pdf of the magnitudes of direction cosines between vorticity at $L_\omega = 5\eta$ and principal strain rates at L_s for case AZ1 at $t = 1.5\tau_f$.

To quantify the straining scale imparting the most stretching on these vortical structures, Fig. 7.8 shows the probability of perfect alignment, P , between these vortical structures at scale $L_\omega = 5\eta$ and larger straining structures for case AZ1. In this figure, the full line is for the unconditioned probability while dashed lines are the probability conditioned on the value of the reaction rate, \dot{Q}^+ . This latter allows to study the effect of heat release on the vortex stretching mechanism. It is observed that the unconditioned probability peaks for a values of \mathcal{L} between 3 and 4, similarly to the results reported in Figs. 3.9 for non-reacting turbulence and 3.14 for premixed flames. Furthermore, even when conditioning on the reaction rate, the location of the peak is not unduly affected indicating that the vortex stretching is not significantly influenced by heat release in MILD combustion. It should be noted that due to the limited range of turbulent scales in the present DNS of MILD combustion, the maximum value of \mathcal{L} is limited to 6. This does not change the results stated above as the peak of P and its decrease at larger values of \mathcal{L} can already be observed. Similar results are obtained for cases AZ2 and BZ1, shown in Fig. 7.9.

7.2 Summary

In this chapter, the multiscale analysis of the turbulence field in MILD combustion showed that the vortex stretching mechanism and the interaction of scales remain similar to

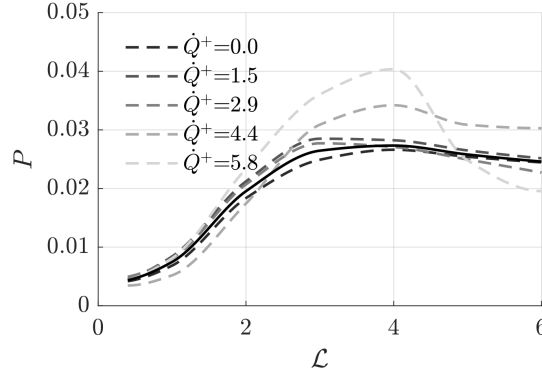


Fig. 7.8 Variation of probability of near perfect alignment of ω with α versus \mathcal{L} for $L_\omega = 5\eta$ for case AZ1. Full line is for the unconditioned probability, dashed lines are for probability conditioned on the reaction rate.

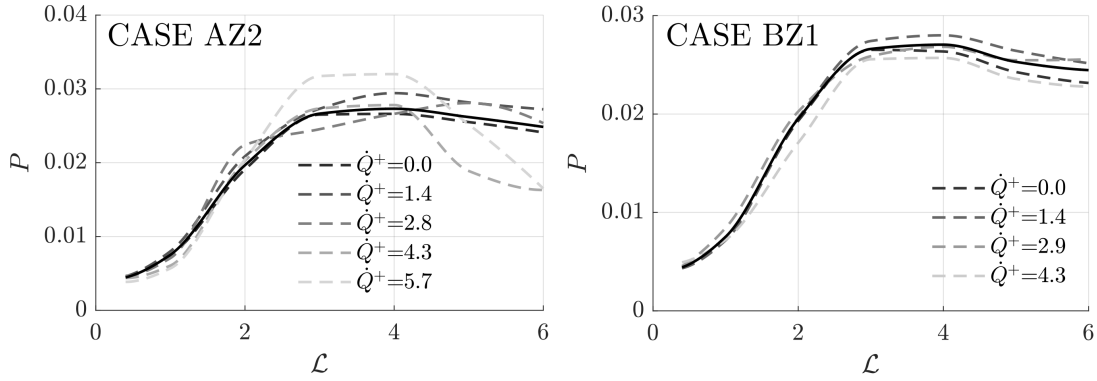


Fig. 7.9 Variation of probability of near perfect alignment of ω with α versus \mathcal{L} for $L_\omega = 5\eta$ for cases AZ2 and BZ1. Full line is for the unconditioned probability, dashed lines are for probability conditioned on the reaction rate.

those observed in non-reacting homogeneous isotropic turbulence and turbulent premixed flames. In particular, the scale-locality of the energy cascade and vortex stretching are retained with a peak of energy transfer found for a ratio S/L between 0.3 and 0.5 and a peak probability of perfect alignment between the α strain from scale L_s and the vorticity at scale L_ω for $\mathcal{L} \approx 4$. This suggests that the interaction of scales in the turbulence field of MILD combustion is relatively unaffected by the presence of heat release, despite the fact that it is volumetrically distributed. This can be explained by the relatively low heat release and low increase in temperature in MILD combustion compared to conventional combustion analysed in the previous studies of Kolla et al. [2014] and O'Brien et al. [2017].

Chapter 8

Conclusions and Future Work

In this work, a multiscale analysis of homogenous isotropic turbulence and premixed flames has been performed. Subsequently, the physics of turbulent non-premixed MILD combustion has been investigated. To this aim, DNS of MILD combustion with mixture fraction variations have been conducted. As MILD combustion involves the recirculation of exhaust gases with fuel and fresh oxidiser, a careful two-stage method has been developed to construct a mixture that includes mixture fraction variations with the presence of fresh, burnt and reacting gases. Furthermore, a specific combustion mechanism was developed to include the chemical kinetics of a chemiluminescent species, OH^* . This final chapter summarises the results presented in the previous chapters and suggests directions for future work.

8.1 Scales interactions in turbulence and premixed flames

The initial analysis, presented in chapter 3, focused on scales interaction in isotropic turbulence and premixed flames. In a first step, using the bandpass filtering method, the energy cascade was analysed and the assumption of scale-locality was assessed. It was shown that structures of a scale L mostly transfer their energy to slightly smaller structures of a scale $0.3L$. This supported the scale-locality of the energy cascade. The analysis of the vortex stretching also showed this scale-locality. Furthermore, similar results were obtained for all the turbulence fields studied which covered Re_λ from 37 to 1131. This indicated that the turbulence field in simulations with a low Reynolds number still exhibits the same interaction of scales as high Reynolds number turbulence. This result provided support for the DNS of MILD combustion conducted in the present

work and more generally for DNS of turbulent reacting flows as the Reynolds number in such simulations is generally limited.

In a second step, a similar analysis was conducted in turbulent premixed flames. It was first shown that the vortex stretching mechanism was not unduly affected by heat release rate as results similar to those for homogeneous isotropic turbulence were found. Furthermore, the flame-turbulence interaction was also analysed using the bandpass filtering method by decomposing the effects of each scales of eddies on the tangential strain-rate. It was observed that eddies larger than the laminar flame thickness imparted the most strain on the flame. This has wider modelling implications for turbulent premixed flames as this indicates that it may not be required to model the effects of these small scales turbulence on the flame.

8.2 Physical insights of MILD combustion

Chapter 4 analysed the inception of MILD combustion. In particular, the S-curve was assessed and an unconventional behaviour was observed with an increase in temperature with SDR for the inception of MILD combustion. This specific behaviour was attributed to the role played by intermediates and radicals. This emphasised the need to revisit the definition of MILD combustion to account for these effects.

Furthermore, in chapter 5, MILD combustion was observed to have highly convoluted reaction zones which thus yielded frequent interactions among them. This resulted in the apparent thickening of the reaction zones observed in MILD combustion. The analysis of the structure of the reaction zones in physical and mixture fraction spaces also highlighted the existence of ignition kernels evolving into propagating flames. Using the flame index, both non-premixed and premixed combustion modes were found in MILD combustion. The non-premixed behaviour observed was the result of opposing fluxes of fuel and oxidiser coming respectively from rich and lean mixtures. The use of conventional measurable species for the reaction zones identification was also investigated using DNS-deduced LIF signals. It was observed that OH was inadequate while HCO or $\text{OH} \times \text{CH}_2\text{O}$ were still well correlated with heat release rate. In addition, the chemiluminescent species OH^* was also found to be an adequate marker of heat release rate for MILD combustion.

Chapter 6 analysed the coexistence of ignition and propagating flames in MILD combustion using a balance of the various terms in the species transport equation. This showed the entanglement between ignition dominated and flame propagation regions. Furthermore, the autoignition was strongly influenced by mixture fraction as lean mixture were observed to be more likely to undergo autoignition in the early stage of the domain.

Propagating flames were subsequently developing further downstream. Ignition of rich mixture was also observed in the downstream. The interplay between autoignition and flame propagation was found to be strongly influenced by the typical lengthscale of the mixture fraction field ℓ_Z . Indeed, sequential autoignition was favoured by a small ℓ_Z while the evolution from ignition towards deflagration was more likely for larger ℓ_Z .

The energy cascade and the interactions of turbulent structures of various scales in MILD combustion was studied in chapter 7. In particular, in MILD combustion, the scale-locality of the energy cascade and the vortex stretching mechanism were observed to have similar features as in non-reacting turbulence. This suggested that the limited heat release rate in MILD combustion did not unduly affect the turbulence field and its dynamical features, despite the volumetrically distributed heat release.

8.3 Future work

The work and analysis presented in this thesis have provided a number of useful insights into the physics of MILD combustion. Nonetheless, there are still various aspects where additional analysis would be of interest. The specific future work recommended is as follows:

- Regarding the multiscale analysis of the energy cascade and vortex stretching mechanism, it may be of interest to also study its temporal aspect, such as the decay, and to analyse how the interactions of scales evolves in time.
- The analysis in turbulent premixed flames was done on a specific configuration, a flame propagating in homogeneous isotropic turbulence. Studying whether the results obtained in that configuration extend to more realistic ones would provide additional insights for the modelling of turbulent reacting flows.
- The previous multiscale analysis in MILD combustion has focused on the effect of heat release on the dynamics of turbulence. However, there is a two-way coupling between turbulence and reaction zones and it would thus be of interest to analyse how the reaction zones in MILD combustion are affected by the various scales of turbulence and in particular if there is a correlation between some specific scales of turbulence and the reaction zones.
- From an experimental point of view, it was shown that the identification of reaction zones could be particularly challenging in MILD combustion. It is thus of interest to assess the suitability of other markers of heat release rate such as those used in

Conclusions and Future Work

[Barlow et al., 2015; Gazi et al., 2013; Nikolaou & Swaminathan, 2014; Tanahashi et al., 2005]. Furthermore, a novel experimental method, which combines the Chemical Explosive Mode Analysis (CEMA) of Lu et al. [2010] and Raman/Rayleigh measurements, was proposed by Hartl et al. [2018] to delineate between premixed and non-premixed modes of combustion. Given the balance between these two modes found in this work, assessing this methodology for MILD combustion would be useful for future experimental works.

- As both autoignition and flame propagation were observed in MILD combustion, it is interesting from an experimental perspective to try to find an appropriate marker that can discriminate between the two phenomena. Some work in that direction has been proposed by Schulz et al. [2017] for a lifted methane-air flame and it would be interesting to assess whether the criterion proposed to distinguish between these remains valid for MILD combustion. Furthermore, Xu et al. [2018] has also suggested an alternative methodology to distinguish between these two modes using the CEMA methodology. It would thus be of interest to assess the adequacy of this method and compare it to the result obtained here using the \mathcal{B} marker. Furthermore, trying to quantify the amount of back-support in MILD combustion compared to conventional stratified flames could provide additional physical insights.
- From the physical understanding obtained here from the DNS of MILD combustion, a modelling framework for MILD combustion can be proposed. In particular, from the large inhomogeneities observed in the reacting mixture and the volumetrically distributed reaction zones, the Partially Stirred Reactor (PaSR) could be used as the basis for modelling. This model could be used in conjunction with a presumed PDF approach similar to the one proposed by Chen et al. [2017].

References

- (2013). International Energy Outlook 2013 (DOE/EIA-0484). Technical report, U.S. Energy Information Administration.
- Abtahizadeh, E., de Goey, L. P. H., & van Oijen, J. A. (2017). LES of Delft Jet-in-Hot Coflow burner to investigate the effect of preferential diffusion on autoignition of CH₄/H₂ flames. *Fuel*, 191:36–45.
- Abtahizadeh, E., Sepman, A. V., Hernández-Pérez, F., van Oijen, J. A., Mokhov, A. V., de Goey, L. P. H., & Levinsky, H. B. (2013). Numerical and experimental investigations on the influence of preheating and dilution on transition of laminar coflow diffusion flames to Mild combustion regime. *Combust. Flame*, 160(11):2359–2374.
- Aluie, H. & Eyink, G. L. (2009). Localness of energy cascade in hydrodynamic turbulence. II. Sharp spectral filter. *Phys. Fluids*, 21(11):1–16.
- Aminian, J., Galletti, C., Shahhosseini, S., & Tognotti, L. (2011). Key modeling issues in prediction of minor species in diluted-preheated combustion conditions. *Appl. Therm. Eng.*, 31(16):3287–3300.
- Aminian, J., Galletti, C., Shahhosseini, S., & Tognotti, L. (2012). Numerical investigation of a MILD combustion burner: Analysis of mixing field, chemical kinetics and turbulence-chemistry interaction. *Flow, Turbul. Combust.*, 88(4):597–623.
- Aminian, J., Galletti, C., & Tognotti, L. (2016). Extended EDC local extinction model accounting finite-rate chemistry for MILD combustion. *Fuel*, 165:123–133.
- Aoyama, T., Ishihara, T., Kaneda, Y., Yokokawa, M., Itakura, K., & Uno, A. (2005). Statistics of energy transfer in high-resolution direct numerical simulation of turbulence in a periodic box. *J. Phys. Soc. Japan*, 74(12):3202–3212.
- Ashurst, W. T., Kerstein, A. R., Kerr, R. M., & Gibson, C. H. (1987). Alignment of vorticity and scalar gradient with strain rate in simulated Navier-Stokes turbulence. *Phys. Fluids*, 30(8):2343.
- Barlow, R. S., Meares, S., Magnotti, G., Cutcher, H. C., & Masri, A. R. (2015). Local extinction and near-field structure in piloted turbulent CH₄/air jet flames with inhomogeneous inlets. *Combust. Flame*, 162(10):3516–3540.
- Batchelor, G. (1953). *The Theory of Homogeneous Turbulence*. Cambridge University Press.

References

- Batchelor, G. K. & Townsend, A. A. (1948). Decay of turbulence in the final period. *Proc. R. Soc. London A*, 194(1039).
- Bermejo-Moreno, I. & Pullin, D. I. (2008). On the non-local geometry of turbulence. *J. Fluid Mech.*, 603:101–135.
- Bermejo-Moreno, I., Pullin, D. I., & Horiuti, K. (2009). Geometry of enstrophy and dissipation, grid resolution effects and proximity issues in turbulence. *J. Fluid Mech.*, 620:121.
- Betchov, R. (1956). An inequality concerning the production of vorticity in isotropic turbulence. *J. Fluid Mech.*, 1(05):497.
- Bhaya, R., De, A., & Yadav, R. (2014). Large Eddy Simulation of Mild Combustion Using PDF-Based Turbulence-Chemistry Interaction Models. *Combust. Sci. Technol.*, 186(9):1138–1165.
- Bilger, R. W. (1979). Effects of Kinetics and Mixing in Turbulent Combustion. *Combust. Sci. Technol.*, 19(3-4):89–93.
- Bilger, R. W., Starner, S. H., & Kee, R. J. (1990). On Reduced Mechanisms for Methane-Air Combustion in Nonpremixed Flames. *Combust. Flame*, 80:135–149.
- Brasseur, J. G. & Wei, C. H. (1994). Interscale dynamics and local isotropy in high Reynolds number turbulence within triadic interactions. *Phys. Fluids*, 6(2):842–870.
- Bray, K. N. C. & Cant, R. S. (1991). Some applications of Kolmogorov’s turbulence research in the field of combustion. *Proc. R. Soc. London A*, 434(1890):217–240.
- Bray, K. N. C., Domingo, P., & Vervisch, L. (2005). Role of the progress variable in models for partially premixed turbulent combustion. *Combust. Flame*, 141(4):431–437.
- Briones, A. M., Aggarwal, S. K., & Katta, V. R. (2006). A numerical investigation of flame liftoff, stabilization, and blowout. *Phys. Fluids*, 18:043603.
- Burgers, J. M. (1948). A mathematical model illustrating the theory of turbulence. *Adv. Appl. Mech.*, 1:171–199.
- Candel, S. M. & Poinot, T. (1990). Flame Stretch and the Balance Equation for the Flame Area. *Combust. Sci. Technol.*, 70(1-3):1–15.
- Cant, R. S. (2013). SENG2 User Guide (CUED–THERMO–2012/04, 2nd edition). Technical report, University of Cambridge.
- Cardesa, J. I., Vela-Martín, A., Dong, S., & Jiménez, J. (2015). The temporal evolution of the energy flux across scales in homogeneous turbulence. *Phys. Fluids*, 27(11):111702.
- Cardesa, J. I., Vela-Martín, A., & Jiménez, J. (2017). The turbulent cascade in five dimensions. *Science*, 7933:1–6.
- Cavaliere, A. & de Joannon, M. (2004). Mild Combustion. *Prog. Energy Combust. Sci.*, 30(4):329–366.

- Chakraborty, N. (2007). Comparison of displacement speed statistics of turbulent premixed flames in the regimes representing combustion in corrugated flamelets and thin reaction zones. *Phys. Fluids*, 19(10).
- Chakraborty, N. & Cant, R. S. (2005). Effects of strain rate and curvature on surface density function transport in turbulent premixed flames in the thin reaction zones regime. *Phys. Fluids*, 17(6):065108.
- Chakraborty, N., Hartung, G., Katragadda, M., & Kaminski, C. F. (2011). Comparison of 2D and 3D density-weighted displacement speed statistics and implications for laser based measurements of flame displacement speed using direct numerical simulation data. *Combust. Flame*, 158(7):1372–1390.
- Chakraborty, N. & Klein, M. (2008). A priori direct numerical simulation assessment of algebraic flame surface density models for turbulent premixed flames in the context of large eddy simulation. *Phys. Fluids*, 20(8):085108.
- Chakraborty, N., Klein, M., & Cant, R. S. (2007). Stretch rate effects on displacement speed in turbulent premixed flame kernels in the thin reaction zones regime. *Proc. Combust. Inst.*, 31(1):1385–1392.
- Charlette, F., Meneveau, C., & Veynante, D. (2002). A power-law flame wrinkling model for LES of premixed turbulent combustion Part I: Non-Dynamic formulation and Initial Test. *Combust. Flame*, 131(02):159–180.
- Chen, Z., Reddy, V. M., Ruan, S., Doan, N. A. K., Roberts, W. L., & Swaminathan, N. (2017). Simulation of MILD combustion using Perfectly Stirred Reactor model. *Proc. Combust. Inst.*, 36:4279–4286.
- Chen, Z., Ruan, S., & Swaminathan, N. (2015). Simulation of turbulent lifted methane jet flames: Effects of air-dilution and transient flame propagation. *Combust. Flame*, 162(3):703–716.
- Christo, F. C. & Dally, B. B. (2004). Application of Transport PDF Approach for Modelling MILD Combustion. In *15th Australas. Fluid Mech. Conf.*, pages 1–4.
- Christo, F. C. & Dally, B. B. (2005). Modeling turbulent reacting jets issuing into a hot and diluted coflow. *Combust. Flame*, 142:117–129.
- Cocke, W. J. (1969). Turbulent hydrodynamic line stretching: consequences of isotropy. *Phys. Fluids*, 12(12):2488–2492.
- Coelho, P. J. & Peters, N. (2001). Numerical simulation of a mild combustion burner. *Combust. Flame*, 124(x):503–518.
- Colin, O., Ducros, F., Veynante, D., & Poinso, T. (2000). A thickened flame model for large eddy simulations of turbulent premixed combustion. *Phys. Fluids*, 12(2000):1843–1863.
- Correia Rodrigues, H. R., Tummers, M. J., van Veen, E. H., & Roekaerts, D. J. E. M. (2014). Spray flame structure in conventional and hot-diluted combustion regime. *Combust. Flame*, 162(162):759–773.

References

- Dally, B. B., Karpetis, A. N., & Barlow, R. S. (2002). Structure of turbulent non-premixed jet flames in a diluted hot coflow. *Proc. Combust. Inst.*, 29(x):1147–1154.
- Dally, B. B., Riesmeier, E., & Peters, N. (2004). Effect of fuel mixture on moderate and intense low oxygen dilution combustion. *Combust. Flame*, 137(4):418–431.
- Davidson, P. A. (2015). *Turbulence : an introduction for scientists and engineers*. Oxford University Press, Oxford, 2nd edition.
- Davidson, P. A., Morishita, K., & Kaneda, Y. (2008). On the generation and flux of enstrophy in isotropic turbulence. *J. Turbul.*, 9(October):1–26.
- De, A. & Dongre, A. (2015). Assessment of Turbulence-Chemistry Interaction Models in MILD Combustion Regime. *Flow, Turbul. Combust.*, 94:439–478.
- De, A., Dongre, A., & Yadav, R. (2013). Numerical investigation of Delft-Jet-In-Coflow (DJHC) burner using probability density function (PDF) transport modeling - GT2013-95390. In *ASME Turbo Expo 2013 Turbine Tech. Conf. Expo*.
- De, A., Oldenhof, E., Sathiah, P., & Roekaerts, D. J. E. M. (2011). Numerical simulation of Delft-Jet-in-Hot-Coflow (DJHC) flames using the eddy dissipation concept model for turbulence-chemistry interaction. *Flow, Turbul. Combust.*, 87(4):537–567.
- de Joannon, M., Cavaliere, A., Faravelli, T., Ranzi, E., Sabia, P., & Tregrossi, A. (2005). Analysis of process parameters for steady operations in methane mild combustion technology. *Proc. Combust. Inst.*, 30(2):2605–2612.
- de Joannon, M., Matarazzo, A., Sabia, P., & Cavaliere, A. (2007). Mild Combustion in Homogeneous Charge Diffusion Ignition (HCDI) regime. *Proc. Combust. Inst.*, 31(2):3409–3416.
- de Joannon, M., Sabia, P., Cozzolino, G., Sorrentino, G., & Cavaliere, a. (2012a). Pyrolytic and Oxidative Structures in Hot Oxidant Diluted Oxidant (HODO) MILD Combustion. *Combust. Sci. Technol.*, 184(7-8):1207–1218.
- de Joannon, M., Sabia, P., Sorrentino, G., & Cavaliere, a. (2009). Numerical study of mild combustion in hot diluted diffusion ignition (HDDI) regime. *Proc. Combust. Inst.*, 32(2):3147–3154.
- de Joannon, M., Sabia, P., Tregrossi, a., & Cavaliere, a. (2004). Dynamic Behavior of Methane Oxidation in Premixed Flow Reactor. *Combust. Sci. Technol.*, 176(5-6):769–783.
- de Joannon, M., Saponaro, A., & Cavaliere, A. (2000). Zero-dimensional analysis of diluted oxidation of methane in rich conditions. *Proc. Combust. Inst.*, 28(2):1639–1646.
- de Joannon, M., Sorrentino, G., & Cavaliere, A. (2012b). MILD combustion in diffusion-controlled regimes of Hot Diluted Fuel. *Combust. Flame*, 159(5):1832–1839.
- Domaradzki, J. A. & Carati, D. (2007). An analysis of the energy transfer and the locality of nonlinear interactions in turbulence. *Phys. Fluids*, 19:085112.

- Domaradzki, J. A., Liu, W., & Brachet, M. E. (1993). An analysis of subgrid-scale interactions in numerically simulated isotropic turbulence. *Phys. Fluids A Fluid Dyn.*, 5(7):1747.
- Donzis, D. A., Yeung, P. K., & Sreenivasan, K. R. (2008). Dissipation and enstrophy in isotropic turbulence: Resolution effects and scaling in direct numerical simulations. *Phys. Fluids*, 20(4):1–16.
- Dopazo, C., Cifuentes, L., Martin, J., & Jiménez, C. (2015). Strain rates normal to approaching iso-scalar surfaces in a turbulent premixed flame. *Combust. Flame*, 162(5):1729–1736.
- Dunn, M. J., Masri, A. R., Bilger, R. W., & Barlow, R. S. (2010). Finite rate chemistry effects in highly sheared turbulent premixed flames. *Flow, Turbul. Combust.*, 85(3-4):621–648.
- Duwig, C., Li, B., Li, Z. S., & Aldén, M. (2012). High resolution imaging of flameless and distributed turbulent combustion. *Combust. Flame*, 159(1):306–316.
- Echekki, T., Chen, J. H., & Gran, I. (1996). The mechanism of mutual annihilation of stoichiometric premixed methane-air flames. *26th Symp. Combust.*, pages 855–863.
- Elsinga, G. E. & Marusic, I. (2016). The anisotropic structure of turbulence and its energy spectrum. *Phys. Fluids*, 28(011701):1–8.
- Ern, A. & Giovangigli, V. (1994). *Multicomponent Transport Algorithms*. Springer-Verlag Berlin Heidelberg.
- Eswaran, V. & Pope, S. B. (1988a). An examination of forcing in direct numerical simulations of turbulence. *Comput. Fluids*, 16(3):257–278.
- Eswaran, V. & Pope, S. B. (1988b). Direct numerical simulations of the turbulent mixing of a passive scalar. *Phys. Fluids*, 31(3):506–520.
- Evans, M. J., Chinnici, A., Medwell, P. R., & Ye, J. (2017a). Ignition features of methane and ethylene fuel-blends in hot and diluted coflows. *Fuel*, 203:279–289.
- Evans, M. J., Medwell, P. R., & Tian, Z. F. (2015). Modeling Lifted Jet Flames in a Heated Coflow Using an Optimized Eddy Dissipation Concept Model. *Combust. Sci. Technol.*, 187(7):1093–1109.
- Evans, M. J., Medwell, P. R., Tian, Z. F., Ye, J., Frassoldati, A., & Cuoci, A. (2017b). Effects of oxidant stream composition on non-premixed laminar flames with heated and diluted coflows. *Combust. Flame*, 178:297–310.
- Evans, M. J., Medwell, P. R., Wu, H., Stagni, A., & Ihme, M. (2017c). Classification of Non-Premixed MILD and Autoignitive Flames. *Proc. Combust. Inst.*, 36:4297–4304.
- Eyink, G. L. & Aluie, H. (2009). Localness of energy cascade in hydrodynamic turbulence. I. smooth coarse graining. *Phys. Fluids*, 21(11):1–9.
- Farge, M. (1992). Wavelet Transforms And Their Applications To Turbulence. *Annu. Rev. Fluid Mech.*, 24(1):395–457.

References

- Frassoldati, A., Sharma, P., Cuoci, A., Faravelli, T., & Ranzi, E. (2010). Kinetic and fluid dynamics modeling of methane/hydrogen jet flames in diluted coflow. *Appl. Therm. Eng.*, 30(4):376–383.
- Frisch, U. (1995). *Turbulence : the legacy of A.N. Kolmogorov*. Cambridge University Press.
- Fujimori, T., Riechelmann, D., & Sato, J. (1998). Effect of liftoff on NO_x emission of turbulent jet flame in high-temperature coflowing air. *27th Symp. Combust.*, pages 1149–1155.
- Galletti, C., Parente, A., Derudi, M., Rota, R., & Tognotti, L. (2009). Numerical and experimental analysis of NO emissions from a lab-scale burner fed with hydrogen-enriched fuels and operating in MILD combustion. *Int. J. Hydrogen Energy*, 34(19):8339–8351.
- Galletti, C., Parente, A., & Tognotti, L. (2007). Numerical and experimental investigation of a mild combustion burner. *Combust. Flame*, 151(4):649–664.
- Gao, Y., Chakraborty, N., & Swaminathan, N. (2014). Algebraic Closure of Scalar Dissipation Rate for Large Eddy Simulations of Turbulent Premixed Combustion. *Combust. Sci. Technol.*, 186(10-11):1309–1337.
- Gazi, A., Vourliotakis, G., Skevis, G., & Founti, M. A. (2013). Assessment of chemical markers for heat-release rate correlations in laminar premixed flames. *Combust. Sci. Technol.*, 185(10):1482–1508.
- Göktolga, M. U., van Oijen, J. A., & de Goey, L. P. H. (2015). 3D DNS of MILD combustion: A detailed analysis of heat loss effects, preferential diffusion, and flame formation mechanisms. *Fuel*, 159:784–795.
- Göktolga, M. U., van Oijen, J. A., & de Goey, L. P. H. (2017). Modeling MILD combustion using a novel multistage FGM method. *Proc. Combust. Inst.*, 36:4269–4277.
- Goodwin, D. G., Moffat, H. K., & Speth, R. L. (2017). Cantera: An Object-oriented Software Toolkit for Chemical Kinetics, Thermodynamics, and Transport Processes.
- Gordon, R. L., Masri, a. R., Pope, S. B., & Goldin, G. M. (2007). A numerical study of auto-ignition in turbulent lifted flames issuing into a vitiated co-flow. *Combust. Theory Model.*, 11(3):351–376.
- Goto, S., Saito, Y., & Kawahara, G. (2017). Hierarchy of antiparallel vortex tubes in spatially periodic turbulence at high Reynolds numbers. *Phys. Rev. Fluids*, 2(6):064603.
- Hamlington, P. E., Poludnenko, A. Y., & Oran, E. S. (2011). Interactions between turbulence and flames in premixed reacting flows. *Phys. Fluids*, 23(12):125111.
- Hamlington, P. E., Schumacher, J., & Dahm, W. J. A. (2008a). Direct assessment of vorticity alignment with local and nonlocal strain rates in turbulent flows. *Phys. Fluids*, 20(11):1–5.

- Hamlington, P. E., Schumacher, J., & Dahm, W. J. A. (2008b). Local and Nonlocal Strain Rate Fields and Vorticity Alignment in Turbulent Flows. *Phys. Rev. E*, 77:026303.
- Hartl, S., Geyer, D., Dreizler, A., Magnotti, G., Barlow, R. S., & Hasse, C. (2018). Regime identification from Raman/Rayleigh line measurements in partially premixed flames. *Combust. Flame*, 189:126–141.
- Hawkes, E. R. & Cant, R. S. (2001). Implications of a flame surface density approach to large eddy simulation of premixed turbulent combustion. *Combust. Flame*, 126(01):1617–1629.
- Haworth, D. C. (2010). Progress in probability density function methods for turbulent reacting flows. *Prog. Energy Combust. Sci.*, 36(2):168–259.
- Heisenberg, W. (1948). Zur statistischen Theorie der Turbulenz. *Zeitschrift für Phys.*, 124:628–657.
- Hu, E., Li, X., Meng, X., Chen, Y., Cheng, Y., Xie, Y., & Huang, Z. (2015). Laminar flame speeds and ignition delay times of methane-air mixtures at elevated temperatures and pressures. *Fuel*, 158:1–10.
- Ihme, M. & See, Y. C. (2011). LES flamelet modeling of a three-stream MILD combustor: Analysis of flame sensitivity to scalar inflow conditions. *Proc. Combust. Inst.*, 33(1):1309–1317.
- Ihme, M., Zhang, J., He, G., & Dally, B. B. (2012). Large-eddy simulation of a jet-in-hot-coflow burner operating in the oxygen-diluted combustion regime. *Flow, Turbul. Combust.*, 89(3):449–464.
- Ishihara, T., Kaneda, Y., & Hunt, J. C. R. (2013). Thin Shear Layers in High Reynolds Number Turbulence—DNS Results. *Flow, Turbul. Combust.*, 91:895–929.
- Jiménez, J. (1992). Kinematic alignment effects in turbulent flows. *Phys. Fluids*, 4:652–654.
- Kathrotia, T., Riedel, U., Seipel, A., Moshhammer, K., & Brockhinke, A. (2012). Experimental and numerical study of chemiluminescent species in low-pressure flames. *Appl. Phys. B Lasers Opt.*, 107(3):571–584.
- Katsuki, M. & Hasegawa, T. (1998). The science and technology of combustion in highly preheated air. *27th Symp. Combust.*, 27:3135–3146.
- Kim, S. H., Huh, K. Y., & Dally, B. B. (2005). Conditional moment closure modeling of turbulent nonpremixed combustion in diluted hot coflow. *Proc. Combust. Inst.*, 30 I(1):751–757.
- Klimenko, A. Y. & Bilger, R. W. (1999). Conditional moment closure for turbulent combustion. *Prog. Energy Combust. Sci.*, 25(6):595–687.
- Knikker, R., Veynante, D., & Meneveau, C. (2004). A dynamic flame surface density model for large eddy simulation of turbulent premixed combustion. *Phys. Fluids*, 16(11):L91.

References

- Knudsen, E., Kolla, H., Hawkes, E. R., & Pitsch, H. (2013). LES of a premixed jet flame DNS using a strained flamelet model. *Combust. Flame*, 160(12):2911–2927.
- Kobayashi, H., Matsumoto, E., Fukushima, N., Tanahashi, M., & Miyauchi, T. (2011). Statistical properties of the local structure of homogeneous isotropic turbulence and turbulent channel flows. *J. Turbul.*, 12(11):1–16.
- Kolla, H., Hawkes, E. R., Kerstein, A. R., Swaminathan, N., & Chen, J. H. (2014). On velocity and reactive scalar spectra in turbulent premixed flames. *J. Fluid Mech.*, 754:456–487.
- Kolla, H. & Swaminathan, N. (2010). Strained flamelets for turbulent premixed flames, I: Formulation and planar flame results. *Combust. Flame*, 157(5):943–954.
- Kolmogorov, A. N. (1941). The local structure of turbulence in incompressible viscous fluid for very large Reynolds numbers. *Dokl. Akad. Nauk SSSR*, 30:299–303.
- Kulkarni, R., Bunkute, B., Biagioli, F., Duesing, M., & Polifke, W. (2014). Large Eddy Simulation of ALSTOM’s Reheat Combustor using Tabulated Chemistry and Stochastic-Fields Combustion Model - GT2014-26053. In *ASME Turbo Expo 2014 Turbine Tech. Conf. Expo*.
- Kulkarni, R. & Polifke, W. (2013). LES of Delft-Jet-In-Hot-Coflow (DJHC) with tabulated chemistry and stochastic fields combustion model. *Fuel Process. Technol.*, 107:138–146.
- Labahn, J. W. & Devaud, C. B. (2015). Large Eddy Simulations (LES) including Conditional Source-term Estimation (CSE) applied to two Delft-Jet-in-Hot-Coflow (DJHC) flames. *Combust. Flame*, 164:68–84.
- Labahn, J. W. & Devaud, C. B. (2016). Species and temperature predictions in a semi-industrial MILD furnace using a non-adiabatic conditional source-term estimation formulation. *Combust. Theory Model.*, 21(3):466–486.
- Labahn, J. W., Dovizio, D., & Devaud, C. B. (2015). Numerical simulation of the Delft-Jet-in-Hot-Coflow (DJHC) flame using Conditional Source-term Estimation. *Proc. Combust. Inst.*, 35(3):3547–3555.
- Lee, J., Jeon, S., & Kim, Y. (2015). Multi-environment probability density function approach for turbulent CH₄/H₂ flames under the MILD combustion condition. *Combust. Flame*, 162(4):1464–1476.
- Lesieur, M. (2008). *Turbulence in Fluids*. Springer Netherlands, 4th edition.
- Leung, T., Swaminathan, N., & Davidson, P. A. (2012). Geometry and interaction of structures in homogeneous isotropic turbulence. *J. Fluid Mech.*, 710:453–481.
- Li, Z., Cuoci, A., Sadiki, A., & Parente, A. (2017). Comprehensive numerical study of the Adelaide Jet in Hot-Coflow burner by means of RANS and detailed chemistry. *Energy*, 139:555–570.

- Lindemann, F. A. (1922). Discussion on "The radiation theory of chemical action". *Trans. Faraday Soc.*, 17:598–606.
- Lipatnikov, A. N., Nishiki, S., & Hasegawa, T. (2014). A direct numerical simulation study of vorticity transformation in weakly turbulent premixed flames. *Phys. Fluids*, 26(10):105104.
- Lozano-Durán, A., Holzner, M., & Jiménez, J. (2016). Multiscale analysis of the topological invariants in the logarithmic region of turbulent channels at a friction Reynolds number of 932. *J. Fluid Mech.*, 803:356–394.
- Lu, T. F., Yoo, C. S., Chen, J. H., & Law, C. K. (2010). Three-dimensional direct numerical simulation of a turbulent lifted hydrogen jet flame in heated coflow: a chemical explosive mode analysis. *J. Fluid Mech.*, 652:45–64.
- Lumley, J. L. (1992). Some comments on turbulence. *Phys. Fluids A Fluid Dyn.*, 4(2):203–211.
- Luong, M. B., Yu, G. H., Chung, S. H., & Yoo, C. S. (2017). Ignition of a lean PRF/air mixture under RCCI/SCCI conditions: Chemical aspects. *Proc. Combust. Inst.*, 36(3):3587–3596.
- Lupant, D. & Lybaert, P. (2015). Assessment of the EDC combustion model in MILD conditions with in-furnace experimental data. *Appl. Therm. Eng.*, 75:93–102.
- Ma, L. & Roekaerts, D. J. E. M. (2016a). Modeling of spray jet flame under MILD condition with non-adiabatic FGM and a new conditional droplet injection model. *Combust. Flame*, 165:402–423.
- Ma, L. & Roekaerts, D. J. E. M. (2016b). Structure of spray in hot-diluted coflow flames under different coflow conditions: A numerical study. *Combust. Flame*, 172:20–37.
- Magnussen, B. F. (1981). On the structure of turbulence and a generalized eddy dissipation concept for chemical reaction in turbulent flow. In *19th AIAA Meet.*, pages 1–6.
- Mardani, A. (2017). Optimization of the Eddy Dissipation Concept (EDC) model for turbulence-chemistry interactions under hot diluted combustion of CH₄/H₂. *Fuel*, 191:114–129.
- Mardani, A., Tabejamaat, S., & Hassanpour, S. (2013). Numerical study of CO and CO₂ formation in CH₄/H₂ blended flame under MILD condition. *Combust. Flame*, 160(9):1636–1649.
- Masri, A. R. (2015). Partial premixing and stratification in turbulent flames. *Proc. Combust. Inst.*, 35(2):1115–1136.
- Mecke, K. R., Buchert, T., & Wagner, H. (1994). Robust morphological measures for large-scales structures in the universe. *Astron. Astrophys.*, 288:697–704.
- Medwell, P. R., Kalt, P. A. M., & Dally, B. B. (2007). Simultaneous imaging of OH, formaldehyde, and temperature of turbulent nonpremixed jet flames in a heated and diluted coflow. *Combust. Flame*, 148(1-2):48–61.

References

- Medwell, P. R., Kalt, P. A. M., & Dally, B. B. (2008). Imaging of diluted turbulent ethylene flames stabilized on a Jet in Hot Coflow (JHC) burner. *Combust. Flame*, 152(1-2):100–113.
- Medwell, P. R., Kalt, P. A. M., & Dally, B. B. (2009). Reaction Zone Weakening Effects under Hot and Diluted Oxidant Stream Conditions. *Combust. Sci. Technol.*, 181(7):937–953.
- Meneveau, C. & Poinso, T. (1991). Stretching and quenching of flamelets in premixed turbulent combustion. *Combust. Flame*, 86(4):311–332.
- Minamoto, Y. (2013). *Physical Aspects and Modelling of Turbulent MILD Combustion*. PhD thesis, University of Cambridge.
- Minamoto, Y., Dunstan, T. D., Swaminathan, N., & Cant, R. S. (2013). DNS of EGR-type turbulent flame in MILD condition. *Proc. Combust. Inst.*, 34(2):3231–3238.
- Minamoto, Y. & Swaminathan, N. (2014a). Modelling paradigms for MILD combustion. *Int. J. Adv. Eng. Sci. Appl. Math.*, 6(1-2):65–75.
- Minamoto, Y. & Swaminathan, N. (2014b). Scalar gradient behaviour in MILD combustion. *Combust. Flame*, 161(4):1063–1075.
- Minamoto, Y. & Swaminathan, N. (2015). Subgrid scale modelling for MILD combustion. *Proc. Combust. Inst.*, 35(3):3529–3536.
- Minamoto, Y., Swaminathan, N., Cant, R. S., & Leung, T. (2014a). Morphological and statistical features of reaction zones in MILD and premixed combustion. *Combust. Flame*, 161(11):2801–2814.
- Minamoto, Y., Swaminathan, N., Cant, R. S., & Leung, T. (2014b). Reaction Zones and Their Structure in MILD Combustion. *Combust. Sci. Technol.*, 186(8):1075–1096.
- Moffatt, H. K., Kida, S., & Ohkitani, K. (1994). Stretched vortices - the sinews of turbulence; large-Reynolds-number asymptotics. *J. Fluid Mech.*, 259:241–264.
- Moisy, F. & Jiménez, J. (2004). Geometry and clustering of intense structures in isotropic turbulence. *J. Fluid Mech.*, 513:111–133.
- Mullin, J. A. & Dahm, W. J. A. (2006). Dual-plane stereo particle image velocimetry measurements of velocity gradient tensor fields in turbulent shear flow. II. Experimental results. *Phys. Fluids*, 18:035102s.
- Nada, Y., Tanahashi, M., & Miyauchi, T. (2004). Effect of turbulence characteristics on local flame structure of H₂-air premixed flames. *J. Turbul.*, 5:37–41.
- Najm, H. N., Knio, O. M., Paul, P. H., & Wyckoff, P. (1998a). A Study of Flame Observables in Premixed Methane - Air Flames. *Combust. Sci. Technol.*, 140(1-6):369–403.
- Najm, H. N., Paul, P. H., Mueller, C. J., & Wyckoff, P. S. (1998b). On the Adequacy of Certain Experimental Observables as Measurements of Flame Burning Rate. *Combust. Flame*, 113(3):312–332.

- Nemitallah, M. A., Rashwan, S. S., Mansir, I. B., Abdelhafez, A. A., & Habib, M. A. M. (2018). Review of novel combustion techniques for clean power production in gas turbines. *Energy & Fuels*, 32:979–1004.
- Nikolaou, Z. M. & Swaminathan, N. (2014). Heat release rate markers for premixed combustion. *Combust. Flame*, 161(12):3073–3084.
- Oberlack, M., Arlitt, R., & Peters, N. (2000). On stochastic Damkohler number variations in a homogeneous flow reactor. *Combust. Theory Model.*, 4(4):495–509.
- O’Brien, J., Towery, C. A. Z., Hamlington, P. E., Ihme, M., Poludnenko, A. Y., & Urzay, J. (2017). The cross-scale physical-space transfer of kinetic energy in turbulent premixed flames. *Proc. Combust. Inst.*, 36(2):1967–1975.
- Obukhov, A. M. (1941). On the distribution of energy in the spectrum of turbulent flow. *Dokl. Akad. Nauk SSSR*, 32(1):22–24.
- Oldenhof, E., Tummers, M. J., van Veen, E. H., & Roekaerts, D. J. E. M. (2010). Ignition kernel formation and lift-off behaviour of jet-in-hot-coflow flames. *Combust. Flame*, 157(6):1167–1178.
- Oldenhof, E., Tummers, M. J., van Veen, E. H., & Roekaerts, D. J. E. M. (2011). Role of entrainment in the stabilisation of jet-in-hot-coflow flames. *Combust. Flame*, 158(8):1553–1563.
- Oldenhof, E., Tummers, M. J., van Veen, E. H., & Roekaerts, D. J. E. M. (2013). Conditional flow field statistics of jet-in-hot-coflow flames. *Combust. Flame*, 160(8):1428–1440.
- Ozdemir, I. B. & Peters, N. (2001). Characteristics of the reaction zone in a combustor operating at mild combustion. *Exp. Fluids*, 30(6):683–695.
- Panoutsos, C. S., Hardalupas, Y., & Taylor, A. M. K. P. (2009). Numerical evaluation of equivalence ratio measurement using OH* and CH* chemiluminescence in premixed and non-premixed methane-air flames. *Combust. Flame*, 156(2):273–291.
- Pao, Y.-H. (1965). Structure of Turbulent Velocity and Scalar Fields at Large Wavenumbers. *Phys. Fluids*, 8(6):1063–1075.
- Parente, A., Malik, M. R., Contino, F., Cuoci, A., & Dally, B. B. (2016). Extension of the Eddy Dissipation Concept for turbulence/chemistry interactions to MILD combustion. *Fuel*, 163:98–111.
- Parente, A., Sutherland, J. C., Dally, B. B., Tognotti, L., & Smith, P. J. (2011). Investigation of the MILD combustion regime via Principal Component Analysis. *Proc. Combust. Inst.*, 33(2):3333–3341.
- Paul, P. H. & Najm, H. N. (1998). Planar laser-induced fluorescence imaging of flame heat release rate. *27th Symp. Combust.*, 27(1):43–50.
- Peters, N. (2000). *Turbulent Combustion*. Cambridge University Press, Cambridge.

References

- Peters, N. (2009). Multiscale combustion and turbulence. *Proc. Combust. Inst.*, 32(1):1–25.
- Pitsch, H. (2006). Large-Eddy Simulation of Turbulent Combustion. *Annu. Rev. Fluid Mech.*, 38(1):453–482.
- Pitsch, H. & Fedotov, S. (2001). Investigation of scalar dissipation rate fluctuations in non-premixed turbulent combustion using a stochastic approach. *Combust. Theory Model.*, 5(1):41–57.
- Plessing, T., Peters, N., & Wüning, J. G. (1998). Laseroptical investigation of highly preheated combustion with strong exhaust gas recirculation. *27th Symp. Combust.*, 27:3197–3204.
- Poinsot, T. (1992). Boundary conditions for direct simulations of compressible viscous flows. *J. Comput. Phys.*, 101:104–129.
- Poinsot, T. & Veynante, D. (2011). *Theoretical and Numerical Combustion*. Aquaprint, Bordeaux, 3rd edition.
- Poinsot, T., Veynante, D., & Candel, S. M. (1991). Quenching processes and premixed turbulent combustion diagrams. *J. Fluid Mech.*, 228:561–606.
- ReactionDesign (2015). CHEMKIN-PRO 15141.
- Rebola, A., Coelho, P. J., & Costa, M. (2013). Assessment of the Performance of Several Turbulence and Combustion Models in the Numerical Simulation of a Flameless Combustor. *Combust. Sci. Technol.*, 185(4):600–626.
- Reddy, V. M., Katoch, A., Roberts, W. L., & Kumar, S. (2015). Experimental and numerical analysis for high intensity swirl based ultra-low emission flameless combustor operating with liquid fuels. *Proc. Combust. Inst.*, 35(3):3581–3589.
- Richardson, E. S., Granet, V. E., Eyssartier, A., & Chen, J. H. (2010). Effects of equivalence ratio variation on lean, stratified methane-air laminar counterflow flames. *Combust. Theory Model.*, 14(6):775–792.
- Richardson, L. F. (1922). *Weather Prediction by Numerical Process*. Cambridge University Press, Cambridge.
- Roberts, W. L., Driscoll, J. F., Drake, M., & Goss, L. (1993). Images of the quenching of a flame by a vortex—To quantify regimes of turbulent combustion. *Combust. Flame*, 94(1-2):58–69.
- Rogallo, R. S. (1981). Numerical Experiments in Homogeneous Turbulence - NASA-TM-81315. Technical report.
- Ruan, S., Swaminathan, N., & Darbyshire, O. R. (2014a). Modelling of turbulent lifted jet flames using flamelets: a priori assessment and a posteriori validation. *Combust. Theory Model.*, 18(2):295–329.
- Ruan, S., Swaminathan, N., & Mizobuchi, Y. (2014b). Investigation of Flame Stretch in Turbulent Lifted Jet Flame. *Combust. Sci. Technol.*, 186(3):243–272.

- Ruetsch, G. R. & Maxey, M. R. (1991). Small-scale features of vorticity and passive scalar fields in homogeneous isotropic turbulence. *Phys. Fluids A*, 3(6):1587–1597.
- Rutland, C. J. & Cant, R. S. (1994). Turbulent Transport in Premixed Flames N95-21040. In *Proc. Summer Program. Cent. Turbul. Res.*, pages 75–94.
- Sabia, P., de Joannon, M., Fierro, S., Tregrossi, a., & Cavaliere, a. (2007). Hydrogen-enriched methane Mild Combustion in a well stirred reactor. *Exp. Therm. Fluid Sci.*, 31:469–475.
- Sabia, P., de Joannon, M., Lubrano Lavadera, M., Giudicianni, P., & Ragucci, R. (2014). Autoignition delay times of propane mixtures under MILD conditions at atmospheric pressure. *Combust. Flame*, 161(12):3022–3030.
- Sabia, P., de Joannon, M., Picarelli, A., & Ragucci, R. (2013). Methane auto-ignition delay times and oxidation regimes in MILD combustion at atmospheric pressure. *Combust. Flame*, 160(1):47–55.
- Sabia, P., Lubrano Lavadera, M., Giudicianni, P., Sorrentino, G., Ragucci, R., & de Joannon, M. (2015a). CO₂ and H₂O effect on propane auto-ignition delay times under mild combustion operative conditions. *Combust. Flame*, 162(3):533–543.
- Sabia, P., Lubrano Lavadera, M., Sorrentino, G., Giudicianni, P., Ragucci, R., & de Joannon, M. (2016). H₂O and CO₂ Dilution in MILD Combustion of Simple Hydrocarbons. *Flow, Turbul. Combust.*, 96(2):433–448.
- Sabia, P., Sorrentino, G., Chinnici, A., Cavaliere, A., & Ragucci, R. (2015b). Dynamic Behaviors in Methane MILD and Oxy-Fuel Combustion. Chemical Effect of CO₂. *Energy & Fuels*, 29(3):1978–1986.
- Sahni, V., Sathyaprakash, B. S., & Shandarin, S. F. (1998). Shapefinders: A New Shape Diagnostic for Large-Scale Structure. *Astrophys. J.*, 495(1):L5–L8.
- Schulz, O., Jaravel, T., Poinso, T., Cuenot, B., & Noiray, N. (2017). A criterion to distinguish autoignition and propagation applied to a lifted methane-air jet flame. *Proc. Combust. Inst.*, 36:1637–1644.
- Shabanian, S. R., Medwell, P. R., Rahimi, M., Frassoldati, A., & Cuoci, A. (2013). Kinetic and fluid dynamic modeling of ethylene jet flames in diluted and heated oxidant stream combustion conditions. *Appl. Therm. Eng.*, 52(2):538–554.
- Sharma, S., Pingulkar, H., Chowdhury, A., & Kumar, S. (2018). A new emission reduction approach in MILD combustion through asymmetric fuel injection. *Combust. Flame*, 193:61–75.
- She, Z.-S., Jackson, E., & Orszag, S. A. (1991). Structure and dynamics of homogeneous turbulence: models and simulations. *Proc. R. Soc. London A*, 434:101–124.
- Sheth, J. V. & Sahni, V. (2005). Exploring the geometry, topology and morphology of large scale structure using Minkowski functionals. *Curr. Sci.*, 88:1101–1116.

References

- Sidey, J. A. M. & Mastorakos, E. (2015a). Simulations of laminar non-premixed flames of methane with hot combustion products as oxidiser. *Combust. Flame*, 163:1–11.
- Sidey, J. A. M. & Mastorakos, E. (2015b). Visualization of MILD combustion from jets in cross-flow. *Proc. Combust. Inst.*, 35(3):3537–3545.
- Sidey, J. A. M. & Mastorakos, E. (2016). Simulations of laminar non-premixed flames of kerosene with hot combustion products as oxidiser. *Combust. Theory Model.*, 163:1–16.
- Sidey, J. A. M., Mastorakos, E., & Gordon, R. L. (2014). Simulations of Autoignition and Laminar Premixed Flames in Methane/Air Mixtures Diluted with Hot Products. *Combust. Sci. Technol.*, 186(4-5):453–465.
- Smooke, M. D. & Giovangigli, V. (1991). Formulation of the premixed and nonpremixed test problems. In Smooke, M. D., editor, *Reduced Kinetic Mechanisms and Asymptotic Approximations for Methane-Air Flames*, volume 384 of *Lecture Notes in Physics*, pages 1–28. Springer Berlin Heidelberg, Berlin/Heidelberg.
- Snyder, A. D., Robertson, J., Zanders, D. L., & Skinner, G. B. (1965). Shock tube studies of fuel-air ignition characteristics - AD470239. Technical report, Air Force aero propulsion laboratory research and technology division.
- Sorrentino, G., Sabia, P., Bozza, P., Ragucci, R., & de Joannon, M. (2017). Impact of external operating parameters on the performance of a cyclonic burner with high level of internal recirculation under MILD combustion conditions. *Energy*, 137:1167–1174.
- Sorrentino, G., Sabia, P., de Joannon, M., Cavaliere, A., & Ragucci, R. (2016). The Effect of Diluent on the Sustainability of MILD Combustion in a Cyclonic Burner. *Flow, Turbul. Combust.*, 96(2):449–468.
- Sorrentino, G., Scarpa, D., & Cavaliere, a. (2013). Transient inception of MILD combustion in hot diluted diffusion ignition (HDDI) regime: A numerical study. *Proc. Combust. Inst.*, 34(2):3239–3247.
- Steinberg, A. M. & Driscoll, J. F. (2009). Straining and wrinkling processes during turbulence-premixed flame interaction measured using temporally-resolved diagnostics. *Combust. Flame*, 156(12):2285–2306.
- Steinberg, A. M. & Driscoll, J. F. (2010). Stretch-rate relationships for turbulent premixed combustion LES subgrid models measured using temporally resolved diagnostics. *Combust. Flame*, 157(7):1422–1435.
- Su, L. K. & Dahm, W. J. A. (1996). Scalar imaging velocimetry measurements of the velocity gradient tensor field in turbulent flows. I. Assessment of errors. *Phys. Fluids*, 8(7):1883.
- Swaminathan, N. & Grout, R. W. (2006). Interaction of turbulence and scalar fields in premixed flames. *Phys. Fluids*, 18(4):045102.
- Tanahashi, M., Murakami, S., Choi, G.-M., Fukuchi, Y., & Miyauchi, T. (2005). Simultaneous CH–OH PLIF and stereoscopic PIV measurements of turbulent premixed flames. *Proc. Combust. Inst.*, 30(1):1665–1672.

- Tanahashi, M., Myauchi, M., & Ikeda, J. (1999). Identification of coherent fine scale structure. In *Simulation and Identification of Organized Structures in Flows, Fluid Mechanics and its applications.*, pages 131–140.
- Taylor, G. I. (1938). Production and Dissipation of Vorticity in a Turbulent Fluid. *Proc. R. Soc. London A*, 164(916):15–23.
- Taylor, G. I. & Green, A. E. (1937). Mechanism of the Production of Small Eddies from Large Ones. *Proc. R. Soc. London A*, 158(895):499–521.
- Tordella, D., Di Savino, S., & Sitzia, L. (2014). Large fluctuations of the nonlinearities in isotropic turbulence. Anisotropic filtering analysis. *Phys. D Nonlinear Phenom.*, 284:16–26.
- Treurniet, T. C., Nieuwstadt, F. T. M., & Boersma, B. J. (2006). Direct numerical simulation of homogeneous turbulence in combination with premixed combustion at low Mach number modelled by the G-equation. *J. Fluid Mech.*, 565:25–62.
- Tsinober, A. (2009). *An Informal Conceptual Introduction to Turbulence*. Springer Netherlands.
- Vagelopoulos, C. M. & Egolfopoulos, F. N. (1998). Direct experimental determination of laminar flame speeds. *27th Symp. Combust.*, 27:513–519.
- Vagelopoulos, C. M., Egolfopoulos, F. N., & Law, C. K. (1994). Further considerations on the determination of laminar flame speeds with the counterflow twin-flame technique. *25th Symp. Combust.*, 25(1):1341–1347.
- van Oijen, J. A. (2013). Direct numerical simulation of autoigniting mixing layers in MILD combustion. *Proc. Combust. Inst.*, 34(1):1163–1171.
- Veríssimo, A. S., Rocha, A. M. A., & Costa, M. (2011). Operational, combustion, and emission characteristics of a small-scale combustor. *Energy & Fuels*, 25(6):2469–2480.
- Veynante, D. & Vervisch, L. (2002). Turbulent combustion modeling. *Prog. Energy Combust. Sci.*, 28:193–266.
- Vincent, A. & Meneguzzi, M. (1994). The dynamics of vorticity tubes in homogeneous turbulence. *J. Fluid Mech.*, 258:245.
- Wang, H., Hawkes, E. R., & Chen, J. H. (2016). Turbulence-flame interactions in DNS of a laboratory high Karlovitz premixed turbulent jet flame. *Phys. Fluids*, 28:095107.
- Wang, H., Hawkes, E. R., Chen, J. H., Zhou, B., Li, Z., & Aldén, M. (2017). Direct numerical simulations of a high Karlovitz number laboratory premixed jet flame – an analysis of flame stretch and flame thickening. *J. Fluid Mech.*, 815:511–536.
- Wei, L., Elsinga, G. E., Brethouwer, G., Schlatter, P., & Johansson, A. V. (2014). Universality and scaling phenomenology of small-scale turbulence in wall-bounded flows. *Phys. Fluids*, 26(035107):1–13.
- Woelk, G. & Wüning, J. (1993). Controlled combustion by flameless oxidation. In *Joint Meeting of the British and German Sections of the Combustion Institute*.

References

- Wünning, J. A. (1991). Flameless oxidation with highly preheated air. *Chemie Ing. Tech.*, 63:1243–1245.
- Wünning, J. A. & Wünning, J. G. (1997). Flameless oxidation to reduce thermal no-formation. *Prog. Energy Combust. Sci.*, 23(1):81–94.
- Xu, C., Park, J. W., Yoo, C. S., Chen, J. H., & Lu, T. (2018). Identification of premixed flame propagation modes using chemical explosive mode analysis. *Proc. Combust. Inst.*
- Yamashita, H., Shimada, M., & Takeno, T. (1996). A numerical study on flame stability at the transition point of jet diffusion flames. *26th Symp. Combust.*, 26(1):27–34.
- Yenerdag, B., Fukushima, N., Shimura, M., Tanahashi, M., & Miyauchi, T. (2015). Turbulence-flame interaction and fractal characteristics of H₂-air premixed flame under pressure rising condition. *Proc. Combust. Inst.*, 35(2):1277–1285.
- Yeung, P. K. & Brasseur, J. G. (1991). The response of isotropic turbulence to isotropic and anisotropic forcing at the large scales. *Phys. Fluids A Fluid Dyn.*, 3(5):884–897.
- Yeung, P. K. & Pope, S. B. (1993). Differential diffusion of passive scalars in isotropic turbulence. *Phys. Fluids A*, 5(10):2467–2478.
- Yoshimatsu, K., Anayama, K., & Kaneda, Y. (2015). Influence of vortex dynamics and structure on turbulence statistics at large scales. *Phys. Fluids*, 27(5):055106.
- Zhou, B., Costa, M., Li, Z., Aldén, M., & Bai, X.-S. (2015). Characterization of the reaction zone structures in a laboratory combustor using optical diagnostics: From flame to flameless combustion. *Proc. Combust. Inst.*, 36(3):4305–4312.

Appendix A

Initial Turbulent Kinetic Energy and Scalar Spectrums

The present appendix provides additional details on the initial spectrums for the turbulent kinetic energy and on the methodology to construct the initial mixture fraction, \hat{Z} , and progress variable, \hat{c}_Y , fields described in section 2.2.2.

A.1 Turbulent energy spectrum

The Batchelor-Townsend spectrum [Batchelor & Townsend, 1948] is used to initialize the turbulence field as described in [Cant, 2013]. It is given by:

$$E(k) = c_0 \frac{k^4}{k_0^5} \exp \left(-2 \left(\frac{k}{k_0} \right)^2 \right) \quad (\text{A.1})$$

where c_0 and k_0 are the two parameters controlling respectively the total kinetic energy and the wavenumber of the maximum energy point in the spectrum. k is the wavenumber magnitude in Fourier space. From this spectrum, the relevant turbulence quantities can be expressed as:

- Turbulent kinetic energy

$$K = \frac{3}{32} \sqrt{\frac{\pi}{2}} c_0 \quad (\text{A.2})$$

- Turbulence energy dissipation rate

$$\epsilon = \frac{15}{16} \sqrt{\frac{\pi}{2}} \pi^2 \nu c_0 k_0^2 \quad (\text{A.3})$$

- Longitudinal integral lengthscale

$$L_p = \frac{1}{\sqrt{2\pi}k_0} \quad (\text{A.4})$$

- Taylor microscale

$$\lambda^2 = \frac{1}{2\pi^2 k_0^2} \quad (\text{A.5})$$

- Kolmogorov lengthscale

$$\eta = \left(\frac{\nu^2}{\frac{15}{16}\sqrt{\frac{\pi}{2}}\pi^2 c_0 k_0^2} \right)^{1/4} \quad (\text{A.6})$$

In this thesis work, the following values were chosen for the parameters: $c_0 = 16000$ and $k_0 = 1.6$. Additional theoretical background can be found in [Batchelor, 1953].

A.2 Scalar spectrum

The methodology developed by Eswaran & Pope [1988b] is used in this thesis to initialize the scalar fields. This method allows to construct a scalar field, ϕ , with a pdf which conforms closely to a double delta function while having smooth variations. A brief summary of this method is provided hereunder.

1. First, the Fourier amplitudes of the scalar field, $\Phi(\mathbf{k})$, are assigned random values so that the scalar-energy spectrum has a specified function $f_\phi(k)$:

$$\Phi(\mathbf{k}) = \left(\frac{f_\phi}{4\pi k^2} \right)^{1/2} \exp(2\pi i \theta(\mathbf{k})) \quad (\text{A.7})$$

where $\theta(\mathbf{k})$ is a uniformly distributed random number between 0 and 1, \mathbf{k} is the wave number and $k = |\mathbf{k}|$. This is performed for each node of the numerical domain.

2. This scalar field is then inverse-Fourier transformed into physical space. In physical space, the scalar value at each node is set to +1 if it is larger than the specified mean $\langle \phi \rangle$, and -1 if it is smaller. This allows to obtain the double-delta distribution.
3. To smooth the previous field, the scalar field is retransformed into spectral space and the Fourier amplitudes of the scalar are multiplied by a filter function, $F(\mathbf{k})$, defined as:

$$F(\mathbf{k}) = \begin{cases} 1, & \text{if } k \leq k_c \\ (k/k_c)^{-2}, & \text{if } k > k_c \end{cases} \quad (\text{A.8})$$

where k_c is a specified cutoff wavenumber.

4. Finally, this scalar field is inverse-Fourier transformed again to return into physical space.

In this methodology, the function $f_\phi(\mathbf{k})$ is chosen to be a "top-hat" function of width k_0 centered on a selected integer wavenumber k_s :

$$f_\phi(k) = \begin{cases} 1, & \text{if } k_s - k_0/2 \leq k \leq k_s + k_0/2 \\ 0, & \text{otherwise} \end{cases} \quad (\text{A.9})$$

Here, the parameter k_s/k_0 essentially determines the integral lengthscale of the scalar field with larger values of k_s/k_0 yielding smaller lengthscales. The second parameter k_c/k_s controls the amount of high wave number scalar energy with a higher value of k_c allowing for more high wave number energy.

The parameters used for the initial $\widehat{c_Y}$ and \widehat{Z} fields are provided respectively in Tables A.1 and A.2. The parameters of $\widehat{c_Y}$ were chosen to be the same as those in the previous work by [Minamoto \[2013\]](#). Those parameters allow for enough variations of the progress variable field given the limited size of the numerical domain. The parameters for \widehat{Z} were chosen using similar considerations while ensuring that typical lengthscales for \widehat{Z} are larger or equal to those of $\widehat{c_Y}$ as explained in section 2.2.2.

Table A.1 Parameters used to construct the initial progress variable field, $\widehat{c_Y}$.

Case	k_0	k_s/k_0	k_c/k_s	$\langle c \rangle$
AZ1	1.5	2.2	0.8	0.3
AZ2	1.5	2.2	0.8	0.3
BZ1	1.5	2.2	0.8	0.3

Table A.2 Parameters used to construct the initial mixture fraction field, \widehat{Z} .

Case	k_0	k_s/k_0	k_c/k_s	$\langle Z \rangle$
AZ1	1.5	1.2	0.392	0.008
AZ2	1.5	2.2	0.4	0.008
BZ1	1.5	1.2	0.392	0.004667

Appendix B

Description of the Chemical Mechanism

Table B.1 and B.2 summarise the Lewis numbers and reaction steps of the proposed modified methane-air skeletal combustion mechanism using reactions steps from Bilger et al. [1990], Smooke & Giovangigli [1991] and Kathrotia et al. [2012]. The Lewis number of each species have been computed using a methodology similar to the one described by Smooke & Giovangigli [1991]. The Lewis numbers for each species are computed using

$$Le_{\alpha} = \frac{\lambda_{th}}{\rho D_{\alpha} c_p} \quad (\text{B.1})$$

where λ_{th} is the mixture thermal conductivity, c_p the mass specific heat capacity of the mixture, ρ the mixture density and D_{α} the binary diffusion coefficient of the species α . The Lewis numbers in function of temperature are presented in Fig. B.1 for each species where it is computed for a 1D laminar premixed CH₄/air stoichiometric flame at $T_r = 298K$ and 1 atm, using CHEMKIN-PRO.

Table B.1 Lewis numbers used for each species in the MS-58 mechanism

	Species	Le
1	CH ₄	0.994
2	O ₂	1.110
3	H ₂ O	0.856
4	CO ₂	1.392
5	H	0.179
6	O	0.708
7	OH	0.722
8	OH*	0.722
9	HO ₂	1.100
10	H ₂	0.298
11	CO	1.108
12	H ₂ O ₂	1.107
13	HCO	1.303
14	CH ₃ O	1.339
15	CH ₂ O	1.313
16	CH ₃	1.002
17	CH ₂	0.980
18	CH	0.661
19	N ₂	1.111

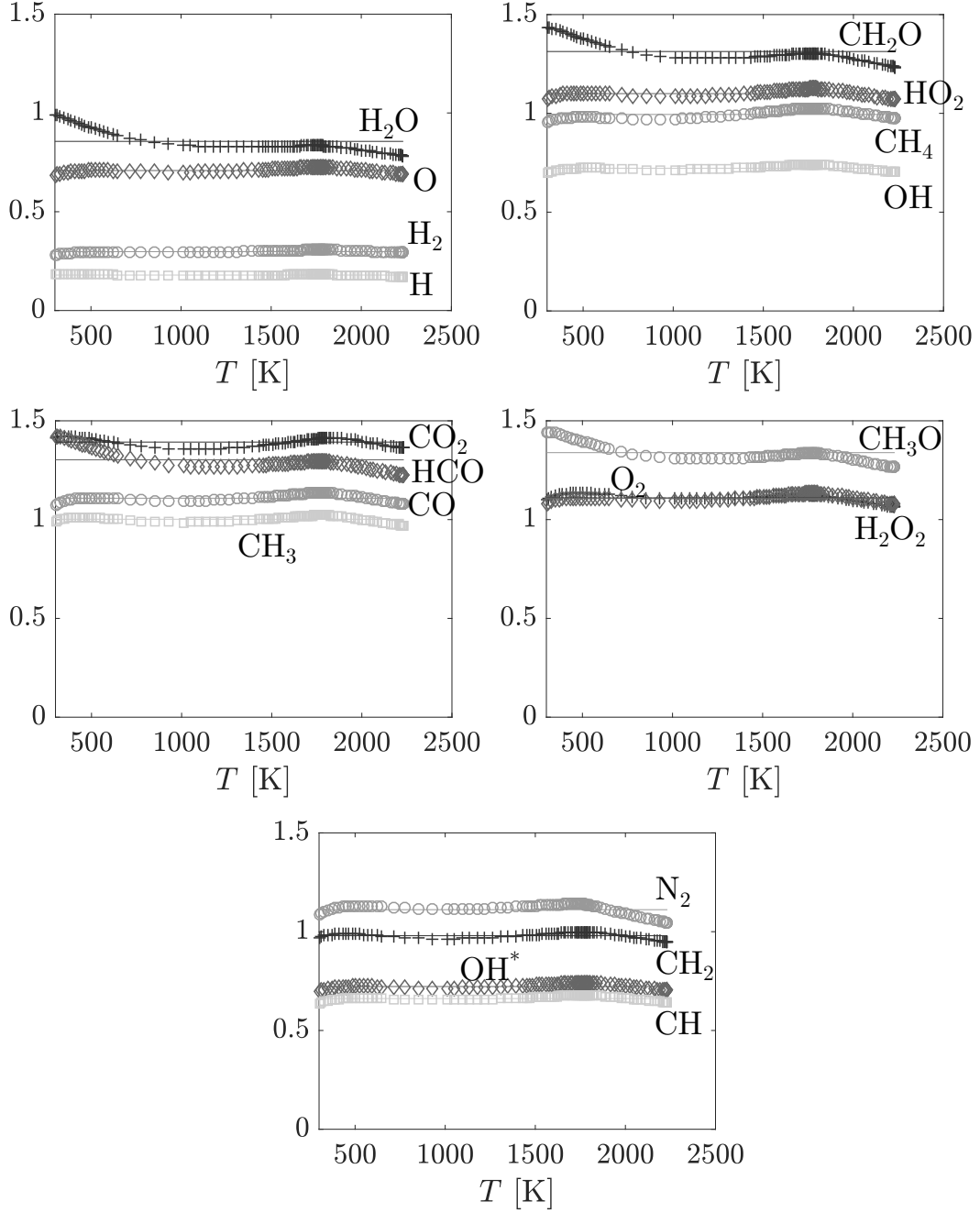


Fig. B.1 Lewis numbers in function of temperature for the species of the MS-58 mechanism.

Description of the Chemical Mechanism

In Table B.2, the third body efficiencies are: for M_1 , $H_2O=18.6$, $CO_2=4.2$, $H_2=2.86$, $CO = 2.11$, $N_2=1.26$, for all other species: 1.0; for M_2 , $H_2O=5.0$, for all other species: 1.0; for M_3 , $H_2=1.00$, $H_2O = 6.50$, $O_2 = 0.40$, $N_2 = 0.40$, for all other species: 1.0; for M_4 $CH_4=6.5$, $H_2O=6.5$, $CO_2=1.5$, $H_2 = 1.0$, $CO=0.75$, $O_2=0.4$ and $N_2=0.4$. For all other species: 1.0. Fall-off coefficient $k_{\text{fall}} = 0.0063 \exp(-18000/(RT))$.

Table B.2 Methane-air combustion mechanism used with OH^* chemistry. Rate coefficients are in the form $k = AT^n \exp(-E/(RT))$, in moles, cc and cal. units. SMOOKE, KEE58 and KATHROTIA in the table denote the reactions from respectively Smooke & Giovangigli [1991], Bilger et al. [1990] and Kathrotia et al. [2012].

	REACTION	A	n	E	Source
1	$CH_4(+M_4) \rightarrow CH_3 + H(+M_4)$	6.30E+14	0.000	104000.0	SMOOKE
2	$CH_3 + H(+M_4) \rightarrow CH_4(+M_4)$	5.20E+12	0.000	-1310.0	SMOOKE
3	$CH_4 + H \rightarrow CH_3 + H_2$	2.20E+04	3.000	8750.0	SMOOKE
4	$CH_3 + H_2 \rightarrow CH_4 + H$	9.57E+02	3.000	8750.0	SMOOKE
5	$CH_4 + OH \rightarrow CH_3 + H_2O$	1.60E+06	2.100	2460.0	SMOOKE
6	$CH_3 + H_2O \rightarrow CH_4 + OH$	3.02E+05	2.100	17422.0	SMOOKE
7	$CH_3 + O \rightarrow CH_2O + H$	6.80E+13	0.000	0.0	SMOOKE
8	$CH_2O + H \rightarrow HCO + H_2$	2.50E+13	0.000	3991.0	SMOOKE
9	$CH_2O + OH \rightarrow HCO + H_2O$	3.00E+13	0.000	1195.0	SMOOKE
10	$HCO + H \rightarrow CO + H_2$	4.00E+13	0.000	0.0	SMOOKE
11	$HCO + M \rightarrow CO + H + M$	1.60E+14	0.000	14700.0	SMOOKE
12	$CH_3 + O_2 \rightarrow CH_3O + O$	7.00E+12	0.000	25652.0	SMOOKE
13	$CH_3O + H \rightarrow CH_2O + H_2$	2.00E+13	0.000	0.0	SMOOKE
14	$CH_3O + M \rightarrow CH_2O + H + M$	2.40E+13	0.000	28812.0	SMOOKE
15	$H + O_2 \leftrightarrow OH + O$	5.13E+16	-0.816	16507.	KEE58
16	$O + H_2 \leftrightarrow OH + H$	1.80E+10	1.000	8826.	KEE58
17	$OH + H_2 \leftrightarrow H_2O + H$	1.17E+09	1.300	3626.	KEE58
18	$2OH \leftrightarrow O + H_2O$	6.00E+08	1.300	0.	KEE58
19	$H + O_2 + M_1 \leftrightarrow HO_2 + M_1$	3.61E+17	-0.720	0.	KEE58
20	$H + HO_2 \leftrightarrow 2OH$	1.40E+14	0.000	1073.	KEE58
21	$H + HO_2 \leftrightarrow H_2 + O_2$	1.25E+13	0.000	0.	KEE58
22	$OH + HO_2 \leftrightarrow H_2O + O_2$	7.50E+12	0.000	0.	KEE58
23	$CO + OH \leftrightarrow CO_2 + H$	1.51E+07	1.300	-758.	KEE58
24	$CH_3 + OH \leftrightarrow CH_2 + H_2O$	1.50E+13	0.000	5000.	KEE58

25	$\text{CH}_3 + \text{H} \leftrightarrow \text{CH}_2 + \text{H}_2$	9.00E+13	0.000	15100.	KEE58
26	$\text{CH}_2 + \text{H} \leftrightarrow \text{CH} + \text{H}_2$	1.40E+19	-2.000	0.	KEE58
27	$\text{CH}_2 + \text{OH} \leftrightarrow \text{CH}_2\text{O} + \text{H}$	2.50E+13	0.000	0.	KEE58
28	$\text{CH}_2 + \text{OH} \leftrightarrow \text{CH} + \text{H}_2\text{O}$	4.50E+13	0.000	3000.	KEE58
29	$\text{CH} + \text{O}_2 \leftrightarrow \text{HCO} + \text{O}$	3.30E+13	0.000	0.	KEE58
30	$\text{CH} + \text{O} \leftrightarrow \text{CO} + \text{H}$	5.70E+13	0.000	0.	KEE58
31	$\text{CH} + \text{OH} \leftrightarrow \text{HCO} + \text{H}$	3.00E+13	0.000	0.	KEE58
32	$\text{CH} + \text{CO}_2 \leftrightarrow \text{HCO} + \text{CO}$	3.40E+12	0.000	690.	KEE58
33	$\text{CH}_2 + \text{CO}_2 \leftrightarrow \text{CH}_2\text{O} + \text{CO}$	1.10E+11	0.000	1000.	KEE58
34	$\text{CH}_2 + \text{O} \leftrightarrow \text{CO} + \text{H} + \text{H}$	3.00E+13	0.000	0.	KEE58
35	$\text{CH}_2 + \text{O} \leftrightarrow \text{CO} + \text{H}_2$	5.00E+13	0.000	0.	KEE58
36	$\text{CH}_2 + \text{O}_2 \leftrightarrow \text{CO}_2 + \text{H} + \text{H}$	1.60E+12	0.000	1000.	KEE58
37	$\text{CH}_2 + \text{O}_2 \leftrightarrow \text{CH}_2\text{O} + \text{O}$	5.00E+13	0.000	9000.	KEE58
38	$\text{CH}_2 + \text{O}_2 \leftrightarrow \text{CO}_2 + \text{H}_2$	6.90E+11	0.000	500.	KEE58
39	$\text{CH}_2 + \text{O}_2 \leftrightarrow \text{CO} + \text{H}_2\text{O}$	1.90E+10	0.000	-1000.	KEE58
40	$\text{CH}_2 + \text{O}_2 \leftrightarrow \text{CO} + \text{OH} + \text{H}$	8.60E+10	0.000	-500.	KEE58
41	$\text{CH}_2 + \text{O}_2 \leftrightarrow \text{HCO} + \text{OH}$	4.30E+10	0.000	-500.	KEE58
42	$\text{HO}_2 + \text{HO}_2 \leftrightarrow \text{H}_2\text{O}_2 + \text{O}_2$	2.00E+12	0.000	0.	KEE58
43	$\text{H}_2\text{O}_2 + \text{M} \leftrightarrow \text{OH} + \text{OH} + \text{M}$	1.30E+17	0.000	45500.	KEE58
44	$\text{H}_2\text{O}_2 + \text{OH} \leftrightarrow \text{H}_2\text{O} + \text{HO}_2$	1.00E+13	0.000	1800.	KEE58
45	$\text{H} + \text{OH} + \text{M}_2 \leftrightarrow \text{H}_2\text{O} + \text{M}_2$	1.60E+22	-2.000	0.	KEE58
46	$\text{H} + \text{H} + \text{M} \leftrightarrow \text{H}_2 + \text{M}$	1.00E+18	-1.000	0.	KEE58
47	$\text{H} + \text{O} + \text{M}_3 \leftrightarrow \text{M}_3 + \text{OH}^*$	1.50E+13	0.000	5975.0	KATHROTIA
48	$\text{CH} + \text{O}_2 \leftrightarrow \text{CO} + \text{OH}^*$	1.80E+11	0.000	0.0	KATHROTIA
49	$\text{OH}^* + \text{H}_2\text{O} \leftrightarrow \text{OH} + \text{H}_2\text{O}$	5.93E+12	0.500	-860.0	KATHROTIA
50	$\text{OH}^* + \text{H}_2 \leftrightarrow \text{OH} + \text{H}_2$	2.95E+12	0.500	-444.0	KATHROTIA
51	$\text{OH}^* + \text{N}_2 \leftrightarrow \text{OH} + \text{N}_2$	1.08E+11	0.500	-1242.0	KATHROTIA
52	$\text{OH}^* + \text{OH} \leftrightarrow \text{OH} + \text{OH}$	6.01E+12	0.500	-764.0	KATHROTIA
53	$\text{OH}^* + \text{H} \leftrightarrow \text{OH} + \text{H}$	1.31E+12	0.500	-167.0	KATHROTIA
54	$\text{OH}^* \leftrightarrow \text{OH}$	1.45E+06	0.000	0.0	KATHROTIA
55	$\text{OH}^* + \text{O}_2 \leftrightarrow \text{OH} + \text{O}_2$	2.10E+12	0.500	-478.0	KATHROTIA
56	$\text{OH}^* + \text{CO}_2 \leftrightarrow \text{OH} + \text{CO}_2$	2.75E+12	0.500	-968.0	KATHROTIA
57	$\text{OH}^* + \text{CO} \leftrightarrow \text{OH} + \text{CO}$	3.23E+12	0.500	-787.0	KATHROTIA
58	$\text{OH}^* + \text{CH}_4 \leftrightarrow \text{OH} + \text{CH}_4$	3.36E+12	0.500	-635.0	KATHROTIA

Description of the Chemical Mechanism

The sensitivity of the ignition delay time to the various chemical steps has been assessed and is shown in Fig. B.2. This analysis has been performed for the mixture of cases AZ1 and AZ2 (see Table 2.1) for a mixture with an equivalence ratio of $\phi = 0.8$ (which is the mean equivalence ratio for those cases). This is done using a 0D adiabatic homogeneous reactor with CANTERA. The mixture for case BZ1 yields similar results. This figure highlights the importance of reactions involving the radicals, H, O, OH and CH_2O on the ignition of MILD combustion mixture.

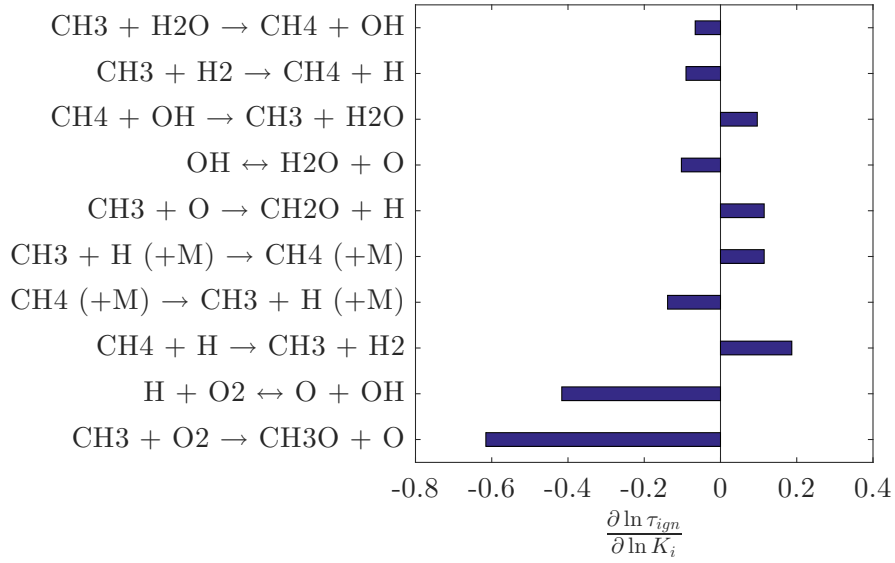


Fig. B.2 Sensitivity of the autoignition delay time to the 10 most important reactions in the MS-58 mechanism.

Appendix C

List of Publications

The results produced from this thesis work have been published, submitted, or are under preparation for publication, in the following:

Journals:

1. N.A.K. Doan, N. Swaminathan & Y. Minamoto. *DNS of MILD combustion with mixture fraction variations*. Combustion and Flame (189), 173-189 (2018).
2. N.A.K. Doan, N. Swaminathan & N. Chakraborty, *Multiscale Analysis of Flame-Turbulence Interaction in Premixed Flames*. Proceedings of the Combustion Institute (36), 1929-1935 (2017).
3. N.A.K. Doan, N. Swaminathan, P. A. Davidson & M. Tanahashi, *Scale-locality of the energy cascade using real space quantities*. Physical Review Fluids (3), 084601.
4. N.A.K. Doan & N. Swaminathan, *Role of radicals on MILD combustion inception*. Proceedings of the Combustion Institute (available online).
5. N.A.K. Doan & N. Swaminathan, *Autoignition and flame propagation behaviours in non-premixed MILD combustion*. Combustion and Flame (submitted Jun. 2018).
6. N.A.K. Doan & N. Swaminathan, *Analysis of Markers for Combustion Mode and Heat Release in MILD Combustion Using DNS Data*. Combustion Science and Technology (submitted Sep. 2018).

Conferences:

1. N.A.K. Doan & N. Swaminathan, *Role of radicals on MILD combustion inception*. 37th International Symposium on Combustion, Dublin, Ireland, 2018.
2. N.A.K. Doan & N. Swaminathan, *Autoignition and Flame Propagation in MILD Combustion*. 6th International Education Forum on Environment and Energy Science, Tenerife, Spain, 2017.
3. N.A.K. Doan, Y. Minamoto & N. Swaminathan, *Modes of Combustion and Reaction Zones Morphology in MILD Combustion*. 10th International Mediterranean Combustion Symposium, Naples, Italy, 2017.
4. N.A.K. Doan, N. Swaminathan & Y. Minamoto, *DNS of Partially Premixed MILD Combustion*. 16th International Conference on Numerical Combustion, Orlando, USA, 2017.
5. N.A.K. Doan, N. Swaminathan & Y. Minamoto, *DNS of MILD Combustion with Inhomogeneous Fuel Distribution*. 5th International Education Forum on Environment and Energy Science, San Diego, USA, 2016.
6. N.A.K. Doan, N. Swaminathan & N. Chakraborty, *Multiscale Analysis of Flame-Turbulence Interaction in Premixed Flames*. 36th International Symposium on Combustion, Seoul, South Korea, 2016.
7. N.A.K. Doan & N. Swaminathan, *DNS of Partially Premixed MILD Combustion: Preliminary Investigations*. Joint Meeting of the British-Spanish-Portuguese Sections of the Combustion Institute, Cambridge, UK, 2016.
8. N.A.K. Doan & N. Swaminathan, *Multiscale Analysis in Turbulence and Premixed Flames*. 4th International Education Forum on Environment and Energy Science, Maui, USA, 2015.